Numerical Investigations of Air Flow and Heat Transfer in Axial Flux Permanent Magnet Electrical Machines

AIROLDI, GIOVANNI

How to cite:

AIROLDI, GIOVANNI (2010) *Numerical Investigations of Air Flow and Heat Transfer in Axial Flux Permanent Magnet Electrical Machines*, Durham theses, Durham University. Available at Durham E-Theses Online: http://etheses.dur.ac.uk/264/

Numerical Investigations of Air Flow and Heat Transfer in Axial Flux Permanent Magnet Electrical Machines

Giovanni Airoldi

A thesis presented for the degree of

Doctor of Philosophy

School of Engineering and Computing Sciences

University of Durham

England

March 2010

Numerical Investigations of Air Flow and Heat Transfer in Axial Flux Permanent Magnet Electrical Machines

Giovanni Airoldi

Submitted for the degree of Doctor of Philosophy

March 2010

Abstract

In this study an investigation of heat transfer in air cooled Axial Flux Permanent Magnet (AFPM) electrical machines is carried out. Efficiency of electrical machines is strongly influenced by an effective cooling which is provided by forced convection: air enters the generator through the opening in the machine enclosure and leaves it radially, as it is forced out by the rotating discs. The main goal is the enhancement of the heat transfer from the stator where heat is generated in the copper windings. On the other hand the heat transfer to the rotor needs to be minimised in order to keep the magnets' temperature as low as possible. The cooling can be improved by acting on design parameters, such as the distance between the stator and the rotors (commonly named running clearance), the magnet depth, and by acting on operational parameters, such as the rotational speed. The investigation is carried out by using Computational Fluid Dynamics (CFD) software to model air flow and heat transfer inside the AFPM machines. The experimental validation of the numerical models confirmed the capability of the CFD software in predicting the air mass flow rate and the heat transfer coefficient in the AFPM machines. The thesis describes the effects of the above mentioned parameters on target quantities, such as the heat transfer coefficients on the generator surfaces, the air mass flow rate through the machine, and the resistive torque. General correlations in non-dimensional form are obtained for the calculation of the heat transfer on the generator surfaces in the AFPM machines as a function of the above parameters. General correlations have also been obtained for the calculations of the non-dimensional air mass flow rate through the machine and for the non-dimensional resistive torque.

It was found that the corresponding relationships between the peripheral Reynolds number and local Nusselt numbers on the generator surfaces and the non-dimensional mass flow rate are linear. However, the dependency of Nusselt number on the non dimensional clearance and the magnet depth is non-linear.

For the investigated range of the parameters the following was established:

- an increase in the peripheral Reynolds number results in higher Nusselt number on both the rotating and stationary surfaces of machines;
- an increase in the running clearance results in the reduction of the Nusselt number on the machine surfaces;
- the magnetic segments installed on the surface of the flat rotor act as blades of a radial compressor increasing the air mass flow rate and the corresponding Nusselt number on the stator surface, however for non-dimensional magnet depths beyond 7.3×10^{-2} no appreciable improvements were observed.

The combination of the non-dimensional running clearance equal to 9×10^{-3} and the non-dimensional magnet depth equal to 7.3×10^{-2} was found to be the one which provides the maximum heat transfer from the stator. This piece of information can be used for improving the cooling of AFPM electrical machines without increasing the windage losses and contribute in this way to the enhancement of the overall efficiency of this type of machines. Data obtained from these investigations can be applied in the design stage of permanent magnet generators for enhancing their performance.

Declaration

The work in this thesis is based on research carried out at the Energy Group, in the School of Engineering and Computing Sciences, at Durham University, England. No part of this thesis has been submitted elsewhere for any other degree or qualification and it is all my own work unless referenced to the contrary in the text.

Acknowledgements

I would like to thank my supervisors, Dr. Khamid Mahkamov and Dr. Grant Laidlaw Ingram, for their enthusiastic guidance during this project. I am also grateful to the other lecturers who, with their invaluable discussions, have contributed to this PhD study at Durham University: Dr. Jim Bumby, Dr. Robert Dominy and Prof. Li He and the engineers at Cummins Generators Technologies: Dr. Neill Brown and Dr. Salem Mebarki. Dr. Martin Shanel, my industrial supervisor, deserves a special thanks for his recommendations and for sharing his expertise in the use of CFD software. I am particularly grateful to Chin Hong Lim, who provided the experimental data necessary for the validation of the CFD results, this is deeply appreciated. Dr. Slim Henk, responsible of the University computing cluster, has always been very supportive and contributed to providing an excellent computational facility. Finally, I would like to thank EPSRC and Cummins Generators Technologies for providing the necessary funding for the project.

Contents

List of Figures

List of Tables

Nomenclature and Symbols

AFPM Axial flux permanent magnet

c Running clearance

C Runing clearance main effect

c_{back} Back running clearance

c_{front} Front running clearance

c^* Non-dimensional running clearance

CFD Computational fluid dynamics

D Inlet diameter

e Heating mat's thickness

EWT Enhanced wall treatment

FDM Finite difference method

FEM Finite elements method

FVM Finite volume method

g Acceleration due to gravity

G Non-dimensional clearance

Gr_L Grashoff number

$h(r)$ Local (radial) heat transfer coefficient

k_{air} Air thermal conductivity

i Internal energy

I Current

L Length from the leading edge

LPM Lumped parameter model

m Magnet depth

M Magnet depth main effect

m^* Non-dimensional magnet depth

$\dot{m}$ Mass flow rate

$\dot{m}^*$ Non-dimensional mass flow rate

N-S Navier-Stokes

Nu Nusselt number

P Pressure

Pr Prandtl number

q Heat flux

r Radial coordinate

r^* Non-dimensional radial coordinate

R Electrical resistance

RANS Reynolds averaged Navier Stokes equations

Re Reynolds number

Re_{out} Peripheral Reynolds number

RNG Re-normalisation group

R_{out} Rotor outer radius

R_{st} Stator outer radius

R_{st_in} Stator inlet radius

R_{in} Inlet radius

s Rotational speed

S Rotational speed main effect

SST Shear stress transport

t Time

T Torque

T^* Non-dimensional torque

T_{mid} Temperature in the middle of the clearance

T_w Wall temperature

T_∞ Free stream temperature

u Velocity component along the x coordinate

u_∞ Free stream velocity

v Velocity component along the y coordinate

w Velocity component along the z coordinate

α Angular coordinate

β Coefficient of volumetric thermal expansion

ϵ Turbulent dissipation rate

κ Turbulent kinetic energy

μ Air dynamic viscosity

ν Air kinematic viscosity

ρ Air density

ω Specific dissipation

$\mathit{\Omega}$ Rotational speed

Chapter 1

Introduction

1.1 Axial Flux Permanent Magnet machines

Axial flux permanent magnet (AFPM) electrical machines are generators or motors in which the magnetic field in the air gap is parallel to the axis of rotation.

When they are used as generators, a mechanical torque is supplied to the shaft, and the machine transforms it into electrical power. In the second case electrical power is provided and the machine produces a mechanical power at the shaft.

AFPM machines are particularly suitable in applications where a high torque at low rotational speeds is required. They are also very attractive for applications where a limited axial overall dimension is desirable, and where a large diameter is not detrimental for the particular installation.

Due to its compactness and high efficiency, this type of machine has recently been the object of extensive research in academia and in the electrical machines industry.

The development of rare earth magnetic materials such as samarium cobalt and neodyum-iron-boron and the recent reduction in their price has made possible the construction of high torque permanent magnet machines.

The aim of this work was to carry out a numerical investigation in order to predict the flow and heat transfer occurring inside AFPM machines. The effect of variation of geometric parameters (the clearance between rotor and stator, the depth of the magnets and rotational speed) on the flow and heat transfer has been investigated and correlations have been obtained which relate these parameters to the heat transfer coefficient on the machine surfaces. Correlations have also been found for the cooling air mass flow rate.

In this chapter a concise overview of the layouts of AFPM machines is given, then the scope and the complete structure of the thesis are described.

Examples of utilisation and research on this kind of machine include electric and hybrid vehicles [1–3], internal combustion engine generators (gen-sets), micro-turbine generators for portable electronic devices [4, 5], wind turbines [6], energy storage flywheels [7], hard drives and pumps [8].

The power rating ranges from a few watts for hard disk drives to several hundreds of kilowatts for AFPM machines coupled to internal combustion engines. A number of configurations is available [9, 10]. The generator could be single or double sided: in the first case one rotor carrying the magnets would be facing the stator as shown in Fig. 1.1; in the second case the stator would be enclosed between two rotors as in Fig. 1.2 or the rotor could be enclosed between two stators as in Fig. 1.3.

AFPM machines can be designed in multi-stage configurations to obtain the desired power or torque (Fig. 1.4). Although a high number of stages would lead to a large axial overall dimension which would partially defeat the purpose of having an AFPM machine which has compactness as its main feature.

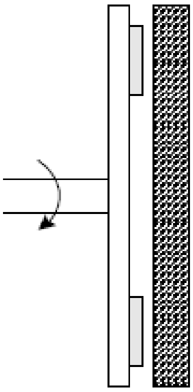

Figure 1.1: Single sided generator

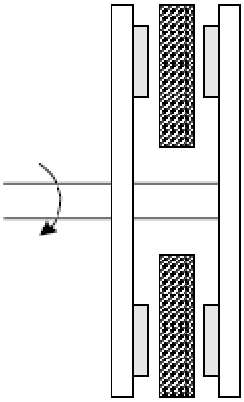

Figure 1.2: Double rotor single stator

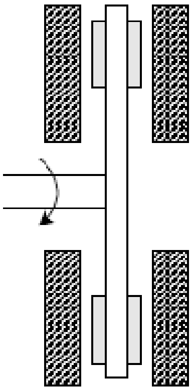

Figure 1.3: Single rotor double stator

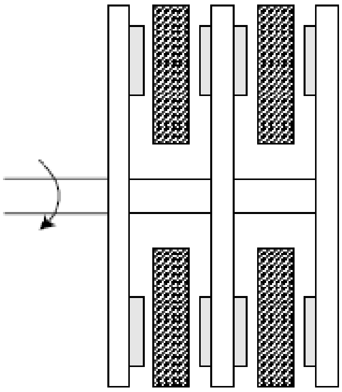

Figure 1.4: Double stage

In an AFPM machine the stator could have an iron core or could be coreless. For a given number of magnets as in a coreless design, the presence of the iron core increases the magnetic flux and therefore the specific power of an electrical machine. On the other hand, a coreless machine would not have the iron losses, and it would have no attraction between the rotor and the stator.

In the case of an iron core stator, a distinction can be made between a slotted and a slotless core. A slotted stator core features recesses in order to house the copper windings. If no recesses are present then the core is called slotless and the windings protrude from the core surface. On slotless stators the gaps between the windings are usually filled with plastic inserts to reduce the windage losses.

The design considered in this thesis is a double sided machine with a slotless stator which consists of an internal stator enclosed between two rotating discs (Fig. 1.5).

The rate of change of the flux density of the magnetic field generated by the rotating magnets induces a current inside the stator coils and consequently heat. The latter is generated according to the Joule law. Fig. 1.6 shows the windings current and magnetic field orientation in a circumferential section of the generator.

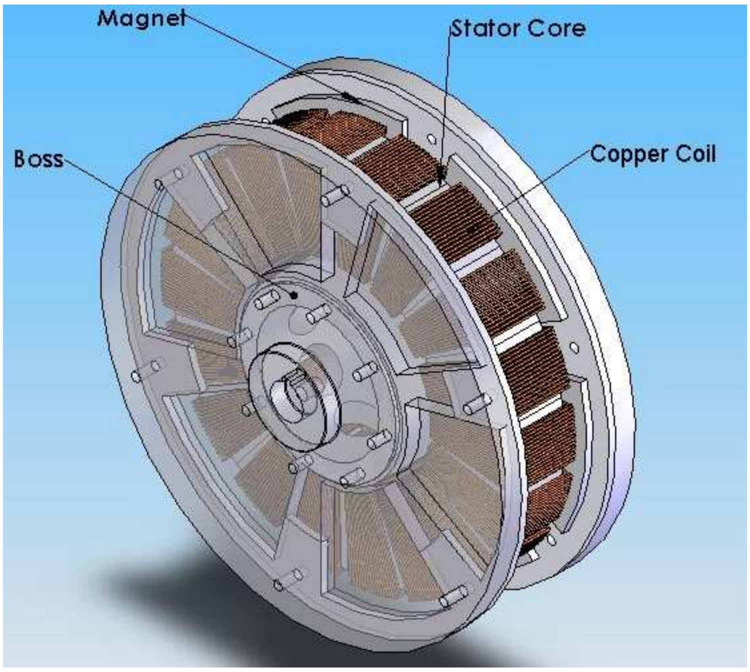

Figure 1.5: Axial Flux Permanent Magnet machine

The heat generated in an electrical machine is dissipated in three main regions:

- In the windings, where the current and the copper resistance cause the Joule losses equal to IR^2.

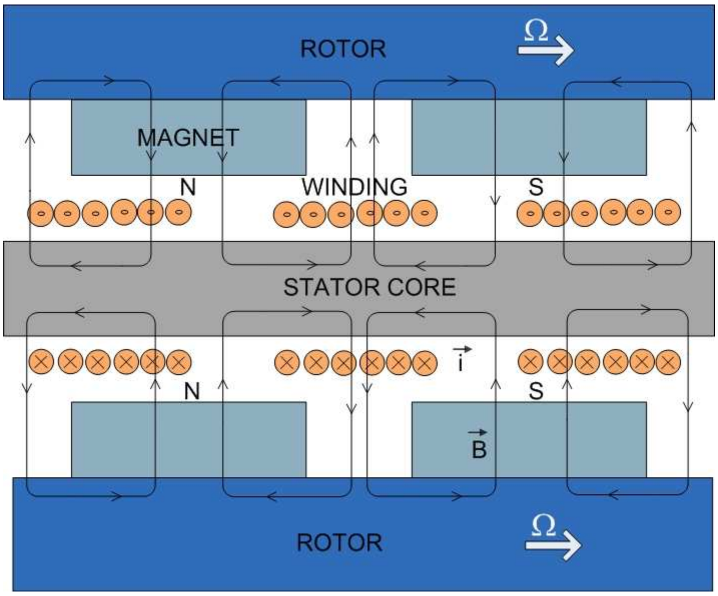

Figure 1.6: Generator's circumferential section: magnetic field and stator currents

- In the laminated core, where the variation of the magnetic field causes eddy currents and therefore iron losses.

- In the bearings, where the mechanical friction results in heat generation.

The heat dissipated in the stator coils causes the stator temperature to rise and heat is also transmitted to the other generator components, such as the magnets and the rotating discs, by means of conduction and convection. Due to the relatively low temperature differences involved radiation can be neglected. High temperatures are detrimental for the high performance operation of electrical machines for the following reasons:

- the winding resistance is proportional to the temperature and a higher resistance causes higher thermal losses;

- the winding insulations would be damaged at high temperatures;

- the magnets would be partially demagnetised when the temperature exceeds a certain limit.

Cooling needs to be provided to maintain the temperature of the generator components below an acceptable maximum level. AFPM machines can be water cooled (Fig. 1.7) or air cooled (Fig. 1.8). Water cooling is generally used when a water cooling system is already available, which is the case of AFPM generators coupled with internal combustion engines. This method of cooling, even if it requires more complex equipment, is more efficient than the air cooling due to the high heat transfer rate to water. Air cooling has the advantage of providing a simpler way of cooling.

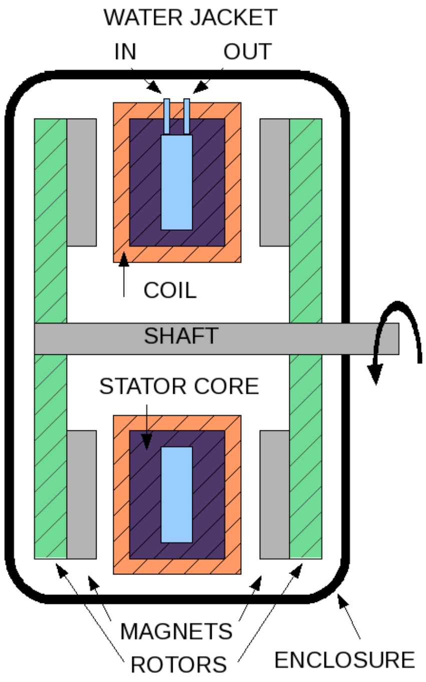

Figure 1.7: Radial section of an AFPM water cooled generator

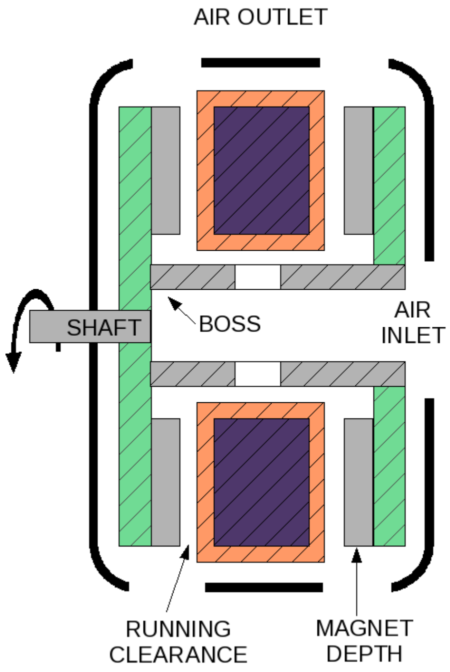

Figure 1.8: Radial section of an AFPM air cooled generator

1.2 Scope of the work

Thermal models for conventional radial flux machines are well established. This is not the case for AFPM machines due to their relative novelty.

So far the research on these machines has concentrated on the electro-mechanical design [11–16].

The research presented in this thesis is part of a larger project being carried out at Durham University and sponsored by Cummins Generators Technologies and EPSRC which aims to build a Thermal Lumped Parameter Model (LPM) to investigate the temperature field in AFPM machines. The whole project is subdivided into three sub-projects:

- Development of a Thermal Lumped Parameter Model (LPM);
- Computational Fluid Dynamics (CFD) study;
- Experimental work on a scaled up version of a generator to validate both the CFD and the LPM results.

The first and the last part of the project are the object of Mr. Chin Hong Lim's PhD.

This thesis presents the work on CFD simulations which has been carried out with two purposes in mind. Firstly, the heat transfer coefficients obtained have been used as an input data for the LPM. Secondly, the detailed effects of a number of running clearances, magnet depths and rotational speeds on the heat transfer and air flow through the machine have been studied.

The CFD study has been completed using the commercial software package Fluent.

1.3 Thesis structure

Computational Fluid Dynamics (CFD) is the main tool used for the investigational object of this thesis. The equations involved in the CFD software and the methods used to solve them are described in chapter 2.

In chapter 3 a review of published literature on thermal models (Thermal networks and CFD models) of electrical machines is presented. Subsequently, available studies on simplified systems, consisting of a rotating disc facing a stator, which have similar flow patterns as in an AFPM machine are presented. A survey of the current literature highlighted the lack of studies and data for systems similar to AFPM machines. Very few studies considered the heat transfer from the stator, and no studies were found for the case of an heated stator facing a slotted rotor which is the object of this thesis.

In chapter 4 validation of the CFD is presented against experimental results obtained from three test rigs. The validation procedure has been carried out, progressively adding more complexity to the rigs:

- Initially, a rig consisting of a flat rotor facing a heated stator was built and a 2D axisymmetric simulation was carried out using Fluent. Throughout this thesis this model will be called the *flat rotor rig*. A mesh dependency study was performed on this model to find the minimum necessary number of elements to obtain a mesh independent solution.

- On the previously described flat rotor, segments were installed to investigate the effect of the magnets on the flow and on the stator heat transfer coefficient; experiment and CFD numerical results have been compared. This model has been named the *magnet rig*. For this test rig the heat transfer coefficient has been obtained in two ways: one includes in the computational mesh the generator's solid components, the other consists of a mesh in which only the air inside the generator has been modelled.

- Finally the CFD model of the 1.5kW AFPM machine built at Durham University was created and simulations performed in Fluent. This has been called the *Durham generator*.

chapter 5 describes the large-scale low-speed test rig model of an AFPM electrical machine built to validate the CFD predicted heat transfer coefficients. The detailed experimental measurements of the heat transfer coefficient in the large-scale low-speed test rig are compared to the results of its CFD model.

The effect of variation of the generator geometrical parameters, such as the running clearance, the magnet depth, and the rotational speed on the heat transfer coefficients is analysed in two chapters.

Initially, a factorial study is presented in chapter 6. Here the parameters under consideration can only have two values: 'high' and 'low'. The main effects and the interdependences of the geometrical parameters on the heat transfer coefficient are discussed. The mean least squares method has been used to find linear correlations to calculate the value of the heat transfer coefficient on the stator, on the rotor, for the mass flow rate through the system and for the resisting windage torque.

In chapter 7 the above parameters have been varied within the range previously defined in chapter 6 and higher order correlations have been found to relate the heat transfer coefficient and the other target quantities to the design (running clearance and magnet depth) and operational (rotational speed) parameters.

Chapter 2

Computational Fluid Dynamics

Computational Fluid Dynamics is the study of fluids mechanics and heat transfer by means of numerical methods. The flow and heat transfer phenomena inside AFPM machines can be described by a set of governing equations: the continuity, the momentum (Navier-Stokes or N-S) and the energy conservation equations. The solution for the time averaged quantities is found by using Computational Fluid Dynamics (CFD) software. In this chapter a general description of Computational Fluid Dynamics is presented, then the equations and the solution methods used in the commercial software Fluent, deployed in the thesis, will be discussed. The standard procedure for a CFD study can be divided into three main parts: pre-processing, solution and post-processing. During the pre-processing procedure the domain is created and the geometry divided into sub-regions which are then meshed to create the control volumes. Each control volume is defined by the bounding nodes (eight for hexahedral structured elements, four for tetrahedral unstructured elements). The mesh, which contains the information about the geometry (volumes, faces, edges and nodes coordinates) is then read into the solver. In the solver the fluid properties, the boundary conditions and the type of flow, laminar or turbulent, are specified. The simulation is then started until a converged solution is reached. The obtained results can be visualised with a post-processing software generally included in the solver. Contour and vector plots, as well as animations of the calculated quantities, can be created.

2.1 Discretisation methods

As already mentioned the domain needs to be divided into cells and nodes. After the grid is generated the governing differential equations are discretised, or in other words replaced in CFD code with a set of algebraic equations. Various well established discretisation methods are used in CFD: Finite difference method (FDM), Finite element method (FEM), Finite volume method (FVM).

2.1.1 Finite difference method

This is the simplest method for discretisation. At an arbitrary point the derivative of a scalar function is substituted with a finite difference approximation. Since the FDM requires a structured grid, this method is difficult to apply to complex geometries and is more suitable to simple cases.

2.1.2 Finite element method

In the finite element method the domain is subdivided in elements. Each of these elements or cells has nodes at its vertices. The number of unknown times the total number of nodes gives the number of degrees of freedom. The solution is found for the nodal values of the unknown. Shape functions are used to link the nodal value of an unknown to its value in any point inside the element. Finite element method are not widely used in CFD because of the higher computational effort required compared to finite volume methods.

2.1.3 Finite volume method

The domain is divided in volumes and the conservation laws of relevant quantities have to be satisfied for each finite volume. The integral form of the conservation laws is discretised directly in the physical space. The possibility of using either structured or unstructured grids have made this method very attractive for implementation in commercial CFD software.

2.2 Finite volume method

As already mentioned the flow in the AFPM machines can be described by the continuity, the Navier-Stokes, and the energy equations. Once the flow is determined the energy equation is solved to calculate the thermal field. In the particular case of AFPM machines the variation of the temperature to which the fluid is subjected is relatively small, like its velocities, therefore the fluid density can be considered constant. This allowed the energy equation to be decoupled from the flow equation and to solve it based on the previously obtained flow solution. The formulation of the N-S equations for incompressible fluids has been used. The general form of the continuity and of the Navier-Stokes equations for incompressible fluids is shown in

Eq.2.1 to Eq. 2.4 as described in [17]:

$$div\mathbf{u} = 0 \tag{2.1}$$

$$\frac{\partial u}{\partial t} + div(u\mathbf{u}) = -\frac{1}{\rho}\frac{\partial p}{\partial x} + \nu div(grad(u)) \tag{2.2}$$

$$\frac{\partial v}{\partial t} + div(v\mathbf{u}) = -\frac{1}{\rho}\frac{\partial p}{\partial y} + \nu div(grad(v)) \tag{2.3}$$

$$\frac{\partial w}{\partial t} + div(w\mathbf{u}) = -\frac{1}{\rho}\frac{\partial p}{\partial z} + \nu div(grad(w)) \tag{2.4}$$

The instantaneous form of the N-S equations is computationally too intensive to be solved for practical problems due to the chaotic nature of turbulent flows. The knowledge of the effects of the time averaged flow and thermal quantities are satisfactory for an industrial study. For this purpose the N-S equations can be rewritten by substituting the instantaneous values of the flow quantities by the time averaged ones. The velocity at an arbitrary point in the domain can be decomposed into its average and fluctuating components: $U_i(t) = U_i + u'_i$ and similar decomposition can be applied to the other scalar quantities involved in the calculation: pressure and temperature. The mean value is averaged on a time interval at least as large as the slowest turbulent fluctuation.

Every term of the continuity and of the Navier-Stokes equations is averaged in time and the previous relationship between instantaneous and time averaged quantities is considered. The Reynolds averaged Navier-Stokes equations (2.5 to 2.8) are obtained as follows:

$$div\mathbf{U} = 0 \tag{2.5}$$

$$\begin{aligned}\frac{\partial U}{\partial t} + div(U\mathbf{U}) &= -\frac{1}{\rho}\frac{\partial P}{\partial x} + \nu div(grad(U)) \\ &+ \frac{1}{\rho}\left[\frac{\partial\left(-\rho\overline{u'^2}\right)}{\partial x} + \frac{\partial\left(-\rho\overline{u'v'}\right)}{\partial y} + \frac{\partial\left(-\rho\overline{u'w'}\right)}{\partial z}\right]\end{aligned} \tag{2.6}$$

$$\begin{aligned}\frac{\partial V}{\partial t} + div(V\mathbf{U}) &= -\frac{1}{\rho}\frac{\partial P}{\partial y} + \nu div(grad(V)) \\ &+ \frac{1}{\rho}\left[\frac{\partial\left(-\rho\overline{u'v'}\right)}{\partial x} + \frac{\partial\left(-\rho\overline{v'^2}\right)}{\partial y} + \frac{\partial\left(-\rho\overline{v'w'}\right)}{\partial z}\right]\end{aligned} \tag{2.7}$$

$$\begin{aligned}\frac{\partial W}{\partial t} + div(W\mathbf{U}) &= -\frac{1}{\rho}\frac{\partial P}{\partial z} + \nu div(grad(W)) \\ &+ \frac{1}{\rho}\left[\frac{\partial\left(-\rho\overline{u'w'}\right)}{\partial x} + \frac{\partial\left(-\rho\overline{v'w'}\right)}{\partial y} + \frac{\partial\left(-\rho\overline{w'^2}\right)}{\partial z}\right]\end{aligned} \tag{2.8}$$

The terms which arise from the time averaging of the time dependent velocity components are known as Reynolds stresses:

$$\begin{aligned}\tau_{xx} &= -\rho\overline{u'}^2 \qquad \tau_{yy} = -\rho\overline{v'}^2 \qquad \tau_{zz} = -\rho\overline{w'}^2 \\ \tau_{xy} &= \tau_{yx} = -\rho\overline{u'v'} \qquad \tau_{xz} = \tau_{zx} = -\rho\overline{u'w'} \qquad \tau_{yz} = \tau_{zy} = -\rho\overline{v'w'}\end{aligned} \tag{2.9}$$

2.2.1 Turbulence models

The need to model these additional terms (Reynolds stresses) arises and this is done by introducing turbulence models. Throughout this project, the $\kappa - \epsilon$ turbulence model [18] has been used for the closure of the system of equations. This turbulent model is based, as many others, on the Boussinesq assumption that the Reynolds stresses are proportional to the mean rate of deformation of the fluid element, like the viscous stresses are proportional to the instantaneous rate of deformation. The proportionality constant is the turbulent viscosity which is assumed to be isotropic (i.e. independent on the direction).

The generic Reynolds stress can be expressed through the suffix notation:

$$\tau_{ij} = -\rho\overline{u_i' u_j'} = \mu_t \left(\frac{\partial U_i}{\partial x_j} + \frac{\partial U_j}{\partial x_i} \right) - \frac{2}{3}\rho\kappa\delta_{ij} \tag{2.10}$$

where δ_{ij}= 1 if $i = j$ and $\delta_{ij} = 0$ if $i \neq j$ and $k = \frac{1}{2}(\overline{u'}^2 + \overline{v'}^2 + \overline{w'}^2)$ is the specific turbulent kinetic energy.

The Realizable $\kappa - \epsilon$ turbulence model [19] has been used in this project. This choice is based on its better performance in rotating flows with separation [20].

2.2.2 Energy equation

Due to the small temperature change and the relatively low velocities, the air has been considered to be incompressible fluid. This allows solving the energy equation independently from the oter governing equations. For the case of an incompressible fluid the derivatives of the density are zero and the internal energy i is the product of the specific heat C and the temperature T. For an incompressible fluid the energy equation can be presented as in Eq. 2.11:

$$\begin{aligned} \rho\frac{DT}{Dt} &= div\,(kgradT) + \tau_{xx}\frac{\partial u}{\partial x} + \tau_{yx}\frac{\partial u}{\partial y} + \tau_{zx}\frac{\partial u}{\partial z} + \tau_{xy}\frac{\partial v}{\partial x} \\ &+ \tau_{yy}\frac{\partial v}{\partial y} + \tau_{zy}\frac{\partial v}{\partial z} + \tau_{xz}\frac{\partial w}{\partial x} + \tau_{yz}\frac{\partial w}{\partial y} + \tau_{zz}\frac{\partial w}{\partial z} + S_i \end{aligned} \tag{2.11}$$

where the term S_i includes the body forces (centrifugal and Coriolis forces in our case).

2.2.3 Mesh

The majority of the simulations performed in this project have been based on structured grids. This allows an increase in the solution accuracy and a lowering of the number of elements.

In structured meshes, the node indexing follows the geometric position of the nodes, which leads to a faster convergence [21] and higher accuracy than in unstructured grids. The use of structured grid elements is also preferable in the viscous region of the domain [17, 21]. This is valid for the whole domain in the case of internal flows.

2.2.4 Wall treatment

Two alternative options are available in Fluent to take into account the presence of walls. The first one is the use of Wall Functions which are applied to model the fluid properties between the wall and the fully turbulent region. The second approach, named Enhanced Wall Treatment (EWT), has been chosen for this study to model the near-wall region. This model solves the RANS equations all the way to the wall throughout the viscous sub-layer: to do so the turbulence model needs to be modified to be valid in the near wall region where a new turbulent viscosity is introduced.

The whole domain is subdivided into a viscosity-affected region and a fully-turbulent region. The boundary between these two regions is defined by a Reynolds number Re_y based on the distance y between the cells centre and the wall:

$$Re_y = \frac{\rho y \sqrt{k}}{\mu} \tag{2.12}$$

where y is the normal distance between the wall and the cell centre. In the region of the domain where $Re_y > 200$ the flow is considered fully-turbulent and the $\kappa - \epsilon$ turbulence model is used. Where $Re_y < 200$ the near-wall region is considered viscosity-affected and a one equation model [22] is employed with a new turbulent viscosity. A blending function allows a smooth transition between the turbulent viscosity in the viscous sub-layer and the turbulent viscosity in the fully turbulent region. If the near-wall region's mesh is fine enough, the EWT will coincide with the two-layer zones model. In order to resolve the laminar boundary layer, and for the EWT to give accurate results, the near-wall grid point needs to be placed inside the viscous sub-layer. This is ensured if the non-dimensional distance satisfies the condition $y^+ \approx 1$ where:

$$y^+ = \frac{\rho u_\tau y}{\mu} \tag{2.13}$$

$$u_\tau = \frac{\tau_w}{\rho} \tag{2.14}$$

$$\tau_w = \mu \frac{\partial \overline{u}}{\partial y} \tag{2.15}$$

The EWT approach has a higher accuracy than the standard wall functions' technique and is more computationally expensive. As a reference for the difference in computational time required between the standard wall functions and the Enhanced

Wall Treatment methods, Rodi [23] reported the computational time required for convergence of a test case of a flow around a bluff body to be 2 hours for the first technique and 8 hours for the second one.

2.2.5 Solver: pressure based and density based

The RANS equations (Eq. 2.5 to 2.8) are strongly coupled as every velocity component appears in each of the momentum equations and in the continuity equation. Non-linear quantities are present in the momentum equations.

The simulations in this study have been completed by using a pressure-based implicit solver. In previous versions of Fluent, the pressure-based solver was referred to as 'segregated solver' and the density based was referred to as the 'coupled solver'. The pressure based scheme is more suited for low Mach numbers and incompressible flows as the pressure is not dependent on the density. However, because of incompressibility the density can not be used to calculate the pressure, as in the density based schemes. Instead, the pressure is obtained from the set of four equations consisting of the Navier-Stokes and of the continuity equation. Pressure-velocity coupling algorithms are used to derive equations for the pressure from the momentum equations and the continuity equation. Various algorithms are available in Fluent for the pressure-velocity coupled discretised equations. The most used are: SIMPLE (Semi-Implicit Method for Pressure-Linked Equations), SIMPLEC, PISO. They consist of an iterative process where i) the initial value of pressure is guessed, ii) the momentum equations are solved to obtain the velocity components, iii) the continuity equation is solved to find the correction value for the pressure,

iv) the value of pressure is updated by adding the correction value obtained from the continuity equation solution, v) a convergence check is carried out. The main difference between the pressure-velocity coupling algorithms is on the convergence speed and solution stability rather than on the actual solution accuracy.

Predicted quantities from numerical, and in particular from CFD software, need to be carefully assessed to verify their validity. As an example, a recent work [24] can be mentioned which assessed three commercial CFD packages and reported poor results on relatively simple test cases. Lacasse *et al.* [25] compared results published by various authors concerning a number of benchmark cases. Initially, they considered the length of the recirculation zone for turbulent flow over a backward facing step. Among the twelve researchers, ten used the same RANS $\kappa - \epsilon$ model. The resulting non-dimensional length varied by 50%. In a second case they examined the Nusselt number downstream of a sudden pipe expansion. The largest calculated value was five times greater than the smallest one. Two sources of error were identified: numerical errors and mathematical modelling errors. The first source is mainly related to the discretisation accuracy of the mesh, while the second source is due to the choice of modelling equations and boundary conditions. In CFD, verification and validation together constitute the procedure to check the accuracy of numerical experiments [26, 27]. The verification process consists of assessing the numerical accuracy of the solution and ensuring that it is grid independent. The validation consists of checking the adequacy of the equations which constitute the model, the accuracy of the assumptions (i.e. incompressible flow, negligible friction heating, etc.), and the accuracy of the boundary conditions. In chapter 4 and chapter 5 the following two tasks will be addressed: Verification will be performed by progressively refining a mesh and validation will be carried out by comparing experimentally measured temperatures and heat transfer coefficients with the numerical results.

Chapter 3

Literature review

A survey of the current literature on thermal modelling of electrical machines is presented in this chapter. Initially, studies on thermal networks (Lumped parameter thermal models) are described; then current literature on CFD studies of electrical machines is discussed; finally, since the flow and heat transfer occurring in AFPM machines are similar to those developed in rotor-stator systems, a survey of the available literature on these systems is presented.

The objective of this thesis is to derive correlations of the heat transfer coefficient on the stator and on the rotor of AFPM machines by means of Computational Fluid Dynamics (CFD) investigations. The mass flow rate and the resistive aerodynamic torque on the rotor are also calculated.

The survey carried out on the published literature highlighted the absence of relevant CFD studies on the flow and the heat transfer in AFPM machines. Instead, studies with the purpose of enhancing the cooling or of predicting the flow and temperatures in conventional electrical machines are widely present in the open literature. The object of those investigations were mainly induction motors, synchronous and direct current (DC) machines. The methods used for the flow and temperature prediction are either experimental or numerical. Experimental studies range from application of particle image velocimetry (PIV) to deploying Laser Doppler anemometry (LDA), whereas numerical methods include CFD, Lumped parameter thermal models (LPM), exact solution of heat transfer equations for simplified models of electric motors. CFD (Finite volume and Finite element) methods require significant computing resources but provide flexibility and a good accuracy. LPM are a fast and reasonably accurate tool to evaluate temperature levels in the design phase. The LPM method consists of dividing the machine into several relatively large elements or nodes which are then connected by corresponding thermal resistances. The thermal capacitances of these elements are concentrated in the nodes. The high speed of execution of LPM made them a widespread method used for the determination of temperatures inside electrical machines and several examples of their use have been found in the literature as shown below.

3.1 Lumped parameter thermal models

Bellettre *et al.* [28] built a lumped parameter thermal network to analyse the effectiveness of a phase change solid-liquid cooling system for a synchronous electrical machine. In their study on switched reluctance motors (SRM) [29] Rouhani *et al.* used a thermal network to find the effects of geometric parameters on the heat transfer and temperature inside the machine. However the shape of the machine they investigated is radically different to that of AFPM machines object of the present study as they are radial flux machines with the cooling provided by a medium different than air. In their paper on high torque low-speed generators for wind turbines Wu *et al.* [30] presented a lumped parameter model designed to find the temperature rise in the machine components. A simpler thermal network which has the advantage of a fast implementation is the one presented by Bumby and Martin [31]. A detailed lumped parameter model for steady and transient modelling of an induction motor is presented in the paper by Mellor *et al.* [32]. The thermal resistances for different parts of the machine are presented, together with Nusselt number correlations used in their calculation. The results from two cases (a 75kW and a 5.5kW motor) showed good agreement with experimental results. In [33] a LPM is presented for water cooled permanent magnet synchronous machines. A good agreement was found between the LPM results and those obtained using FEM simulations for the above two test cases. In both simulations the authors neglected the radiation heat transfer due to the low temperature differences between the surfaces. A description of how to build a thermal network considering all mechanisms of heat transfer (convection, conduction, radiation) is given in [9]. The thermal model developed by Mukhopadhay and Pal [34] calculates the convective heat transfer by subtracting the radiative contribution from the total heat. The model built for induction motors and validated using the experimental results from a 1.5kW motor is able to perform both transient and steady simulations.

For through-flow air cooled machines, where the heat generated is taken away by forced convection of air, in addition to the temperature prediction, there is the necessity of predicting the air flow rate. This can be done by either using CFD, by exploiting dimensional analysis and dimensional analysis of known similar machines, or by using a fluid flow model based on the application of momentum and steady flow energy equations as described in [35] and [36]. An example of LPM on an AFPM machine is presented in the paper of Belicová and Hrabovcová [37] where a coupled electro-magnetic and thermal design method is used. The motor layout differs from the one presented in this thesis as it consists of a rotor located between two slotted stators rather than a stator between two rotors. The advantage of the coupled method is that it can utilise results from one model as boundary conditions in the other. In this case the temperature obtained from the thermal network is used to calculate iteratively the temperature dependent copper resistivity and hence the thermal losses.

3.2 CFD flow and thermal modelling of electrical machines

Air flow and thermal studies have been conducted to enhance the cooling of electric motors and these considered either the internal or the external flow and heat transfer. Numerical CFD methods have been widely used to study conventional machines, such as induction motors and radial flux synchronous motors.

In the case of completely enclosed induction motors, the external flow and heat transfer from the external surface has a considerable importance in the machine cooling. The heat dissipated inside induction motors is conveyed outside through the casing and a fan mounted on the engine shaft forces the air through the fins casted over the enclosure. In [38] a study of the external flow of a closed type induction machine has been conducted and the external hot spot temperatures determined. The velocities between the fins were found to be non-uniform. This was due to the rotating flow leaving the fan, which lead to higher velocities in some inter-fin regions. A modified casing, including a cylindrical shroud conveying the flow from the fan over the first region of the fins, lead to a more homogeneous flow and temperature.

A machine with design close to that of the generator studied in this thesis was considered in the study on temperature rise inside induction motors by Huai *et al.* [39]. They performed a FEM simulation of the internal flow and experiments which were then used to develop a control algorithm to avoid thermal damage to the motor. As a result of their investigations, they found that the end winding area was the one having the highest temperatures.

The internal flow induced by a fan and the heat transfer in a high speed electric motor were also the subject of the CFD study in [40]. The results show that the temperature rise and the pressure change are such that the air density inside the machine can be considered constant. An interesting study is presented by Min-Soo Kim *et al.* [41] who studied an optimisation of the mass flow rate through a DC motor in order to improve the cooling of the stationary windings. The cooling flow is conveyed on the windings by a rotating shroud and by the magnets. The heat is dissipated from the windings and from the peripheral surface of the core. They correlated the mass flow rate with geometrical parameters through a second order polynomial response function. A combination of these parameters was found which improved the heat transfer by 24%. They found that recirculation areas on the windings surface reduced the heat transfer and that direct flow over the windings was more effective than a high flow rate. Among the $\kappa - \epsilon$ turbulence models used (Standard, RNG and Realizable) it was found that the RNG was the one providing the closest match with experimental data.

Another example of investigations where the cooling is provided by a rotating impeller mounted on the motor shaft is the paper by Li [42], where CFD simulations were used to predict the flow and suggest modifications to improve the heat transfer rate. The whole motor was modelled, including its solid components. The radiation heat transfer was neglected, due to the small temperature difference between the armature and the permanent magnet surfaces. Three computational grids were created and the mass flow rate was taken as a parameter to verify that the solution was mesh-independent. Li [42] found a linear relationship between the rotational speed and the cooling air flow rate. This is in agreement with the results obtained in this PhD study and presented in chapter 7 where both the mass flow rate and the heat transfer coefficient are shown to be linearly dependent on the rotational speed.

Several numerical studies concerning thermal modelling of permanent magnet machines are available in the literature. However, these usually consider the radial flux configuration, where the main component of the flow velocities are the axial and the tangential, rather than the radial and the tangential as in the case of axial flux machines. In their paper on Radial Flux Permanent Magnet machines, Kolondzovski *et al.* [43] show three methods for the thermal analysis of these generators. The first consists of considering the domain to be axisymmetric and in performing a finite element 2D CFD simulation of the flow and heat transfer from which the heat transfer coefficients are obtained. These heat transfer coefficients are then specified as boundary conditions in a 3D thermal model of the machine to find the temperature in the solid domain. This procedure was employed because the heat transfer coefficient and the temperatures of the flow could be considered constant in the tangential direction. However, the geometry of the domain does not seem to be axisymmetric since because of the slots, the rotor could not be produced as a solid body of revolution, therefore it seems that a 3D analysis of flow and heat transfer would be necessary. The temperatures from the 3D model were validated by comparing them to those obtained from a thermal network and found to be in good agreement.

It is often difficult to access the internal part of an electrical machine to measure the heat flux and temperatures. To overcome this problem, Huang *et al.* [44] used commercial CFD software to implement a 3D inverse method to estimate the heat flux from the rotor and the stator of a water cooled high speed motor. The method they used consists of three separate stages: solving the direct problem, considering the inverse problem and analysing the steepest descent problem. In the direct problem an arbitrary heat flux is specified, together with other known quantities on the machine surfaces. A simulation is run to find the temperature distribution. In the inverse problem the solution obtained from the direct problem is used as a boundary condition and the heat flux is the only unknown parameter. The solution of the inverse problem is found by minimising a function of the difference between the measured and CFD predicted temperature. The minimisation algorithm is the core of the steepest descent method.

CFD analysis is often employed on large scale machines in the power sector. An example is the study of Ryuichi *et al.* [45] who modelled a synchronous generator with CFD and obtained data on the mass flow rate, heat transfer coefficient on the machine surfaces and compared their predictions with experimental measurements from a test rig. The difference in the calculated and measured mass flow rate was 7%. A model representing the fluid flow and heat transfer occurring in a radial flux electrical machine was the object of the study of Boufia *et al.* [46]. They investigated an annular volume with an inner rotating cylinder. The outer cylinder could either be smooth or feature axial grooves. For the several models investigated it was found that the grooved outer cylinder (stator) carried an improvement in the heat transfer coefficient on the stationary surface. The cooling of disc brakes is a particular case where the flow structures and the heat transfer could be similar to those occurring in an AFPM generator. Tirović [47] used an experimental rig and CFD modelling to study a new layout for ventilation of railway disc brakes and related the cooling efficiency with the aerodynamic power losses caused by the cooling system. The proposed layout which featured a radial vane/pillared disc rather than the traditionally employed radial vane disc lead to power losses which were 50% of the original system's, but kept the same cooling capacity. A further interesting result from Tirović work is the linear dependency of the convective cooling (kW) on the rotational speed.

3.3 Rotor-stator systems

Rotor-stator systems consist of a rotating disc facing a stationary one. It is a simple arrangement which has been studied by a number of researchers in order to understand flow and heat transfer patterns in more complex devices. Traditionally, rotor-stator systems have been investigated to better understand the flow and the heat transfer in order to improve the cooling of gas turbines. More recently, interest in heat transfer modelling of AFPM electrical machines has further extended the amount of research conducted in this field.

3.3.1 Flow structure studies

Several geometrical layouts of rotor-stator systems can be found in the literature: the stator facing the rotor can have an axial opening to allow for the flow intake or it can be closed; the system can either be enclosed in a casing or can be open; the stator could carry a shroud on its periphery; a combination of the previous cases is also possible. The most extensive review of the available literature on rotor-stator systems with various layouts is given by Owen and Rogers in their monograph [48].

The main flow structures existing between two disks are commonly named after the two researchers who first identified them: Batchelor [49] and Stewartson [50]. In the case of a rotor facing a stator without throughflow and without shroud, Batchelor identified that there are two boundary layers: one on the rotor and one on the stator separated by a rotating core of fluid. The radial flow is concentrated on the stator (centripetal flow) and on the rotor (centrifugal flow) surfaces. The boundary layer on the stator is also called ‘Bödewadt layer’ and the one on the rotor ‘Ekmann layer’. Stewartson, for the same system, instead described a flow structure consisting of a boundary layer on the rotor where the tangential velocity is maximum (with no boundary layer on the stator). Later studies [51, 52] observed the occurrence of a rotating core for shrouded systems and the absence of the core rotation for open systems.

Daily and Nece [53] in their experimental and theoretical investigation of a totally enclosed rotor-stator system found that four different flow regimes can occur inside the clearance depending on the combination of non dimensional air gap $G = s/R_{out}$ (with s the air gap and R_{out} the outer radius) and peripheral Reynolds number Re:

1. Laminar boundary layers on both (rotor and stator) surfaces with the two BL covering the whole gap thickness (this happens for low air gap ratios).
2. For high G values there are two separated boundary layers: one on the rotor and one on the stator and they are separated by a core fluid rotating at a fraction of the rotor angular speed $\mathit{\Omega}$.
3. Equivalent to regime 1, but with turbulent boundary layers.
4. Equivalent to regime 2, but with turbulent boundary layers.

As already mentioned, the type of flow building up in a rotor-stator system depends on the presence of a shroud and on the discs' peripheral layout. This was investigated by Debuchy *et al.* [54] who studied the effect of the rotor-stator radius difference on the flow inside the air gap. They considered a system open at the periphery, but without the forced flow. They defined the ratio $\lambda = \Delta R/a$ with ΔR being the difference in the stator-rotor radius and a being the axial distance between the rotor and the stator. They related the velocity field in the vicinity of the air gap outlet (at $r/R_{out} = 1.027$) to the type of flow obtained inside the rotor stator cavity. The variation of λ mainly affected the tangential velocity v_θ. Low values of

λ corresponded to low values of the tangential velocity and vice versa. The reversed flow observed at the periphery, for low values of λ only involves the quiescent fluid on the stator side, whereas for high values of λ the fluid near both stator and rotor is affected by the re-injection. The tangential velocity which characterises the reversed flow from the rotor side causes the core rotation (or Batchelor type of flow) inside the air gap. The transition to a Batchelor flow occurs gradually: Debuchy *et al.* [54] found no evidence of a λ value at which the change in the flow pattern occurs. Instead values of $\lambda > 0.4$ do not cause a significant increase of a swirl velocity and a significant change in flow patterns inside the cavity. The study of Djaoui *et al.* [55] shows how the through-flow affects the flow pattern inside the rotor-stator cavity. A valve is used at the axial inlet to control the air inflow in the experimental apparatus. When the valve is fully closed, a rotating core of fluid is observed which separates the rotor and the stator boundary layers. Instead, with a superposed flow rate through the system a variation in the tangential velocity can be seen along the axial coordinate. The tangential velocity axial variation can be observed, especially at small radii, whereas the radial velocity variation is detected for all the radii.

Poncet *et al.* [56] carried out a numerical and an experimental work on the flow structures developing in three different layouts of a rotor-stator apparatus. They studied the totally enclosed system (without throughflow), as well as the systems with centripetal and centrifugal superimposed flows. They investigated various peripheral Reynolds numbers Re_{out} and non dimensional air gap ratios G. They found that in the totally enclosed system and in the system with the centripetal radial inflow the flow is of Batchelor type. Two boundary layers exist: one on the stator

(Bödewadt layer) and one on the rotor (Ekmann layer) which are separated by a rotating core of fluid. The radial flow only occurs in the two boundary layers and is centripetal on the stator and centrifugal on the rotor. In the case of the centrifugal superimposed flow Poncet *et al.* [56] found that at the periphery ($r/R_{out} = 0.8$) a Batchelor type flow occurs. By progressing towards the rotational axis they found that the rotating core vanished and all the flow became centrifugal along the whole axial distance (Stewartson flow). The radius at which the transition between Batchelor and Stewartson types of flow did not depend on the non-dimensional air gap G. They showed that if the through flow was weak enough then the Batchelor type flow could exist as long as the Bödewadt layer was centripetal (negative radial velocity on the stator). For higher levels of the flow rate the rotating core disappeared and the flow became of the Stewartson type. The Reynolds stress model used for the closure of the system of equations lead to a satisfactory agreement between numerical and experimental data.

3.3.2 Heat transfer studies

While considerable attention has been given to the description of the flow inside rotor-stator systems, less data concerning both numerical and experimental studies of heat transfer are available in the literature. As far as heat transfer is concerned, researchers have directed their efforts to the case of heated rotors rather than heated stators. In the two systems modelled by Poncet and Schiestel [57] turbulent flow structures and heat transfer patterns were obtained. Firstly they analysed the experimental model built by Sparrow and Goldstein [58] consisting of a stator carrying a heated shroud and a rotor subject to a centrifugal throughflow. Secondly the experiment of Djaoui *et al.* [55] was numerically modelled. The Reynolds stress model was used for the problem closure. The Nusselt number, which is the non-dimensional convective heat transfer coefficient ($Nu = hL/k$, where h is the local heat transfer coefficient, L the characteristic length, and k the air thermal conductivity), on the shroud and on the stator was calculated based on the local mean fluid temperature and the authors found a good agreement with the experimental data.

Other authors have analysed the flow patterns and the heat transfer in rotor-stator systems, however the various layouts and heat boundary conditions analysed are different from those considered in this thesis. In their heat transfer measurements on an open system without throughflow Pellé and Harmand [59] have found the influence of the peripheral Reynolds number Re_{out} and that of the non-dimensional air gap G on the rotor local Nu. Raguenet and Laroche [60] studied the rotor-stator cavity to find the respective influence of the walls on the heat exchanges. They expressed the respective influence by means of influence coefficients. The two CFD near wall modelling techniques used (wall functions and low Re formulation) lead to similar results in terms of velocity profiles. Also the wall functions method proved to provide accurate heat transfer predictions in the near wall region. In their study concerning secondary flow for cooling of gas turbines, Roy *et al.* [61] investigated the convective heat transfer from a rotor facing a stator. They suggested correlations for the local radial heat transfer coefficient and compared their experimental with the numerical results. Their study featured a flat rotor and they found that the heat transfer was influenced by both the rotational speed and the mass flow rate.

The cooling of a heated rotor facing a stator has been the subject of the work of Boutarfa and Harmand [62]. The experimental investigation involved the use of infrared thermography. The system consisted of an open system featuring a rotor facing a stator with an axial inlet. Correlations have been proposed for the rotor local Nusselt number as a function of the rotational Re and non dimensional running clearance G. Different flow patterns have been observed for various values of G. For $G = 0.01$, the flow is outward for the whole running clearance. The cooling air could enter the gap between the rotor and the stator axially through the stator opening and leave radially at the outer radius. From their experiments Boutarfa and Harmand obtained a correlation for the local Nusselt number on the rotor which depends on the local rotational Reynolds number and on the non-dimensional air gap.

The effect of a controlled impinging jet through an axial opening in the stator on the cooling of a heated rotor was studied by Pellé and Harmand [63]. Harmand *et al.* [64] considered a stator facing a heated rotor and identified the flow field through Particle Image Velocimetry (PIV). For small values of G they found Couette type of flow inside the air gap. The measured local Nusselt number on the rotor was found to be independent of the non-dimensional radial coordinate which is equivalent to a decreasing local heat transfer coefficient for an increasing radius.

In their numerical simulations of rotating cavities [65] Iacovides and Chew analysed the convective heat transfer for three different layouts of rotor-stator systems. A comparison of the turbulence models used for the closure of the RANS equations lead to the conclusion that none of the models is fully satisfactory for all the layouts. However the $\kappa - \epsilon$ model with one equation near wall treatment was the one which performed best. Yuan *et al.* [66] analysed an open rotor-stator system with no throughflow and used a 2D axysimmetric model with the commercial code Fluent to simulate their experimental apparatus. Results were obtained for various peripheral Reynolds number and various air gap distances. The Stewartson flow structure was generally observed in the cavity. The numerical simulations in general overpredicted the Nusselt number on the heated stator. From the numerical results Yuan *et al.* [66] found that the rotational Reynolds number Re_{out} had less influence the further away the rotor was from the stator. However, an excessively low clearance would have reduced the mass flow rate in the system. They concluded that an optimum distance exists at which the heat transfer is maximised. The obtained pattern of the Nusselt number varied for different rotor-stator distances. For small clearances, Nu steadily increased with the radius. For greater clearances after a peak reached for a non-dimensional radius of about 0.95, Nu started decreasing and reached a relative minimum on the stator periphery. The recirculation bubble on the stator surface at high clearances was believed to be responsible for the Nusselt number drop at the periphery. The same pattern for the Nusselt number on the stator has been found by Hill and Ball in their DNS study on counter rotating discs [67]. Both results are in agreement with the heat transfer coefficient behaviour in [68] where the maximum heat transfer coefficient was found at about $r/R_{out} = 0.85$ and dropped at the periphery. Owen and Rogers [48] report experimental measurements of the radius averaged Nusselt number Nu_{av} on the stator surface as a function of the rotational Reynolds number Re_{out} for a constant air gap ratio G. Nu_{av} increases for increasing Re_{out} up to $Re_{out} = 3 \times 10^6$ after which it levels off. The radius averaged

Nusselt number is found to be a decreasing function of the non-dimensional air gap G. A substantial challenge in the determination of the heat transfer coefficient on a surface is the measurement of the heat flux from that surface. A method consisting of the use of a Printed Circuit Board (PCB), and which does not involve a heat flux measurement is described by Astarita in [69]. The heat flux is calculated by dividing the power supplied to the PCB tracks by the surface exposed to the cooling air. A similar method was used by Howey *et al.* [70] to determine the local Nusselt number on a stationary disc. Several peripheral Reynolds numbers and non-dimensional clearances were investigated. A description of experimental methods to measure the heat flux from the stator was provided. The inlet temperature was used as a reference in the definition of the Nusselt number. A transition radius was found between the laminar and the turbulence region of the flow. An increase in Nusselt number was observed on the stator peripheral area. This was due to the ingress of cold air from the region close to the stator. This was also described in [68] where the reference temperature was taken in the middle of the clearance. In [70] the reversed flow of ambient air increases with the rotor-stator clearance. If the incoming air is at a lower temperature this reversed flow is beneficial for the stator cooling.

In [71] a review of studies available in the literature on stator-rotor systems with various configurations is presented. The effect of protruding objects from the rotor (bolts in this case) on the drag losses, on the boundary layer losses and on the pumping losses has been described.

From the survey of the available literature it appears that few studies have been carried out concerning heat transfer from a stator facing a rotor. The available research focuses in particular on systems featuring flat rotors. Studies on the effect of slots in the rotor on the flow and on the stator heat transfer (which is the subject of the present thesis) are not available in the literature.

As mentioned above, the purpose of the project which includes this PhD is to build a thermal lumped parameter model for AFPM machines. In this model the machine is subdivided into a number of sub-domains which are connected with thermal resistances. The convective heat transfer coefficients need to be provided in order to calculate the value of the thermal resistances. The published data provides correlations for the Nusselt number on the rotor surface (see [72] and [48]). However these correlations are for the Nusselt number averaged on the rotor surface area, whilst to build a lumped parameter model the value of the local radial Nusselt number is required. Furthermore, the geometries investigated in previously published works are always very different from the one in the current research. There are only few studies concerning the heat transfer from the stator. For example Owen [48] reports on a correlation for the average Nusselt number on a stationary disc facing a rotor. The most relevant findings on the heat transfer from the stator are those of Howey [70] in which a local radial Nusselt number is found on a heated stationary disc. However, the test rig was built with a flat rotor which is a considerably different setup compared to a rotor featuring segments. In this PhD, in order to calculate the local convective heat transfer coefficients on the surfaces of AFPM machines, CFD simulations have been carried out using models featuring slotted rotors and heated stators.

Chapter 4

Preliminary validation of CFD results with the small test rigs

A fundamental area of interest for the cooling of AFPM machines is the running clearance between the rotor and the stator. Published works exist on systems consisting of a stator facing a rotating disc. However, from the literature survey it has been found that whereas a considerable amount of work has been carried out on the flow developing inside rotor-stator systems, limited information is available concerning heat transfer, and in particular heat transfer from the stator. Furthermore, the available literature is relevant to systems featuring flat rotors without protruding magnets which is the main object of this study. In this chapter, the basis for studying heat transfer from the stator facing a rotor with protruding sectors is presented. The numerical results obtained have been compared with experimental data in order to validate the computational models. Three computational models with increasing complexity have been analysed and the numerical results compared with available experimental data:

- The first rig consists of a rotor-stator system with a flat rotor. This is referred to as *flat rotor rig.*
- The second rig consists of the same system, but six segments have been placed on the rotor to represent the magnets. This is referred to as *magnet rig.*
- The third model is a 1.5kW AFPM generator built at Durham University. This is referred to as *Durham generator.*

As a part of the work presented in this chapter it was necessary to establish the minimum number of cells across the running clearance which guarantees a mesh independent solution. The results from steady and unsteady simulations carried out for the magnet rig have been compared and discussed.

4.1 Flat rotor rig

4.1.1 Test rig

The flat rotor rig consists of a rotor and a stator both of 300mm diameter. The stator has an opening of 70mm diameter to allow the air inflow, its thickness is 8mm and is connected to an aluminium pipe which serves as both an inlet and a holder for the stator (Fig. 4.1 and Fig. 4.2). The stator structure is supported by adjustable stands mounted on the floor which allow the stator structure to be positioned in the axial direction so as to obtain the required axial clearance for the different test cases. The rotor is flat, without any protruding magnets and has a thickness of

10mm. The rotor is made of transparent plastic material (perspex) to allow for flow visualisation. The rotor disc is driven by a 3kW 2-pole 50Hz induction motor (Fig. 4.1). The rotor speed is controlled by a 4kW AC vector drive speed ABB inverter.

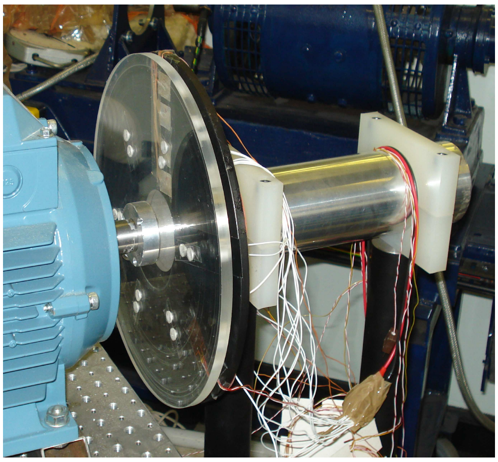

Figure 4.1: Flat rotor rig

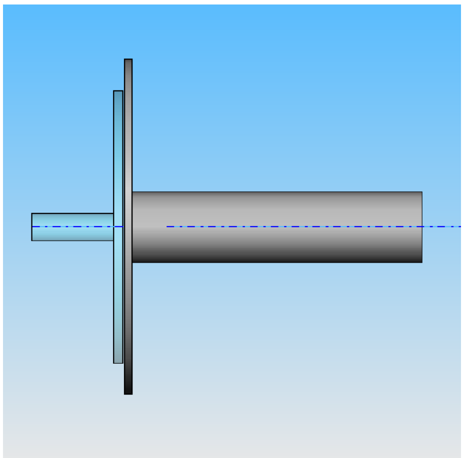

Figure 4.2: Model of flat rotor rig

4.1.2 CFD model

The above system has been modelled in Fluent. Due to the geometric symmetry a 2-dimensional axisymmetric model of the rig has been created. The mesh consists of structured quadrilateral elements. The computational domain has been extended at the inlet and at the outlet to include a part of air which is not enclosed between the two discs. This allowed the simulations to converge faster by incorporating the reversed flow occurring at the outlet boundary. The applied boundary conditions are a zero total pressure at the inlet and a zero static pressure at the outlet boundary. The rotational speed applied to the rotor is 1500rpm. Two running clearances of 2mm and 3mm have been investigated. The computational domain is shown in Fig. 4.3 where the rotor is displayed in white and the stator in blue. Simulations have been run in Fluent by using the (RANS) equations. The realizable κ-ϵ turbulent

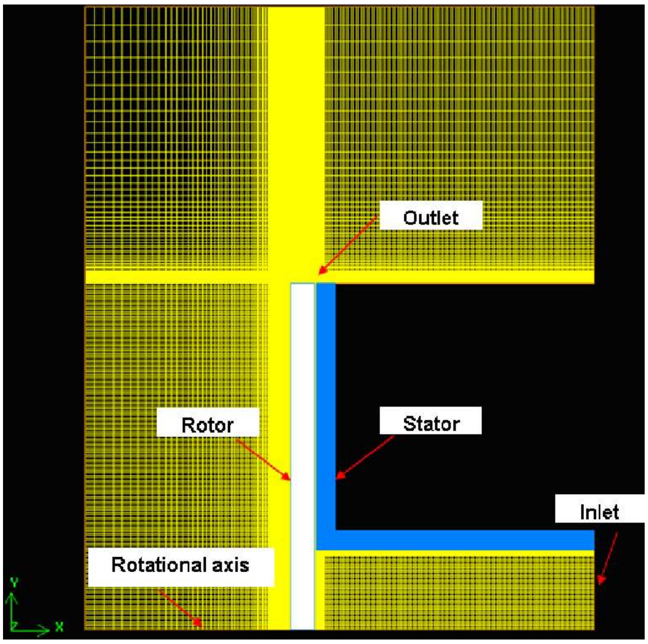

Figure 4.3: 2D axisymmetric domain

model has been used for the closure of the system of equations. The Enhanced Wall Treatment (EWT) which uses a two layer approach, has been applied in Fluent to model the near wall regions. This approach requires the non-dimensional wall distance y^+ to be ≈ 1 in the whole domain, although values of $y^+ < 5$ are considered to be acceptable. Steady state solutions have been obtained. The solutions were considered converged when the residuals dropped below 10^{-3} and when the mass flow rate and the velocity components (v_x and v_y) at a monitored point in the middle of the running clearance became independent of the iterations. At convergence the continuity, velocity and turbulent residuals were in fact about 10^{-5}. The residuals criterion was therefore the least conservative and the easiest to fulfill.

4.1.3 Mass flow rate measurements

The boundary layer developed on the rotor causes the air to enter the pipe and to leave the system in the radial direction. The mass flow rate through the rig has been estimated at the pipe inlet by using a TSI portable hot wire anemometer which had previously been calibrated using an orifice plate. An inlet pipe has been added to the rig to allow more accurate velocity measurements in a region not affected by the skewed flow occurring in the vicinity of the rotor-stator system. The TSI anemometer has a settling time of 1.8s. Therefore, to make sure the reading was accurate each velocity reading was recorded 5s after the anemometer probe was moved into a new position. The inlet velocity has been measured at 17 different positions along the vertical and the horizontal inlet diameters and the mass flow rate was calculated on the basis of these measurements. Fig. 4.4 shows that there is a good agreement between the measured mass flow rate and the one obtained from the numerical simulation for the two considered running clearances with the largest discrepancy ($\approx$ 9%) between measurement and numerical results occurring at the 3mm clearance. This indicates that the CFD model is capable of predicting with a satisfactory accuracy the mass flow rate resulting from the disc rotation and it is a good basis for further work involving the heat transfer. A more accurate validation of

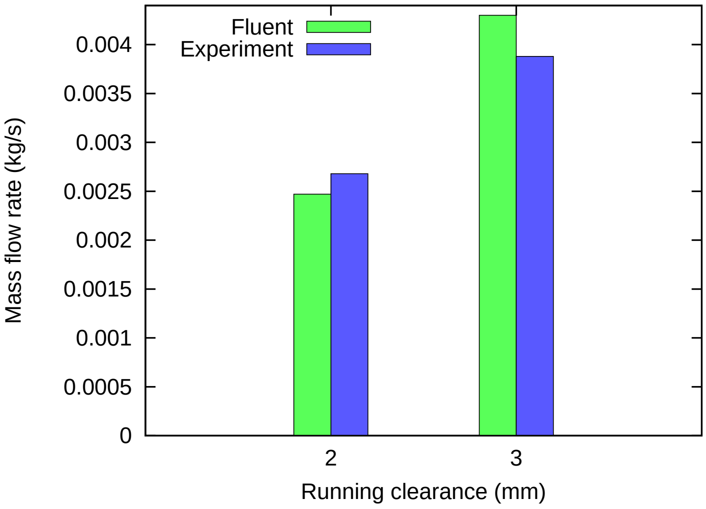

Figure 4.4: Flat rotor rig mass flow rate comparison

the flow patterns would require measurements of the velocities developing inside the running clearance. This could be carried out by using pressure probes on the stator or flat Pitot tubes inside the clearance. The small size of the running clearances of this small rig (2mm) makes the measurement of velocities inside the gap very challenging. Larger gaps are needed to carry out this kind of measurement. For this reason, the flow validation is limited to the measured air mass flow rate. More detailed validation of the obtained CFD results will be carried out in section 4.2 by comparing them with the measured temperatures and heat transfer coefficients. Further validations of the heat transfer coefficient will be presented in chapter 5.

4.1.4 Mesh dependency study

An analysis to determine the minimum number of cells needed to obtain a mesh independent solution has been performed on the system with the 2mm running clearance. The flow and thermal boundary conditions used for these CFD simulations are shown in Table 4.1 and Fig. 4.5.

Table 4.1: Flat rotor rig CFD boundary conditions

Location	Quantity	Value	Units
Inlet	P_{tot}	0	Pa
Outlet	P_{static}	0	Pa
Stator wall	Heat Flux	1000	W/m^2
Inlet air temperature	T	300	K
Rotor walls	Heat Flux	0	W/m^2
Rotational speed	Ω	1500	rpm

Neither the stator nor the rotor were modelled in CFD, but these are shown for clarity as dotted lines in Fig. 4.5. A heat flux boundary condition (see Table 4.1) has been specified on the stator wall facing the cooling air and the rotor wall was considered to be adiabatic. The mesh size has been progressively refined in both

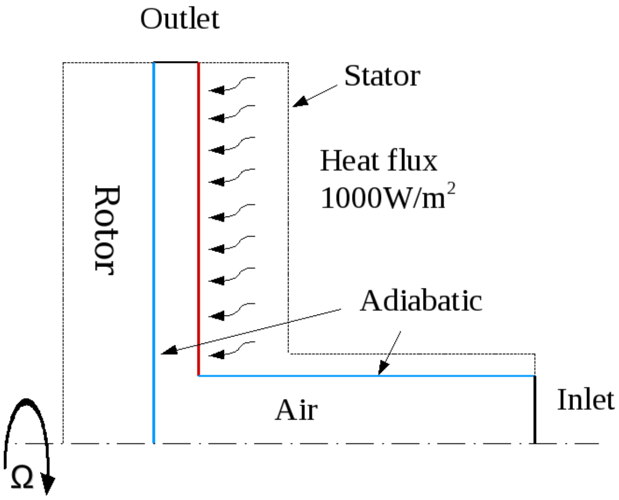

Figure 4.5: Mesh refinement boundary conditions

axial and radial direction (as shown in Fig. 4.6) as follows:

- Axial cells size refinement: the radial cells' size has been kept constant ($\Delta R =$ 1mm) while the number of cells across the running clearance varied between 13 and 43 elements.

- Radial cells size refinement: the number of cells across the clearance has been kept equal to 23, while the radial cells size has been varied (0.3mm $< \Delta R <$ 2mm).

Since the heat transfer coefficient depends on the velocity field which develops in the running clearance, the radial velocity in the air gap has been plotted in Fig.4.8 against the axial distance between the rotor and the stator. A mesh with more than 23 elements in the clearance does not lead to an appreciable radial velocity change as shown in Fig. 4.8. In order to have such a high number of elements in the considered running clearance of 2mm, the cells dimension in the axial direction

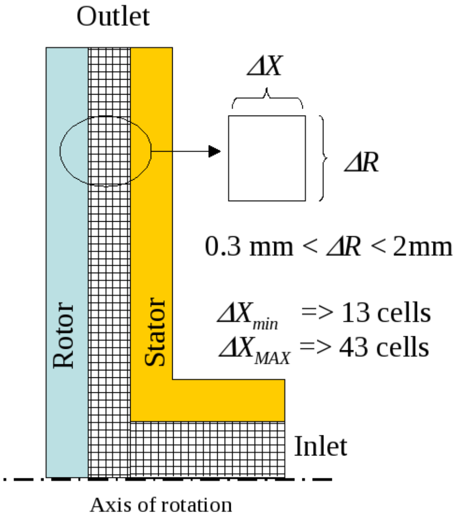

Figure 4.6: Mesh refinement

is (2/23)≈0.09mm. A cell size in the radial direction of 1mm leads to an aspect ratio of 11.1 which is very high as the cells are stretched in the radial direction. Such a high aspect ratio should be avoided in order for the mesh to provide accurate results. Since a high number of elements is necessary along the clearance axial direction in order to accurately resolve the thermal boundary layer, the only way to reduce the aspect ratio is to refine the mesh in the radial direction. This can be done in this case because of the low memory requirements for the 2D grid. However, since the bulk of this PhD study involves 3D simulations a radial cell size less than 1mm would involve an unacceptable increase in the mesh size. Therefore there is an interest in investigating the effect of a high aspect ratio on the results (see Fig. 4.6). As mentioned above, the radial size of the cells has been varied between 0.3 and 2mm keeping the number of elements in the clearance equal to 23 (≈0.09mm axial cell size) which corresponds to an aspect ratio variation between 3.3 and 22.2, respectively. From Fig. 4.7 it can be seen that the cells radial size in the considered range does not affect the accuracy of the prediction of the radial velocity, therefore, the high aspect ratio is not detrimental for the determination of the flow quantities inside the clearance.

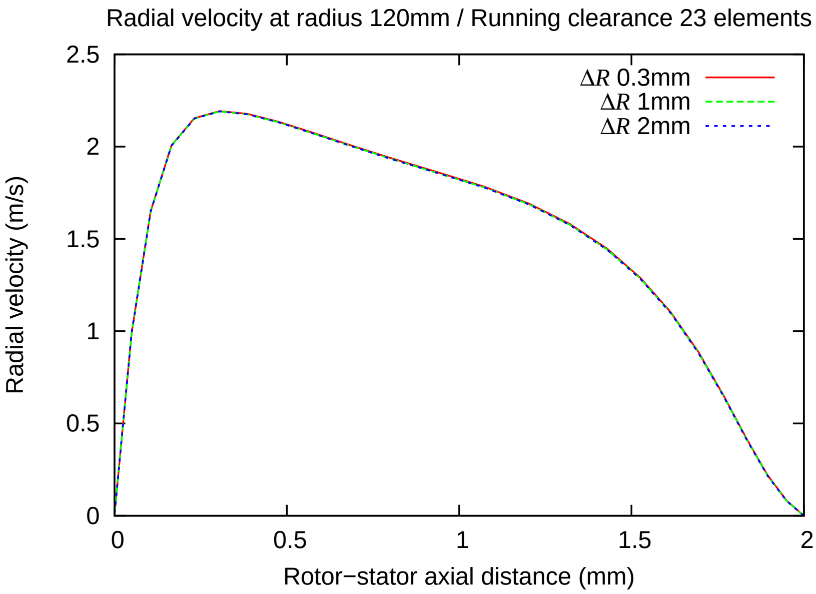

Figure 4.7: Radial cell size refinement, radial velocity

The typical aspect ratio of the 3D meshes used in this study is ≈11 corresponding to ≈20 cells in the axial direction and a cell radial size of 1mm. This apect ratio is well within the range found to be acceptable. The temperatures of the stator have been obtained and plotted in Fig. 4.9 whereas Fig. 4.10 illustrates the temperature in the middle of the running clearance. The results in terms of the accuracy of the temperature distribution reflect those previously obtained for the radial velocity: meshes with a number of cells greater than 23 across the running clearance give a satisfactory converged temperature on both the stator surface and in the running clearance. The heat transfer coefficient is linearly dependent on the difference between the stator and the running clearance temperatures. Hence if the temperatures are mesh independent the same can be affirmed for the heat transfer coefficient. The obtained value of y^+ with a mesh with 23 cells across the running clearance is ≈ 1.1 on the stator and ≈ 3 on the rotor, whereas for the 13 cells mesh y^+ is greater than 5, which is the maximum recommended value, on most of the rotor wall. Therefore the criterion of $y^+ \approx 1$ and $y^+ < 5$ at the maximum proved to be necessary when the EWT method is used in Fluent.

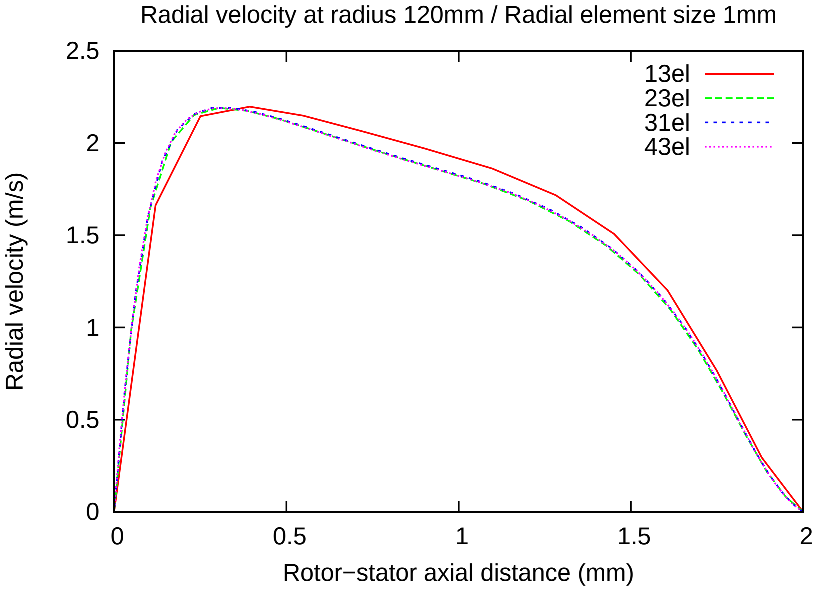

Figure 4.8: Axial cell size refinement, radial velocity

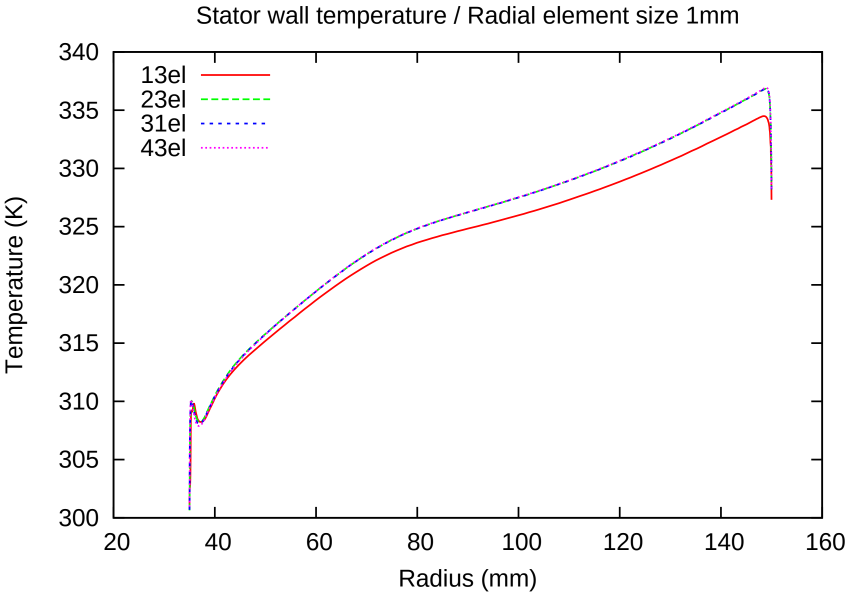

Figure 4.9: Radial cell size 1mm stator temperature

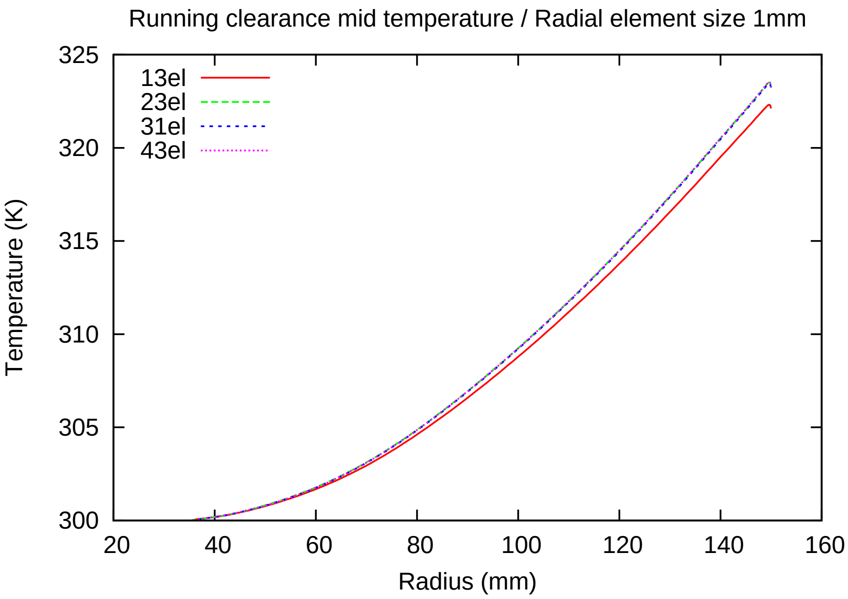

Figure 4.10: Radial cell size 1mm middle temperature

The radial and tangential velocities obtained at various radii (Fig. 4.11 and Fig. 4.12 respectively) show that the flow in this case (running clearance of 2mm and rotational speed of 1500rpm) is of the Stewartson type [50]. This is characterised by a maximum tangential velocity on the rotor which progressively decreases to become zero on the stator. The radial velocity instead is zero on the rotor due to the non-slip condition, then increases due to the centrifugal effect to reduce to zero on the stator surface. The values of the velocities in the running clearance are displayed for radii ranging from 40mm to 140mm.

The heat transfer coefficient on the stator has been calculated in two ways. In the first case (case ‘A’) it was obtained by dividing the local heat flux on the surface by the difference between the surface temperature and the temperature in the centre of the air gap as in Eq. 4.1.

$$h(r) = \frac{\dot{Q}(r)}{T_{wall}(r) - T_{mid}(r)} \tag{4.1}$$

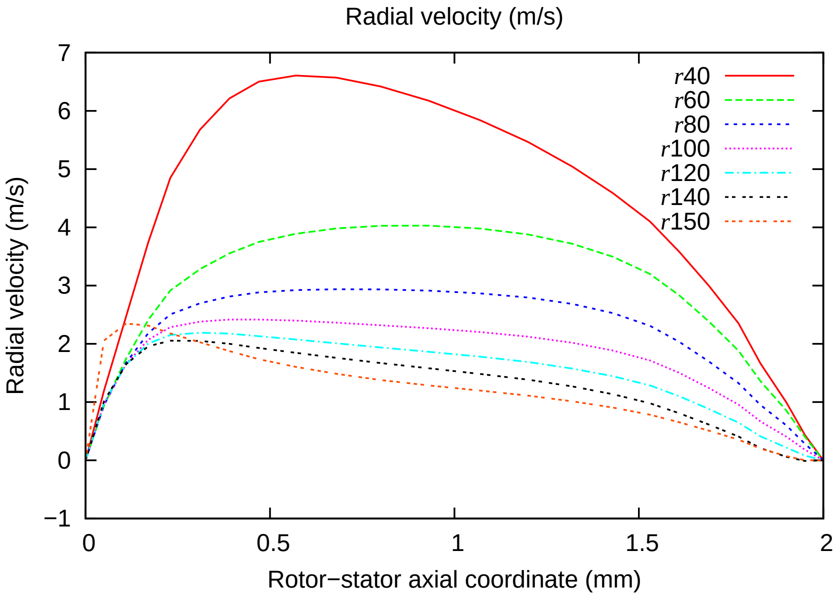

Figure 4.11: Flat rotor 2mm running clearance; radial velocity

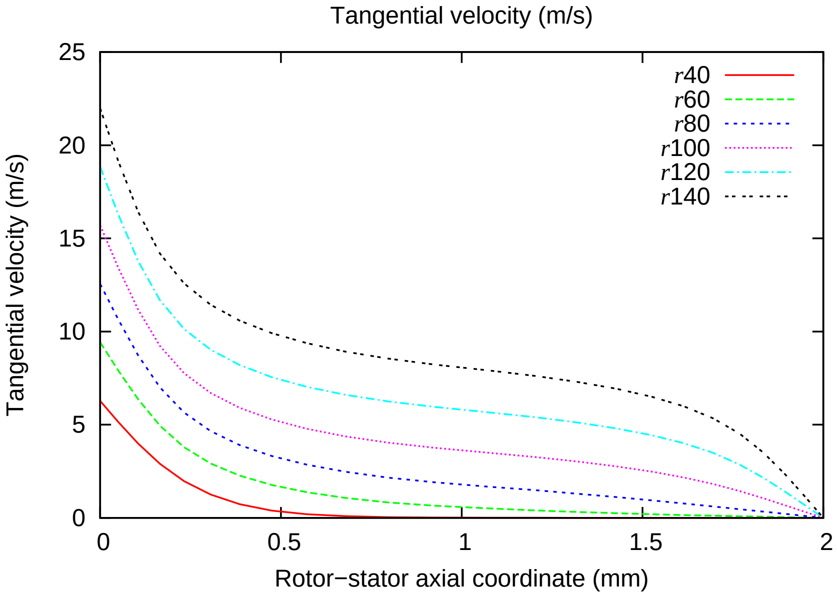

Figure 4.12: Flat rotor 2mm running clearance; tangential velocity

where $T_{wall}(r)$ is the local radial wall temperature, $T_{mid}(r)$ is the local temperature in the middle of the clearance at the same radius, and $\dot{Q}$ is the local heat flux. In the second case (case 'B') the inlet temperature has been used as a reference as in Eq. 4.2.

$$h(r) = \frac{\dot{Q}(r)}{T_{wall}(r) - T_{inlet}} \tag{4.2}$$

where T_{inlet} is constant and equal to 300K.

The heat transfer coefficient calculated using the local temperature in the running clearance is shown in Fig. 4.13, whereas the one calculated by using the inlet temperature as a reference is shown in Fig. 4.14. The two heat transfer coefficients have the same magnitude at the inlet radius (equal to 120W/(m^{2}K)), as the temperature in the middle of the running clearance is the same as the inlet temper-

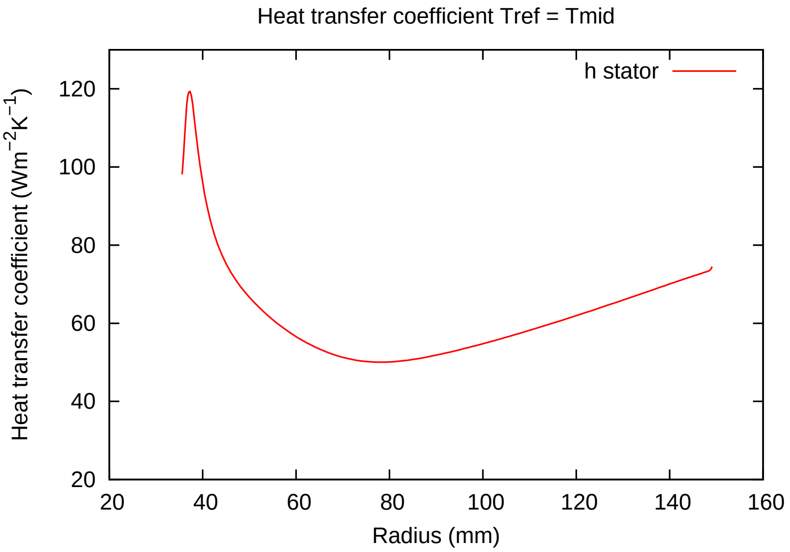

Figure 4.13: Stator local heat transfer coefficient (Case‘A’), 2 mm running clearance

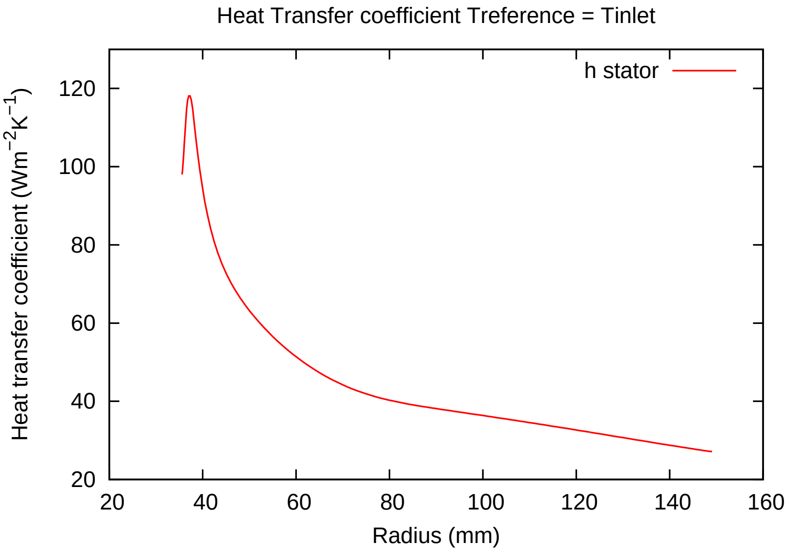

Figure 4.14: Stator local heat transfer coefficient (Case ‘B’), 2mm running clearance

ature at the inner radii. Since the inlet temperature in case 'B' is constant and the surface temperature increases with the radius as shown in Fig. 4.9, the heat transfer coefficient decreases with the radius to reach its minimum value (25W/(m^{2}K)) at r = 150mm. In case 'A' the heat transfer coefficient initially decreases from 120W/(m^{2}K) at the inlet to the minimum value of 52W/(m^{2}K) at r = 80mm, then it starts increasing due to the temperature gap becoming narrower (the stator temperature increases slower than the temperature in the middle of the clearance). The heat transfer coefficient reaches value of 67 W/(m^{2}K) at r = 150mm. In the published work on rotor-stator systems the heat transfer coefficient is usually calculated according the definition in Equation 4.2 due to the inherent difficulty of measuring the temperature in the middle of the clearance. The same approach has been followed in this study to calculate the heat transfer coefficient in order to compare it to experimental values. However, in the LPM briefly described in chapter 1 the definition of heat transfer coefficient in Equation 4.1 has been used. Therefore in chapter 6 and 7 it has been calculated as defined in Equation 4.1.

4.2 Magnet rig

The rotor has subsequently been modified by adding 6 Perspex sectors with a 20mm depth. A picture and a CAD drawing of the test rig are shown in Fig. 4.15 and Fig. 4.16 respectively. The magnets are made as 45° segments with the inner and the outer radius of 55 and 110mm, respectively. Since there are six segments, each of 45°, the inter-sector angle is 15°. On the back of the stator, six 8W silicon heating mats have been placed with thermal resistant glue (see Fig.4.17). These heaters are connected in parallel and powered by an 18Vdc 360W rated adjustable DC power supply to reproduce the heat generation due to Joule losses in the axial flux generator. The DC power supply is adjusted so that it does not exceed the power rating of the silicon heaters. Due to the high aluminium thermal conductivity the aluminium temperature is uniform when the rotor is stationary. To minimise the measuring errors it is recommendable to increase the stator front temperature as much as possible. Since the rating of the heaters is fixed, the stator heated surface and the inlet pipe have been insulated with a fibreglass blanket as shown in Fig. 4.18. Therefore in the simulation the pipe has been considered adiabatic and it has been assumed that all the heat generated by the heating mats was transferred to the stator.

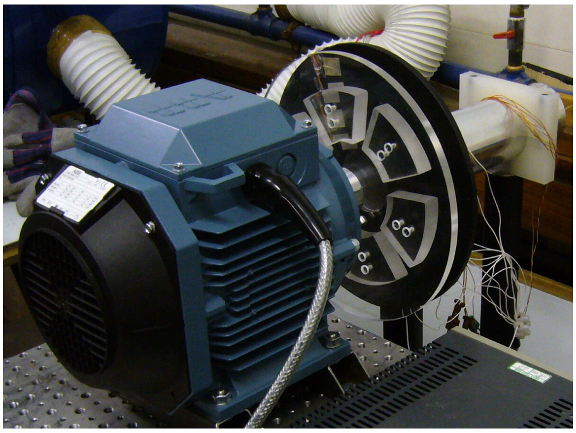

Figure 4.15: Magnet rig

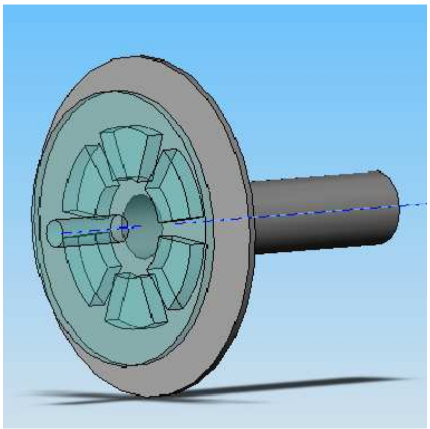

Figure 4.16: Magnet rig: CAD model

4.2.1 Experimental apparatus

Temperature measurements

The temperature of the stator at the fluid interface has been measured at four radii, namely 45mm, 70mm, 102.5mm and 130mm, by means of surface thermocouples. In

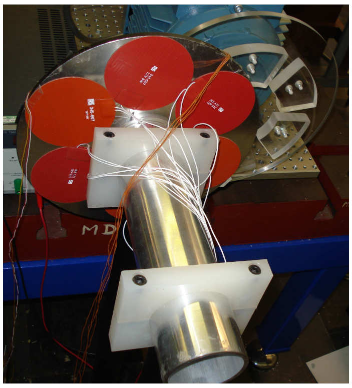

Figure 4.17: Stator heating mats

Figure 4.18: Stator insulation

order to minimise the disturbance on the air flow thin thermocouple wires, 32AWG (0.2mm diameter) were used. However, the thin wires have high resistance which can make the system sensitive to noise. One solution is to use thick thermocouple extension wires which have a low resistance outside the rotor-stator system. Hence the total series resistance is kept small for long distances. The surface temperature is measured by Omega SA1-T type surface thermocouples. The working range for these thermocouples is 270°C to 400°C with an accuracy of ±0.2K. On the top of the thermocouple a fiberglass reinforced polymer insulation layer is applied to minimise the effect of the fluid temperature on the thermocouple and make sure that it measures the wall temperature. The bottom side thermocouple is attached to the wall where the temperature is being measured by using high temperature resistant acrylic double sided tape (Fig. 4.19).

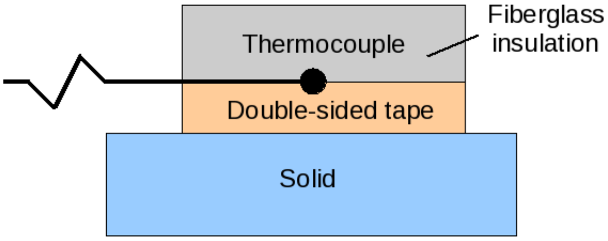

Figure 4.19: Omega SA1-T type film thermocouple attached to a wall with acrylic double-sided tape

This set-up means that the temperature measured by the thermocouple is the one at the top of the double sided tape. Due to the high thermal resistance, the temperature drop across the acrylic double-sided tape is significant. The conduction equation is used to obtain the wall temperature from the thermocouple:

$$T_{wall} = \frac{q \times L}{k} + T_{thermocouple}, \tag{4.3}$$

where T_{wall} is the temperature on the solid surface; q is the heat flux; L is the double-sided tape thickness; k is the double sided tape thermal conductivity.

Heat flux measurements

Heat flux sensors Omega HFS3 (Fig. 4.20) were used to measure the heat flux on the stator surface. They are differential thermocouple sensors: they measure the heat transfer rate by measuring the temperature difference across a thermal barrier. The centre of the sensor consists of Kapton material with known thermal characteristics. On either side of this Kapton sheet 50 copper/constatan junctions are wired in series on the alternate side of the Kapton layer. One of the copper leads is attached to

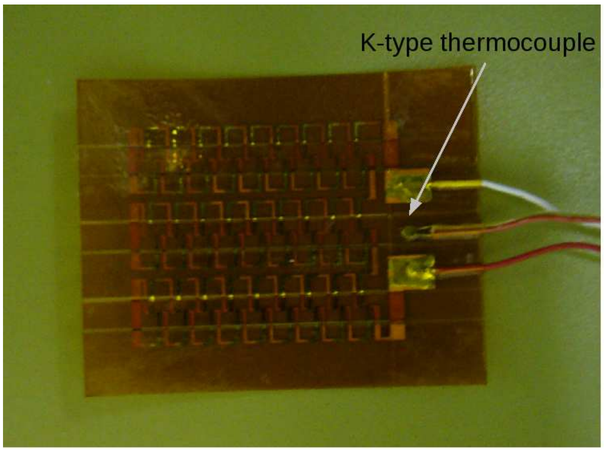

Figure 4.20: Heat flux sensor

the first junction at the bottom surface, and the other one to the last junction at the top surface. The thermal properties of the Omega HFS3 sensor are reported in Table 4.2. A simple experiment allowed the calibration of each of the heat flux sensors used throughout the project. The set-up consists of an aluminium disc, a heating mat, a heat flux sensor and fiberglass for thermal insulation, as shown in Fig. 4.21 and 4.22. The aluminium disc is heated until a steady thermal state is reached. The heat flux sensor is initially placed on the disc top surface, then at the bottom surface of the heating mat. The sum of the EMFs measured for the two positions of the heat flux sensor are used to calibrate it against the total power input from the power supply. The calibration for each of the heat flux sensors has been repeated 5 times and the calibration factor varies between 3.5% and 8.7% depending on the heat flux sensor. The heat flux is calculated using the value of the voltage output and of the calibration factor:

Table 4.2: Thermal properties of the Omega HFS3 heat flux sensor

Property	Quantity	Unit
Thermal resistance	0.002	°C/(W/m^2)
Thermal capacitance	600	Ws/(°Cm^2)
Response time	0.6	s
Sensitivity	0.8-0.13 (Varies with sensors)	μV/(W/m^2)
Temperature limit	150	°C
Heat Flux limit	100	kW/m^2

$$\text{Measured heat flux} = \frac{V_{HF}}{K_{calibration}}, \tag{4.4}$$

where V_{HF} is the voltage output from the sensor in μV; $K_{calibration}$ is the calibration factor in μV/(W/m^2).

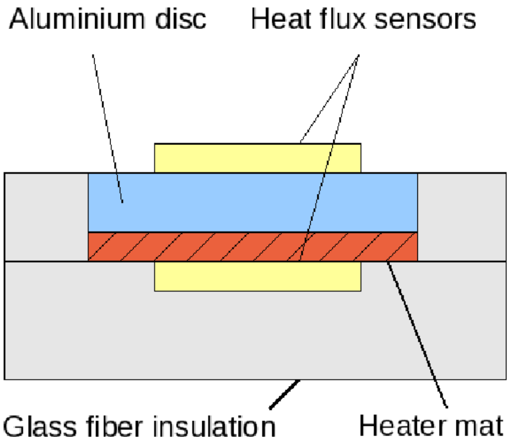

Figure 4.21: Heat flux sensor calibration scheme

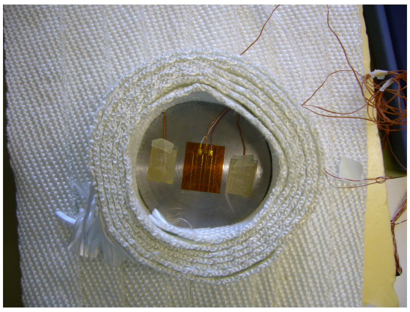

Figure 4.22: Heat flux sensor calibration

The uncertainty of each heat flux sensor is recorded and taken into account, together with the uncertainty of the thermocouples in the measurement of the heat transfer coefficients.

Mass flow rate measurements

Mass flow measurements have been carried out as in the case of the flat rotor by means of the TSI portable anemometer. Compared with the case of a flat rotor, the mass flow rate in the running clearance increases considerably ($\approx$ ten times) due to the magnets which act as blades of a radial compressor.

4.2.2 Steady and unsteady simulations of magnet rig

Two approaches are available in Fluent to model rotating flows. The first one consists of a moving reference frame (MRF) steady simulation, and the second of an unsteady (U-RANS) sliding mesh simulation. The first one is considerably less expensive from a computational point of view (up to ten times in our case) and is equivalent to fixing the rotating fluid in a particular position to evaluate the flow field developing for that position [20].

The unsteady simulation is more robust and takes into account the large scale transient effects which might develop inside the domain. The flow time was discretised into time steps (corresponding to 1° angular increment). The governing equations describing the air flow and heat transfer are solved as a function of time. The flow and heat transfer for each position of the rotor at each time step were modelled. Due to the time constraint for the CFD simulation study there is the need of establishing whether the MRF method can be used to obtain acceptably accurate results.

While the steady approach can only provide a time averaged value of the heat transfer coefficient on the stator surface, the unsteady simulation calculates the instantaneous value of the flow and heat transfer quantities at each time step for each angular position of the rotor.

In both cases (MRF and U-RANS) a part of the domain has been considered stationary while the other rotating. Since the same mesh has been used for the two simulations it had to be compatible with both the steady and the unsteady approaches.

This has required the explicit definition of a grid surface interface between the rotating and the stationary domain. As a requirement for the sliding mesh and for the MRF model the two regions of the domain (stationary and rotating) could not intersect: no displacement normal to the grid interface was allowed. The stationary domain includes the air inside the inlet pipe, the stator annulus, the air in the vicinity of the stator and the outlet plenum. The rotating region of the domain consists of the region of the running clearance surrounding the rotor: it is contained inside the interface displayed in yellow in Fig. 4.23 for a rotor position of 10°. The periodic boundaries are shown in light blue and the outlet in red.

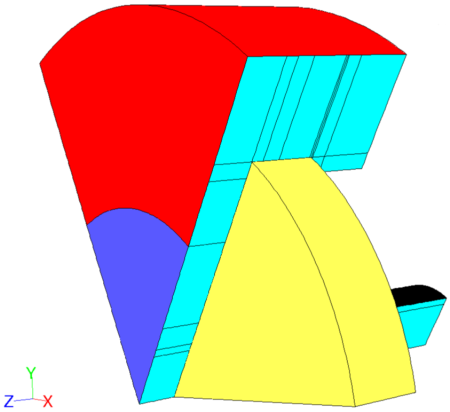

Figure 4.23: Rotating and stationary regions of the domain

The mesh consists of hexahedral elements only and satisfies the condition of $y^+ < 5$ as required by the EWT approach used in Fluent. Fig. 4.24 shows the computational domain and the inlet and outlet boundary conditions. The geometry

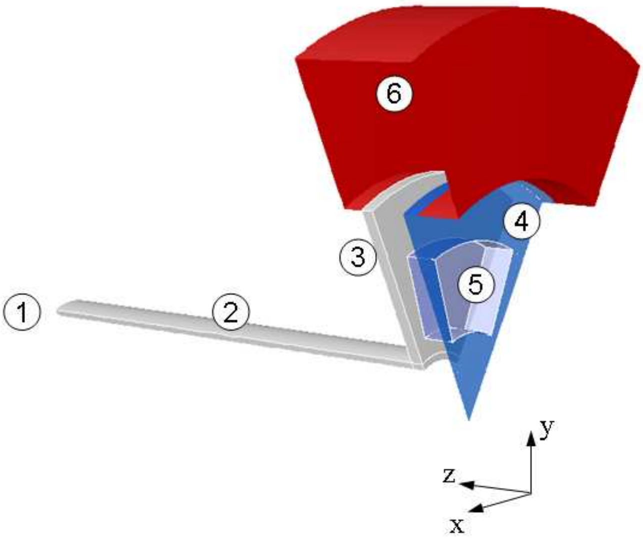

Figure 4.24: Magnet rig computational domain; (1) Inlet, (2) Inlet pipe, (3) Stator, (4) Rotor, (5) Magnet, (6) Extended domain

of the system is periodic, with a 60° periodicity. Therefore only a 60° sector has been modelled and periodic boundary conditions applied. A plenum at the inlet and a plenum at the outlet have been added to extend the domain.

A multi-block structured mesh has been created which includes the stationary and the rotating part of the domain (Fig. 4.25). The whole domain has been split into smaller elementary volumes connected to each other by sharing a common face. The grid is made of 3.8 million hexahedral elements. The clearance between stator and rotor contains about 2.2 million elements in total. The clearance has been meshed with 22 elements across the axial direction.

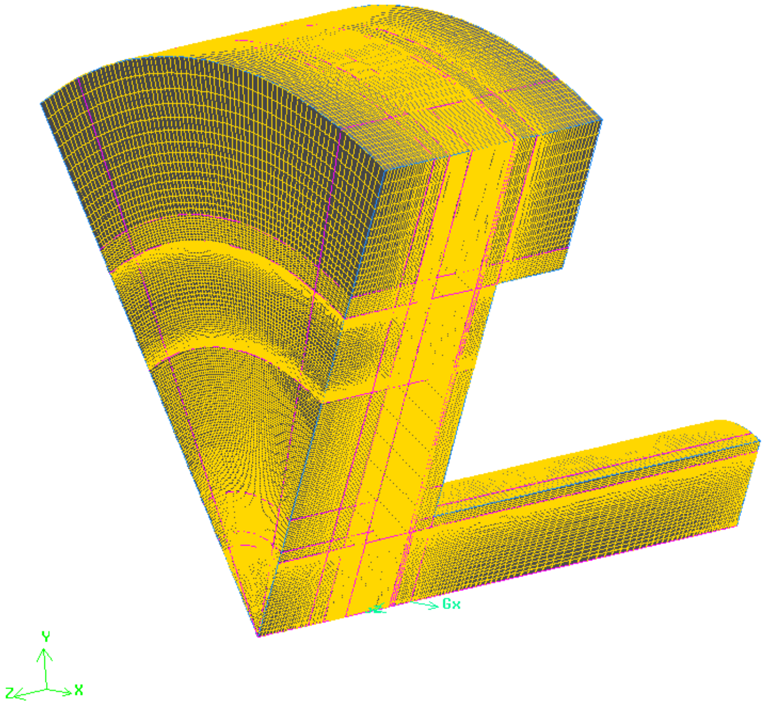

Figure 4.25: Magnet rig mesh

Zero inlet total pressure and zero outlet static pressure boundary conditions have been applied. A rotational speed of 1500rpm has been specified. The heat generated has been calculated by multiplying the voltage and the current read on the power supply connected to the 6 heaters. A uniform heat flux of 800W/m^2 has been specified on the stator in the CFD model. The room temperature of 24°C measured in the experiment has been specified at the CFD model inlet. In order to get an accurate prediction of the temperatures, the solids components of the system have been included in the model. The thermal boundary conditions are shown in Fig. 4.26 for a section of the three dimensional model.

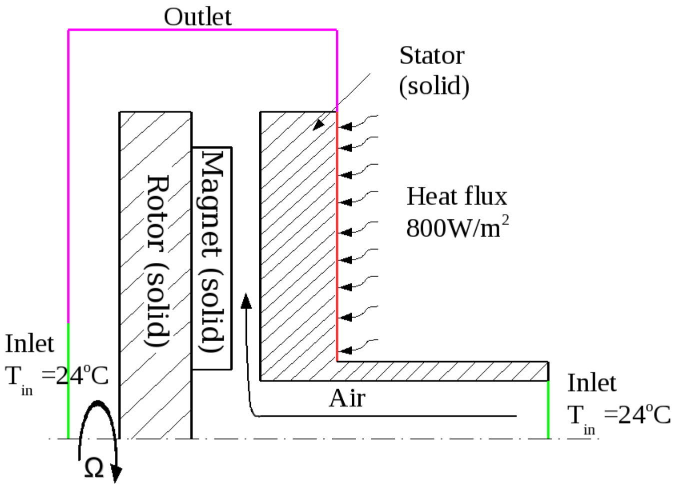

Figure 4.26: Magnet rig boundary conditions

In Fluent, the flow equations and the energy equation have been solved separately: once the flow and turbulence equations converged, the energy equation was solved on the basis of the obtained flow field. This method resulted in faster convergence.

The unsteady results have been obtained for an angular increment of 1°, hence the time step defined in Fluent has been calculated by dividing the angular increment by the constant rotational speed.

Due to the inherent difficulty of measuring the temperature inside the running clearance it has been decided to use as a reference for the calculation of the heat transfer coefficient the temperature of the air at the inlet of the system according to Equation 4.2. This approach was followed in the experimental test and in the two numerical simulations (MRF and U-RANS).

In order to obtain the circumferential averaged heat transfer coefficient two specific methods have been used for the steady and unsteady simulations. In the case of the steady MRF simulation, 60 radial lines have been created on the stator surface at angular distances of 1°, as shown in Fig. 4.27. The temperature and the heat transfer coefficient on each of these lines have been exported from Fluent and then averaged in order to obtain a circumferential averaged value.

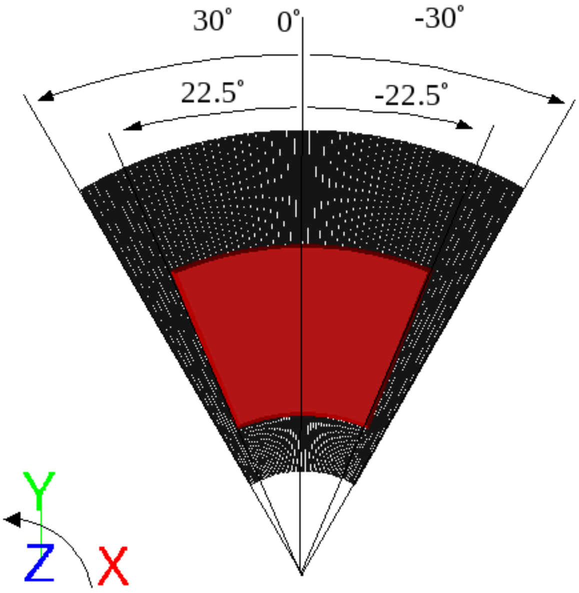

Figure 4.27: Steady state MRF simulation: reference lines

In the case of the U-RANS, one radial line has been created on the stator. As a reference also the symmetry line of the magnet on the rotor is considered. An angle called α can be introduced which defines the position of the symmetry line on the magnet with respect to the line created on the stator. In the instance when $\alpha = 0°$ the rotor is exactly aligned with the stator therefore the magnet symmetry line is facing the line on the stator. For $0° \leq \alpha \leq 22.5°$ the trailing region of the magnet faces the line on the stator. For $22.5° < \alpha < 37.5°$ the disc groove faces the line and for $37.5° < \alpha < 60°$ the leading region of the magnet is facing the stator line.

The heat transfer coefficient on this line has been exported from Fluent for each of the 60 angular positions of the rotor. These values too have been averaged to find the circumferential averaged heat transfer coefficient. Fig. 4.28 shows the reference line and the relative position of the rotor at various angles. These two numerical averaged values are compared to the heat transfer coefficient measured in the experiments and to each other.

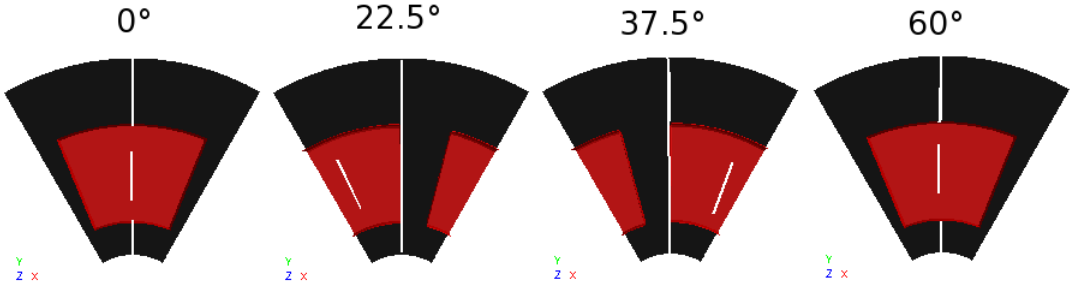

Figure 4.28: Unsteady simulation: reference line and relative rotor positions

4.2.3 Steady state simulation results

In order to visualize the flow inside the magnet rig path lines of the air are plotted in Fig. 4.29. The rotor is not displayed and the periodic 60° domain has been repeated for clarity. The incoming air maintains a low speed until it reaches the running clearance. In the pipe connected to the stator the swirl and the radial component of the velocity are negligible. Once the air reaches the clearance the swirl velocity component becomes the major one. The pathlines coloured according to velocity magnitude show that the highest velocities (≈ 23.5m/s) are obtained in the rotor grooves on the magnet pressure side ($\alpha \approx 23°$). Relatively low velocities ($3\text{m/s} < V < 11\text{m/s}$) are observed in the clearance between the magnets and the stator. Vortex shedding from the magnet pressure side at the magnet peripheral radius ($r = 110$mm) can be observed at an angle $\alpha \approx 12°$.

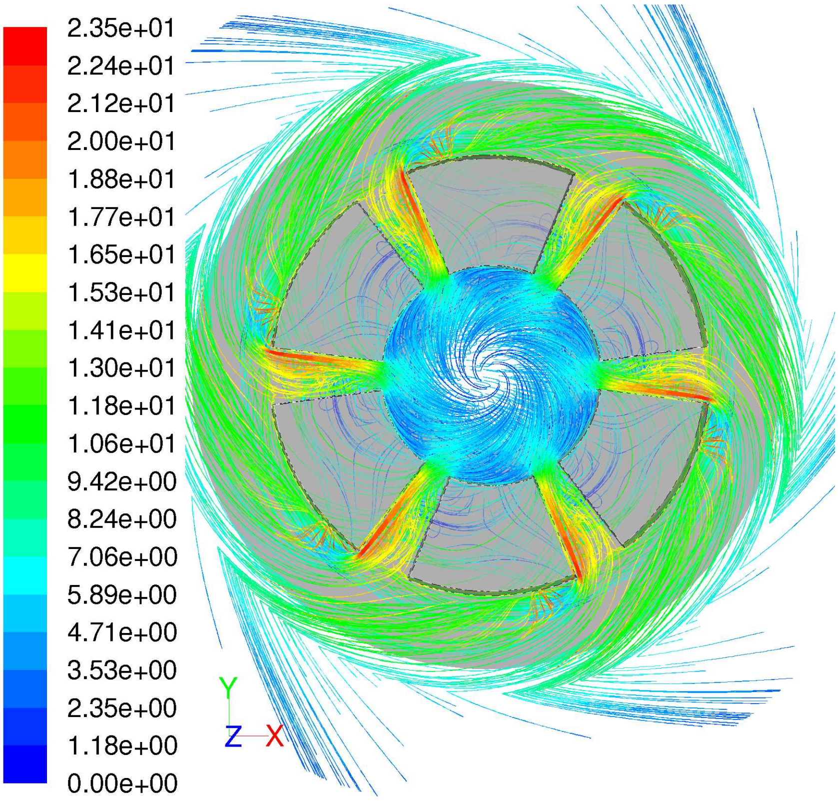

Figure 4.29: Steady state pathlines coloured by velocity magnitude (m/s)

The high aluminium conductivity causes the stator temperature to be relatively uniform over the whole area as shown in Fig. 4.30: the difference between the lowest and the highest temperatures is limited to 1°. A temperature increase occurs proceeding from the inner radius towards the running clearance outlet. This is due to the air heating in the clearance. Some features of the heat transfer coefficient obtained with the steady state MRF model are evident from Fig.4.31. Proceeding from the clearance inlet radius of 35mm the heat transfer coefficient increases re-

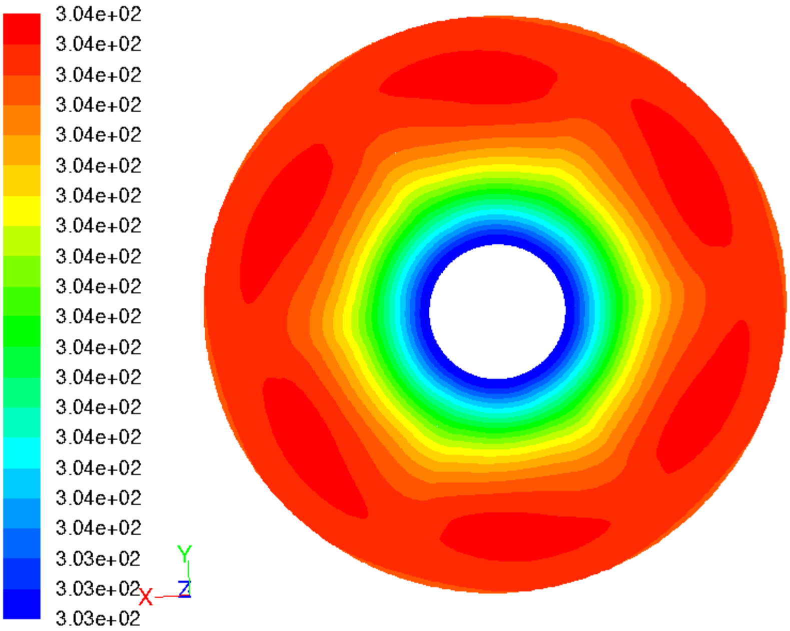

Figure 4.30: Steady state contours of temperature on the stator surface

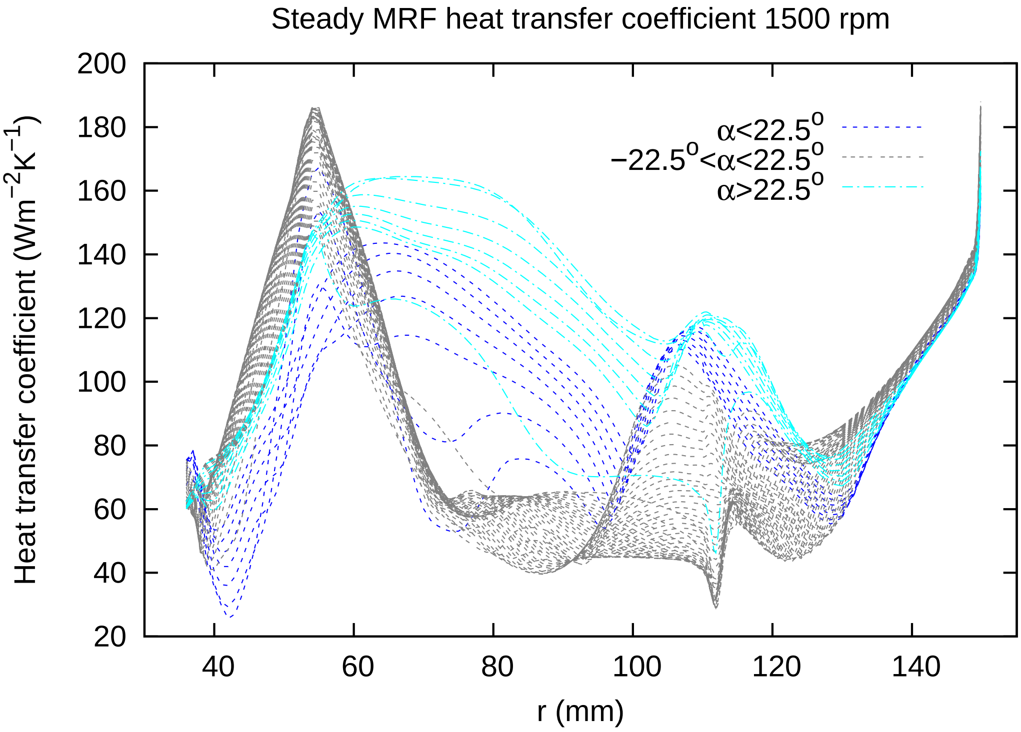

Figure 4.31: Steady state heat transfer coefficient

gardless of the angle until $r = 55$mm, where it reaches its maximum. At this radial location a difference between the heat transfer coefficient obtained at the various angles can be observed.

For -22.5° $< \alpha <$ 22.5° the axial distance between rotor and stator is lowest and the radial velocities highest. This causes the heat transfer coefficient to be the highest in this angular range at the clearance inlet (r = 55mm). The calculated maximum value of the heat transfer coefficient is 184W/m^{2}K for α = -19° and r = 5mm (Fig. 4.31 and 4.32).

The contours of heat transfer coefficient in Fig. 4.32 follow the same pattern as in the bidimensional graph in Fig. 4.31. The areas where the high heat transfer coefficient is calculated coincide with the position of the groove in the rotor disc where the bulk of the mass flow rate occurs and where the highest velocities are obtained. The effect of the vortex shedding from the magnet pressure side shown in Fig. 4.29 on the heat transfer coefficient is not observed. Due to the large depth of the sectors (20mm) the vortex effects remain far from the stator surface.

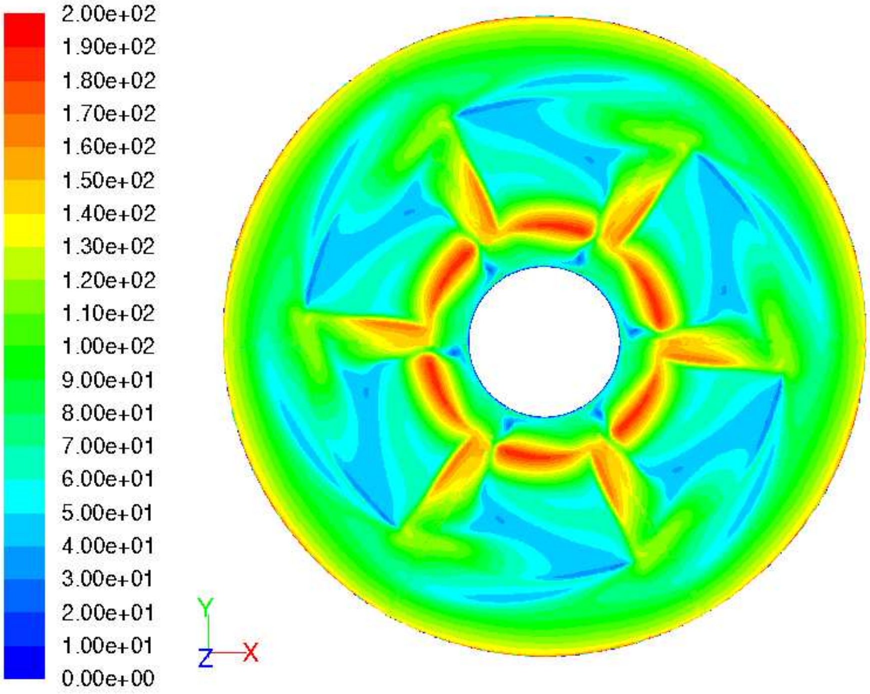

Figure 4.32: Steady state heat transfer coefficient on the stator surface

4.2.4 Unsteady simulation results

In order to clarify the graph of the unsteady simulation it is useful to point out that the angular extension of the domain is 60° and the angle of the magnet is 45°. The heat transfer coefficient has been obtained on a stator radial line for all the 60 angular positions of the rotor. Similarly as for the steady case the air pathlines coloured according to velocity magnitude are shown in Fig. 4.33. The pathlines are plotted for a rotor angle $\alpha = 0°$. The same flow pattern, but rotated, has been found for the other rotor angles. Vortex shedding from the magnet pressure side has been found as in the steady case. The heat transfer coefficient on the stator for

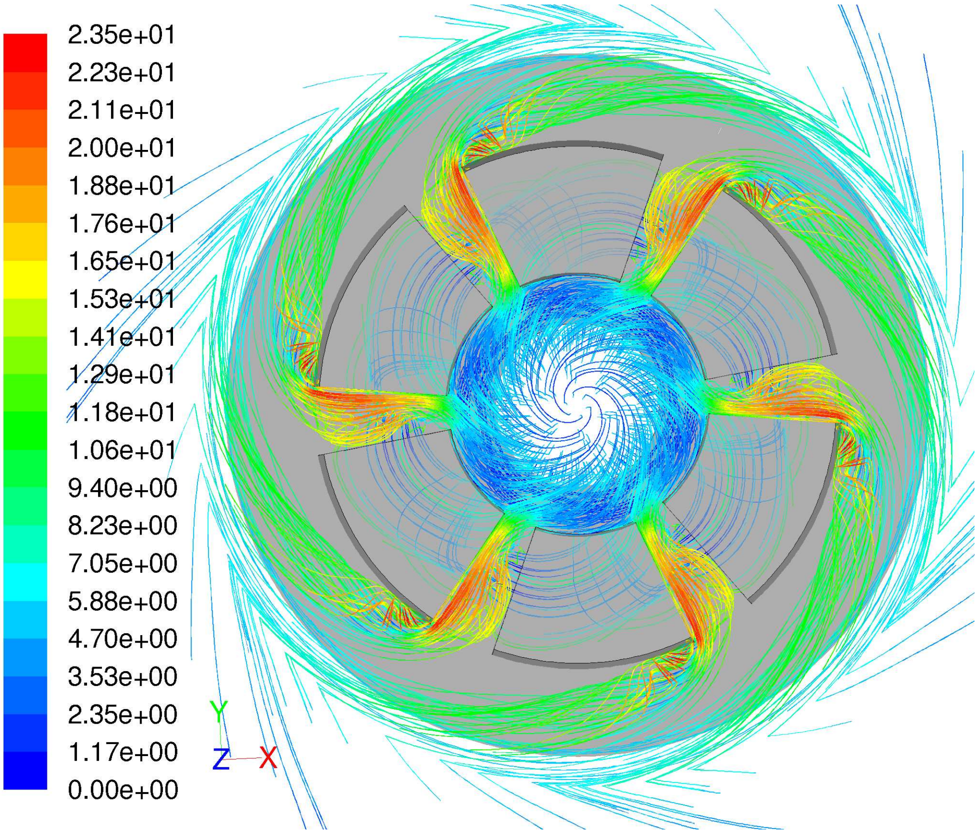

Figure 4.33: Unsteady case pathlines coloured by velocity magnitude (m/s)

the unsteady case is shown in Fig. 4.34 in different colours corresponding to the rotor angle α. For all angular positions of the rotor the heat transfer coefficient is maximum at the clearance inlet ($r = 55$mm) because, due to the low passage area the radial velocity component is maximum. The maximum heat transfer coefficient decreases fast (from 185W/(m^{2}K) at $r = 55$mm to 100W/(m^{2}K) at $r = 65$mm) when the trailing part of the magnet is opposite to the reference line on the stator ($0° < \alpha <22.5°$) whereas its value still drops although it is maintained comparatively high ($\approx$ 160W/(m^{2}K) at 55 mm$< r <$65 mm) when the groove in the rotor is facing the line on the stator ($22.5° < \alpha <37.5°$). Therefore the effect of the groove passage is to increase the heat transfer coefficient further inside the clearance even if its local maximum decreases.

At the radial locations without the magnet (35mm $< r <$ 55mm and 110mm $< r <$ 150mm) the U-RANS simulation predicts a relatively uniform heat transfer coefficient independent on the rotor angle. This is expected considering the axisymmetric geometry of the rotor shape.

In order to better visualise the heat transfer coefficient from the U-RANS simulation a 3D graph (Fig. 4.35) has been created where the heat transfer coefficient on the reference line has been plotted for each of the 60 positions of the rotor.

The variation of the heat transfer coefficient with the rotor angle is shown in Fig. 4.36 at two radii (70mm and 105mm). The effect of the recess in the rotor (which passes the reference line for $22.5° < \alpha < 37.5°$ is clear at the higher radius of 105mm whereas its influence is delayed at the lower radius and the highest heat transfer coefficient (185W/(m^{2}K)) is found for a rotor angle of 40° which corresponds to the first half of the magnet facing the reference line. The wall temperature (Fig. 4.37) varies with the rotor angle within a very limited range (for $r = 70$mm 303.9888K

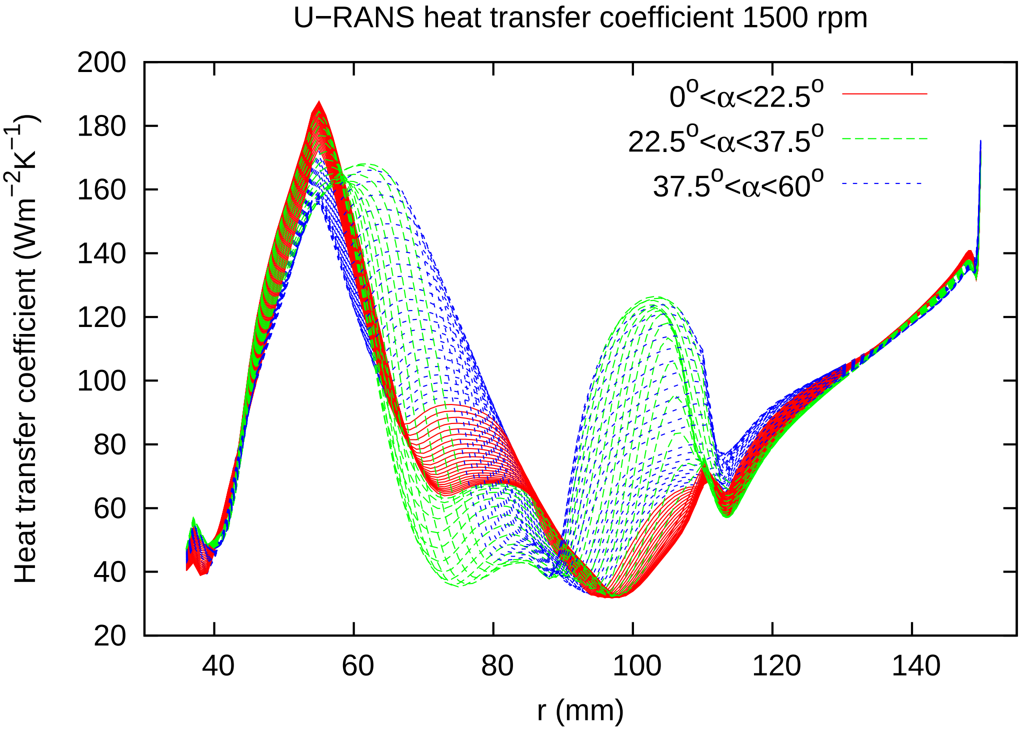

Figure 4.34: Unsteady heat transfer coefficient

$< T_{70} < 303.9905$K; for $r = 105$mm 303.9928 K $< T_{105} < 303.9940$K) due to the high heat capacity of the aluminium stator. On the contrary, the limited temperature variation with radius is due to the high conductivity of the aluminium. For the rotor position at which $\alpha = 0°$ the maximum temperature difference over the radius is observed: 303.9893K $< T_{0°} <$ 303.9937K. Similarly to the heat transfer coefficient, the temperature for $r = 105$mm drops as soon as the rotor groove faces the reference line, whereas the temperature reduction takes place at 40° for $r = 70$mm.

The contours of heat transfer coefficient calculated with the unsteady case simulation are shown in Fig. 4.38 for the rotor angle $\alpha = 0°$. The pattern observed at this angle does not change relative to the moving rotor. This has been verified for rotor angles ranging from 0° to 60° in 10° steps. It can be concluded that there are no considerable transient effects and the steady state MRF approach can be

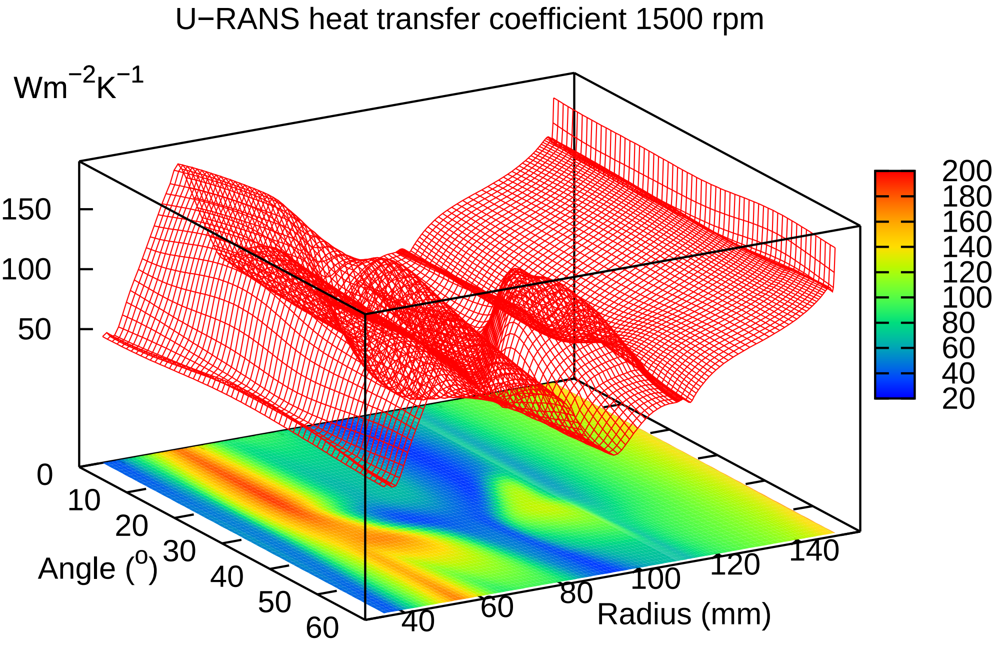

Figure 4.35: Unsteady heat transfer coefficient

successfully employed in further calculations.

At the clearance inlet ($r = 55$mm) the heat transfer coefficient is maximum at the trailing edge ($0° < \alpha < 22.5°$) and has an average value of 180W/(m^{2}K). The minimum value is observed for $r \approx$90mm where the velocity magnitude inside the clearance is minimum (Fig. 4.38). The comparison between the steady and the unsteady cases (Fig. 4.32 and Fig. 4.38 respectively) shows that the steady simulation is capable of predicting the high heat transfer coefficient at the clearance inlet, but at the magnet leading edge it predicts a higher heat transfer coefficient than the unsteady case. A further difference is the prediction of the heat transfer coefficient at the magnet outlet: in the steady case a low heat transfer coefficient is calculated at the magnet leading edge whereas in the unsteady case there is a strip of low heat transfer coefficient at $r \approx$90mm. This is more significant at the trailing

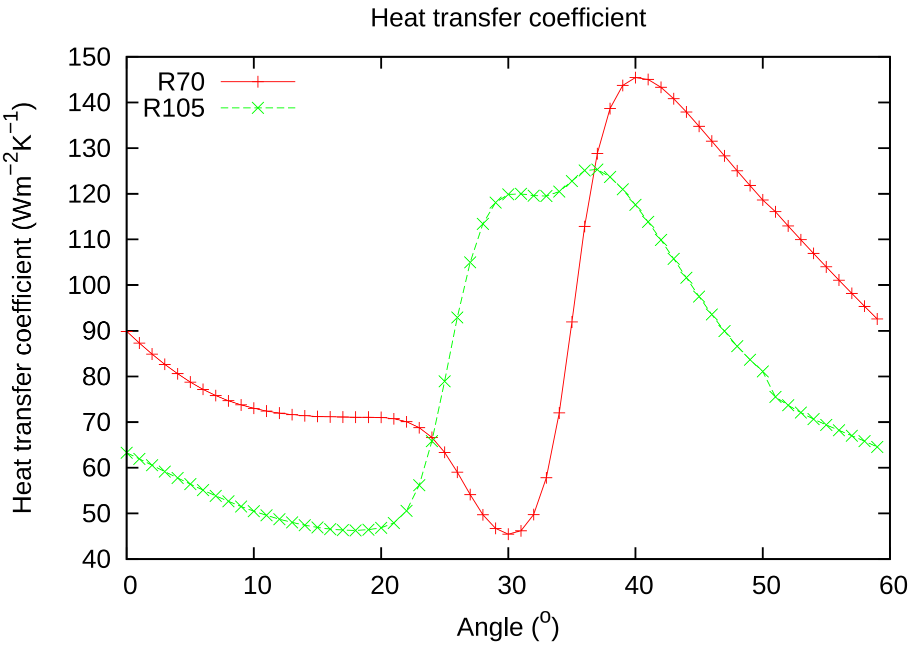

Figure 4.36: Unsteady heat transfer coefficient angular variation

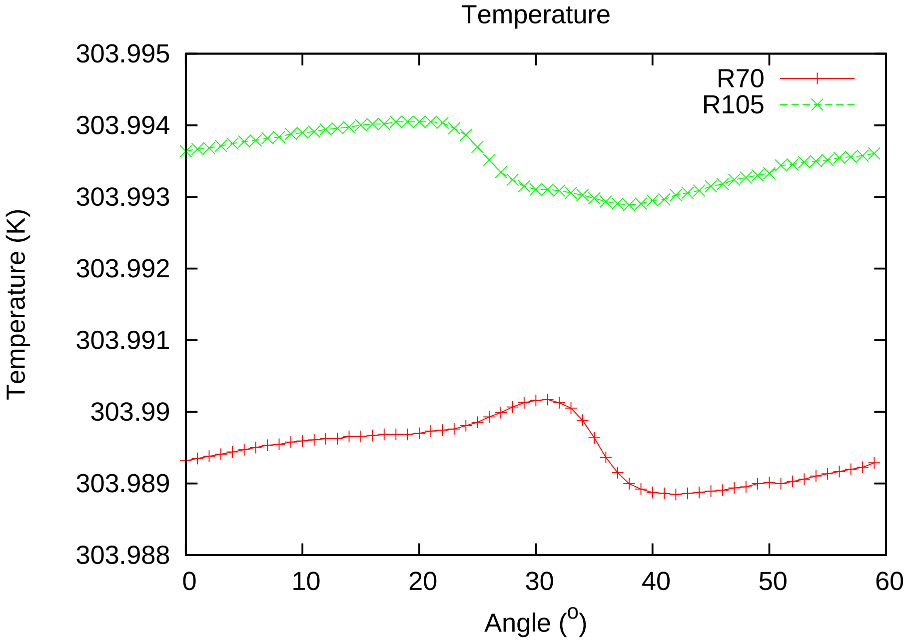

Figure 4.37: Unsteady temperature angular variation

edge of the magnet.

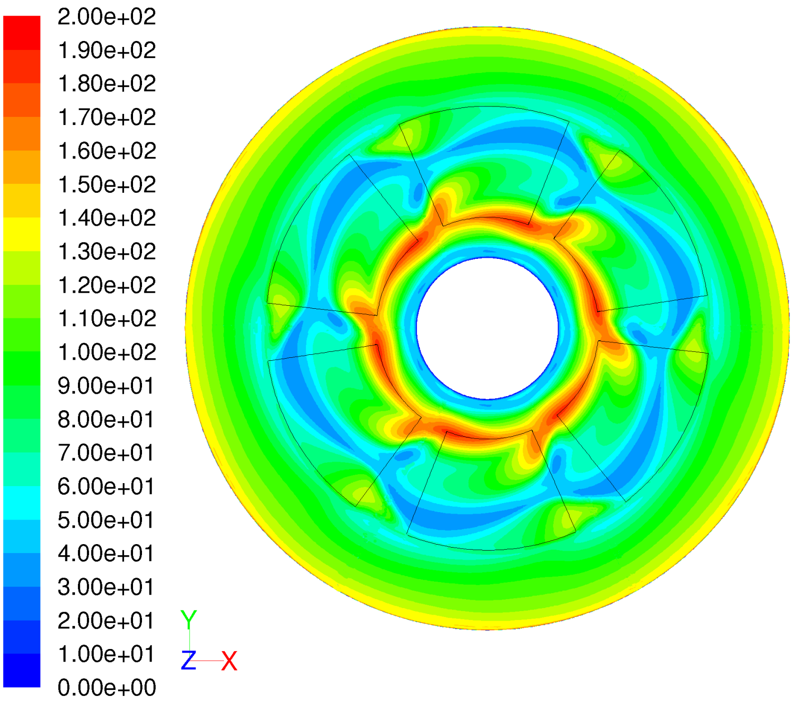

Figure 4.38: Unsteady heat transfer coefficient contours

4.2.5 Comparison between steady and unsteady simulations results

The calculated and the measured mass flow rate through the system are presented in Table 4.3.

Table 4.3: CFD predicted and experimental mass flow rate

	Steady (MRF)	Unsteady (U-RANS)	Experiment	Unit
Mass flow rate	0.0232	0.0220	0.0254	kg/s

The temperatures measured and obtained from the simulation are illustrated in Fig. 4.39. From the temperatures graph it can be seen that whereas the temperatures have a good agreement on the stator mid radius, at the periphery and at the inner radius the difference is more significant. The outer radius of the inlet pipe has been specified in Fluent as adiabatic but, in practice, even an insulated pipe will

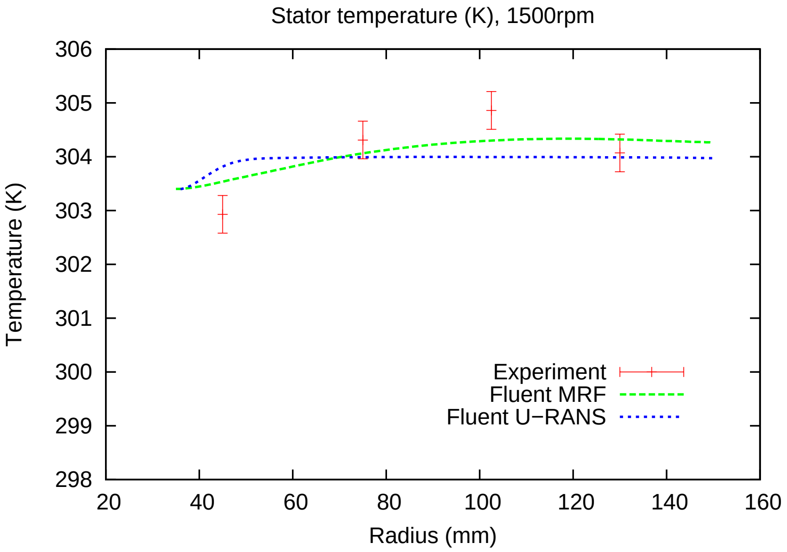

Figure 4.39: Magnet rig temperatures

conduct some heat which explains why the stator temperature at the inner radius is lower than in the simulated case. The heat transfer coefficient calculated with the steady MRF model in the region corresponding to the disc grooves ($\alpha < 22.5°$ and $\alpha > 22.5°$) is higher than that calculated with the unsteady model (U-RANS) as shown in Fig. 4.40. This is particularly more evident in the region of $r \approx 90$ mm where the mis-match between transient and steady simulation results is larger.

By comparing the steady (MRF) and the unsteady sliding mesh (U-RANS) simulations it can be concluded that the matching between the results is overall satisfactory. However, the steady simulation over predicts the non-axisymmetric effects outside the magnet region; namely for r <55mm and r >110mm. A further difference is the over-prediction of the heat transfer coefficient in the periphery of the magnet region (80mm $< r$ <100mm).

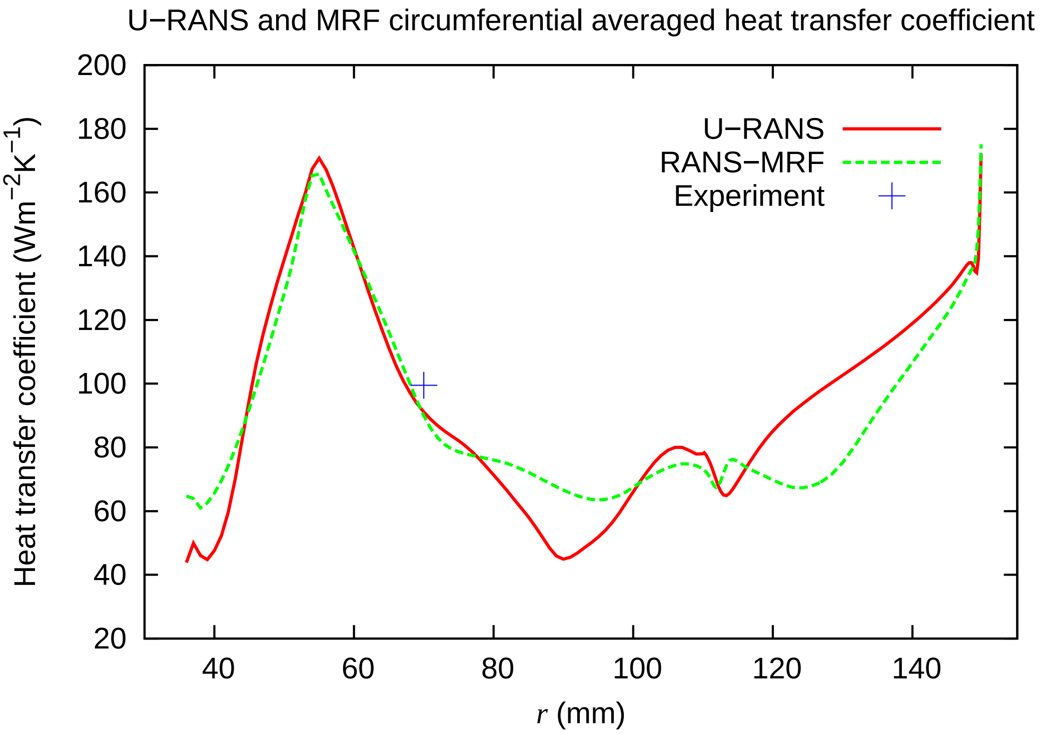

Figure 4.40: Unsteady and steady heat transfer coefficient

4.3 Durham 1.5kW AFPM generator

4.3.1 Description of the generator and of the CFD model

A study of the 1.5kW, 1500rpm AFPM generator built at Durham has been performed. The generator (Fig. 4.41 and Fig. 4.42) consists of a stator and two discs carrying 6 magnets each, fixed on the boss. The stator includes a laminated core and 16 copper windings. The generator's components are displayed in Fig. 4.43 and Fig. 4.44. In the modelling process care has been taken in order to closely reproduce all the dimensions of the actual machine. However, some details in the model, such as the ring retaining the magnets, the stator windings and the conductive cables, slightly differ from the real machine.

Since the generator has a periodicity of 180° only half of it has been modelled

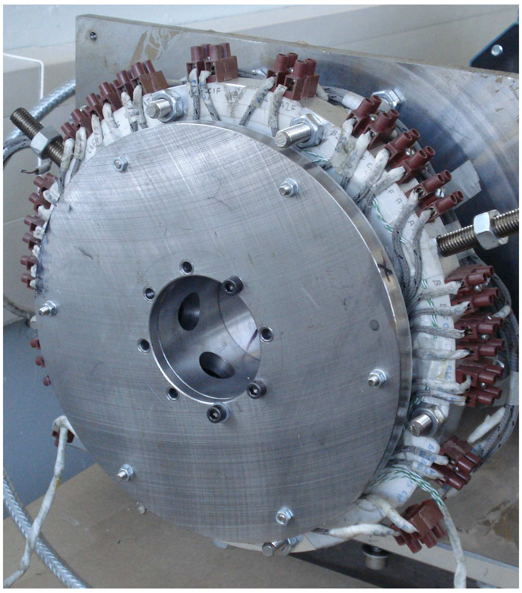

Figure 4.41: AFPM Generator

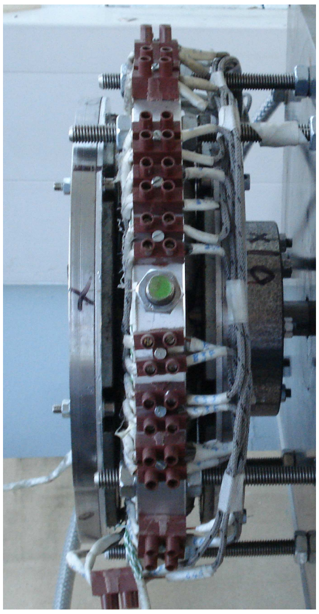

Figure 4.42: Durham generator's side view

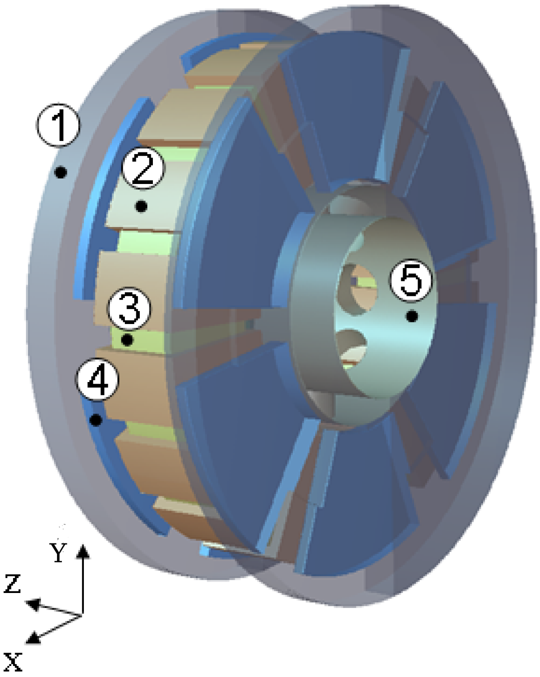

Figure 4.43: Generator components: (1) Disc, (2) Coils, (3) Stator core, (4) Magnets, (5) Boss

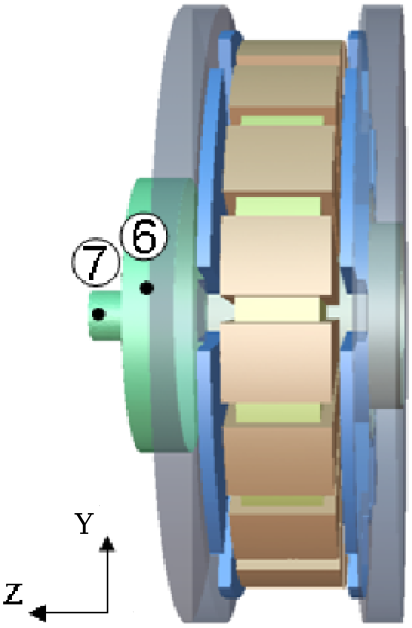

Figure 4.44: Durham generator components side view; (6) Flange, (7) Shaft

and periodic boundary conditions have been applied to the matching faces. The geometric periodicity is 180° because the rotor carries six magnets which have 60° periodicity and in the boss there are 8 holes with 45° periodicity. 180 is the minimum angle divisible by 45 and 60. The pre-processor software, Gambit, has been used to split the domain into elementary volumes which could be meshed with hexahedral elements. The mesh consists of 8 million hexahedral elements. In Fig. 4.45 the generator's domain is displayed. In this model both fluid and solid components of the generator, such as the rotors, the magnets, the stator, the coils and the boss, have been meshed. Hexahedrons have been used to mesh the running clearance, the discs, the magnets, the coils and the stator, and most of the fluid domain. The running clearance is the most critical region where the heat transfer coefficient is calculated and the generated structured mesh is shown in Fig. 4.46. The rotating discs and the surrounding fluid structured mesh is shown in Fig. 4.47. The stator coils and the core enclosed between the two clearances are displayed in Fig. 4.48. Tetrahedrons have been used to mesh volumes surrounded by complex surfaces and which could not be reduced to elementary volumes. These include the volume close to the generator's outlet and a part of the boss (Fig. 4.49). The remaining part of the boss has also been meshed with hexahedrons (Fig. 4.50). The running clearance between the rotor and the stator coils has been meshed with 32 elements. This number of elements has been found to be such that it allows a mesh independent solution and it satisfies the requirements of the EWT scheme. Further increases in the mesh density in the axial direction would cause an unacceptable increase of the aspect ratio of the running clearance cells. This could be avoided by reducing the cells' size in both circumferential and radial direction but it would generate an extremely large mesh.

The boundary conditions applied are shown in Table 4.4. The heat dissipated by the coils has been calculated based on the maximum current of 7A in the generator's coils and on constant copper resistivity.

Table 4.4: 3D Durham generator model boundary conditions

Location	Quantity	Value	Units
Inlet	P_{tot}	0	Pa
Outlet	P_{static}	0	Pa
Coils	Heat generation	340	kW/m^3
Inlet air temperature	T	293	K
Enclosure temperature	T	293	K
Boss, magnets, discs rotational speed	Ω	1500	rpm

The steady RANS equations (continuity, momentum and turbulence) have been solved in Fluent prior to solving the energy equation. A multiple reference frame approach has been employed. The κ-ϵ realizable turbulence model has been used for the closure of the system of equations. As a convergence criterion the residuals have been monitored. Furthermore the mass flow rate at inlet and outlet have been controlled. The three velocity components at a point in the middle of the air gap have been monitored during the iterations. The solution has been considered converged when the residuals reached the required values specified in Fluent, and when the mass flow rate and velocity components reached stability (were constant with iterations) at the monitored point. For all the simulations in this study when convergence was obtained all the residuals reached the magnitude of 10^{-5}, and the energy residual was in the order of 10^{-15}.

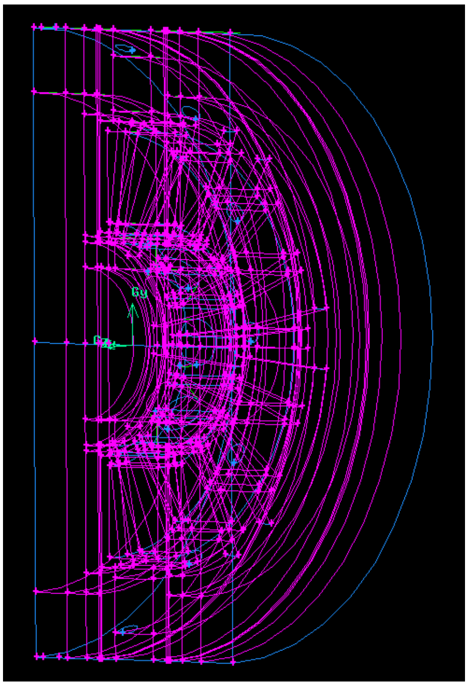

Figure 4.45: Durham generator model domain

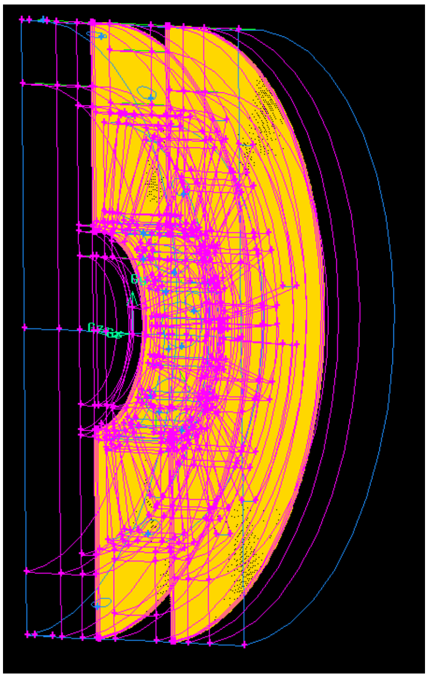

Figure 4.46: Running clearance mesh

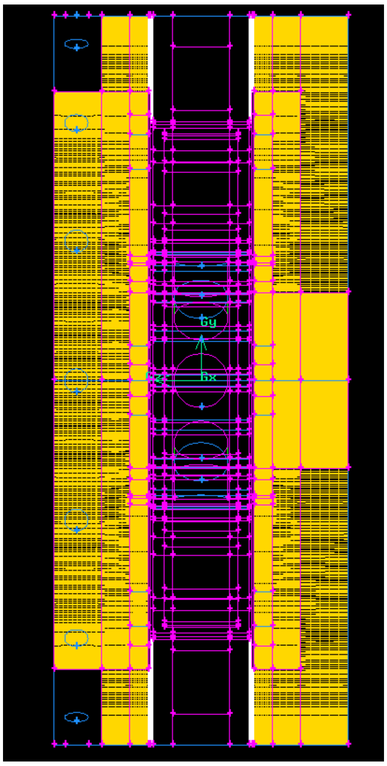

Figure 4.47: Hexahedral rotors' mesh

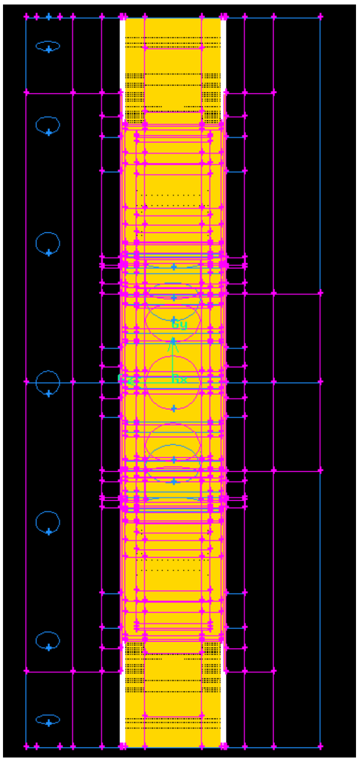

Figure 4.48: Hexahedral stator's mesh

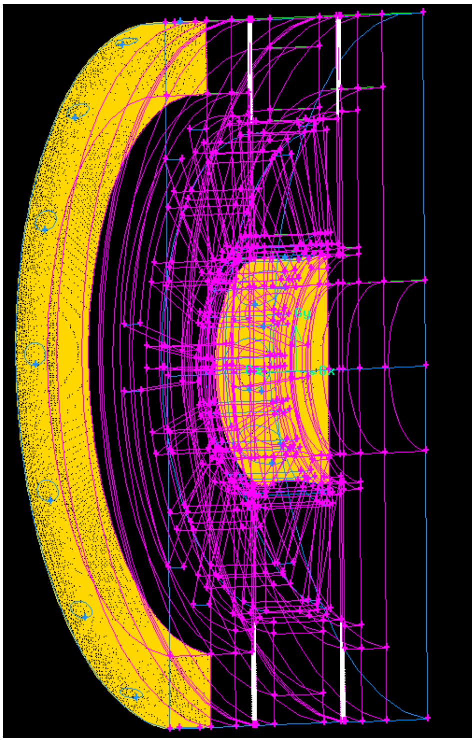

Figure 4.49: Tetrahedral mesh

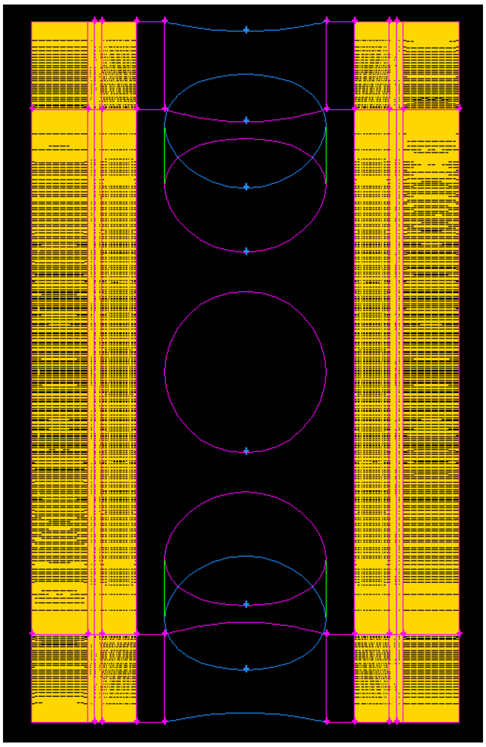

Figure 4.50: Boss mesh

4.3.2 Durham generator results

The mass flow rate through the machine has been estimated with the TSI hot wire anemometer which had previously been used for the simpler rigs. Measurements have been carried out at the generator's inlet along the vertical and the horizontal diameter. The simulations resulted in a mass flow rate of 7.2g/s whereas on the actual generator a mass flow rate of 6g/s was experimentally measured. The difference lies mainly in the inevitable approximations which had to be made in order to build the geometric model. As an example, the stator windings shape has been simplified as their geometry is quite irregular and protruding screws included in the real generator have not been modelled. It is also worth noting that the mass flow rates obtained here are very small compared to those in actual real sized generators. As a reference, a 2kW generator running at 2300rpm has a cooling mass flow rate of ≈ 100g/s. This significant difference is due to the very important area restriction at the generator's outlet (Fig. 4.51). In an actual generator the narrowest cross sectional area is usually the running clearance, whereas in this case it is the outlet area.

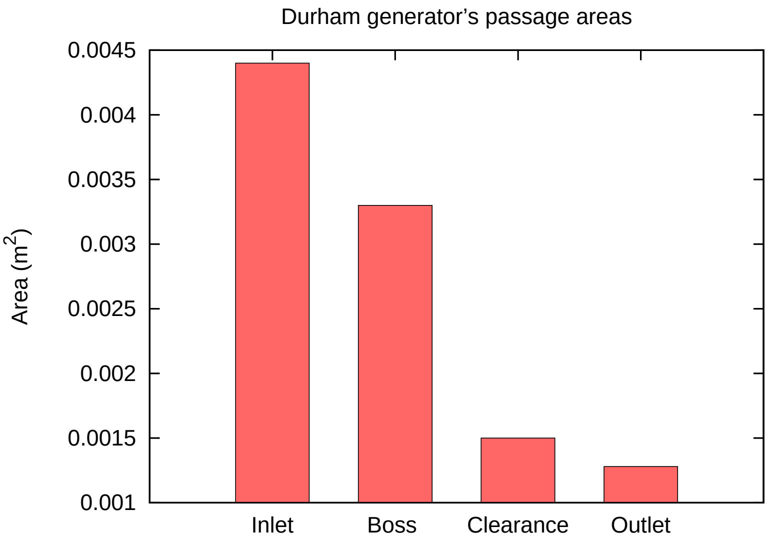

Figure 4.51: Durham generator's passage areas

The velocity contours on the vertical ($x = 0$) plane are shown in Fig. 4.52. The maximum velocities (V ≈12m/s) are obtained at the rotor outer radius where the tangential velocity is the highest. The symmetry of the velocity field with respect to the horizontal axis is noticeable. This is a consequence of neglecting the buoyancy effects. From the velocity contours it can be seen that boundary layers are present on the outer surface of the disc and that not all the air flows through the air gaps. The rise in the static pressure with the radius can be seen in Fig. 4.53. The pressure varies from -10 Pa at the inlet to 140 Pa on the casing surface. In the plot of velocity vectors in Fig. 4.54 the cooling air path is shown on the $x = 0$ plane. The air enters the generator in the axial (z) direction, then passes through the boss openings in the radial direction and through the running clearance. The velocity vectors on the $y = 0$ plane in Fig. 4.55 also show the prevailing axial flow at the inlet. On this plane, as opposed to the case of the $x = 0$ plane, after the bend in the radial direction the cooling air passes through the groove between the magnets and the velocity magnitude is greater.

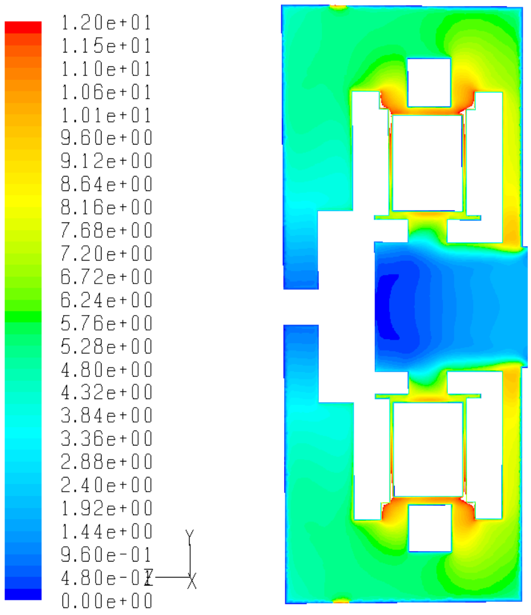

Figure 4.52: Velocity magnitude (m/s)

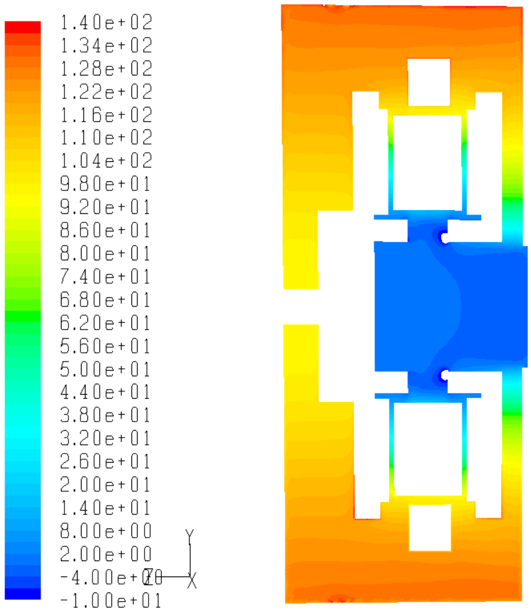

Figure 4.53: Static pressure (Pa)

Temperatures and heat transfer coefficients on the magnets and on the coils have been plotted in the radial direction in the location illustrated in Figs. 4.56 and 4.57, respectively. The temperature on the coils' surfaces reaches 337K and varies within a 0.5K range on both sides of the generator and can be considered to be independent of the radius and of the coil side. This is due to the high conductivity of the copper, and to the fact that the coils have been assumed to be made only of copper. This is a simplifying assumption because the real coils consist of enamel coated copper wire and the space between wires is filled with resin. The temperatures on a zy plane ($x = 0$) are displayed in Fig. 4.61 where the higher temperature of the air leaving the generator is evident. From the temperature contours on the zx plane ($y = 0$)

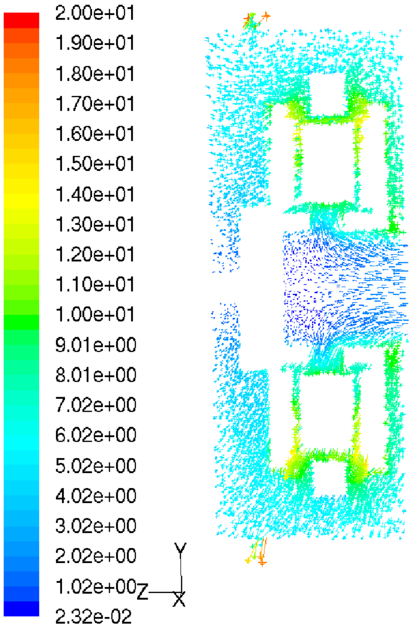

Figure 4.54: Velocity vectors (m/s) on $x = 0$ plane

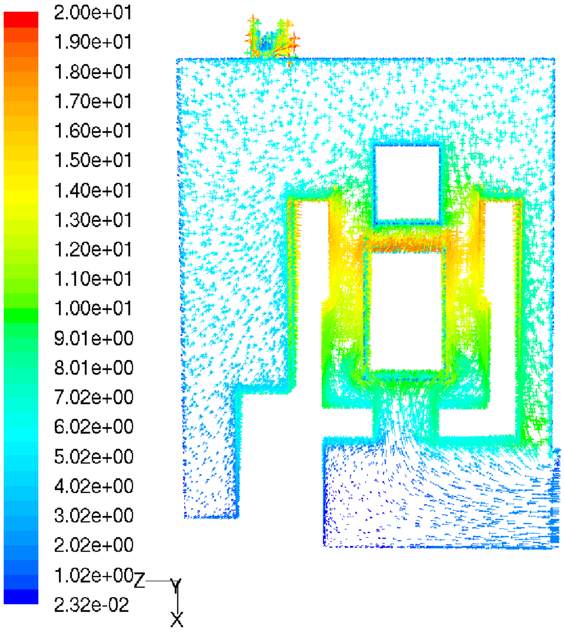

Figure 4.55: Velocity vectors (m/s) on $y = 0$ plane

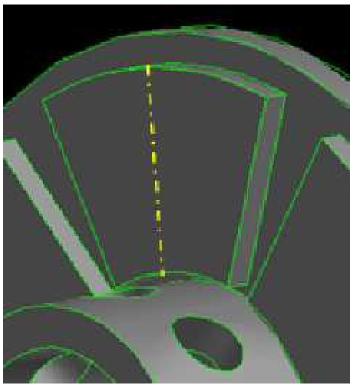

Figure 4.56: Magnet heat transfer coefficient location

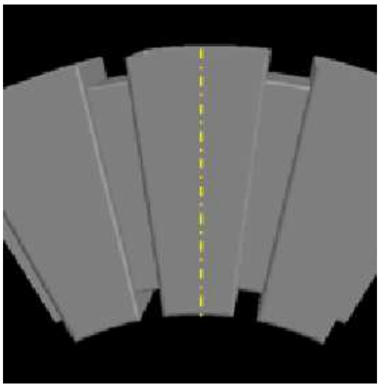

Figure 4.57: Stator heat transfer coefficient location

the thermal boundary layer on the stator is visible for both running clearances. The location with the highest temperature is also shown which corresponds to the stator part close to the stator holder annulus.

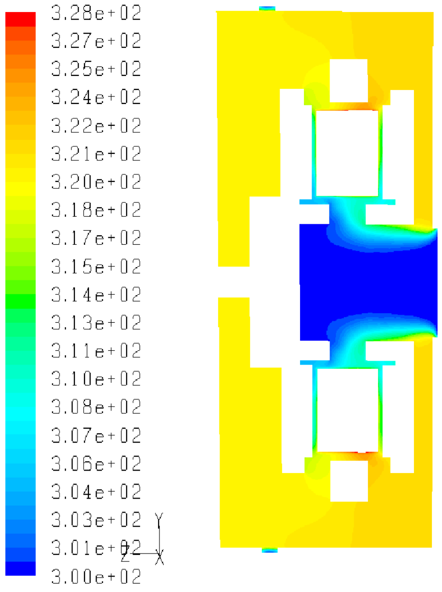

Figure 4.58: Static temperature (K); $x = 0$ plane

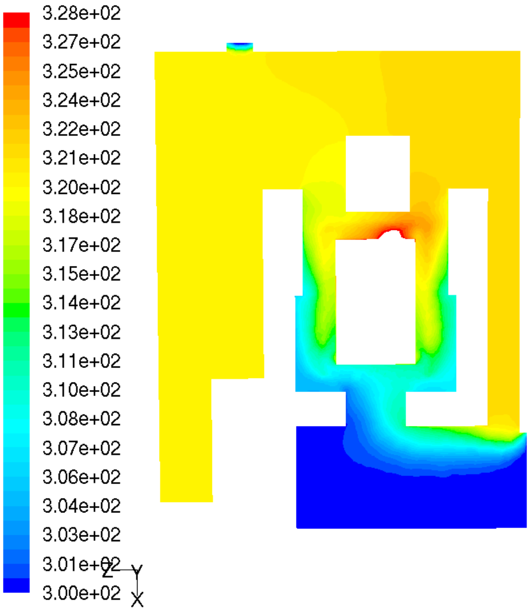

Figure 4.59: Radial plane static temperature contours (K); $y = 0$ plane

The local heat transfer coefficient has been calculated by using as a reference the local temperature in the middle of the running clearance as in Eq. 4.1.

The heat transfer coefficients in the radial direction on either side (left and right clearance) of the stator coils show very good agreement (Fig. 4.60). The heat transfer coefficients on the stator coils increase with radius and vary in a range between 30 and 73W/(m^{2}K). The stator coils have heat transfer coefficients lower than those on the magnets due to the lower flow velocity and lower shear stresses on the coils' surfaces. The heat transfer coefficients on both magnets are equal and increase with radius varying in a range between 40 and 105W/(m^{2}K). The equivalence of the heat transfer coefficients (Fig. 4.60) on either side of the coils

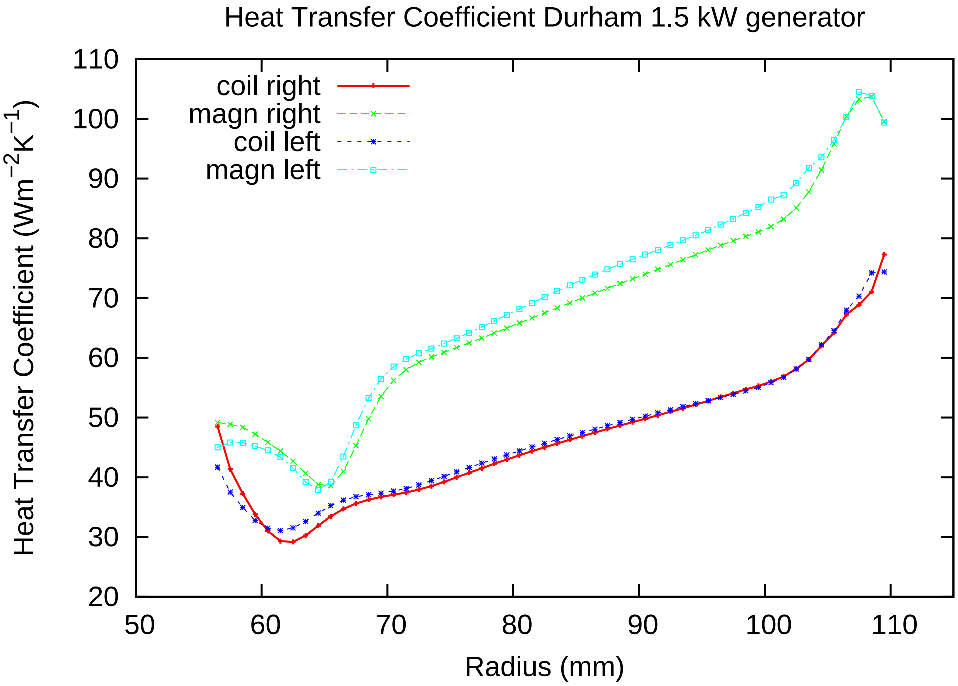

Figure 4.60: Generator's heat transfer coefficients

(left and right clearance) and on either magnet (left and right) shows that the inlet condition (the right clearance is the closest to the air intake and the left one is the furthest away) is not able to influence the heat transfer coefficient. Therefore, the heat transfer coefficient on both stationary surfaces (coils) and rotating ones (magnets) for the given clearance, magnet depth and speed only depends on the radius. Since the temperature on the coils' surface is varying in a narrow range (Fig. 4.61), the parameters which define the variation of heat transfer coefficient on the stator are the running clearance mid temperature and the heat flux. The heat transfer coefficients obtained for this machine are relatively low because of the low radial velocities in the running clearance. The heat transfer coefficients on the stator and on the rotor show the same pattern, although due to the higher shear stresses it is higher on the rotor. Due to the small outlet area, the mass flow rate through the generator (hence the radial velocity) is small and the heat transfer coefficient is only influenced by the tangential velocity.

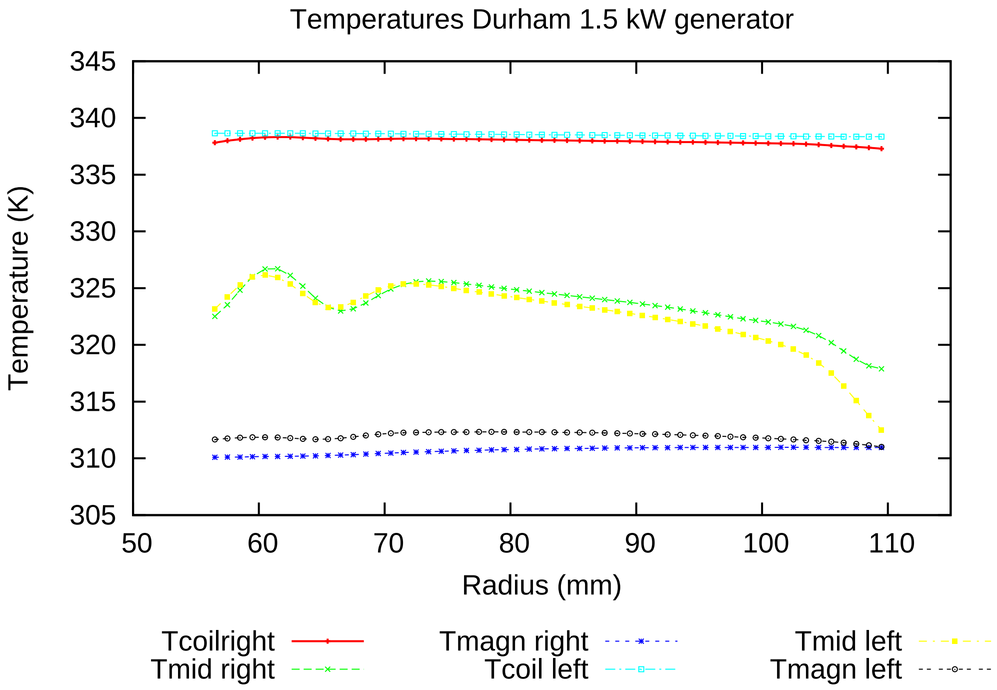

Figure 4.61: Radial temperatures

4.4 Conclusions

In this chapter two rotor-stator systems were analysed: the first one consisting of a flat rotor and a stator (*flat rotor rig*) and the second consisting of a rotor carrying protruding magnets and a stator (*magnet rig*). An experimental apparatus was built, together with CFD models of the two systems. A further simulation has been run for the model of the 1.5kW *Durham generator*. As a result of this study it can be concluded that:

- The CFD models are able to predict the mass flow rate through the rotating systems and through the Durham generator model with satisfactory accuracy. In the case of the flat stator the largest difference in the mass flow rate observed between the simulation and the experiment was about 9%. Considering the low absolute value of the mass flow rate obtained, and taking into account that the mass flow for the flat rotor case is solely due to the shear stresses on the rotor surface, this is a satisfactory result. The accuracy of the mass flow rate prediction from the magnet rig model consisting of a rotor with magnets was higher because of the higher absolute value of the mass flow rate due to the magnets acting as blades.

- Both steady and unsteady CFD models of the magnet rig produced information on temperatures which is in good agreement with measured data.
- A study of the mesh refinement demonstrated that for the system analysed a mesh with 13 cells across the running clearance is not sufficient to provide a mesh independent solution. Increasing the number of cells higher than 23 across the clearance does not lead to a further gain in temperature prediction accuracy. Furthermore, it has been found that the radial cell size does not affect the solution accuracy in terms of predicted velocities and temperatures.
- The stator heat transfer coefficient obtained from both steady and unsteady models of the magnet rig is in good agreement with the experimental value.
- No large scale transient effects have been found from the transient simulation, therefore the steady state MRF approach is an acceptable approximation which will be used to carry out further CFD studies.

Chapter 5

Validation of CFD results using the low speed large scale test rig

5.1 Description of the test rig

The CFD models which are used to obtain the heat transfer coefficient on the generator surfaces need to be validated against experimental data. For this purpose a test rig which is a scaled-up model of an actual AFPM machine has been designed by Mr. Chin Lim and built in the School of Engineering at Durham University. The actual design which has been used in the scaling-up process is that of the Durham AFPM Generator with a rated power of 1.5kW at a rotational speed of 1500rpm.

The scaled-up model has been built according to the theory of similarity in which in geometrically similar systems the Nusselt number is solely dependent on the Reynolds and Prandtl numbers. However, since the fluid used for the machine cooling is always air, the dependence of Nusselt number on the Prandtl number does not need to be considered. A scale factor of 4 has been used to obtain the dimensions of the low-speed large-scale perspex model of the AFPM generator. The critical dimensions of the Durham generator which have been re-created in the scaled-up model are: the running clearance, the magnet depth, the rotor and stator inner and outer radii and the rotor inlet diameter. Some of the dimensions, such as the rotor thickness, have not been considered in the scaling process. This is because they have been found to have a negligible influence on the flow and heat transfer inside the machine. This was established through CFD analysis carried out with Fluent. Therefore, the rotor thickness has been determined in such a way that it withstands the stresses arising from the rotational motion and the weight of the rotating parts. The test rig main dimensions are shown in Table 5.1.

Table 5.1: Test rig dimensions

Dimension	Symbol	(mm)
Rotor outer radius	R_{out}	400
Stator outer radius	R_{st}	440
Stator inner radius	R_{st_in}	200
Front clearance	c_{front}	10
Back clearance	c_{back}	9
Magnet depth	m	26
Inlet diameter	D	150
Heating mats thickness	e	2.5

The rotor outer radius has been chosen as the characteristic length to calculate the Reynolds number shared by the *Durham generator* and the large scale test rig. In order to fulfill the similarity requirements, the large scale model of the generator had to have the same peripheral Reynolds number Re_{out}:

$$Re_{out} = \frac{\rho \Omega R_{out}^2}{\mu}, \tag{5.1}$$

where Ω is the rotational speed, R_{out} the rotor outer radius, ρ and μ the air density and viscosity, respectively.

The similarity relationship expressed through the equivalence of Reynolds numbers $Re_{out,Gen} = Re_{out,Rig}$ allowed the finding of the required rotational speed for the large model:

$$\Omega_{Rig} = \Omega_{Gen} \frac{R^2_{out,Gen}}{R^2_{out,Rig}} \tag{5.2}$$

From Eq. 5.2 it can be seen that for similar systems the rotational speed necessary to guarantee a thermodynamic similarity between the *Durham generator* and the large-scale test rig is independent of the choice of the characteristic length.

This is a consequence of the similarity of the two systems where the ratio between an arbitrary quantity (e.g. the clearance) considered in the two systems is constant and equal to the scale factor.

It has been calculated that a rotational speed of the Durham generator of 1500rpm corresponds to a speed of 93rpm for the large perspex model by using Eq. 5.2.

The larger dimensions of the test rig compared to the original generator allows an easier access to the running clearance and to the parts of the generator where measurements need to be carried out. Large dimensions also reduce the disturbing effect of the measuring tools, such as thermocouples, heat flux sensors and pressure probes on the air flow.

The model built is shown in Fig.5.1 and Fig.5.2 and consists of an annular stator, a stator holder and two rotors each carrying 16 sectors representing the magnets. The stator, its holder, the rotors and the magnets are made of Perspex.

Figure 5.1: Test rig: front view (air inlet)

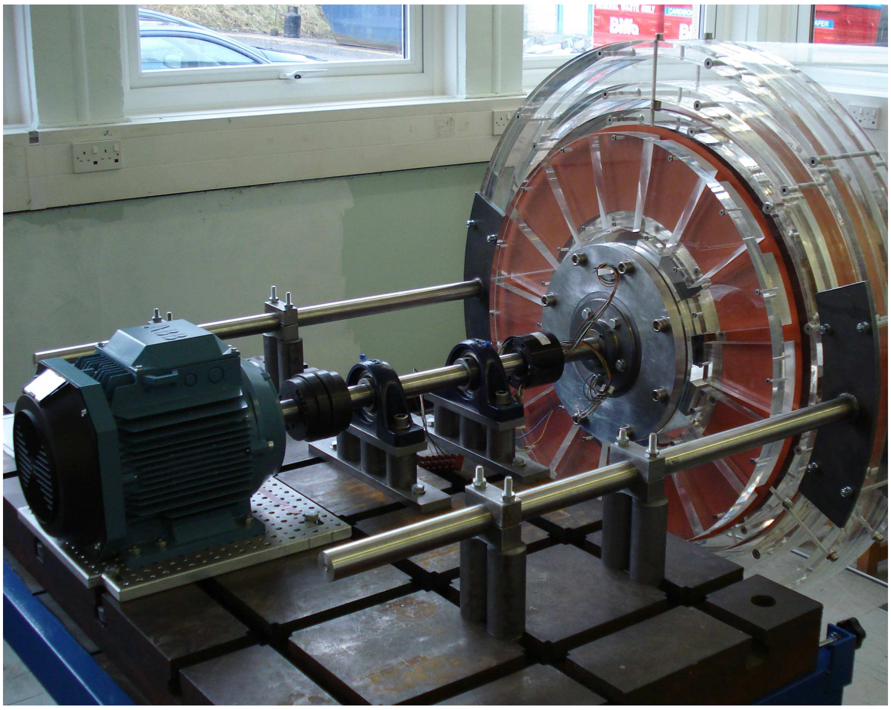

Figure 5.2: Test rig: back view

Since this polymer has a density seven times lower than the density of steel and three times lower than the one of aluminium, the model is relatively light weight. As a consequence considerable savings could be achieved due to the use of smaller and lighter supporting units, smaller diameter shaft and smaller bearings. The other advantage of Perspex is its transparency which will allow to carry out flow visualisation experiments inside the clearance in the future.

The perspex model has been built on the basis of the Durham generator. However, there are two components which are different from those in the Durham generator: the magnets and the boss are similar to those in the generators built by Cummins Generators Technology. Since the rotational speeds in commercial generators could be lower than 1500rpm, in order to have a frequency output as close as possible to the standard 50Hz, the number of pole pairs needs to be increased. This is achieved by augmenting the number of stator coils and the number of magnets on the rotor. Therefore the commercial generators have 16 magnets per rotor rather than 6 like in the Durham generator. The perspex model has been built with 16 magnets on each rotor. In actual generators the boss plays an important role in their cooling. The air enters through a circular opening at the front of the rotor, it then flows through the running clearance due to the rotation of the boss and of the magnets which act as the blades of a radial compressor. The second function of the boss is to provide a structural support for the rotors. The boss consists of 8 aluminium prisms. The number of prisms has been chosen to obtain a necessary periodicity in the generator design. Etched foil silicone rubber heaters have been glued on the outer surfaces of the stator (Fig. 5.3). Four heaters were used: one on each of the annular faces, one on the stator's inner cylinder, and one on the stator's outer cylinder. The heat dissipated in the heating mats is controlled by varying the electrical current in the mats using variac autotransformers. The stator has been made of 30mm thick extruded perspex sheets and in the original design the inner surfaces of the stator were planned to be heated by rubber heaters. However the CFD simulations carried out on the preliminary design demonstrated that because of the perspex low conductivity the temperatures on the stator outer surfaces would have been too low. In order to calculate the heat transfer coefficient on the stator walls, a sufficient temperature difference ($\approx 10°C$) between the inlet temperature and the wall temperature needs to be obtained and this would not have been possible. Two options were considered: rebuilding the stator with a higher conductivity material (aluminium) or placing the heaters on the stator's outer surface.

Numerical simulations based on the first option were performed and the results presented in non-dimensional form in [73]. However, building an aluminium stator like the one presented in the CFD model in [73] would be prohibitively expensive therefore the second option has been adopted in the test rig and a new computational model has been built by taking into account the modifications. A CAD drawing of the stator carrying the heater mats is shown in Fig. 5.3.

The different size of the clearances at the front and at the back of the generator allowed their effect on the heat transfer coefficient on the stator annular surface to be observed. The two rotors connected by the boss were driven by an ABB 5.5kW induction motor. The induction motor speed is controlled by an ABB 5.5kW 380-480V 11.9A, 3-phase inverter.

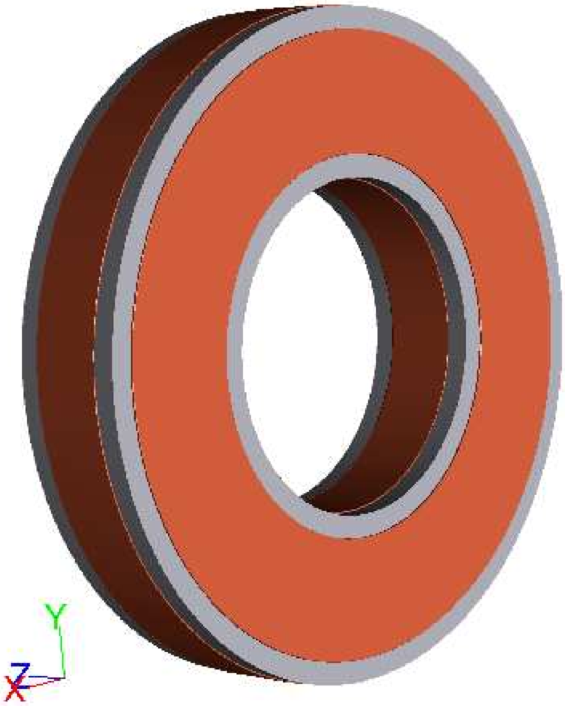

Figure 5.3: Stator with heating mats

5.2 Measuring equipment

The convective heat transfer coefficient on the stator surfaces is measured by using an Omega HFS3 heat flux sensor which also has an integrated K-type thermocouple to measure the wall temperature. Omega SA1 T-type thin film thermocouples have been used to measure the surface temperatures. The heat flux sensors calibration procedure and the set-up of thermocouples are described in detail in section 4.2.1. Heat flux sensors and thermocouples have been attached directly on the heating mats by using TESA acrylic double-sided adhesive tape. The positions of the thermocouples and those of the heat flux sensors on the stator are shown in Fig. 5.4. The heat flux sensors and thermocouples are directly connected to PICO TC-08 USB data-loggers, the heat fluxes and temperatures are recorded at 1s intervals.

The mass flow rate in the test rig has been estimated by measuring the air

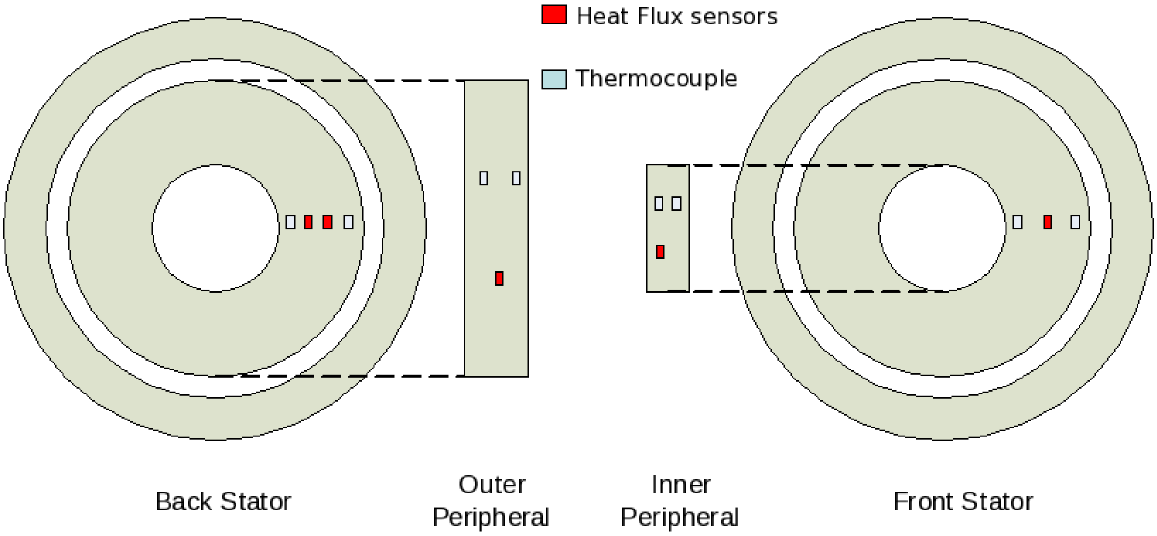

Figure 5.4: Position of the thermocouples and heat flux sensors

velocities at the test rig inlet. To do so the same equipment and the same procedure described in section 4.1.3 have been used. The mass flow rate has been estimated by measuring the velocities along the horizontal and vertical directions on the inlet by means of the hot wire portable anemometer TSI and by integrating the experimental readings over the area.

5.3 Experimental test procedure

The silicone heating mats were heated for 3 hours until a thermal steady state was reached prior to starting the electric motor connected to the shaft driving the rotors and recording the heat transfer coefficient measurements. The signals from the thermocouples and from the heat flux sensors were logged in the computer at 1 second intervals for four hours until a new thermal steady state was reached. Every experiment was repeated three times to minimise the experimental error.

5.4 CFD model

A three dimensional CFD analysis of the test rig has been performed. The CFD model has been built by simulating the air domain inside the test rig model. The solid components of the test rig have not been included in the computational mesh. This approach was used under the assumption that the heat transfer coefficient is independent of the thermal boundary conditions and of whether the solids were included or not in the model. Fig.5.5 shows the CFD model. An additional fluid domain has been considered around the generator due to the absence of an enclosure.

Since the generator has a geometrical periodicity of 45°, only $1/8^{th}$ of it has been modelled and periodic boundary conditions have been applied to the cut planes. The geometric periodicity is 45° because the rotor carries 16 magnets which have 22.5° (360/16) periodicity and in the boss there are 8 prisms with 45° (360/8) periodicity. 45° is the minimum angle divisible by 45 and 22.5.

Exploiting the periodicity of the geometrical features of the generator allowed a considerable reduction of computational time. At the same time the mesh could be refined and a large number of elements could be used to create the mesh in the running clearance.

The mesh shows the inlet, outlet, and periodic boundaries and consists of 8 million hexahedral elements (Fig. 5.6).

The steady state RANS equations have been solved in Fluent to determine the air flow and temperatures. The Multiple Reference Frame (MRF) method has been used in order to take account of the rotation of the generator components and of the cooling air. The realizable $\kappa - \epsilon$ model has been chosen for the closure of the system of equations.

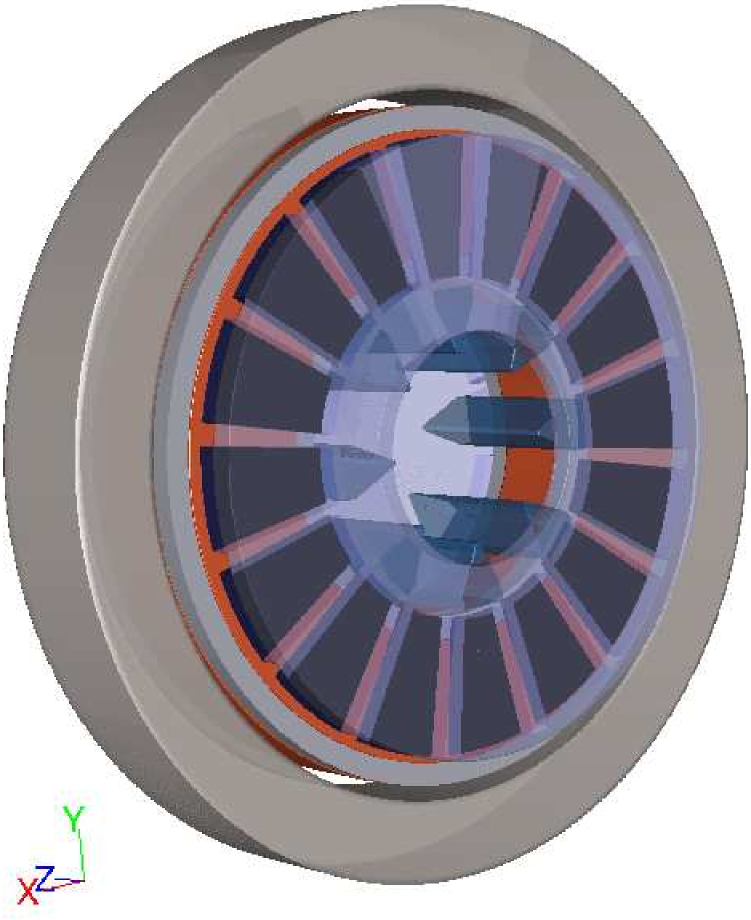

Figure 5.5: Test rig: CFD model

Due to the relatively small temperature differences the radiation between the stator and the rotor has been neglected and it has been assumed that the heat transfer is solely due to convection.

The air density has been considered to be constant due to the relatively small temperature variations to which the rig is subjected (≈ 25K) i.e. the buoyancy effects and the natural convection heat transfer were neglected. This assumption is valid for flows with high velocities but, it needs to be verified for the model test conditions. This assumption was made with the aim of reducing the size of the

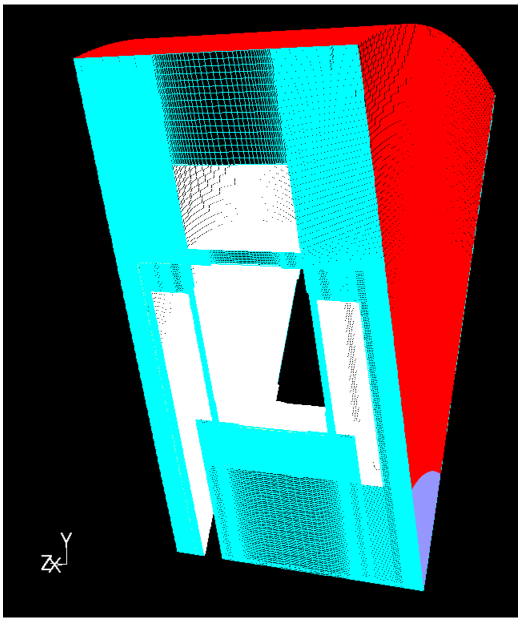

Figure 5.6: Test rig: computational mesh

computational domain. If the natural convection were to be considered, then the model of the rig would not have its 45° periodicity and, as minimum, half of the test rig geometry would have to be numerically simulated.

Table 5.2 shows the boundary conditions used in the CFD modelling process.

Table 5.2: Test rig boundary conditions

	Quantity	Value	Unit
Inlet	P_{tot}	0	Pa
Outlet	P_{static}	0	Pa
Front heating mat	Heat Flux	670	$\mathrm{W/m^2}$
Back heating mat	Heat Flux	691	$\mathrm{W/m^2}$
Outer heating mat	Heat Flux	479	$\mathrm{W/m^2}$
Inner heating mat	Heat Flux	862	$\mathrm{W/m^2}$
Inlet	Air temperature	298	K
Angular speed	Ω	93	rpm

A vertical section (zy plane) of the machine is displayed in Fig. 5.7 to highlight the air flow direction.

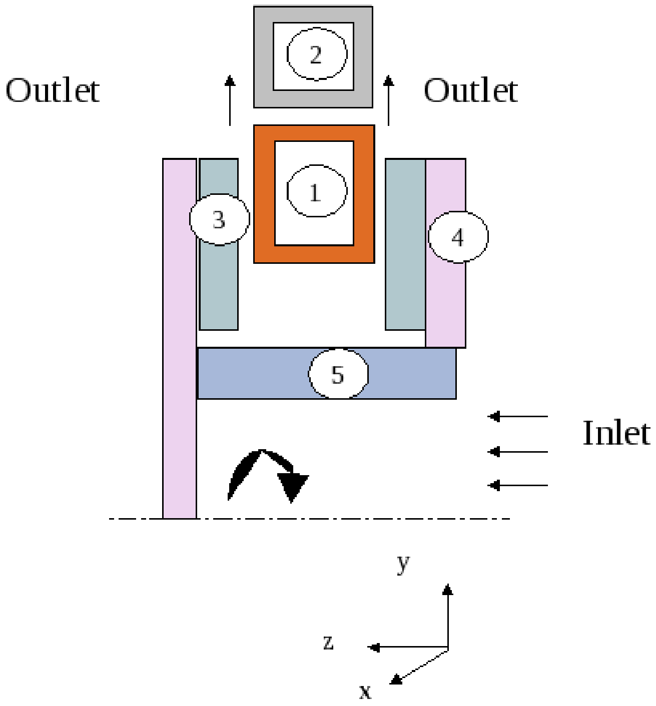

Figure 5.7: Vertical section of the rig: 1. Stator, 2. Stator holder, 3. Magnets, 4. Rotor, 5. Boss

5.5 Results

5.5.1 Air flow

To determine whether the CFD model is capable of accurately predicting the flow in the rig, the mass flow rate has been estimated using a portable hot wire anemometer. Velocity readings have been taken in the horizontal and vertical directions in the vicinity of the rig inlet. The average value of these velocities multiplied by the air density and the inlet area has been compared with the mass flow rate predicted by the CFD steady and unsteady simulations (Fig. 5.8).

The pathlines coloured by the particle ID demonstrate that the outer portion of the inlet axial flow is drawn into the front clearance (Fig. 5.9) whilst the inner portion continues to flow through the back clearance (Fig. 5.10). The pathlines in

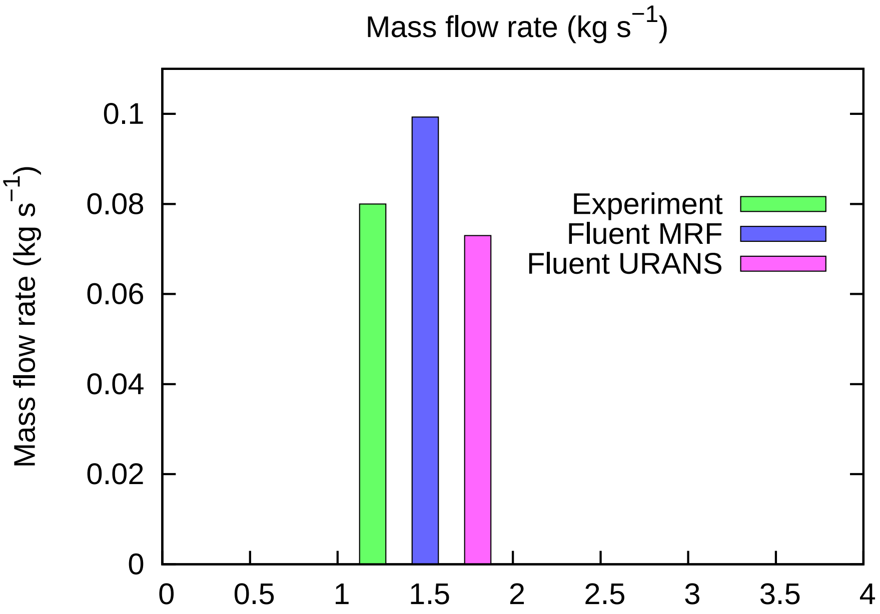

Figure 5.8: Air mass flow rate through the test rig

Fig. 5.10 show that a recirculation region exists on the suction side of the boss-prisms. This results in low velocities in the relevant recess located at the outlet of the prism suction region. Vice versa, the high pressure on the prism pressure side is the reason for the high velocity inside the clearance in the region at the same angular location as on the prism pressure side. The velocity magnitude

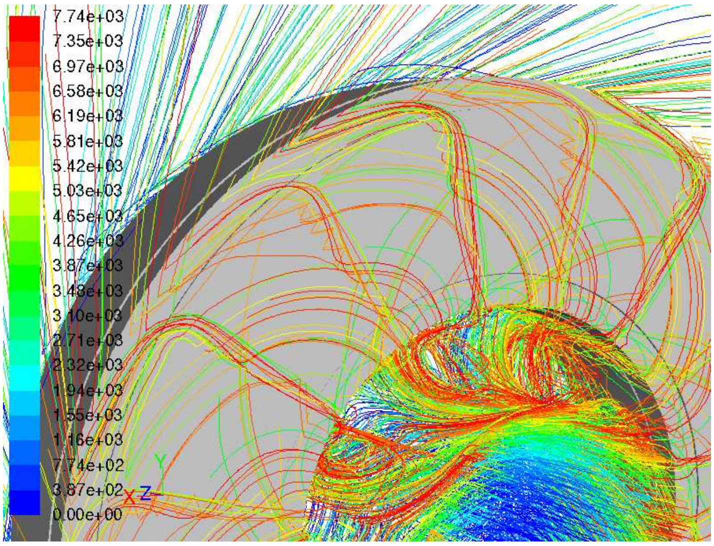

Figure 5.9: Pathlines on the front clearance coloured by particle ID

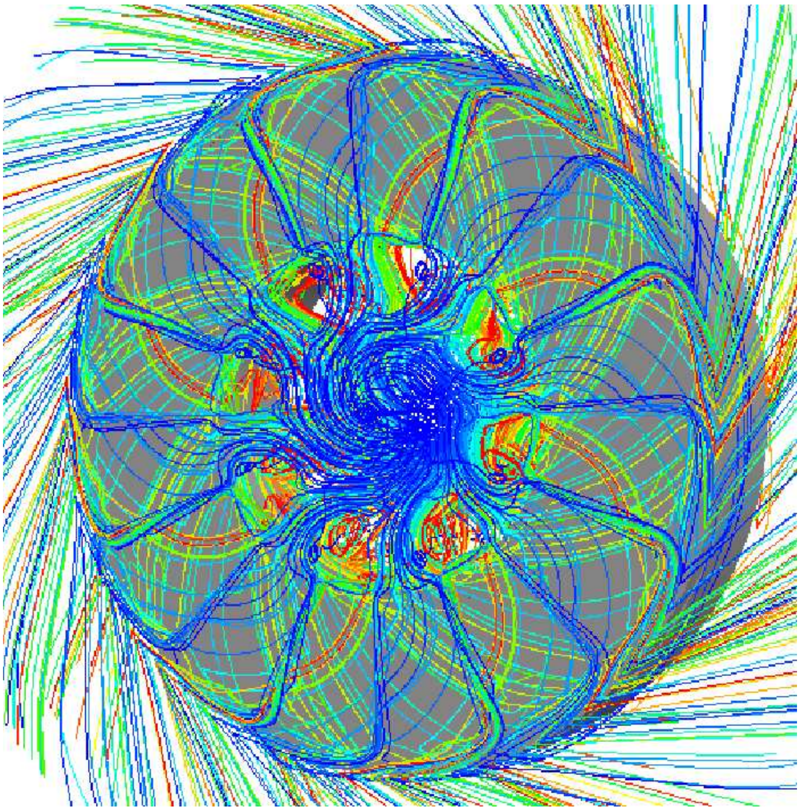

Figure 5.10: Pathlines on the back clearance coloured by particle ID

contours on a radial plane are shown in Fig. 5.11. Developing boundary layers are observed on the rotors outer surfaces. The contours of velocity magnitude show that the additional air domain modelled around the rig is large enough to contain the boundary layers formed on the rotor. The two clearances, and in particular the inlet of the back clearance, are the areas where the highest velocities have been calculated. This corresponds to the region with the highest heat transfer coefficient on the stator annular surface.

The radial velocity in the back clearance (v_r=2.2m/s at the clearance inlet) is higher than in the front one (v_r= 1.3m/s at the clearance inlet) because of its smaller size (Fig. 5.12). A negative radial velocity region (v_r = -4m/s) is visible at the front rotor inlet where the air intake occurs.

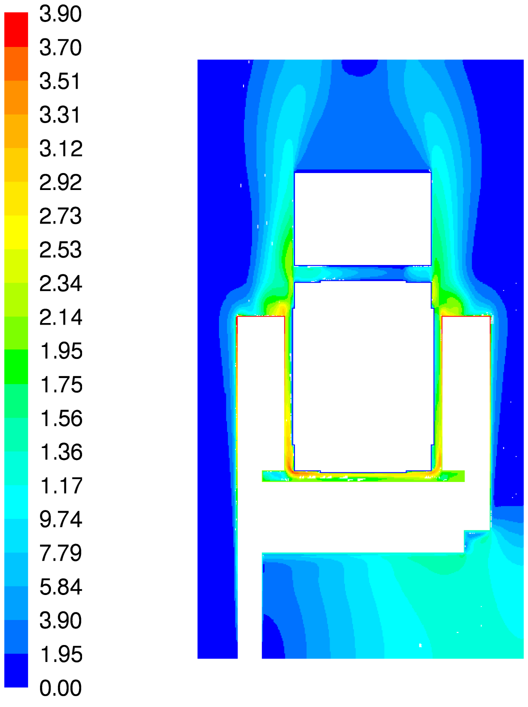

Figure 5.11: Velocity magnitude (m/s)

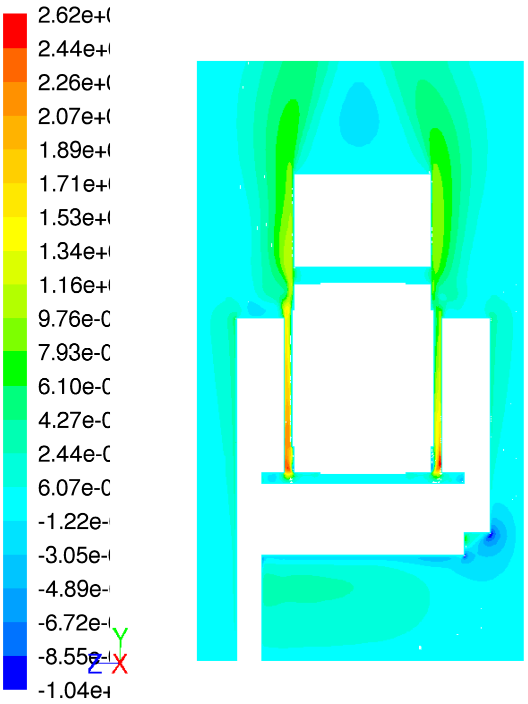

Figure 5.12: Radial velocity (m/s)

5.5.2 Heat transfer

The heat transfer coefficient has been calculated using the room temperature as a reference. This was due to the inherent difficulty of measuring the local air temperature inside the running clearance.

In order to calculate the heat transfer coefficient from the experimental rig the value of the heat flux, the wall and the room temperatures were measured.

The heat transfer coefficient on the stator back mat was greater (on average 30%) than the one on the front mat (Fig. 5.13 and 5.14). This confirms that a low clearance is beneficial for increasing the heat transfer coefficient on the stator surface. For clarity the whole stator is displayed including the surfaces not covered by the heating mats where an adiabatic boundary condition was specified. The heat transfer coefficient on the outer cylinder is very low due to the small velocities between stator and stator holder. In the actual test rig, the heat transfer there is dominated by the natural convection.

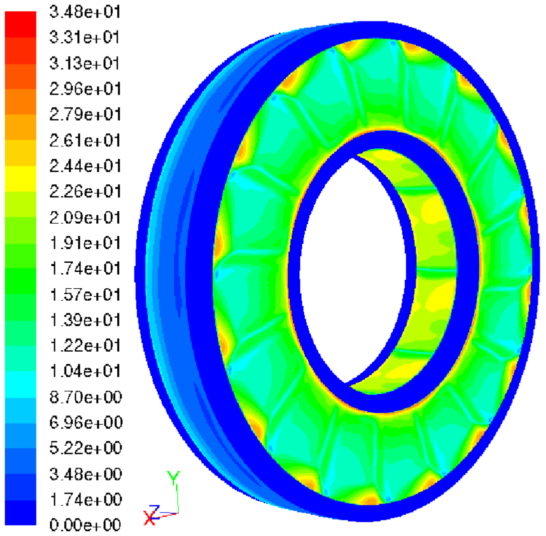

Figure 5.13: Stator front clearance heat transfer coefficient (W/(m^{2}K))

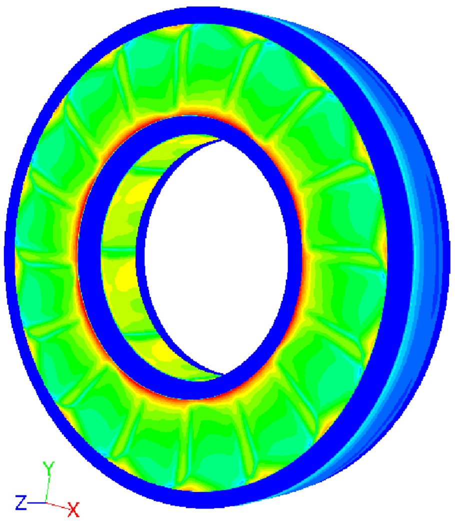

Figure 5.14: Stator back clearance heat transfer coefficient (W/(m^{2}K))

The value of circumferential averaged heat transfer coefficient from the CFD simulation has been obtained on the stator at four locations: top, bottom, front and back. For each of these locations the heat transfer coefficient has been obtained on radial lines spaced in one degree steps and then the average over the 45° segment has been calculated. The heat transfer coefficient has been calculated over the whole annular front and back heating mats which have an inner and outer radius of 250mm and 410mm, respectively. The error indetermination of the heat transfer coefficient caused by measuring tools (the data logger, the thermocouples, the heat flux sensors and the test rig dimensions measurements) has been presented in the graphs by means of error bars. It has been calculated that these lead to an experimental error of ±15%.

The heat transfer coefficient on the stator front and back annular surfaces shows the characteristic decreasing slope (Fig. 5.15). On the back stator the heat transfer coefficient decreases from its maximum value of 60W/(m^{2}K) at the inner radius of 260mm to its minimum of 20W/(m^{2}K) at the outer radius of 380mm.

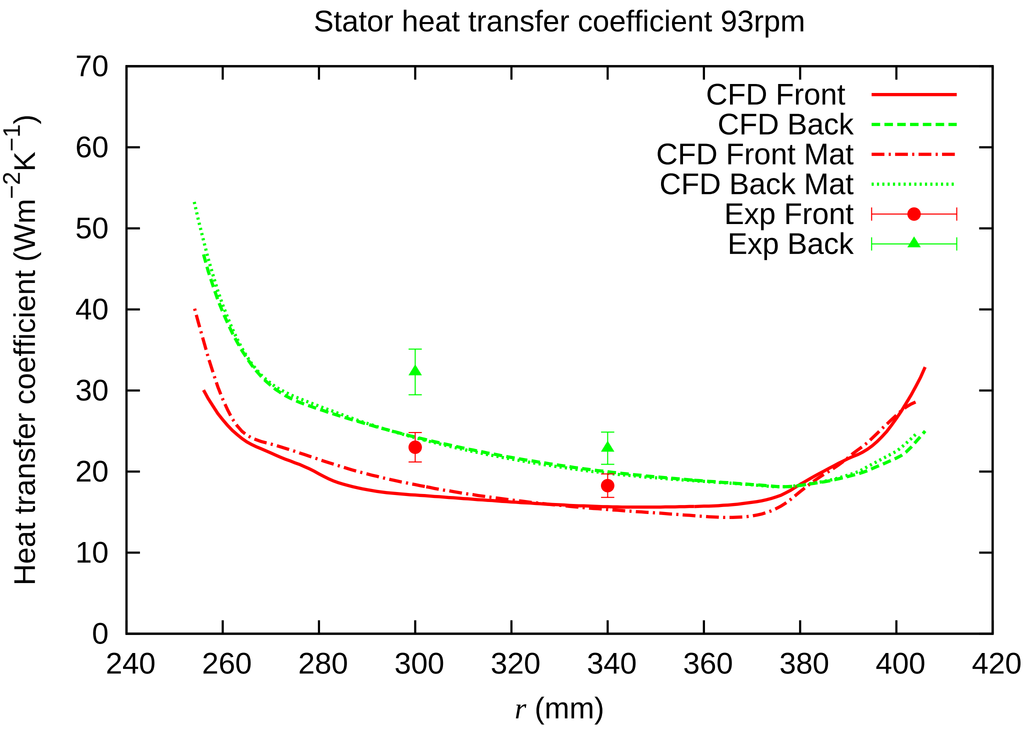

Figure 5.15: Heat transfer coefficient on the front and back stator annular surfaces

The higher velocity magnitude (due to high radial velocity) at the clearance inlet causes a higher heat transfer coefficient. The lowest velocity magnitudes at the mid radius corresponds to the lowest heat transfer coefficient and to the highest temperatures on the stator annulus. The agreement between the numerical and the measured heat transfer coefficient on the stator annular mats is reasonably good with the CFD always predicting the lower heat transfer coefficient value. The highest discrepancy is observed at the inner radius ($r = 300$mm) for both the front and the back annular mats. At this radius the difference is 25% and 36% for the front and back mats, respectively. At the higher radius ($r = 340$mm) the agreement is better and the discrepancy is reduced to 12% and 7% on the front and back of the stator, respectively.

The heat transfer coefficient has also been obtained over the inner and outer mats for the whole axial span (137mm $< z <$ 237mm). The axial coordinate z has been measured from the edge of the front stator.

The beneficial effect of the boss is evident when the two heat transfer coefficients on the stator's inner and outer cylindrical surfaces are compared (Fig. 5.16). The heat transfer coefficient on the inner surface is uniform (about 27W/(m^{2}K)) and independent of the axial position. A good agreement is observed for the heat transfer coefficient on the stator inner cylinder with a difference between CFD and empirical results of 8%. The heat transfer coefficient on the outer stator's cylindrical surface is the one which has the highest difference between the CFD prediction and the experimental measurement (61%). Since the effect of the forced flow is negligible on the outer cylindrical mat, the heat exchange in this area is mainly attributed to the natural convection which had to be ignored in the CFD model, hence the strong discrepancy.

Due to the CFD constantly under-predicting the heat transfer coefficient on the stator surfaces, the impact of application of other turbulence models, of including the solids mats and of the thermal boundary conditions on the magnitude of the heat transfer coefficient have been investigated. The heat flux boundary condition has been changed and additional simulations have been run with other heat fluxes from the heating mats. Since in the main case the heat flux was specified to be between 479 and 862W/m^2 depending on the silicon mat, the additional CFD simulations have been run with 200 and 1000W/m^2 heat fluxes. The energy equation has been solved based on the previously obtained flow solution. The results for the case with the heat fluxes of 200W/m^2 and 1000W/m^2 are not presented here because they exactly coincide with those in Fig. 5.15 and Fig. 5.16. The reason for this is the independence of the heat transfer coefficient from the thermal boundary conditions. The heat transfer coefficient only depends on the flow which develops in the clearance. A higher heat flux specified on a wall will cause an increase on the wall temperature to keep the heat transfer coefficient constant.

A further attempt has been made to investigate the dependency of the heat transfer coefficient on the inlet boundary conditions. At the inlet, in addition to the pressure boundary condition values of the hydraulic diameter and the turbulence intensity have been specified. Further simulations have been run with different values of the hydraulic diameter and the turbulence intensity. It has been found that neither the mass flow rate through the domain nor the heat transfer coefficient on the stator surfaces are affected by the value of the above two parameters.

In addition to the $\kappa-\epsilon$ turbulence model, the SST $\kappa-\omega$ model has been used and no noticeable differences in the mass flow rate and in the heat transfer coefficient on the stator surfaces have been obtained. The results presented to this point have been obtained without modelling the solid components which constitute the rig.

Additional simulations have been run by modelling the solid heating mats. Simulations with two values of the heat generation 200kW/m^3 and 340kW/m^3 from the solid mats have been run. Another simulation has been run by setting the temperature on the inner faces of the mats (the ones not in contact with the cooling air) to 400K.

In Fig.5.15 and 5.16 the results for the model including also the meshed mats and a heat generation of 340kW/m^3 are shown; they are indicated in the label with 'Mat'.

The heat transfer coefficient obtained from the model including the solid mats and the one including only the fluid region of the test rig confirmed the assumption previously made that the heat transfer coefficient is independent of the modelling of solids and independent of the thermal boundary conditions used.

There is an equivalence of heat transfer coefficients in a model where solids are included and in one where only the fluid is modelled, even if the temperatures and heat fluxes obtained in the two models are different.

It can be concluded that if the interest lies in the heat transfer coefficient, significant preprocessing and computational effort can be saved by excluding the generator's solid components from the model. However, if the solids are not included in the model then the temperatures obtained from the numerical simulations will be different from the measured ones and their comparison would be meaningless.

A conclusion can be drawn that the CFD model built by considering forced convection only underestimates the magnitude of the heat transfer coefficient on the stator. This was demonstrated at all locations where experimental data was available for comparison. The location where this is most evident is on the stator's outer cylinder over which the air velocity is negligible therefore nearly the whole rate of heat transfer recorded in the experiment can be attributed to the natural convection occurring on this surface. In the next section a comparison between the

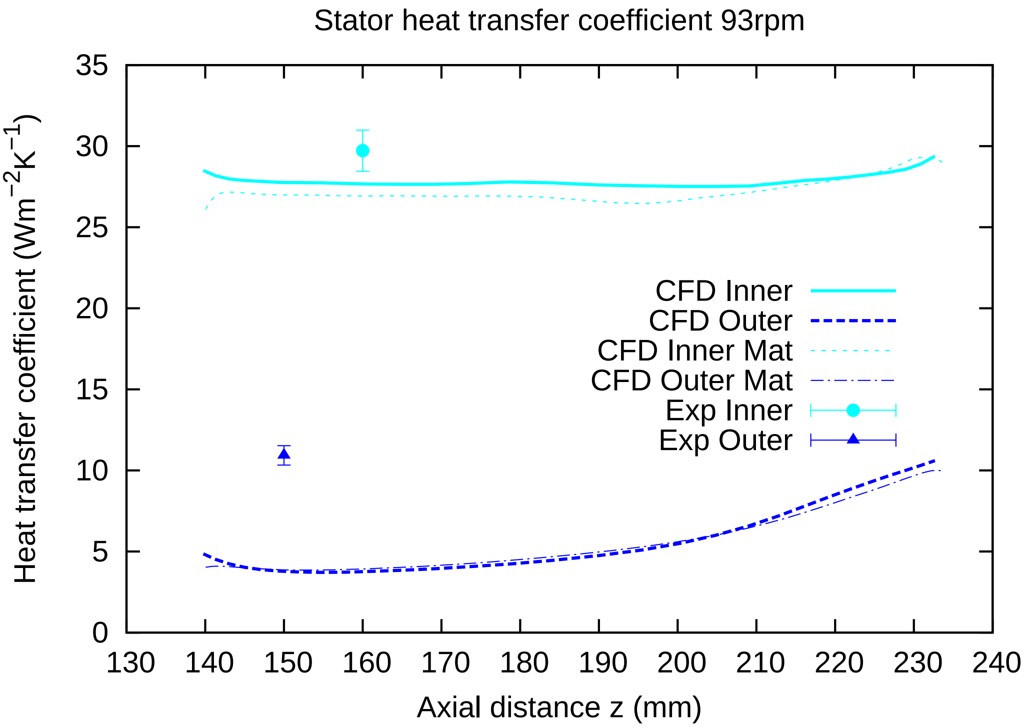

Figure 5.16: Heat transfer coefficient on the stator outer and inner cylindrical surfaces

effects of the forced convection from the experimental and from the CFD results is presented.

5.6 Forced convection comparison

In all the CFD models the effect of the natural convection has been previously neglected. This is a reasonable assumption as long as the buoyancy effect is negligible compared to the inertial forces [74]. As described in [75] this can be checked for a particular case by considering the ratio between the Grashof number and the square of the Reynolds number. The Reynolds and Grashof numbers are defined as:

$$Re_L = \frac{u_\infty L}{\nu} \tag{5.3}$$

and

$$Gr_L = \frac{g\beta\left(T_w - T_\infty\right)L^3}{\nu^2}, \tag{5.4}$$

where β is the coefficient of volumetric thermal expansion (β=3.3 for air); T_w is the wall temperature; ν is the kinematic viscosity ($\nu = 16.2 \times 10^{-6}\mathrm{m}^2/s for air$);T$_\infty$ is the free stream temperature (T_∞=298K); u_∞ is the free stream velocity and L is the distance from the leading edge of the vertical plate. If the ratio $(Gr_L/Re_L^2) << 1$ then the free convection can be considered negligible and the forced convection is the only mechanism of heat transfer.

If $(Gr_L/Re_L^2) >> 1$ then the opposite is true and the buoyancy effects play a predominant role in the heat transfer phenomenon.

However, when $(Gr_L/Re_L^2) \approx 1$ the forced and natural convection contribute in equal terms to the heat transfer.

For the points on the stator annular heating mats considering a distance from the leading edge $L = 0.06$m it can be found that (Gr_L/Re_L^2)=1.35. This corresponds to the condition in which the natural and the forced convection both contribute to the heat transfer.

This kind of flow is called ‘mixed convection flow’ and the natural convection could either be augmenting or cancelling the effect of the forced convection as suggested in [76]. These two are commonly referred to as ‘assisting’ and ‘opposing’ effects.

In the ‘assisting’ situation the buoyancy forces act along the forced flow as shown on the left in Fig. 5.17. The resulting heat transfer is obtained as the superimposition of the natural and the forced convection Nusselt numbers considered with the exponent n as shown in Eq. 5.5:

$$Nu^n_{mixed-assisting} = Nu^n_{forced} + Nu^n_{natural} \tag{5.5}$$

In the 'opposing' case the buoyancy forces act in the direction opposite to the forced flow like on the right in Fig. 5.17. The resulting heat transfer is obtained by subtracting the Nusselt number due to the natural convection from the one due to the forced convection (Eq. 5.6).

$$Nu^n_{mixed-opposing} = Nu^n_{forced} - Nu^n_{natural} \tag{5.6}$$

The exponent n is a correlation parameter based on the particular flow pattern. It has been rationalised by Churchill for flows around immersed bodies [77] and in channel flows [78]. Various configurations of uniformly and isothermally heated vertical planes were analysed and it was found that n = 3 is a good approximation. However this exponent is dependent on the flow patterns, on the boundary conditions, and on the reference temperature used for the calculation of the heat transfer coefficient in the Nusselt number expression. Therefore for the test rig it is impossible to use one of these case-specific exponents.

Instead, further experiments were carried out to find the effect of the natural convection in the large scale test rig. Additional heat flux sensors were added on both sides of the test rig front clearance (Fig. 5.17). By measuring the heat transfer coefficient on both sides of the stator surface the effect of the natural convection could be calculated by subtracting Eq. 5.6 from Eq. 5.5 which leads to:

$$Nu_{mixed-assisting} - Nu^{n}_{mixed-opposing} = 2 \times Nu^{n}_{natural} \tag{5.7}$$

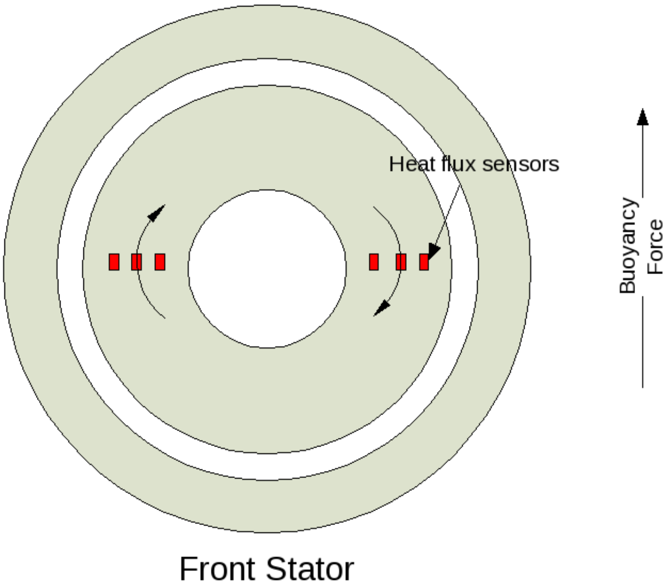

Figure 5.17: Heat flux sensors' position for mixed convection investigation

The mixed assisting and opposing convective coefficients were measured with the discs rotating at the speed of 93rpm, whereas the natural convection coefficients were measured with the rig stationary. To measure the natural convective coefficient the electric power supplied to the heating mats was such as to obtain the same temperatures on the stator walls as in the case with the rotors moving at the angular speed of 93rpm. Table 5.3 shows the assisting (first row), the opposing (second row), and the natural convection (third row) convective coefficients. The exponent n was calculated by Newton-Raphson method using Eq. 5.7. The heat transfer coefficient due to forced convection only was calculated using Eq. 5.5 and is shown in Table 5.3.

In the actual generator the velocities are higher and the effect of the natural

Table 5.3: Front clearance convection coefficients

	Radial coordinate (mm)		
Heat transfer coefficients (W/(m^{2}K))	290	330	370
Assisting flow	19.16	16.13	18.04
Opposing flow	24.50	17.79	21.99
Natural convection	6.47	8.61	13.52
Forced convection	21.9	17.00	20.21
n exponent	1.43	2.88	3.05

convection is negligible. For this reason in the validation of the CFD model it is important to compare the fraction of the heat transfer coefficient due to the forced convection only. The n exponent depends on the specific case. In order to find the forced convection coefficient for the back clearance the value of n obtained for the front clearance has been used. However, for the convective heat exchanges on the stator outer and inner cylindrical surfaces n=3 has been used as calculated for similar cases in [78].

The agreement between the forced convection fraction of the heat transfer coefficient is satisfactory for all of the locations considered (Fig. 5.18 and 5.19).

5.7 Conclusions

In this chapter a validation study has been presented for the CFD model of the large-scale low-speed test rig.

- The mass flow rate through the rig was measured and found to be in good agreement with the values predicted by the CFD model.
- The heat transfer coefficient has been measured at various points on the rig

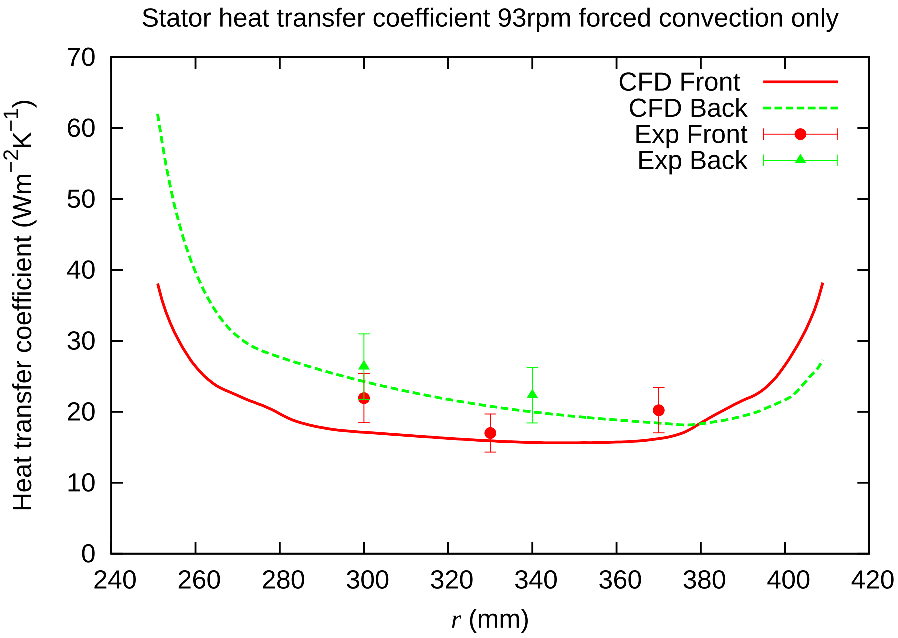

Figure 5.18: Heat transfer coefficient due to forced convection on the stator front and back annuli

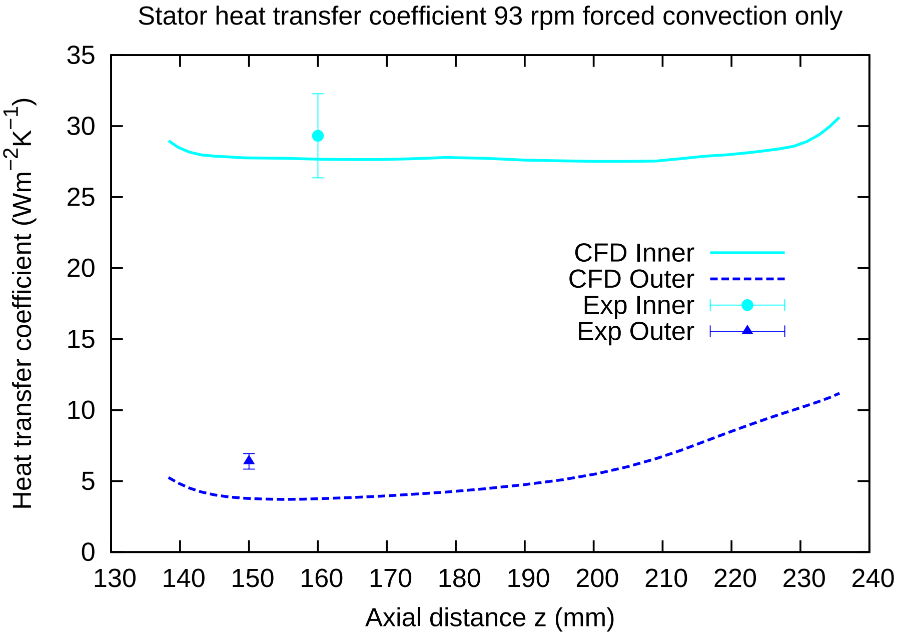

Figure 5.19: Heat transfer coefficient due to forced convection on the stator cylindrical surfaces

stator.

- It has been demonstrated that the heat transfer coefficient is independent of the heat boundary conditions therefore the solid parts can be excluded from the CFD model to save pre-processing and computational effort.

- It has been found that at the low speed at which the test has been carried out the CFD under-predicts the heat transfer coefficient if the effect of the natural convection is not included in the model. Instead a good agreement has been established between CFD and experiments when the heat transfer coefficients due to the forced convection only were considered.

Simulations were conducted for various values of the heat flux from the stator surface. The heat transfer coefficient has been found to be independent of the thermal boundary condition: a higher heat flux from the surface leads to a higher surface temperature which results in a constant heat transfer coefficient value. This confirmed the initial assumption that the heat transfer coefficient depends only on the flow patterns and not on the thermal boundary conditions.

In the next chapter results are presented from a study where the magnet depth, the running clearance and the rotational speed have been varied.

Due to the findings obtained in this chapter and in chapter 4, section 4.2.5 a steady state MRF model has been used for the investigation, with no solid components being modelled, and meshes featuring between 20 and 34 elements in the running clearance have been used.

Chapter 6

Factorial design CFD study

In this chapter a factorial design study is presented. This is a preliminary investigation to find out the influence of the running clearance c, of the magnet depth m, and of the rotational speed s on the heat transfer, on the air flow rate and on the resistive torque.

The heat generated according to the Joule law in the stator of an air cooled AFPM machine needs to be dissipated outside the machine by the cooling air. The amount of energy transferred outside the machine is proportional to the air mass flow rate, and to the heat transfer coefficient on the stator surface. An increase of these quantities would be beneficial in order to achieve an increment of heat transferred to the environment. However, an increase of the air mass flow rate would be relatively expensive as more work would need to be done to force extra air through the system. The inlet temperature would be dependent on external factors and is usually not controlled.

The convective heat transfer coefficient can be augmented without necessarily increasing the windage losses in the machine by changing some of the machine's critical dimensions.

The study has been conducted on the basis of the 1.5kW Durham generator described in chapter 4. The models have been built considering the shape and the components included in this machine. However, the range of dimensions considered in the study is based on the dimensions of generators built by Cummins Generators Technologies (CGT). In this chapter the results from a three dimensional Factorial study are presented. In the next section the general setup of the CFD models is described, and subsequently the Factorial study structure will be explained.

6.1 CFD model

The model and its components (disc, magnet, stator and boss) are shown in Fig. 6.1. The domain has been simplified by excluding the inlet region and the boss as shown in Fig. 6.2. It has been assumed that a rotor is carrying 6 magnets, hence a 60° periodic domain (Fig. 6.3) is used. Due to the elimination of the boss from the domain there is no axial flow inlet as in a real AFPM machine, but the air flow enters and leaves the domain in the radial direction. Hence the domain is symmetric with respect to the vertical mid plane. Due to this symmetry about the xy plane only half of the periodic domain has been modelled in Fluent (Fig. 6.4). By invoking periodicity and symmetry the model in Fig.6.2 can be simplified to that shown in Fig. 6.4.

The periodicity and the symmetry of the generator allowed a reduction of the computational time and an increase in the mesh density in the running clearance between stator and magnets, which is the region of main interest in studying heat transfer. A typical run time for the deployed computational model is around 18 hours using two Dual-core 2.2GHz Opteron processors.

The stator has been considered flat, without protruding windings as a smooth stator reduces windage losses and is the most common configuration of AFPM machines.

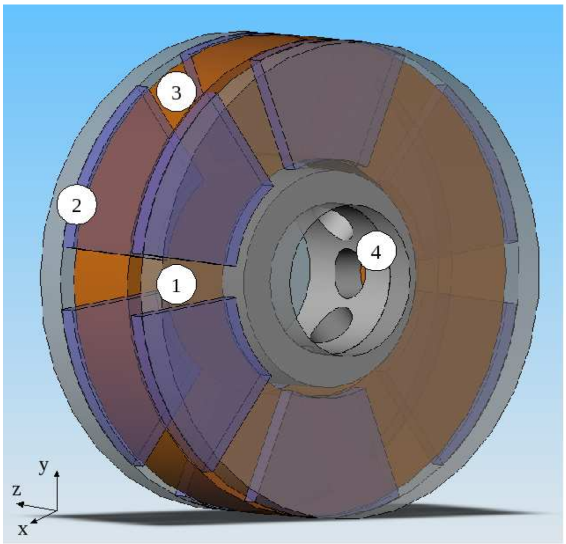

Figure 6.1: Generator model: 1. Disc, 2. Magnet, 3. Stator, 4. Boss

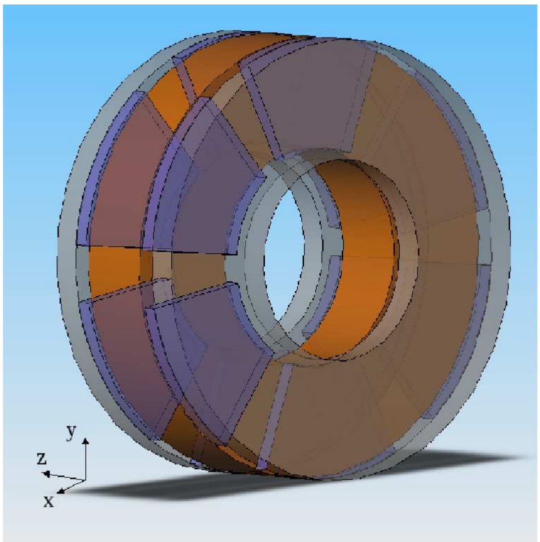

Figure 6.2: Generator without boss

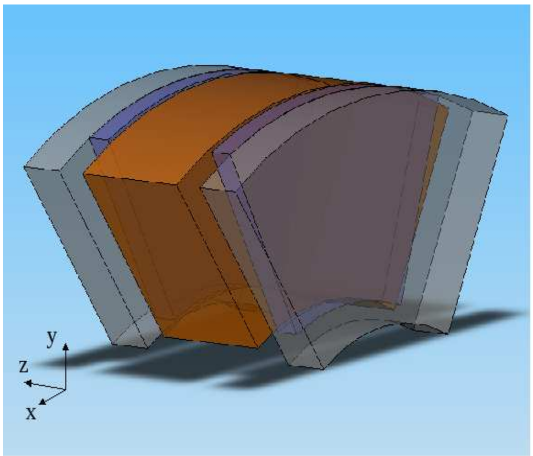

Figure 6.3: Generator's periodic domain

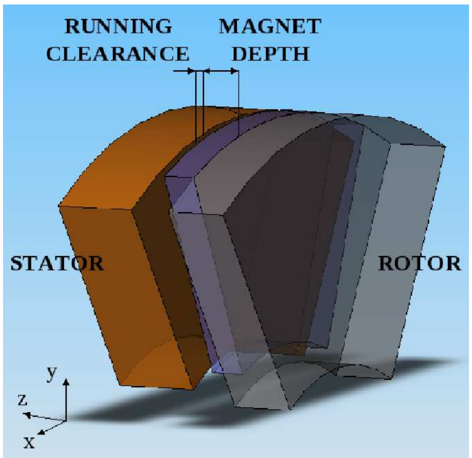

Figure 6.4: Generator's domain: periodic and symmetric about the z axis

The domain has been extended at the outlet. The boundary conditions have been specified as follows: a zero static pressure at the outlet, a constant heat flux on the stator surface, an adiabatic rotor surface, a zero total pressure at the inlet. The modelled system can be schematised as shown in Fig. 6.5. A reversed flow occurred at the outlet, even if the domain was extended. The temperature for the reversed flow specified as the boundary condition at the outlet has been assumed to be the same as that of the flow leaving the generator. The energy balance of the system has been used to determine its value.

The results presented in chapter 4 and chapter 5 have been used to build the CFD model:

- No generator solid components have been included in the model. Instead, a constant heat flux has been specified on the stator walls. This was possible because, as shown in chapter 5, the heat transfer coefficient does not depend on the thermal boundary conditions.

- The steady state MRF approach has been used. In chapter 4 it has been shown that large scale transient effects are not present and a steady state simulation produces reasonable results.

The air has been considered incompressible and its properties (density, specific heat, viscosity, conductivity) independent of the temperature. Therefore in the energy balance the only unknown is the air temperature at the outlet. The simulations have been run by using the EWT method, the realizable κ-ϵ turbulence model, and the MRF approach. The local (radial) heat transfer coefficient *h(r)* has been calculated at three angular positions: -26°, 0°, and 26° on the stator surface on the lines shown in Fig. 6.5. These values correspond to the mid angles of the projection of the magnet on the stator. The angle of -26° corresponds to the trailing region of the domain, 0° corresponds to the central narrowest part of the running clearance, and 26° corresponds to the leading region of the domain. The local *h(r)* obtained at these angles have been averaged over the angle value to find a radial heat transfer coefficient on the stator. From a thermal point of view, a high heat transfer coefficient is desirable, as this at a constant temperature difference, leads to a higher heat flux which will cool the stator more effectively.

The grid has been generated to obtain $y^+ \approx 1$ as required by the EWT approach. A typical mesh used for the 60° section of the stator-rotor system is presented in Fig. 6.6. A typical mesh consists of 3 to 4 million nodes, 2 million of which are located in the running clearance.

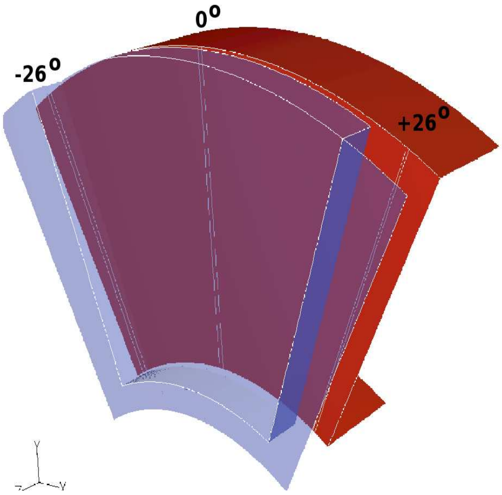

Figure 6.5: Computational domain

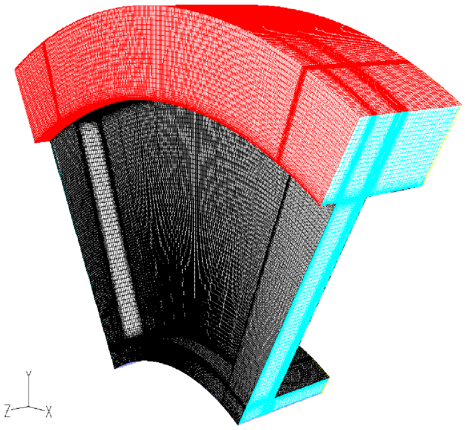

Figure 6.6: Computational mesh

For each model, graphs have been plotted displaying the local heat transfer coefficient *h(r)* at the three angle values and their averaged value. The calculation of the local *h(r)* has been carried out by using as a reference temperature the local temperature in the middle of the running clearance. The heat transfer coefficient has been calculated as shown in Eq. 6.1

$$h(r) = \frac{\dot{Q}}{T_{wall}(r) - T_{mid}(r)} \tag{6.1}$$

where $T_{wall}(r)$ is the local radial wall temperature, $T_{mid}(r)$ is the local temperature in the middle of the clearance at the same radius. The temperature values are exported from Fluent at mesh points which are not, in general, at the same radius as required in order to calculate the heat transfer coefficient with Equation 6.1. Therefore, in order to obtain the two temperatures $T_{mid}(r)$ and $T_{wall}(r)$ at the same radius, a linear interpolation has been performed.

Since the heat transfer coefficients at the three angle values have been averaged, the temperatures had to be obtained at the same interpolated radius for all the six lines (two at each angle: one on the stator surface and one in the mid clearance). For this reason, the same interpolating radius for the six lines has been used. A programme has been written with the scripting language Perl which gives as an output the temperatures on the six lines at the same radii so allowing the calculation of the local heat transfer coefficient. An example of interpolation is shown in Fig. 6.7 where the temperature obtained from Fluent on a line on the stator is compared to the relevant interpolated temperature.

6.2 Factorial study range

The main purpose of the factorial study is to investigate the effect of the parameters and their interactions on the target quantities. The analysis is a *three dimensional*

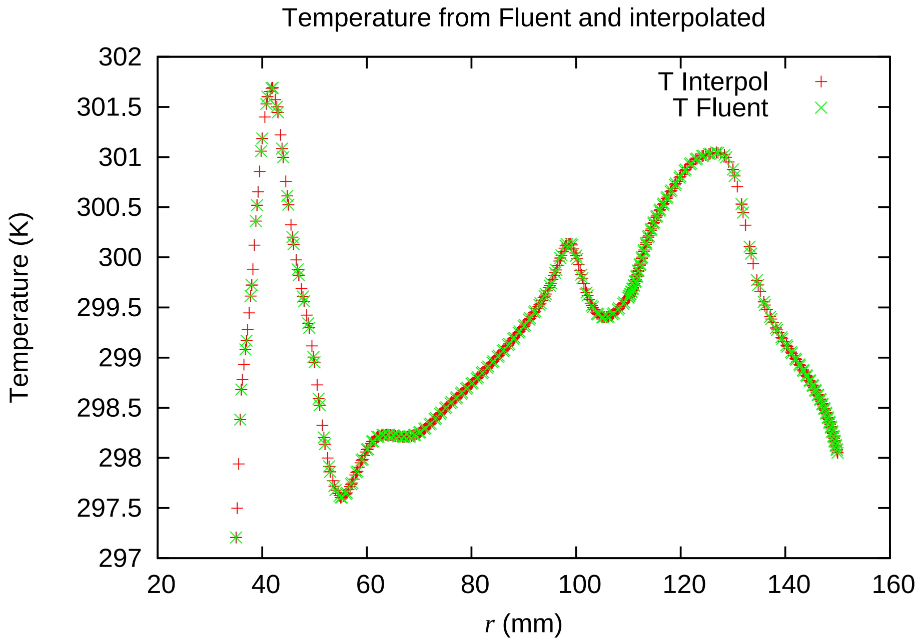

Figure 6.7: Temperature interpolation

two level factorial study. It is called ‘two level’ because each of the investigated parameters could only have two values: ‘high’ and ‘low’. It is defined as ‘three dimensional’ because it involves three factors or parameters. In this study, the parameters (or factors) are:

- the running clearance;
- the magnet depth;
- the rotational speed.

The target quantities are:

- the local heat transfer coefficient on the stator surface which is the most important quantity and needs to be maximised.
- the heat transfer coefficient on the rotor surface;
- the air mass flow rate through the machine;

- the rotor torque.

The two values given to each of the parameters define the boundaries of the factorial study [79]. The factors main effects and their interdependence have been analysed. As a result of the factorial study linear response functions have been obtained which correlate the parameters to the target functions. A regression function has been obtained for each of the following target functions: the heat transfer coefficient on the stator, the heat transfer coefficient on the rotor, the air mass flow rate through the generator and the torque. Since the number of parameters considered was three (running clearance, magnet depth, and rotational speed), and there were two levels, the total number of investigated cases was 2^3. The dimensions of two generators have been provided by Cummins Generator Technologies. The investigated range of the parameters has been obtained by considering the original dimensions of two generators and by incrementing and decreasing them by 20%, to find the upper and lower boundary. The parameters range is summarised in Table 6.1.

Table 6.1: Parameters range

	Running clearance (mm)	Magnet depth (mm)	Rotational Speed (rpm)
min	1	2	1400
MAX	5	18	3000

A three dimensional graphical representation of the factors range is given in Fig. 6.8 where the three coordinates represent the running clearance c, the magnet depth m and the rotational speed s, respectively.

The cases of the 2^3 factorial study are summarised in Table 6.2 where the 'low' value of a parameter is shown with the '-' sign and the 'high' value with '+' sign.

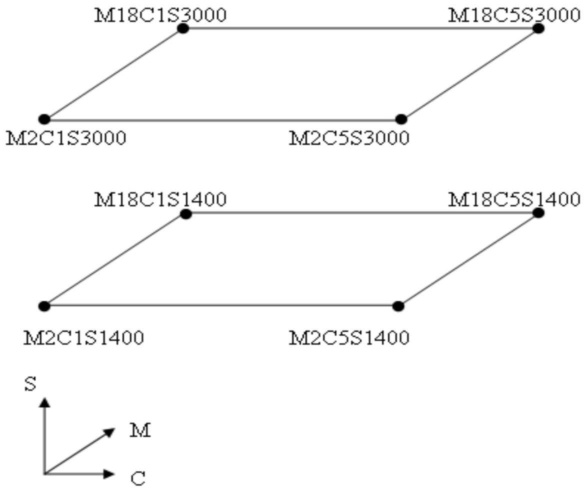

Figure 6.8: Factorial study simulations

Table 6.2: Factorial cases

Case	Running clearance c	Magnet depth m	Rotational Speed s	Combinations
1	-	-	-	(1)
2	+	-	-	c
3	-	+	-	m
4	+	+	-	cm
5	-	-	+	s
6	+	-	+	cs
7	-	+	+	ms
8	+	+	+	cms

For convenience the common practice of factorial design studies has been followed where each case is identified by a combination of characters. In the combinations identifier (in the last column of Table 6.2) the small font letter represents the high value of the corresponding parameter (shown in the last column of Table 6.2). The first combination (1) represents the case where all the parameters have their low values. In an experimental factorial study each case would generally present results from several repetitions; here the results have been obtained from numerical computations hence only one set of data is available.

A parameter can have a main effect and a combined effect with another parameter. The main effect is defined as the average effect of a factor on the target function. The main effects are the effect of the running clearance here indicated with 'C', the effect of the magnet depth 'M' and the rotational speed 'S'. The effect of 'C' is the average target function resulting from the simulations with 'C' at the high level minus the average of the simulations where 'C' is at the low level.

$$\begin{aligned} C = h_{C^+} - h_{C^-} &= \frac{c + cm + cs + cms}{4} - \frac{(1) + m + s + ms}{4} \\ &= \frac{1}{4}[c + cm + cs + cms - (1) - m - s - ms] \end{aligned} \tag{6.2}$$

The 'M' effect is the average of the target function obtained with the four simulations where the magnet was maximum minus the average of the simulations where 'm' is at the low level.

$$M = h_{M^+} - h_{M^-} = \frac{1}{4}[m + cm + ms + cms - (1) - c - s - cs] \tag{6.3}$$

Similarly the 'S' effect is the difference between the four cases with the high rotational speed and the four with the low rotational speed.

$$S = h_{S^+} - h_{S^-} = \frac{1}{4}[s + cs + ms + cms - (1) - c - m - cm] \tag{6.4}$$

Also the effect of interactions between factors have been calculated. The effect of interaction between the running clearance 'C' and the magnet depth 'M' is defined as the difference between the average running clearance effects at the two levels of 'M'. The average 'C' effects are:

$$\text{Average}C\text{effect} = \begin{cases} \frac{[(cms-ms)+(cm-m)]}{2} & \text{High}M \\ \frac{[(cs-s)+(c-(1))]}{2} & \text{Low}M \end{cases}$$

The CM interaction is half of the difference between the two 'C' average effects:

$$CM = \frac{[cms - ms + cm - m - cs + s - c + (1)]}{4} \tag{6.5}$$

The running clearance and the rotational speed interaction and the magnet and rotational speed interaction can be obtained similarly:

$$CS = \frac{[(1) - c + m - cm - s + cs - ms + cms]}{4} \tag{6.6}$$

and

$$MS = \frac{[(1) + c - m - cm - s - cs + ms + cms]}{4} \tag{6.7}$$

The last interaction which needs to be investigated is the one between all the factors which is defined as the average difference between the 'CM' interaction at the two levels of speed:

$$CMS = \frac{[cms - ms - cs + s - cm + m + c - (1)]}{4} \tag{6.8}$$

These effects have been evaluated for the heat transfer coefficient on the stator, the heat transfer coefficient on the rotor, for the mass flow rate, and for the rotor torque.

6.3 Flow patterns

The case (1) (see Table 6.2, on page 122) is taken as an example to describe the flow developing inside the clearance. The pathlines in Fig. 6.9 and Fig. 6.10 allow a qualitative description of the flow which is dominated by the tangential velocity and the radial velocity component is considerably smaller. It can be seen that the region in the clearance where the radial velocities are high correspond to the first half of the magnet (the pressure side). On the low pressure side (the suction side) the contribution to the velocity magnitude is mainly due to the tangential velocity. Most of the cooling air is flowing through the recesses formed by the magnets as can be seen from the velocity magnitude and the radial velocity which are higher in the recess than in the clearance: whereas the velocity magnitude is about 8m/s in the clearance, its value reaches 17m/s in the magnet grooves.

The velocity magnitude contours have been obtained on the radial surfaces shown

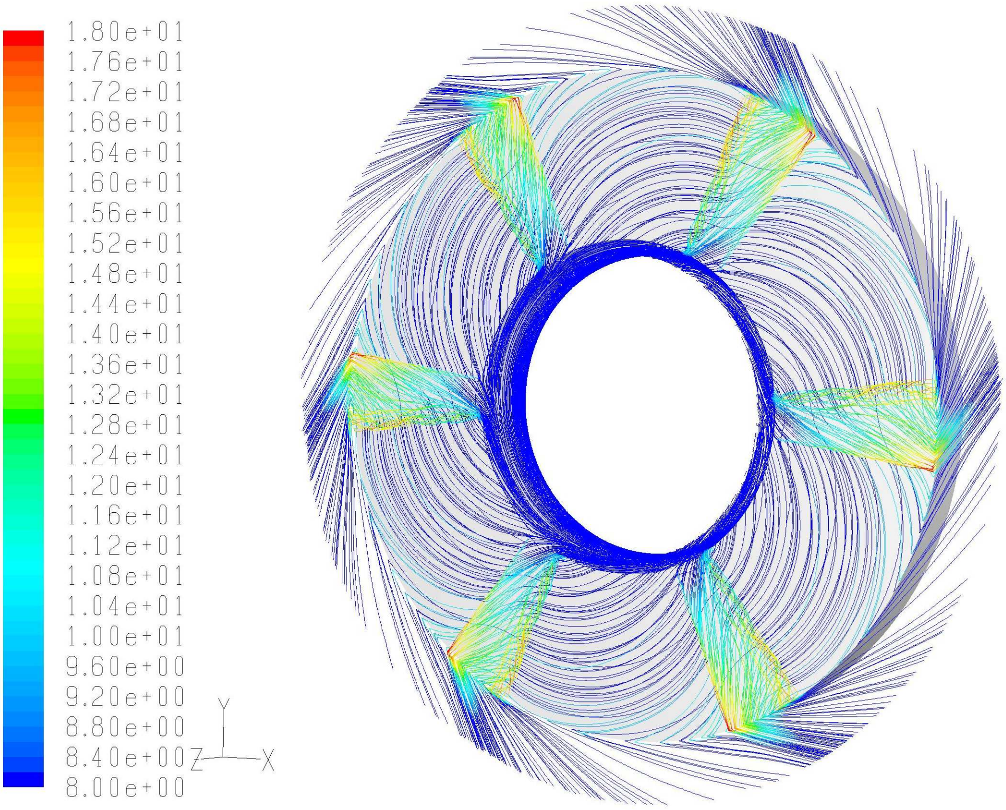

Figure 6.9: Pathlines coloured by velocity magnitude

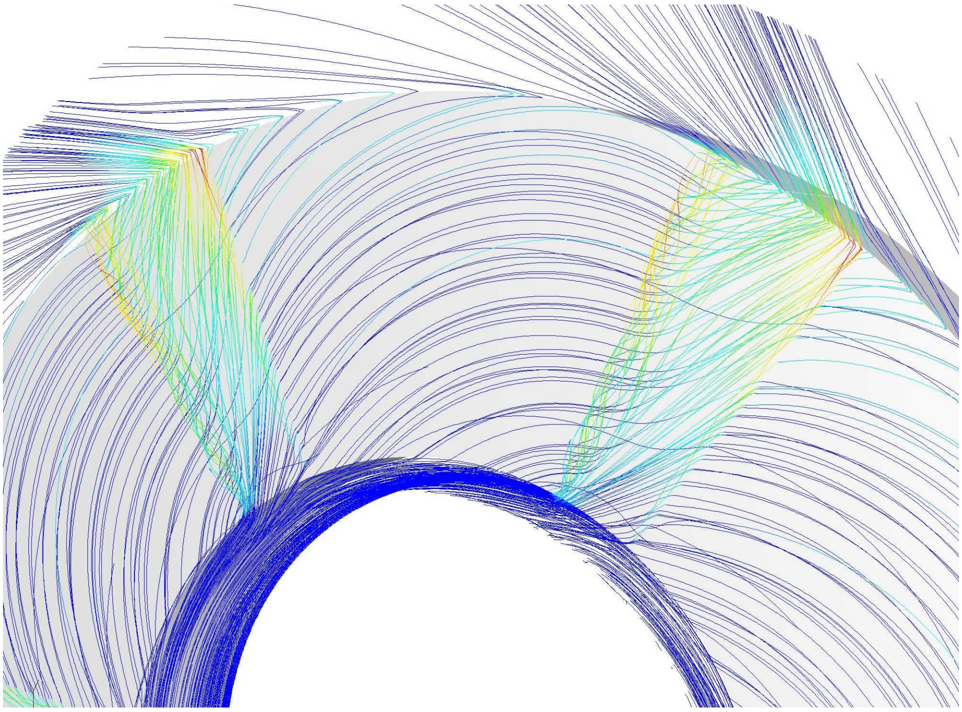

Figure 6.10: Pathlines coloured by velocity magnitude: closeup

in Fig. 6.11 (at angles -26°, 0° and +26°).

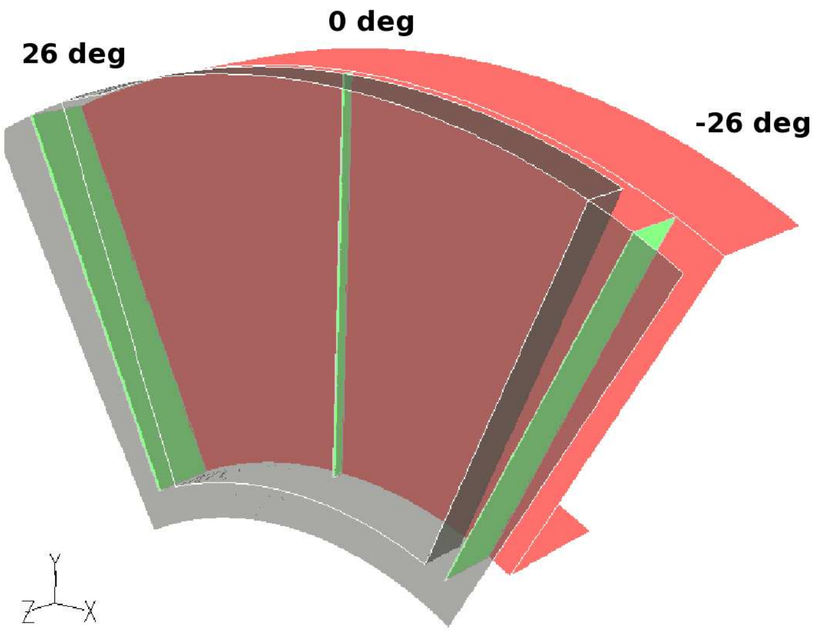

Figure 6.11: Velocity contours planes

The region of the running clearance close to the rotor shows higher velocities than the one close to the stator (see Fig. 6.12). It is therefore desirable to have a low running clearance as it increases the turbulent mixing. As an example the velocity magnitude in the clearance at $r = 100$mm is about 11m/s on the rotor and 2m/s on the stator. For a given mass flow rate a lower running clearance increases the radial velocity in the clearance due to the reduction of the cross sectional area.

However, an excessively low running clearance could reduce the flow rate due to the excessive flow resistance. For given values of the magnet depth and the rotational speed an increase of the clearance to a certain value results in the rise of the mass flow rate, however further widening the clearance would not result in further increase of mass flow rate. This would reduce the radial velocity and the beneficial effect on the heat transfer coefficient.

In this case the search for an ideal clearance which maximises the heat transfer coefficient is made more complex by the presence of the grooves in the rotors. A clearance value which would be ideal for a stator facing a flat rotor might not be the best one when the rotor features radial grooves typical for this study work.

The radial velocity is positive on the radial surfaces at 0° and +26° as shown in Fig. 6.13 on page 129. The reversed flow is observed on the radial surface at the angle of -26° (Fig. 6.13) and for angles between -22° and -29° on the mid plane in the clearance, as shown in Fig. 6.14. The negative velocities reach a value of -2m/s. This is not desirable because of the high temperature of the air re-entering the system. The low velocities and the reversed flow on this area (the peripheral region of the stator surface) causes the temperature to increase locally from 314 K to 322 K (Fig. 6.15 on page 130).

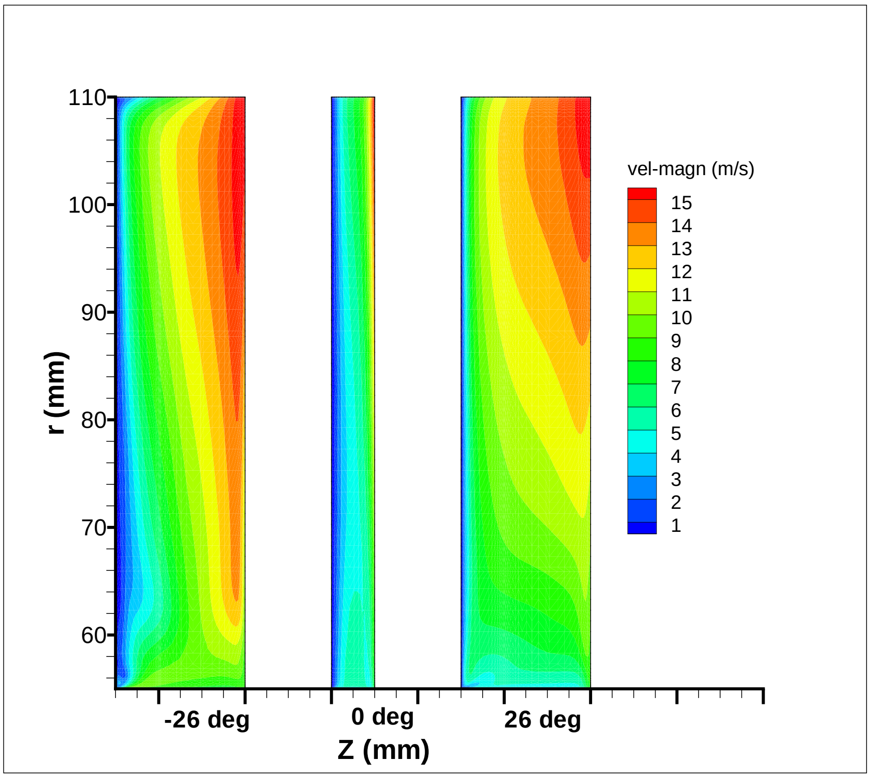

Figure 6.12: Velocity magnitude on zy plane, case (1)

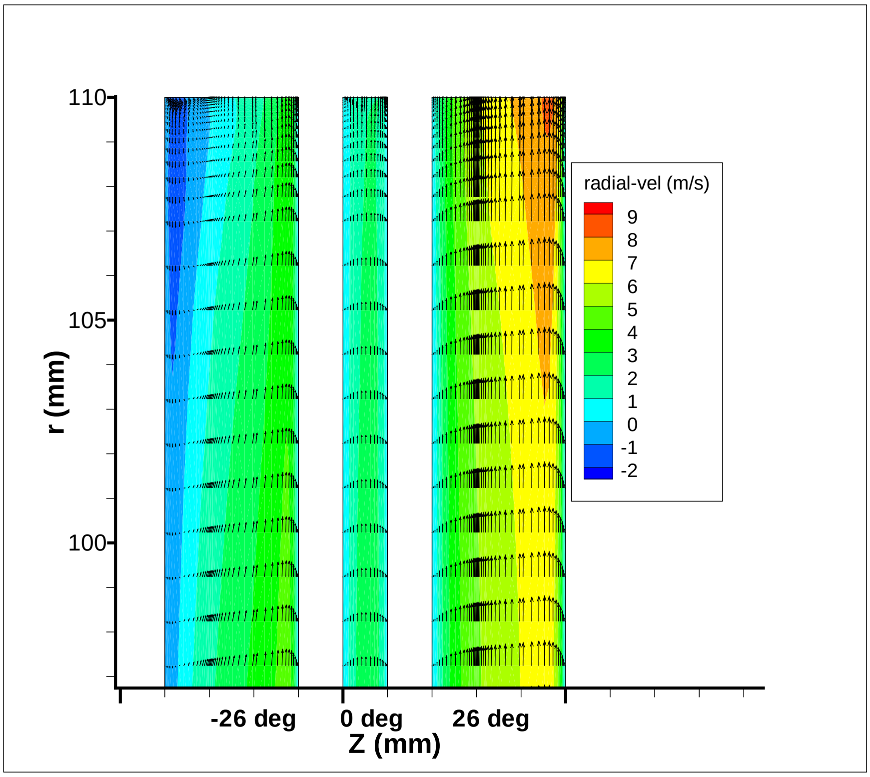

Figure 6.13: Radial velocity on zy plane, case (1)

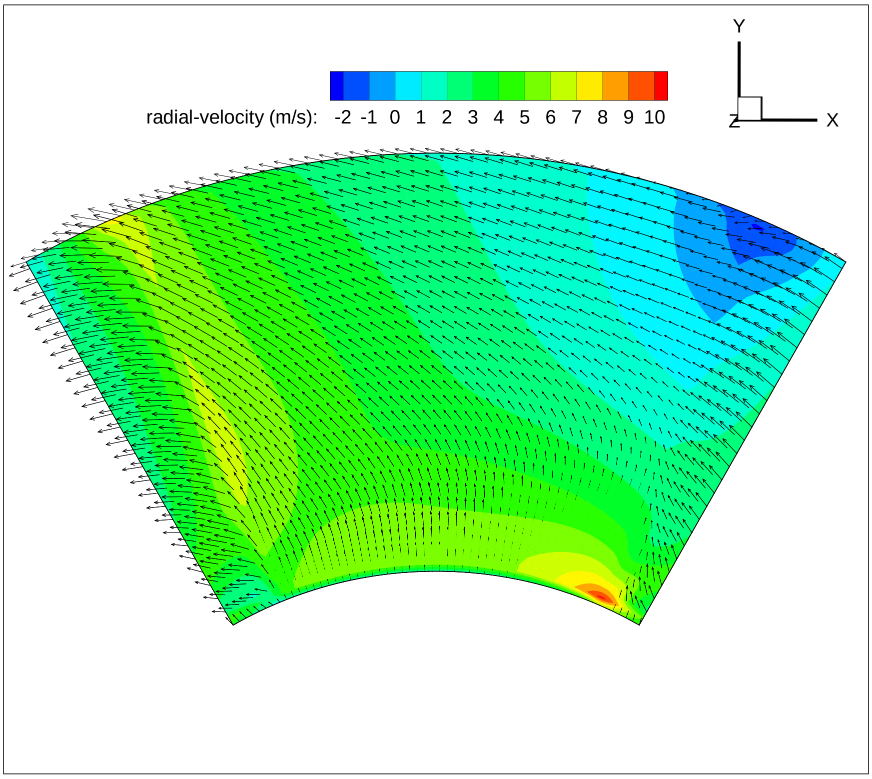

Figure 6.14: Radial velocity and velocity vectors on mid plane, case (1)

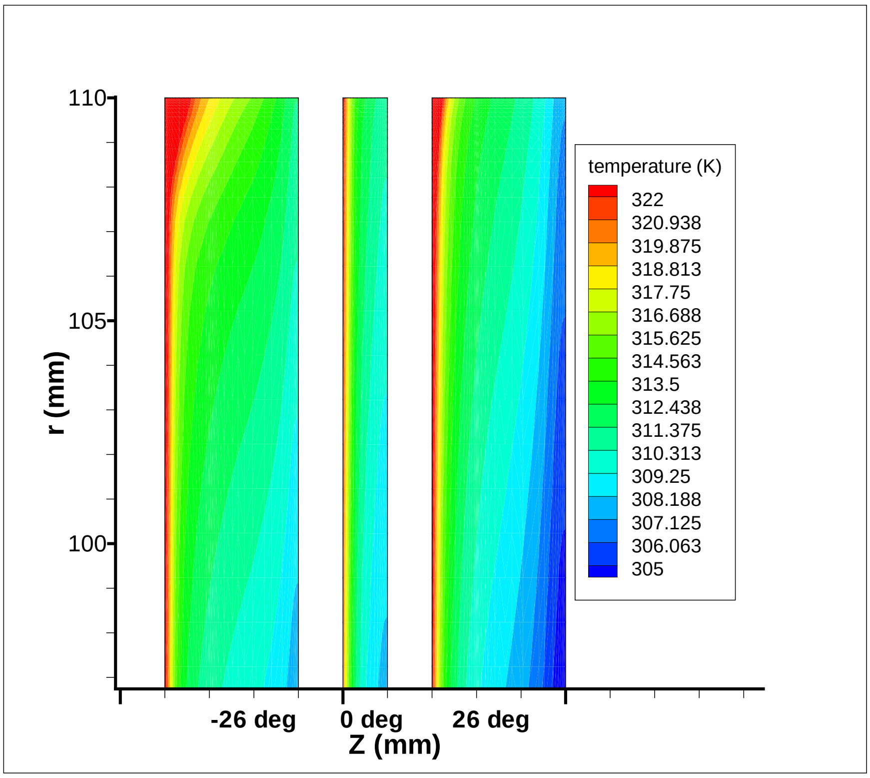

Figure 6.15: Temperature on zy plane, case (1)

6.4 Stator heat transfer coefficient

In order to show the dependency of the heat transfer coefficient on the velocities, information on the tangential and the radial velocities and the velocity magnitude have been obtained in the mid-line in the center of the clearance which is the interception between the clearance mid plane and the zero angular coordinate. The local heat transfer coefficient on the stator surface at the same angle of 0° has been plotted together with the velocities (Fig. 6.16). The velocity magnitude contours have been obtained on the radial surfaces shown in Fig. 6.11. The heat transfer coefficient has been calculated using the temperature in the middle of the clearance as a reference temperature as in Equation 4.1, on page 49). A distinct pattern has been found for the heat transfer coefficient on the stator surface for all cases analysed. At the inlet of the running clearance it is maximum, further in the running clearance it decreases relatively steeply depending on the clearance and magnet values, then it increases again at the clearance outlet. This can be explained by considering the velocity magnitude of the flow in the middle of the air gap. Assuming a negligible axial velocity in the clearance, only the radial and the tangential velocities contribute to the velocity magnitude. At the running clearance inlet the radial velocity is maximum (the minimal cross-sectional area), and the tangential velocity is minimum (the smallest radius). At the clearance outlet the tangential velocity is maximum (the maximum radius) and the radial velocity is minimum (the maximal passage area). Therefore a point close to the average radius exists where the velocity magnitude in the clearance is at its minimum. This minimum velocity magnitude corresponds to a minimum in heat transfer coefficient. It can also be noticed that the heat transfer coefficient at the inlet of the running clearance is in general higher for the two angles of -26° and 26°. This is because the radial flow is mainly occurring through the rotor groove which corresponds to these two angles as already seen in Fig. 6.10, on page 126. From the graphs of velocity magnitudes on the radial surfaces in the clearance and from the heat transfer coefficient graphs it can be seen that:

- A large clearance leads to a low velocity magnitude, hence to a low heat transfer coefficient.
- A deep magnet results in a high flow rate, hence in higher velocities and in a greater heat transfer coefficient.
- A high rotational speed results in a high flow rate, hence in a greater heat

transfer coefficient.

A detailed description of the velocity contours and of the heat transfer coefficient patterns for each of the cases is presented in the following sections.

Case '(1)' local *h(r)*

In the case where all the parameters are at their low values (case '(1)', Table 6.2, on page 122) the heat transfer coefficient at all angles and over the whole radius is quite uniform as shown in Fig. 6.17. The heat transfer coefficient varies in a range between 70 and 90W/(m^{2}K) for radii between 65 and 105mm. The two regions where a high heat transfer coefficient is observed are at the inlet of the clearance at -26° and 26° because of the high radial velocities obtained where the cross sectional area is minimum.

Case 'c' local *h(r)*

The values of velocities due to the large running clearance are lower than the previous case, and as a consequence the heat transfer coefficient is lower over the whole radius (Fig. 6.19). The contours of the velocity magnitude for the case 'c' are shown in Fig. 6.20, on page 137. The velocity magnitude in the middle of the clearance (0°) at the radial periphery is about 4m/s as compared to 10m/s calculated in case '(1)' at the same location.

The variation in heat transfer coefficient over the radius is smaller than in the case with the small clearance (the heat transfer coefficient varies between 34W/(m^{2}K) at the radius of 70mm to 40W/(m^{2}K) at the radius of 105mm). Also the variability at the three angular location is reduced. This is because the relative difference in the axial distance between the rotor and the stator at the three angular locations is reduced due to the larger clearance and the effect of the protrusions on the rotor are taken further away from the stator. By comparing Fig. 6.18 and Fig. 6.19 the relationship between the velocity magnitude and the heat transfer coefficient can be observed as in the case with the small clearance; the high velocities at the clearance inlet and at the outlet lead to the high heat transfer coefficient in these areas. At the two angles of -26° and 26° the heat transfer coefficient suddenly drops at the clearance exit from 48W/(m^{2}K) to 40W/(m^{2}K). This is explained by the variation of the velocity magnitudes at the outlet (Fig. 6.20) which decrease causing an increase of the stator wall temperature and of the temperature difference between the clearance and the stator wall.

Case 'm' local *h(r)*

While in case '(1)' the stator heat transfer coefficient was steadily increasing, for case 'm' it continuously decreases until the radius is 95mm as shown in Fig. 6.22, on page 138. The cross sectional areas are greater for this case due to the deeper rotor grooves, hence the radial velocities decrease with a higher rate of change: in this case the radial velocity linearly decreases from 8m/s for the radius of 55mm to 1m/s for the radius of 110mm, whereas in case '(1)' the radial velocity varies from 7m/s to 2m/s at the same radii. However, the deeper magnets induce a higher tangential velocity in the running clearance and a higher radial velocity at the running clearance inlet which results in the higher heat transfer coefficient on the stator surface. The increment in the velocity magnitude for $r > 95$mm (Fig. 6.21 and Fig. 6.23) causes a rise of the local heat transfer coefficient at the angle of 0° displayed in Fig. 6.22.

For case ‘m’ as for the case ‘ms’ the velocity magnitudes on the plane 26° are higher than at -26° as opposed to all the other cases.

Case ‘cm’ local *h(r)*

The results for the case ‘cm’ in Fig. 6.25 on page 139, show the uniform heat transfer coefficient on the stator at all three angles considered. As for case ‘c’ a wide running clearance reduces the effect of the rotor on the stator heat transfer coefficient and smooths the difference of the heat transfer coefficient at these three angles. The low velocity magnitudes for r = 80mm on the 0° plane displayed in Fig. 6.26 are the reason for the reduction of the heat transfer coefficient at the same radius. The heat transfer coefficient decreases from 65W/(m^{2}K) at the clearance inlet to 36W/(m^{2}K) for r = 80mm then it increases again to reach 60W/(m^{2}K) at the clearance outlet. Also the heat transfer coefficient reduction at the outlet radius (106mm $< r <$ 110mm) is caused by the low velocity magnitude at the 0° plane.

Case ‘s’ local *h(r)*

The velocities for case ‘s’ are displayed in Fig. 6.27, on page 140 and the heat transfer coefficient for the three angles is shown in Fig. 6.28. The velocity contours are presented in Fig. 6.29. The heat transfer coefficient and velocity patterns observed in case ‘(1)’ are also present in this case. However all the calculated quantities are augmented due to the higher rotational speed: the radial velocity linearly decreases from 14m/s to 5m/s moving from the inner radius (55mm) to the outer radius (110mm). The heat transfer coefficient linearly increases with the radius from 125W/(m^{2}K) at r = 60mm to 130W/(m^{2}K) at r = 105mm.

Case 'cs' local *h(r)*

The results for the case 'cs' in Fig. 6.31, on page 141 show a different shape of heat transfer coefficient compared to case 'c'. This is in contrast to the results obtained for cases '(1)' and 's' where the same velocity and heat transfer patterns were observed. This indicates that an interaction between the rotational speed and the running clearance exists: the effect of the rotational speed depends on the value of the running clearance. The effect of the interaction between the rotational speed and the running clearance has been named 'CS' and is discussed in more detail in Section 6.4.2.

The highest heat transfer coefficient was found for this case at the clearance inlet and outlet (75W/(m^{2}K)) whereas the lowest was calculated for 80mm $< r <$ 100mm (50W/(m^{2}K)).

Case 'ms' local *h(r)*

The stator heat transfer coefficient for the case 'ms' follows the patterns already described for the case 'm', but its value is increased due to the higher rotational speed. This shows that the interaction between speed and magnet depth, named 'MS' is negligible as discussed in Section 6.4.2. The heat transfer coefficient decreases relatively steadily from the maximum value of 250W/(m^{2}K) at the clearance inlet to the value of 150W/(m^{2}K) at the clearance outlet.

The correlation between the velocity of the mid line at 0° and the local heat transfer coefficient is in this case very strong as shown in Fig. 6.33, on page 142. The stator heat transfer coefficient has a minimum at r = 90mm which corresponds to the minimum of the velocity magnitude contours observed in the running clearance at 0° in Fig. 6.35, on page 142. The velocity magnitude and the local heat transfer coefficient are at their highest value at the clearance inlet and outlet due to the high radial and tangential velocities respectively.

Case ‘cms’ local *h(r)*

The results for the case ‘cms’ show the same patterns as for the case ‘cm’, but with heat transfer coefficients approximately doubled in value (whereas the maximum heat transfer coefficient coefficient at the inlet of the clearance is 120W/(m^2K) for the case ‘cms’, it is 65W/(m^2K) for the case ‘cm’). The fact that the heat transfer coefficient for the two cases follows the same pattern means that the effect on the stator heat transfer coefficient of a system with high magnet and high clearance is independent of the rotational speed in the considered range. The ‘*CMS*’ interaction is therefore negligible, as discussed later in Section 6.4.2. The heat transfer coefficients at the three angles are relatively homogeneous apart from the inlet and outlet zones. At the inlet the heat transfer coefficient is higher at the two angles -26° and 26° than at 0° whereas at the outlet *h(r)* is higher at 0°.

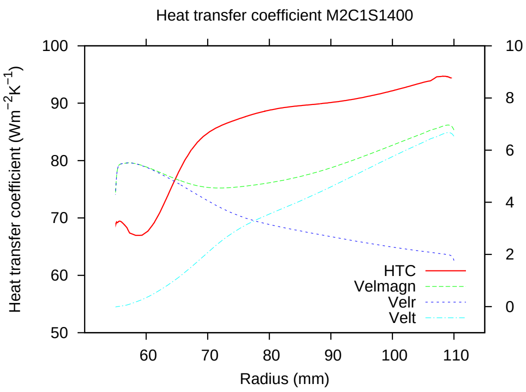

Figure 6.16: Velocities at 0°, case (1)

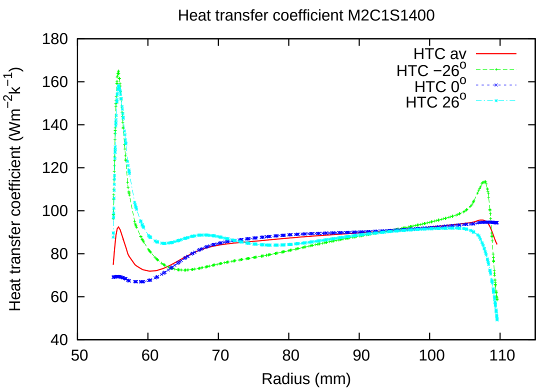

Figure 6.17: Stator local *h(r)*, case (1)

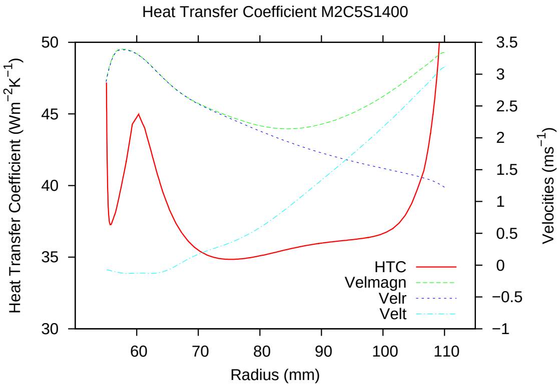

Figure 6.18: Velocities at 0°, case c

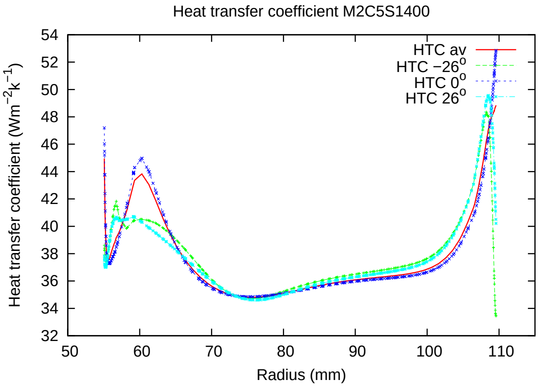

Figure 6.19: Stator local *h(r)*, case c

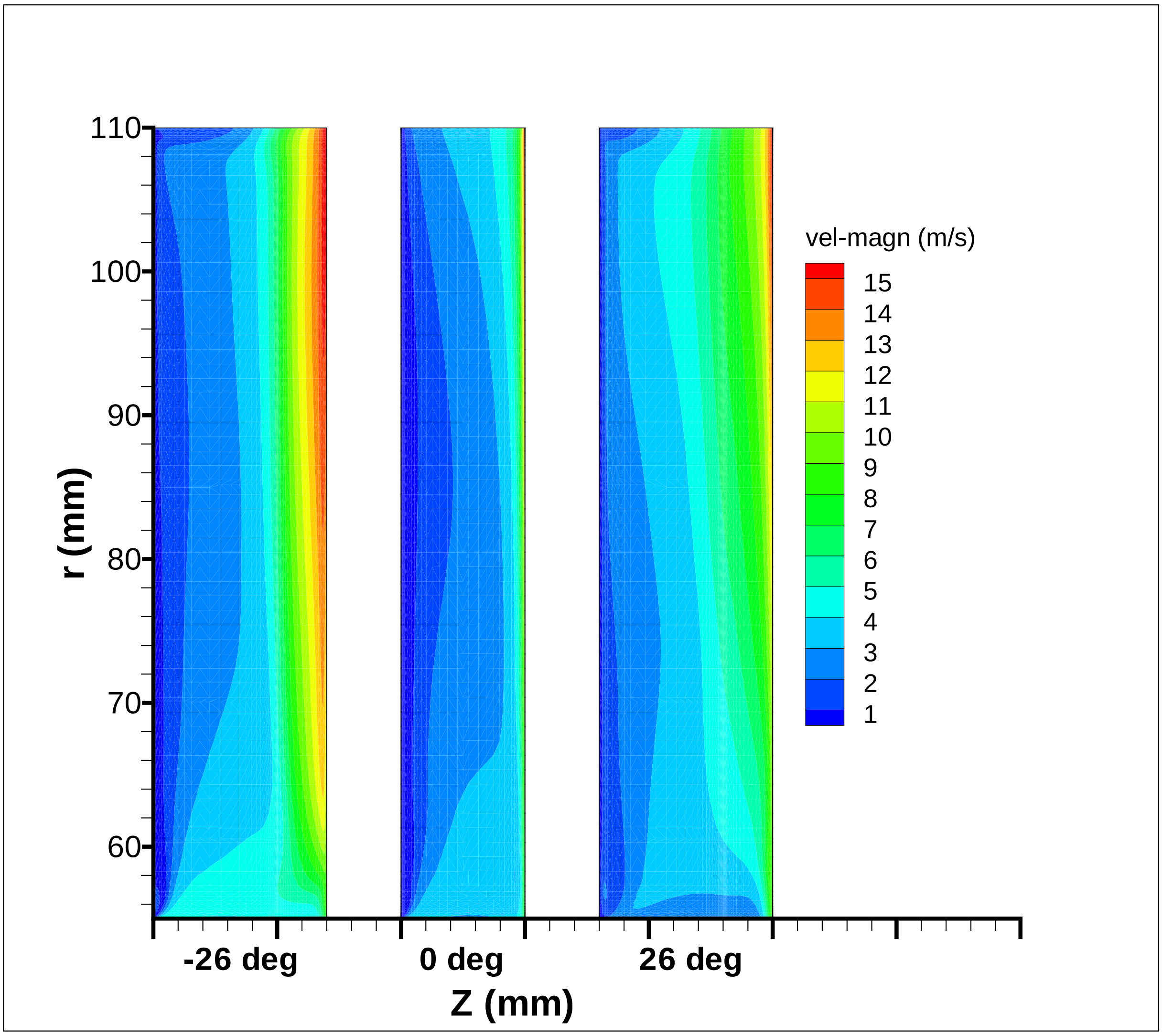

Figure 6.20: Velocity magnitude contours, case c

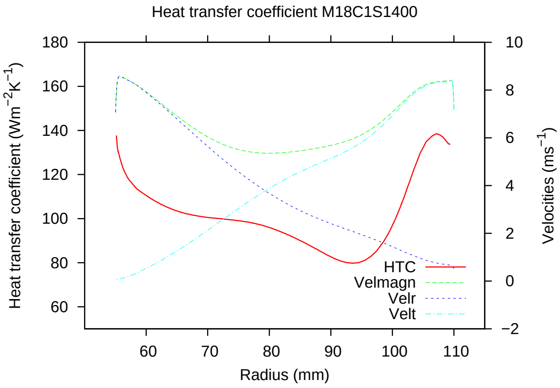

Figure 6.21: Velocities at 0°, case m

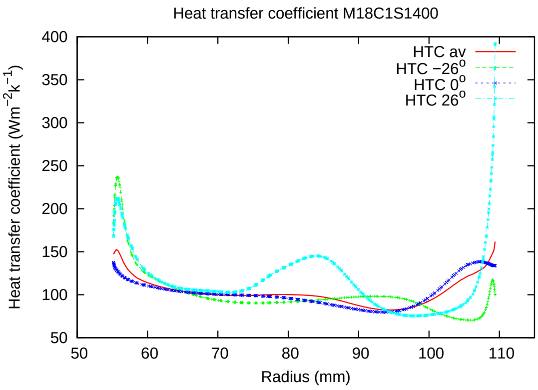

Figure 6.22: Stator local $h(r)$, case m

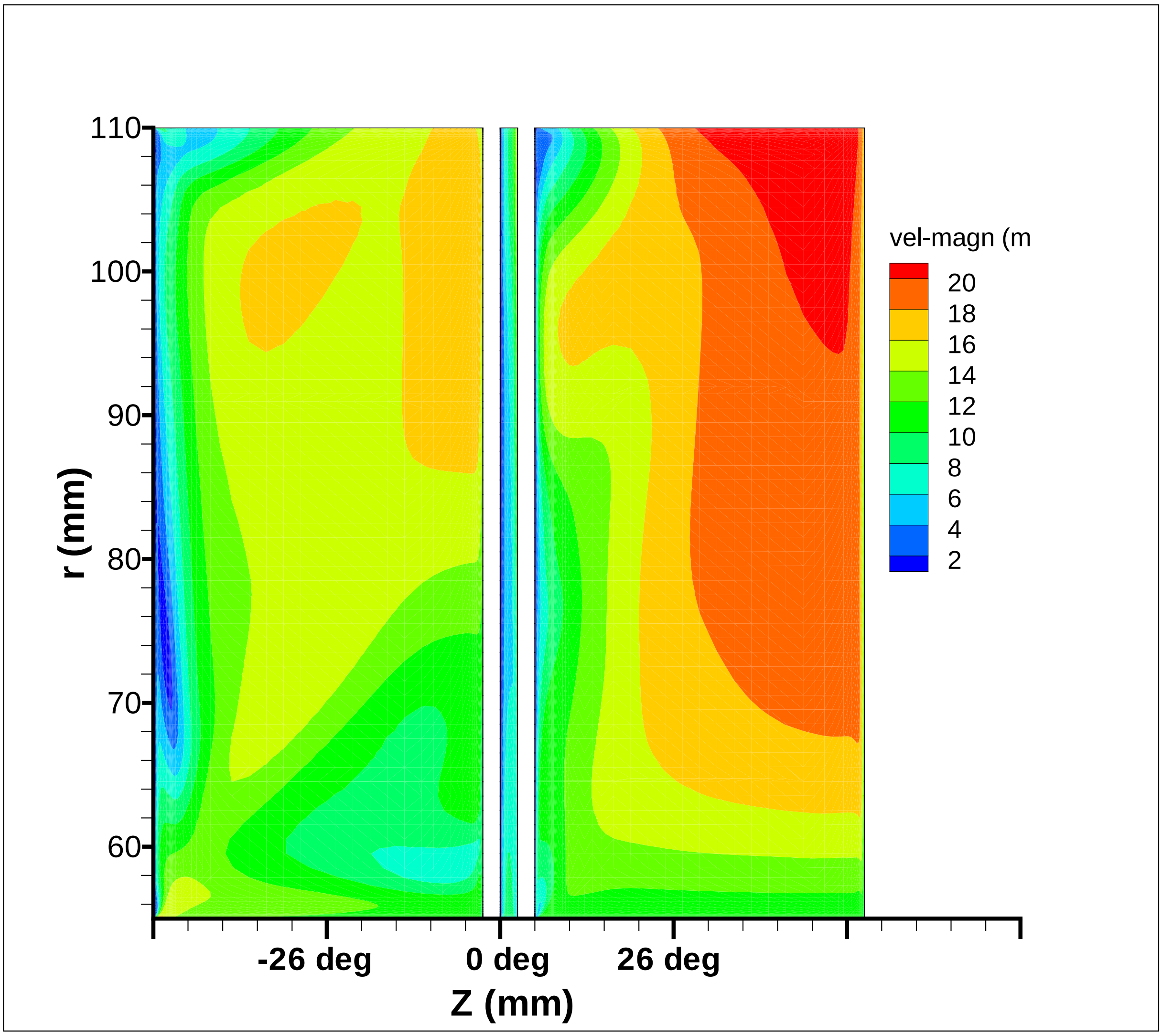

Figure 6.23: Velocity magnitude contours, case m

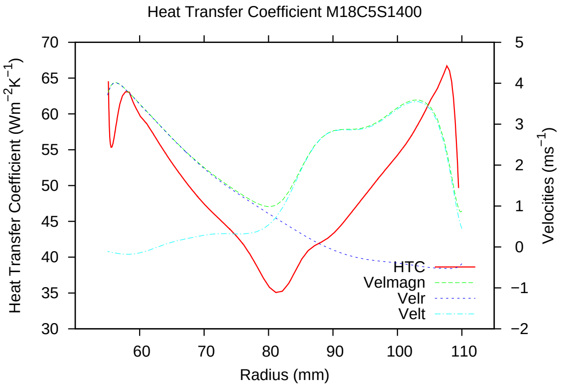

Figure 6.24: Velocities at 0°, case cm

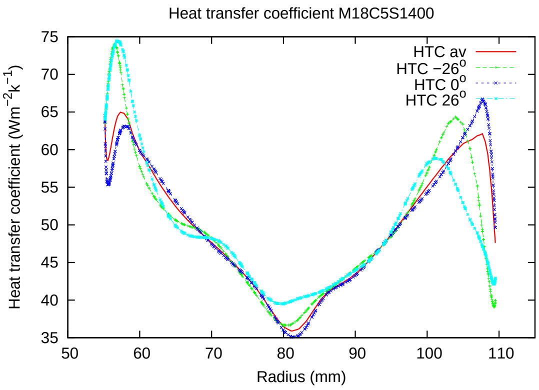

Figure 6.25: Stator local *h(r)*, case cm

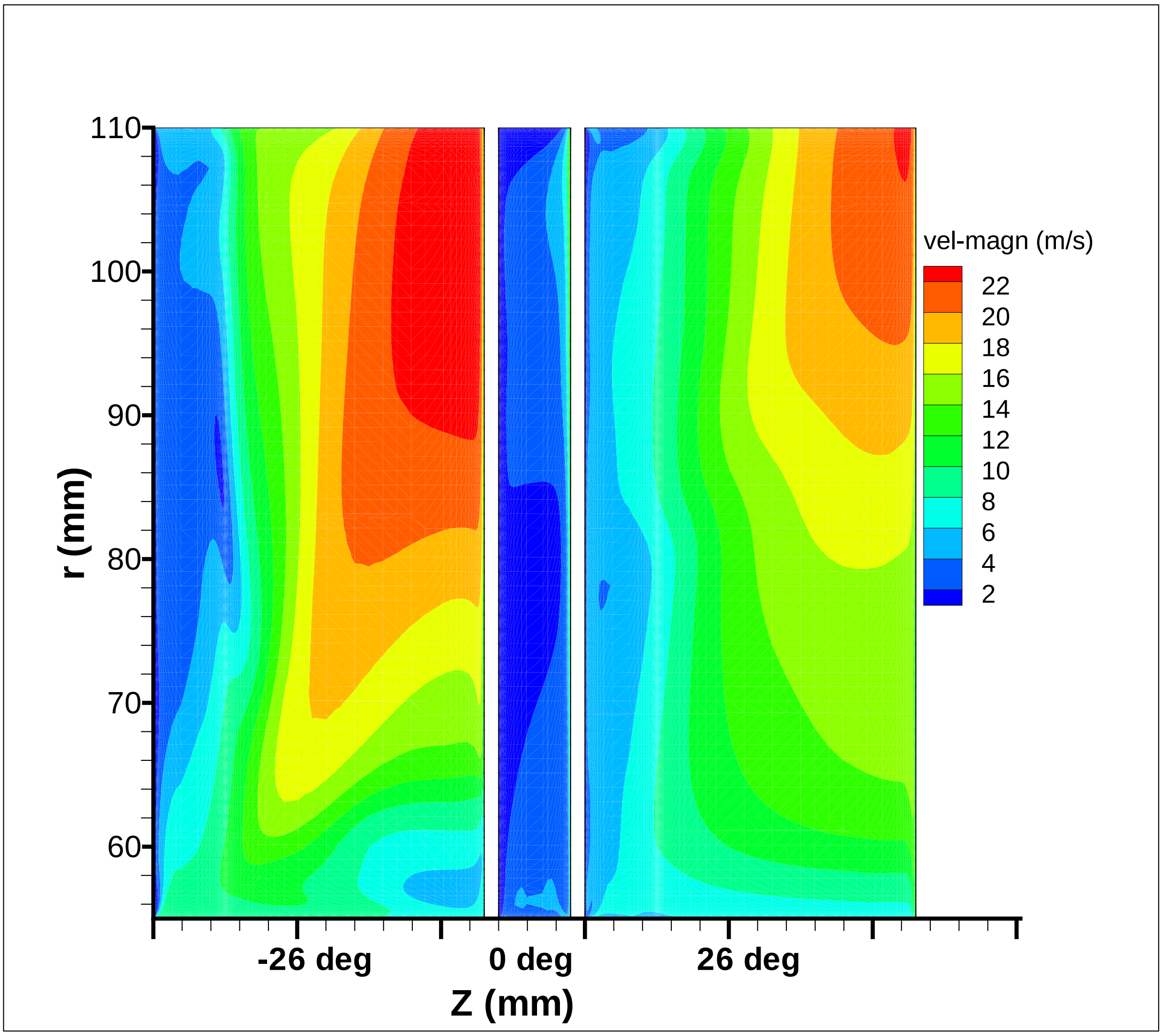

Figure 6.26: Velocity magnitude contours, case cm

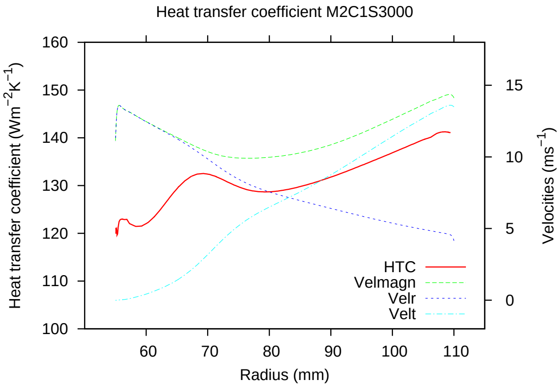

Figure 6.27: Velocities at 0°, case s

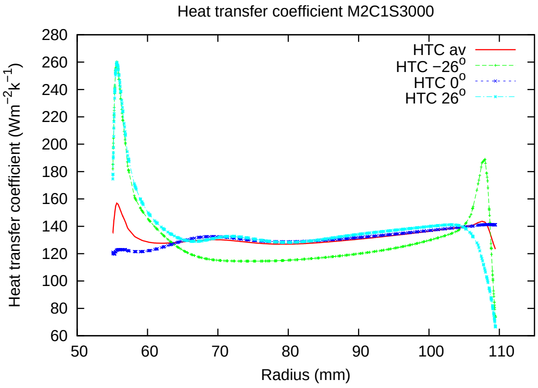

Figure 6.28: Stator local $h(r)$, case s

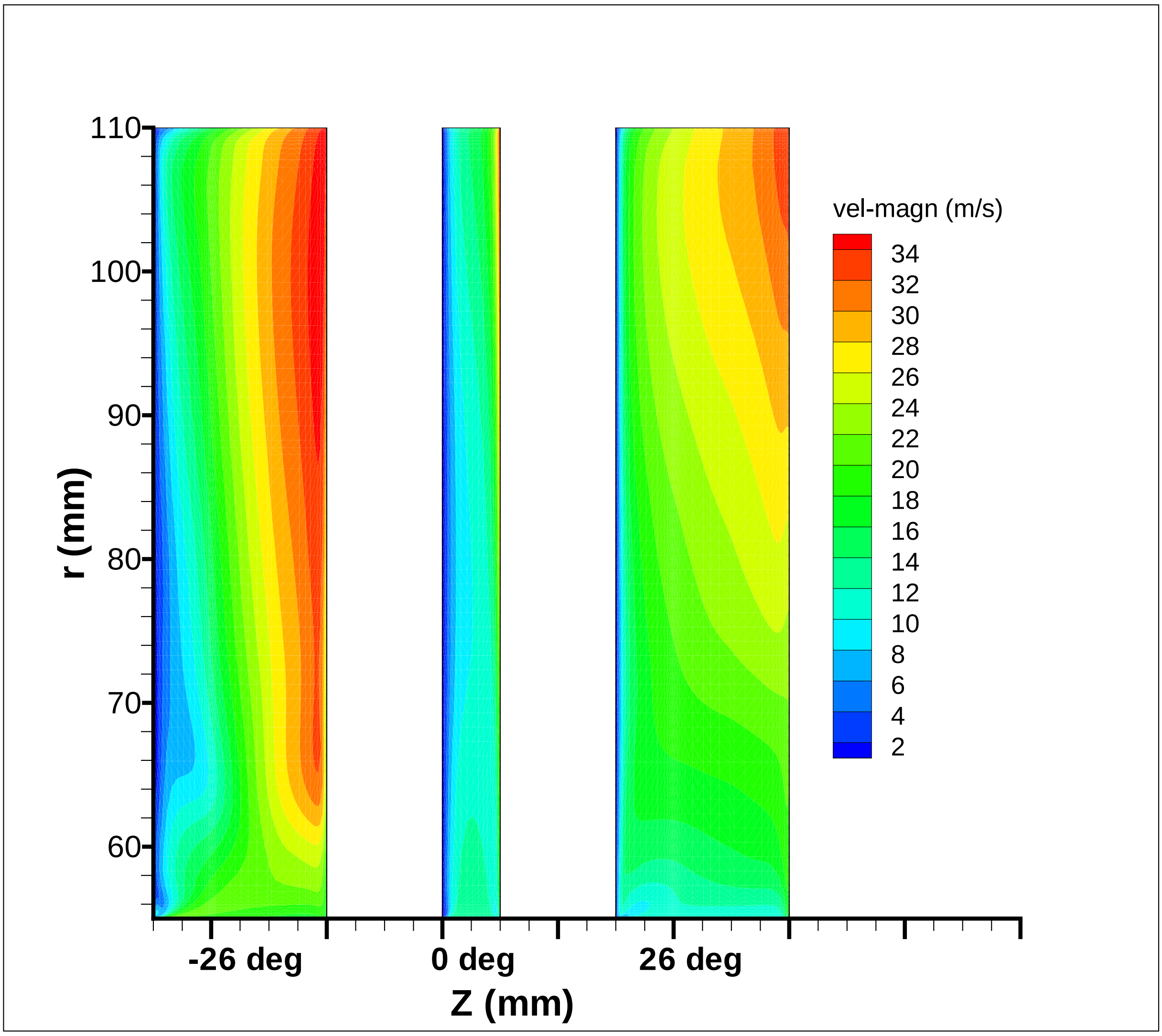

Figure 6.29: Velocity magnitude contours, case s

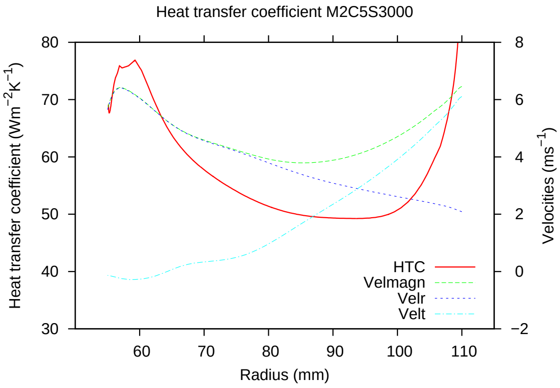

Figure 6.30: Velocities at 0°, case cs

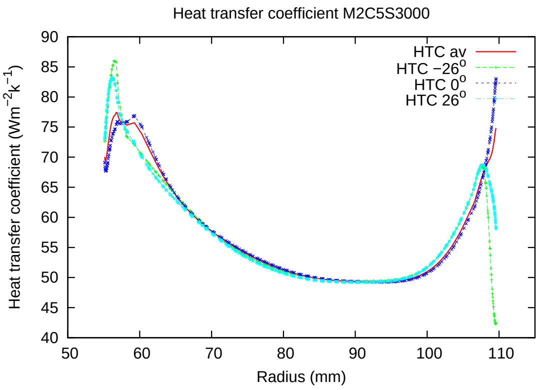

Figure 6.31: Stator local $h(r)$, case cs

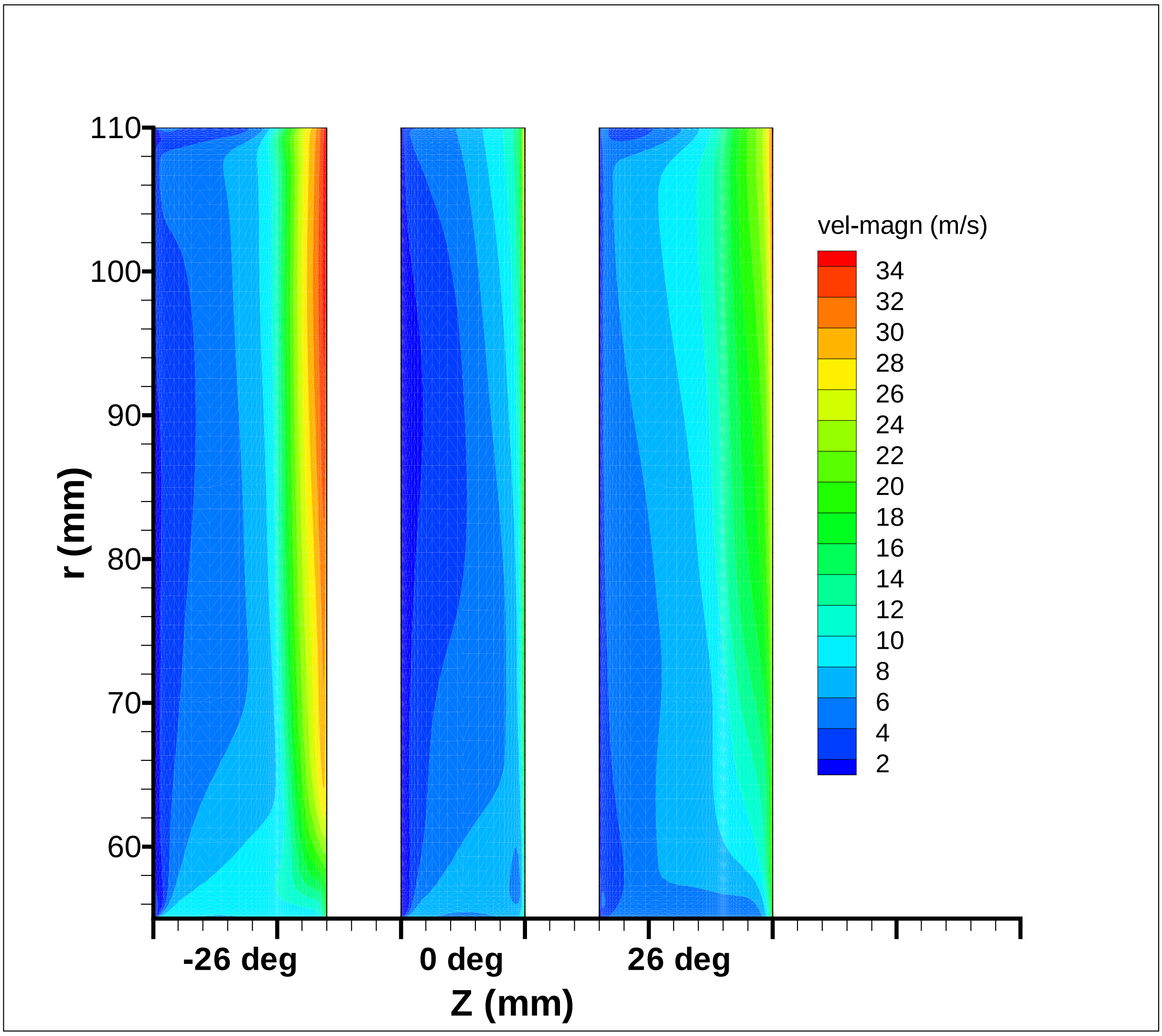

Figure 6.32: Velocity magnitude contours, case cs

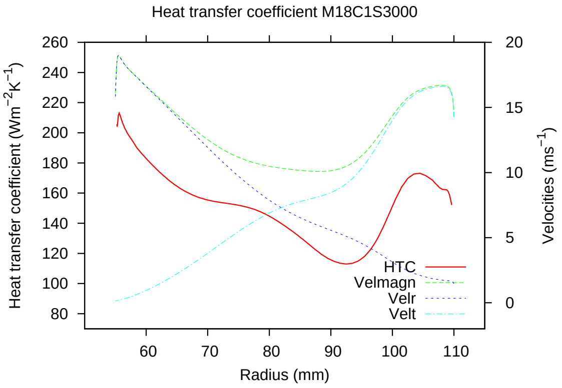

Figure 6.33: Velocities at 0°, case ms

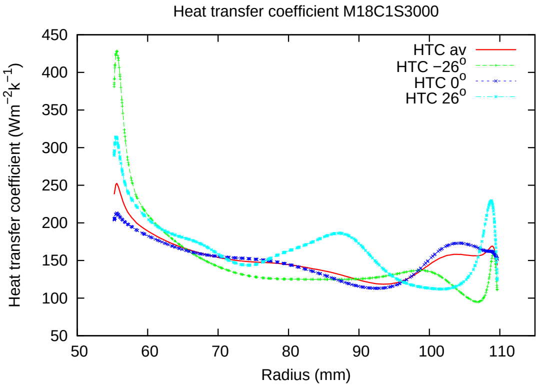

Figure 6.34: Stator local $h(r)$, case ms

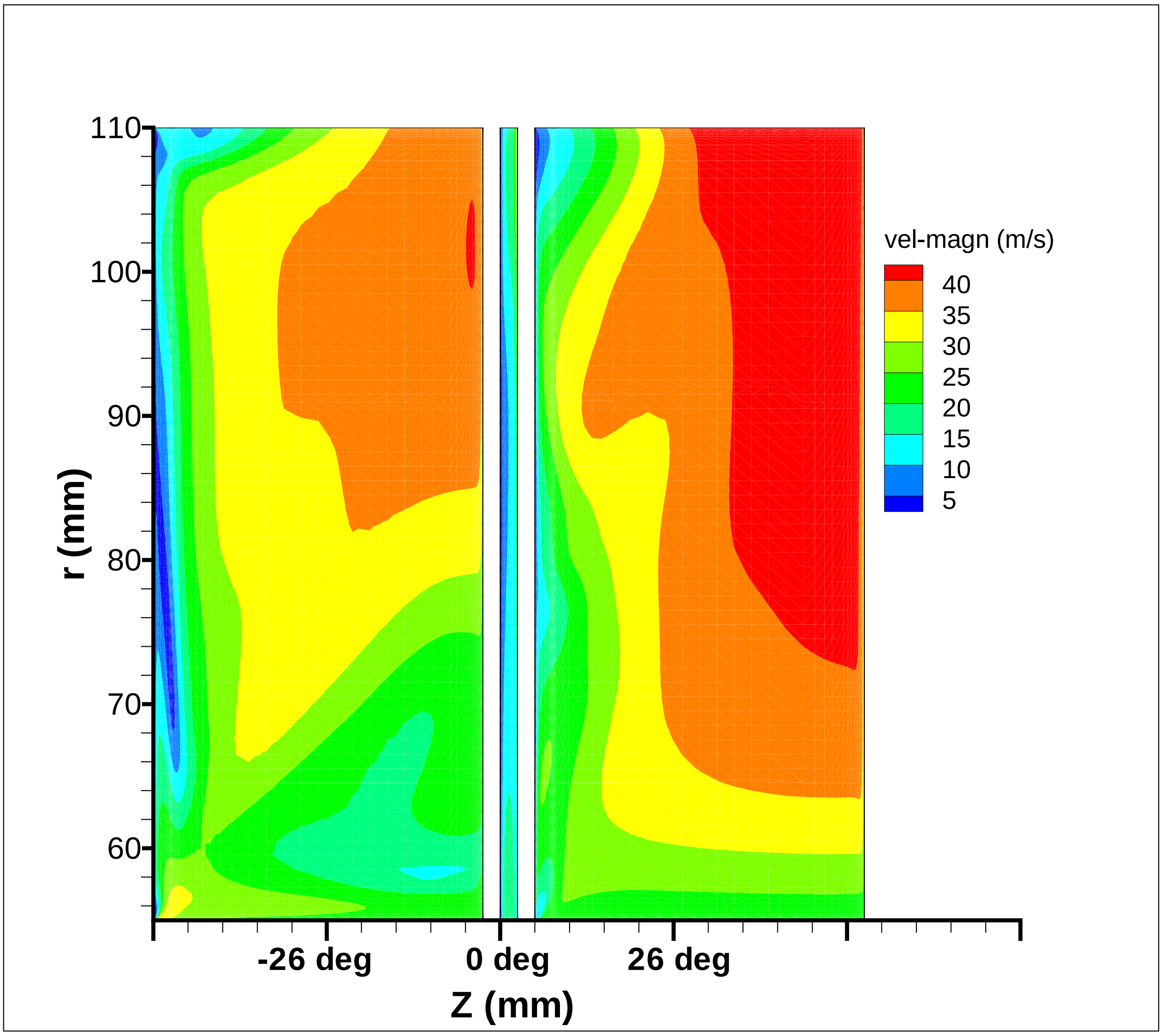

Figure 6.35: Velocity magnitude contours, case ms

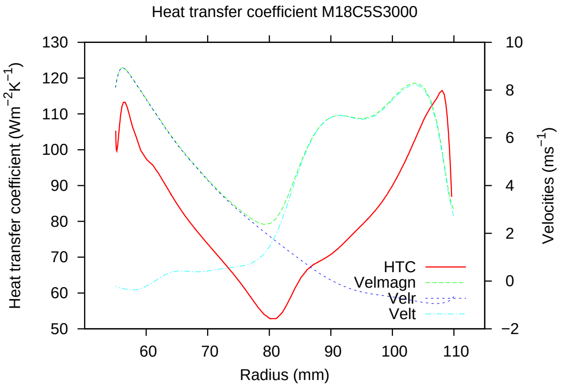

Figure 6.36: Velocities at 0°, case cms

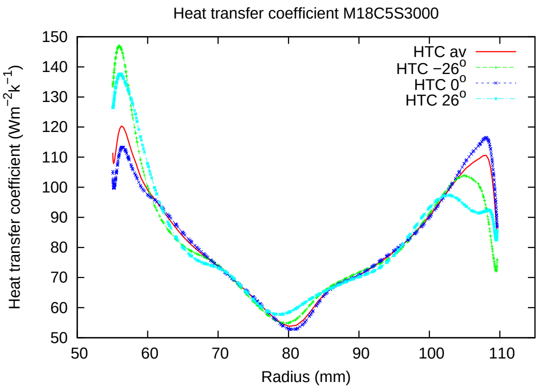

Figure 6.37: Stator local *h(r)*, case cms

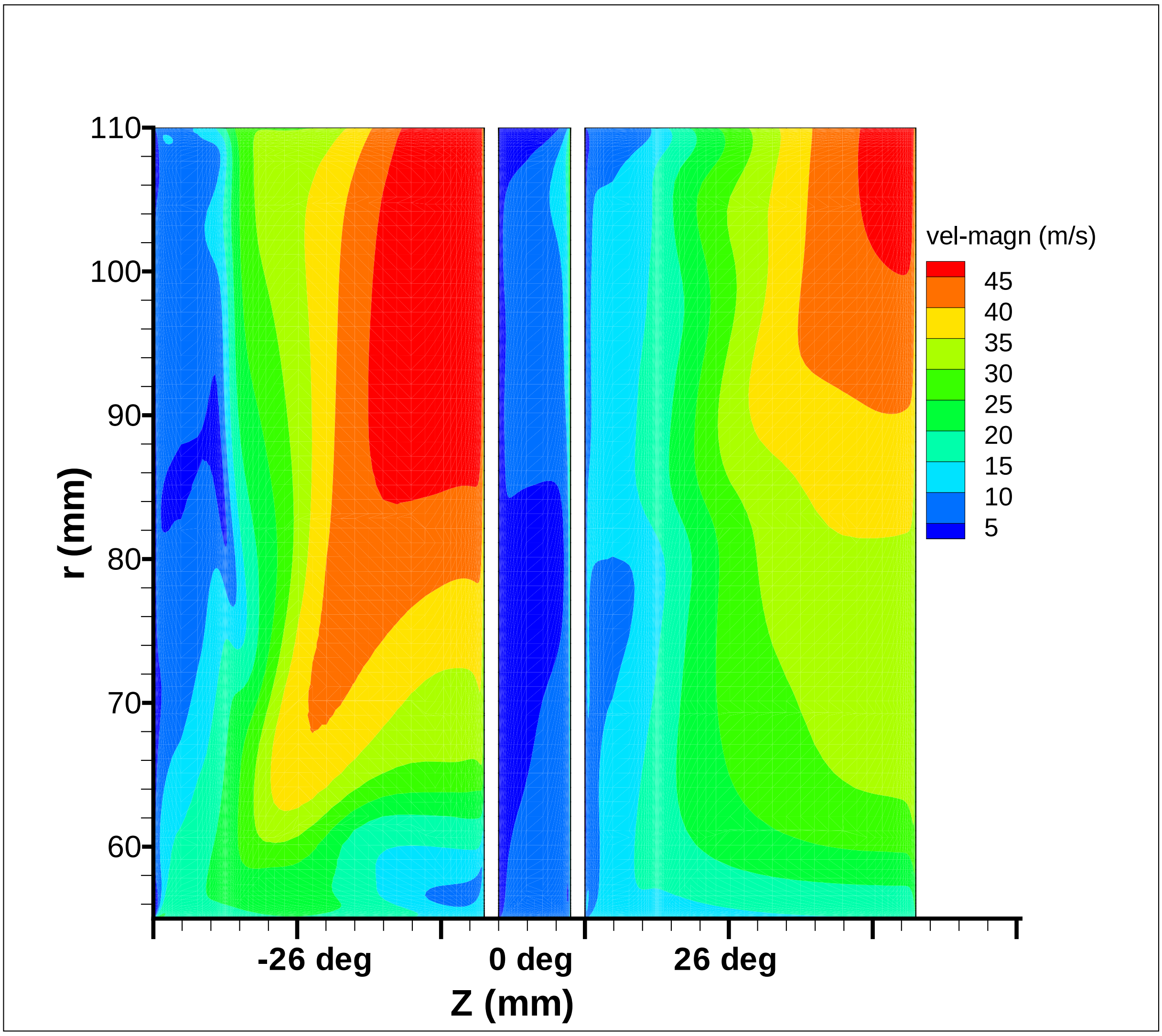

Figure 6.38: Velocity magnitude contours, case cms

The stator averaged heat transfer coefficients are displayed together in Fig. 6.39 to allow graphic comparison of the heat transfer obtained for all the cases. It can be observed that the configuration with the highest heat transfer coefficient is the one with the deepest magnet (18mm), the narrowest clearance (1mm) and the highest speed (3000rpm). However, this configuration leads to considerable resistive torque because of the deep magnet. The second highest heat transfer coefficient was found for the configuration with the 1 mm clearance, the 2mm magnet and the 3000rpm angular speed. Although this configuration has a lower heat transfer coefficient at the clearance inlet (140W/(m^{2}K) as opposed to 250W/(m^{2}K)), it has the same heat transfer coefficient as the one featuring a deep magnet for $r > 85$mm.

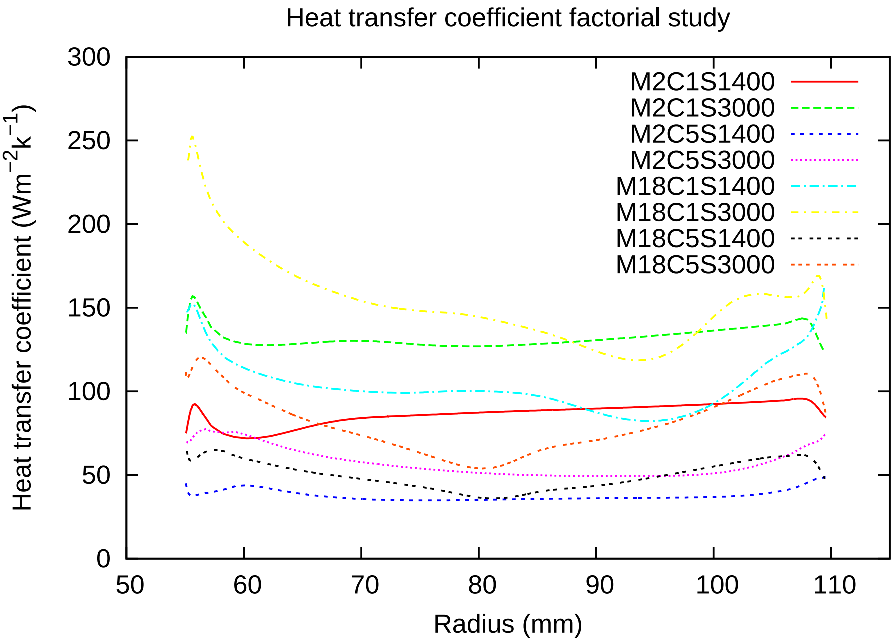

Figure 6.39: Average stator heat transfer coefficient for all the cases

6.4.1 Main effects on the stator heat transfer coefficient

The running clearance has been split into ten control volumes at the ten radial locations at which the heat transfer coefficient on the stator surface has been evaluated (Fig. 6.40). Each control volume spans over a radial range of 5 mm and is identified by its radial coordinate. The main and interaction effects have been calculated and response surfaces have been obtained at each of these radii.

From the graph of the main effects on the stator heat transfer coefficient in Fig. 6.41 it can be seen that the running clearance is the factor with the strongest effect. The consequence of the wide running clearance is the lower heat transfer coefficient (negative effect) at all radii considered (in the order of -60W/(m^{2}K)). The magnets' depth has a positive contribution to the heat transfer coefficient and this is more noticeable at the inner and outer radii regions with values of 40 W/(m^{2}K). The magnet depth does not seem to substantially increase the heat transfer for intermediate radii (80mm $< r <$ 95mm) where its effect is in the order of 5 to 10W/(m^{2}K).

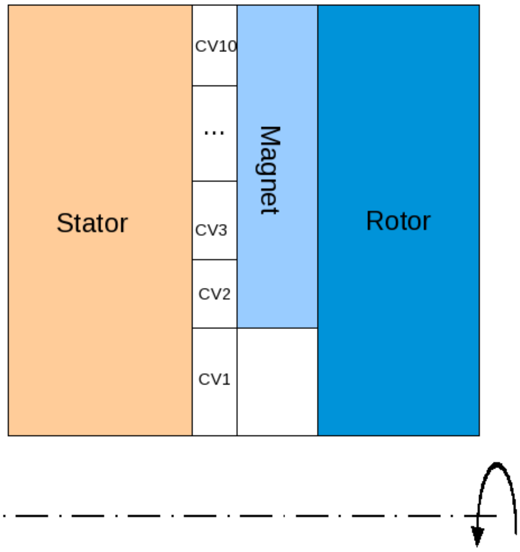

Figure 6.40: Running clearance division

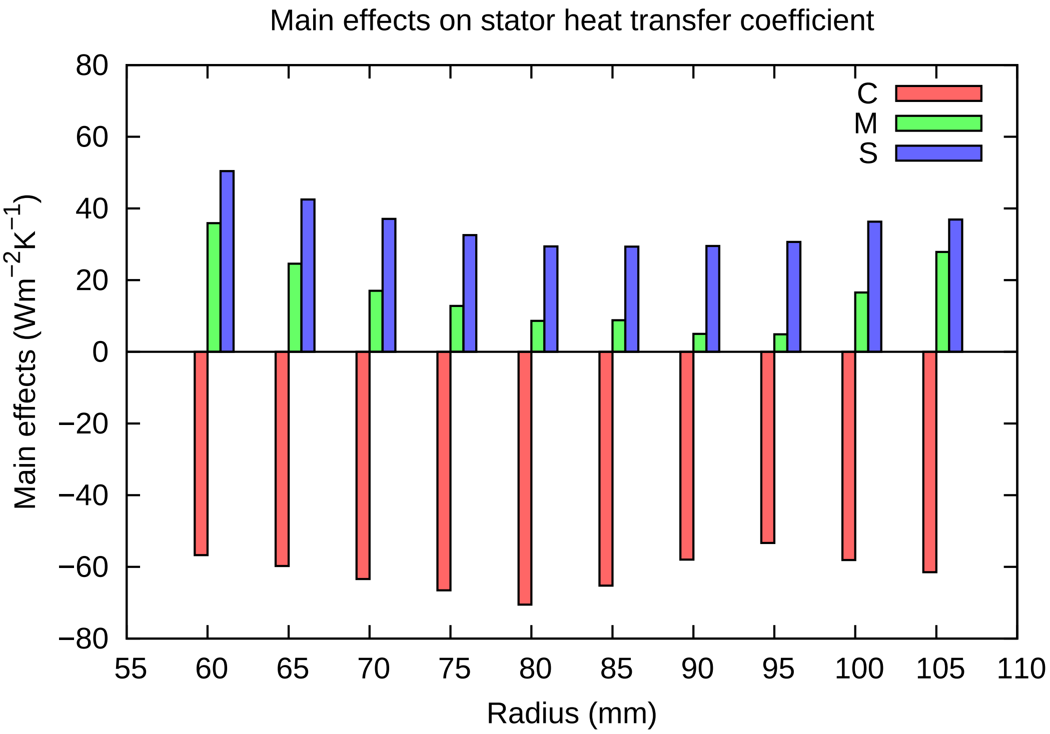

Figure 6.41: Main effects on the stator heat transfer coefficient

The rotational speed has a positive effect on the stator heat transfer coefficient. Its contribution is mostly uniform over the radius, with a slightly higher effect at the running clearance inlet where the effect is 50W/(m^{2}K) as opposed to the 40W/(m^{2}K) at the outlet.

6.4.2 Interaction effects on the stator heat transfer coefficient

The interaction effects are fairly weak compared to the main effects. They are displayed in Fig. 6.42 which has been scaled to the same range of the main effects to allow for comparison. It is worth underlying that the main and interaction effects are valid for the range of the parameters investigated. A narrower range of the parameters could lead to weaker interactions and a wider range to stronger ones.

The '*CM*' interaction is negative for the inner region (60mm $< r <$ 80mm) whereas it is positive on the outer region (80mm $< r <$ 105mm). Values of the '*CM*' interaction range from -18W/(m^{2}K) at the inlet to -5 for r = 80mm to 20 W/(m^{2}K) for r = 95mm. This means that a deeper magnet has a higher effect on a narrower clearance for the inner region and the opposite for the outer region of the running clearance.

The '*CS*' effect is negative over the whole radius and in the range of -15W/(m^{2}K).

The '*MS*' and '*CMS*' effects have a negligible magnitude over the whole radius when compared to the other discussed effects. The interactions can be visualised by fixing one of the three parameters and by plotting the heat transfer coefficient as a function of the remaining two. The '*CM*' interaction has been plotted for the rotational speed of 1400rpm, the '*CS*' for the magnet depth of 2mm, and the '*MS*'

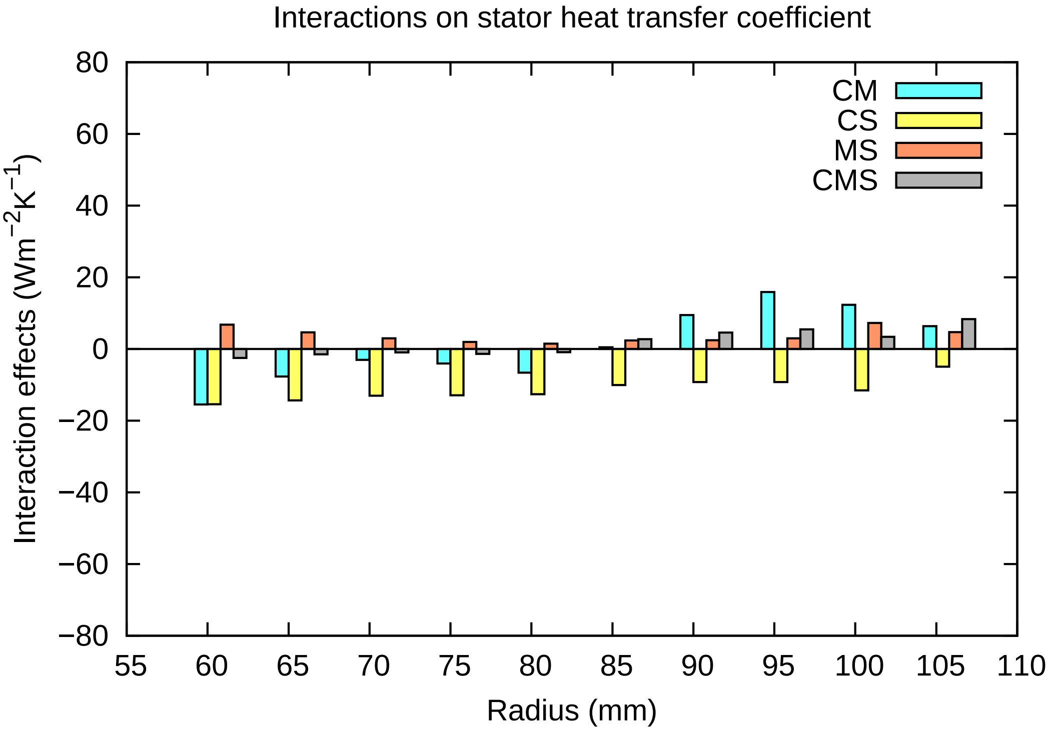

Figure 6.42: Interaction effects on the stator heat transfer coefficient

for the clearance of 1mm. The interactions are slightly different at different radii, as illustrated in Fig. 6.42, however the stator heat transfer coefficient at $r = 60$mm can be taken as an example. At the radius of 60 mm the '*CM*', '*CS*' and '*MS*' interactions have been plotted.

The '*CM*' interaction is presented in Fig. 6.43 where it is clear that the increase of the magnet depth leads to the higher heat transfer coefficient at low clearances than at high ones. This corresponds to the negative value of the '*CM*' interaction effect at $r = 60$mm in Fig. 6.42.

Also the '*CS*' interaction has a negative effect on the stator heat transfer coefficient as illustrated in Fig. 6.44: an increase of the rotational speed is more beneficial if a reduction of the running clearance takes place, hence the '*CS*' interaction is negative again as shown in Fig. 6.42.

Even if the '*MS*' interaction at $r = 60$mm is the second highest among all radii, it is negligible compared to the main effects and to the other interactions. Its effect is illustrated in Fig. 6.45: an increase in the rotational speed has approximately the same effect for low or high magnet depths. The effect of the higher velocity at the high magnet depth is actually slightly increased. For this reason the '*MS*' interaction is positive as it can be seen in Fig. 6.42.

The '*CMS*' interaction has been shown to be negligible by plotting the '*CM*' interaction at the rotational speed of 3000rpm. From the comparison of the '*CM*' interaction at 1400rpm (Fig. 6.43) and at 3000rpm (Fig. 6.46) it is evident that no difference in the '*CM*' interdependence exists at the two rotational speeds which means that the '*CMS*' interdependence is negligible. This is also confirmed by the values of the '*CMS*' interactions displayed in Fig.6.42.

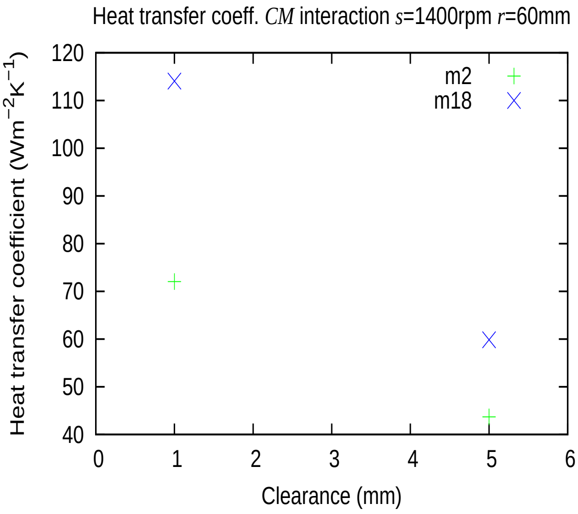

Figure 6.43: *CM* interaction, r=60mm

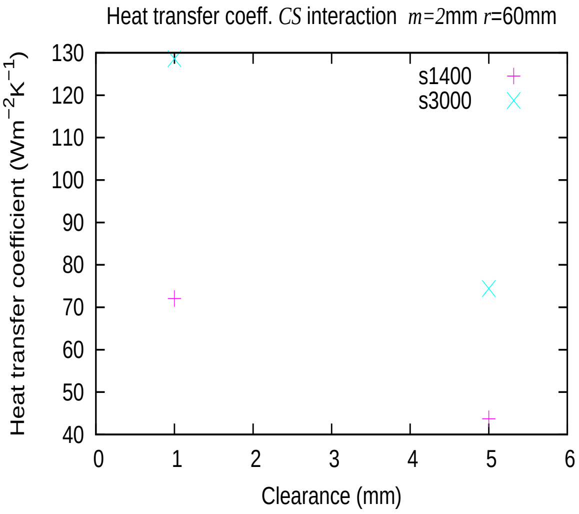

Figure 6.44: *CS* interaction, r=60mm

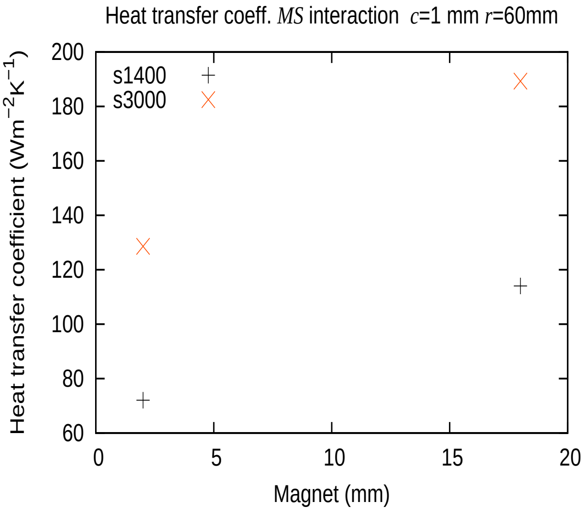

Figure 6.45: *MS* interaction: r=60mm

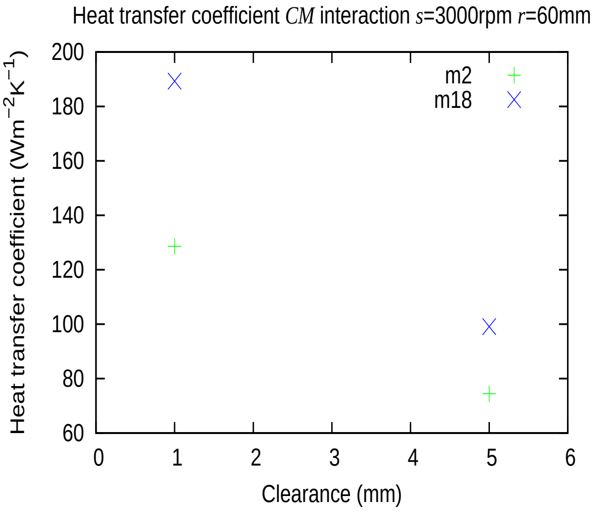

Figure 6.46: *CM* interaction: r=60mm

6.4.3 Stator heat transfer coefficient first order correlation

A first order response function for the heat transfer coefficient on the stator has been derived at each of the radii in which the domain has been divided. Due to the fact that this is a 2 level factorial study, a regression function with higher order than a linear one can not be obtained. The least mean squares method has been used to find the regression constant coefficients. The heat transfer coefficient regression function has a polynomial form as in Eq. 6.9. The equation has been written and the coefficients have been obtained for the running clearance and the magnet depth expressed in mm, the rotational speed in rpm and the heat transfer coefficient in W/(m^{2}K).

$$h(r) = b_0(r) + b_1(r)c + b_2(r)m + b_3(r)s \tag{6.9}$$

The complete list of coefficients of the linear polynomial response function is reported in Table 6.3, on page 151. The coefficients obtained at each of the ten control volumes are given in this table.

By fixing the rotational speed at one of the two values (1400 or 3000rpm) the heat transfer coefficient depends on the two remaining factors: the running clearance and the magnet depth. The first order linear regression surfaces are therefore planes which can be obtained at every radius. In Fig. 6.47 to Fig. 6.52 the heat transfer coefficient correlation plane is plotted at the radii of 60, 80 and 100mm for both the rotational speeds of 1400 and 3000rpm. The main effects of the clearance and magnet depth can be recognised in the two slopes of the planes. The negative slope along the clearance axis corresponds to its negative effect whereas the positive slope along the magnet's depth axis corresponds to the magnet's positive effect. The positive effect of the rotational speed can be observed by comparing the two planes at a constant radius (e.g. $r = 60$mm): the slopes about the two coordinates are similar, but the plane at the highest rotational speed features greater values of heat transfer coefficient. It can be seen that the range over which the clearance and the magnet depth vary is relatively broad therefore higher order response functions need to be

Table 6.3: Stator $h(r)$ correlation coefficients

	Radius (mm)									
	60	65	70	75	80	85	90	95	100	105
b_0	48.3917	60.5434	71.2976	79.155	86.5819	83.1205	78.6961	74.7296	70.7515	74.8198
b_1	-14.1818	-14.9354	-15.8526	-16.642	-17.6355	-16.3151	-14.5009	-13.3362	-14.53	-15.3678
b_2	2.2433	1.5353	1.0626	0.7984	0.5385	0.5512	0.3132	0.3044	1.0342	1.7402
b_3	0.0315	0.0266	0.0232	0.0204	0.0184	0.0183	0.0185	0.0192	0.0227	0.0231

found in order to obtain a more accurate correlation between the parameters (clearance, magnet depth and rotational speed) and the stator heat transfer coefficient. This will be addressed in chapter 7 where further simulations and a second order response function will be built. As a result of the factorial design study of the stator heat transfer coefficient it can be concluded that the main effects are predominant over the interaction ones. The running clearance has a negative effect, whereas the magnet depth and the rotational speed have a positive effect. The positive effect of the rotational speed is the most significant.

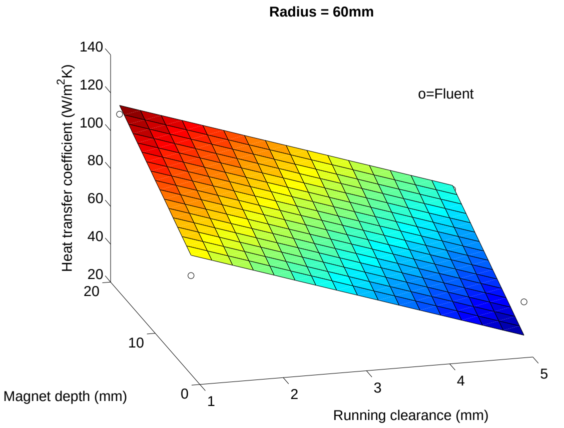

Figure 6.47: Stator *h(r)*, r=60mm, s=1400rpm

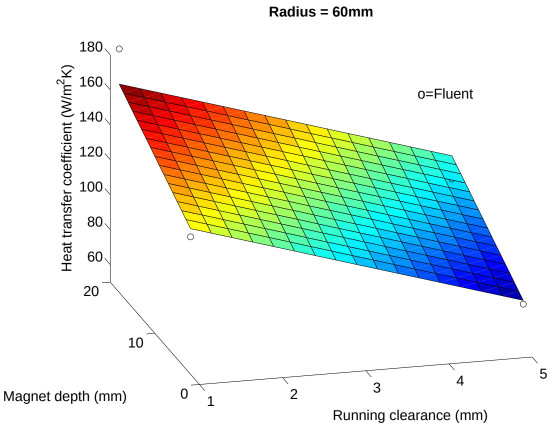

Figure 6.48: Stator *h(r)*, r=60mm, s=3000rpm

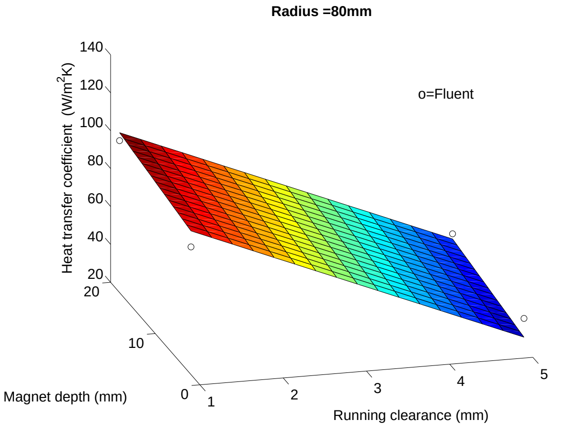

Figure 6.49: Stator *h(r)*, r=80mm, s=1400rpm

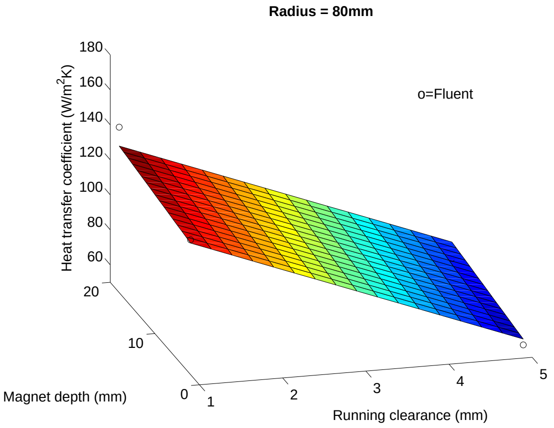

Figure 6.50: Stator *h(r)*, r=80mm, s=3000rpm

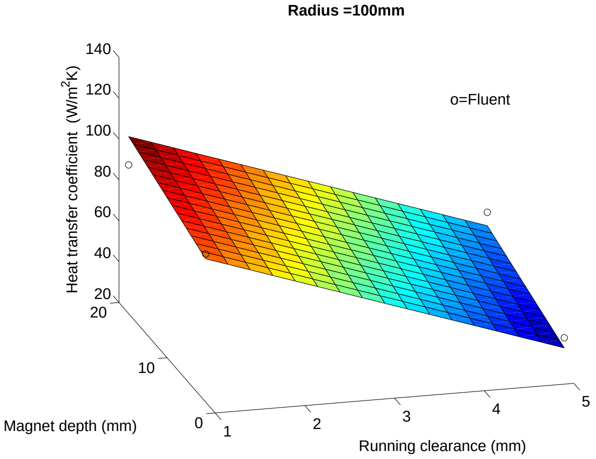

Figure 6.51: Stator *h(r)*, r=100mm, s=1400rpm

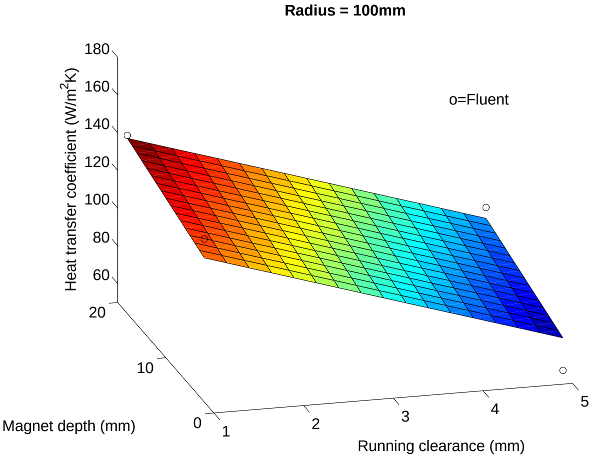

Figure 6.52: Stator *h(r)*, r=100mm, s=3000rpm

6.5 Rotor heat transfer coefficient

As already discussed the heat transfer coefficient on the surfaces of the generator will be used as an input data for the thermal LPM. Therefore it is necessary to find its magnitude on the rotor as well as on the stator. The magnet's temperature prediction is of a particular importance in order to keep it below the critical value [80]. When AFPM machines are used in certain applications, such as in wind turbines, the cooling of the magnets is not of the same particular concern as it is when these generators are coupled to an engine in an internal combustion engine driven Genset. The heat transfer coefficient on the rotor has been calculated by using as a reference temperature the temperature in the middle of the running clearance. The heat transfer coefficients have been evaluated at three equally spaced locations on the magnets' surface: -15°, 0°, and 15°. The dashed lines on the magnet surface where the heat transfer coefficient on the rotor has been calculated are shown in Fig. 6.53. The average of the heat transfer coefficient at these angles has then been obtained. For all the investigated cases (see Table 6.2 on page 122) the heat

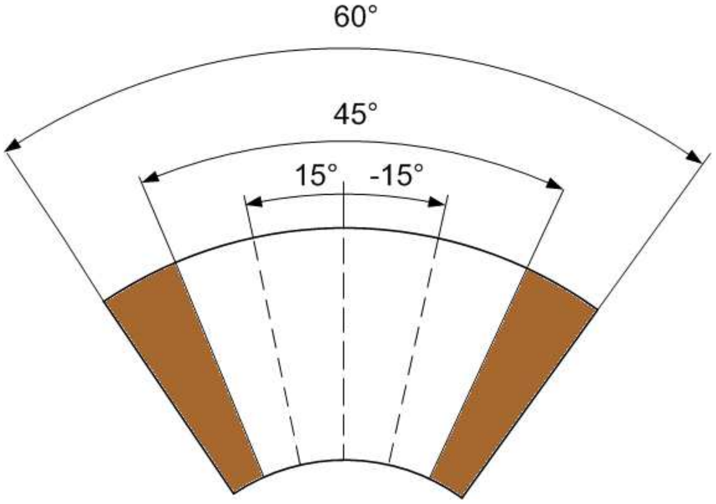

Figure 6.53: Lines where the heat transfer coefficient on the magnet has been calculated

transfer coefficient on the rotor is higher than the relevant heat transfer coefficient on the stator. In this case, as opposed to the case of the stator, a low heat transfer coefficient is desirable. This is because heat is not generated in the magnets, and a high heat transfer coefficient would have the effect of transferring the thermal energy that the air acquired from the stator to the magnets.

In an AFPM electrical machine the heat generated in the stator windings is transmitted to the cooling air by convection, a part of this heat leaves the machine from the outlet and part of it is transferred to the rotor.

The heat transfer coefficient on the rotor follows a characteristic pattern for every model investigated (Fig. 6.54 to Fig. 6.62): the heat transfer coefficient is maximum at the running clearance inlet due to the high radial velocities then it decreases as the air flows towards the outlet. For all the cases with the high magnet depth (indicated with the letter 'm' in the case description in Table 6.2 on page 122) a steep increase in the heat transfer coefficient occurs at the peripheral radius. This is caused by the flow pattern at the trailing edge of the magnet where the low pressure causes the reverse flow to enter the clearance from the outlet.

The average heat transfer coefficients on the rotor is displayed in Fig. 6.62 for all the cases analysed in this factorial study. The highest heat transfer coefficient is obtained with the narrowest clearance, the deepest magnet and the highest speed. However, the heat transfer coefficient for case ‘s’ (high speed) is greater than for case ‘ms’ (high magnet and speed, low clearance). This can also be observed in Fig. 6.63 on page 159 which shows that the magnet’s main effect on the rotor heat transfer coefficient is weak at the outlet radius.

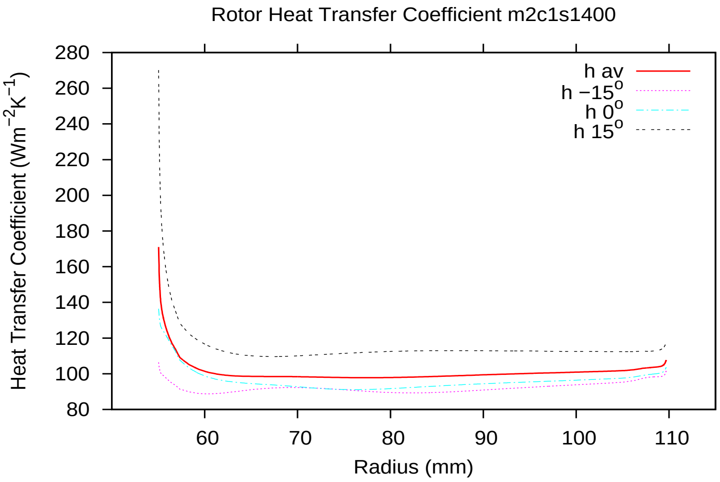

Figure 6.54: Rotor local *h(r)* case ‘(1)’

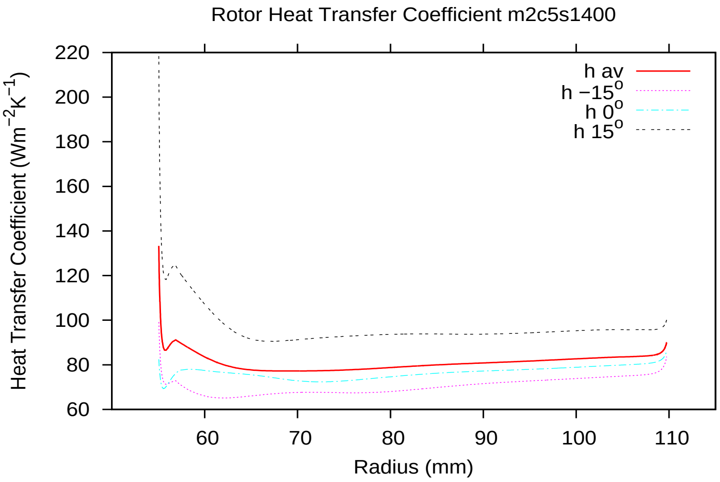

Figure 6.55: Rotor local *h(r)* case ‘c’

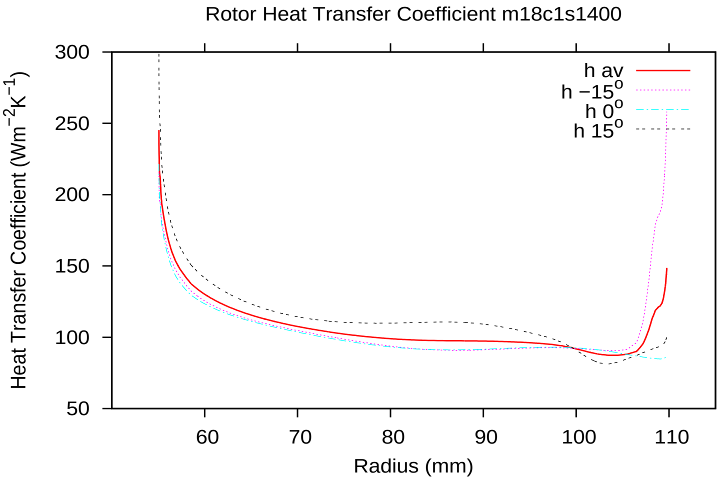

Figure 6.56: Rotor local *h(r)* case 'm'

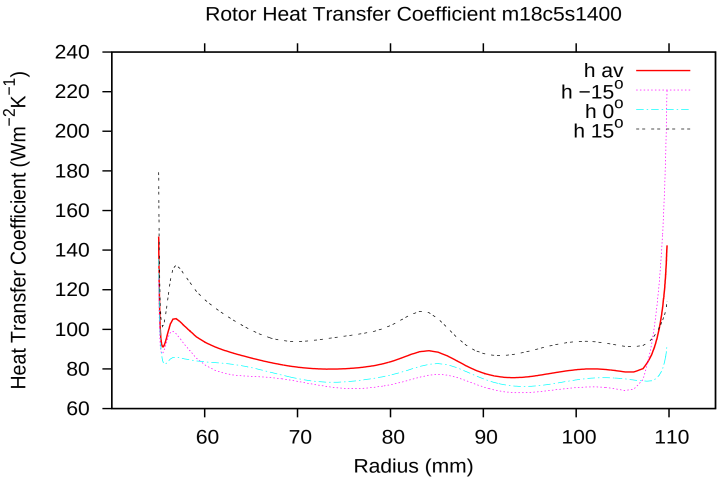

Figure 6.57: Rotor local *h(r)* case 'cm'

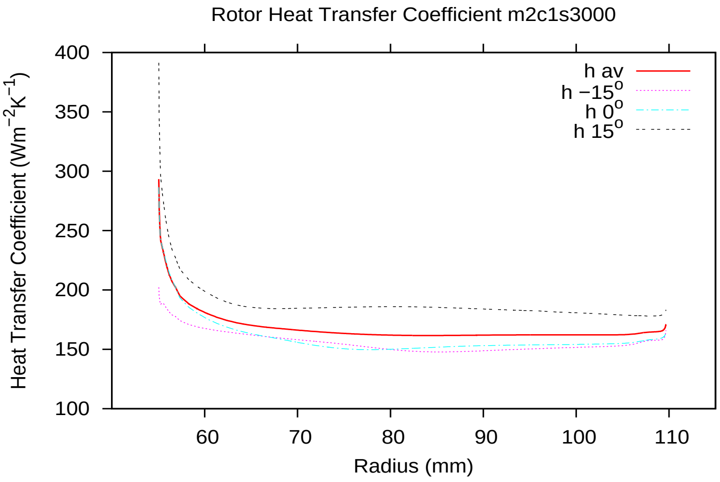

Figure 6.58: Rotor local *h(r)* case 's'

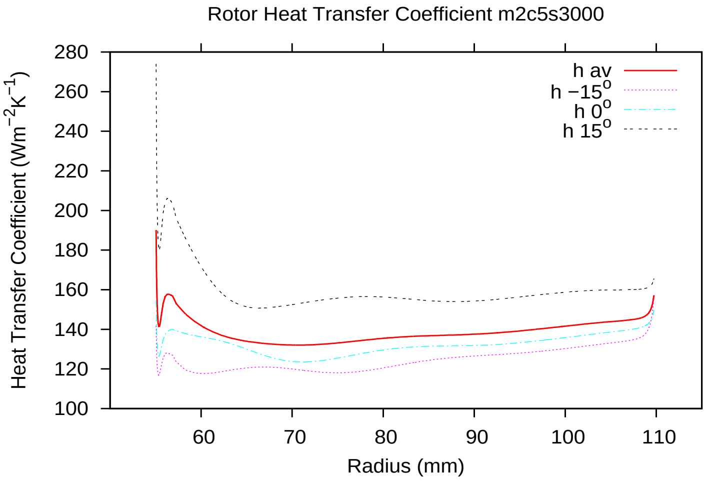

Figure 6.59: Rotor local *h(r)* case 'cs'

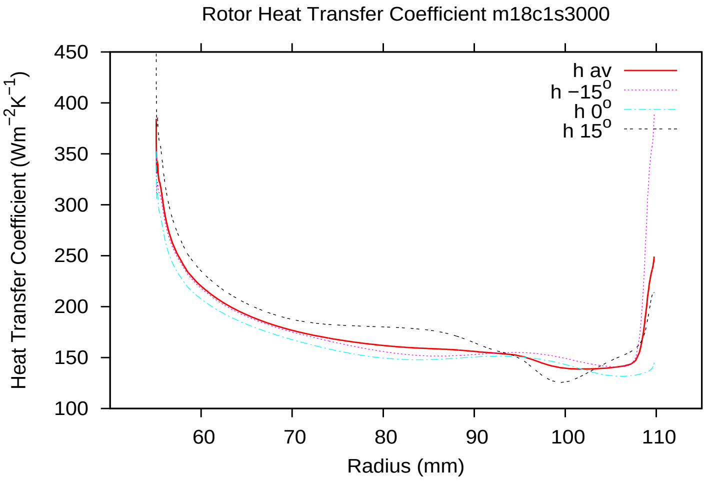

Figure 6.60: Rotor local *h(r)* case 'ms'

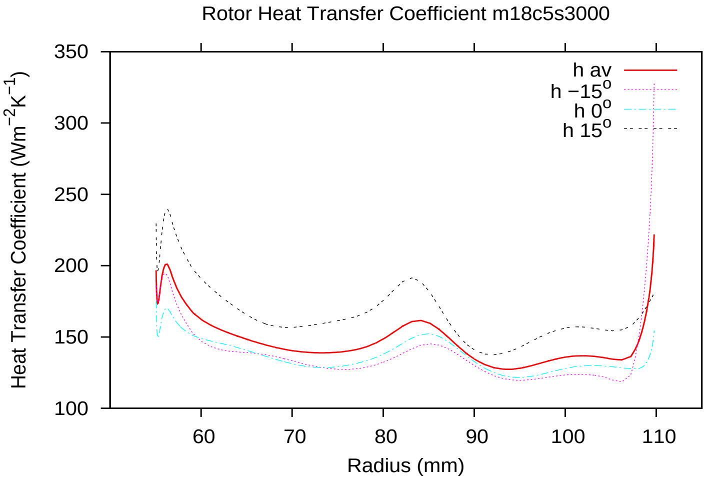

Figure 6.61: Rotor local *h(r)* case 'cms'

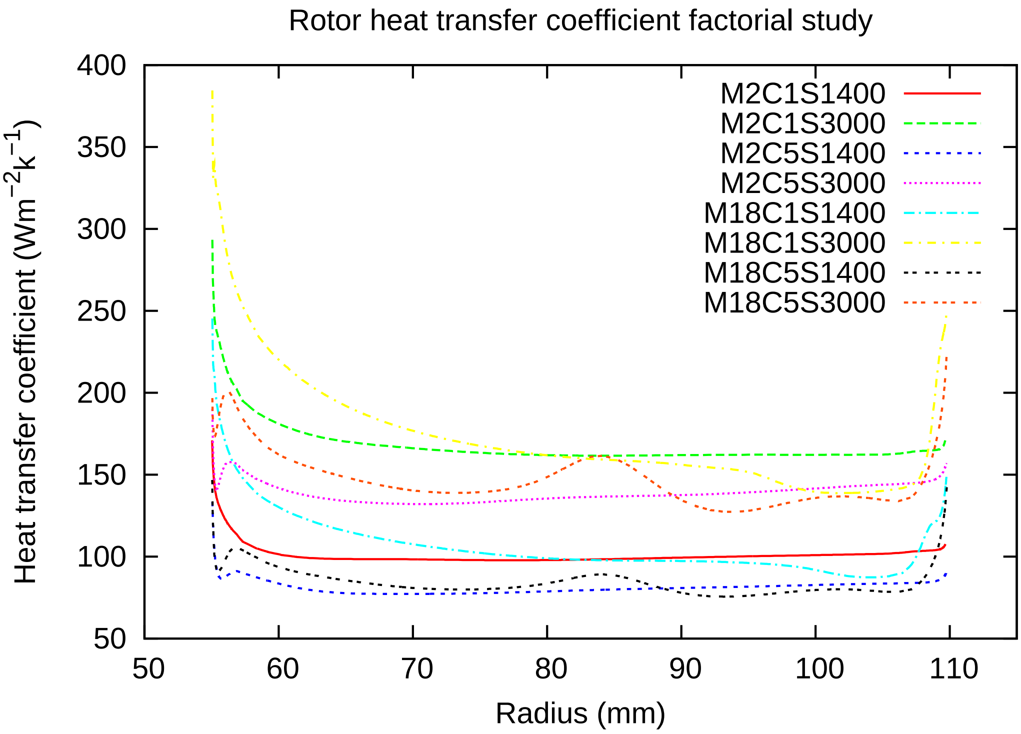

Figure 6.62: Average rotor local *h(r)* for all cases

6.5.1 Main effects on the rotor heat transfer coefficient

The main effects of the parameters on the rotor heat transfer coefficient are shown in Fig. 6.63. The effects of the factors on the rotor heat transfer coefficient are similar to those on the stator. The running clearance has a negative effect: that is wider running clearances lead to a lower heat transfer coefficient on the rotor. The magnet's depth has a positive effect which is greater for mid radii. The rotational speed also has a positive effect as it increases the shear stresses on the rotor and consequently the heat transfer. Whereas a positive effect of the rotational speed is desirable for the heat transfer on the stator, this is not the case for the rotor, as heat transfer to the rotor would increase the temperature of the magnets.

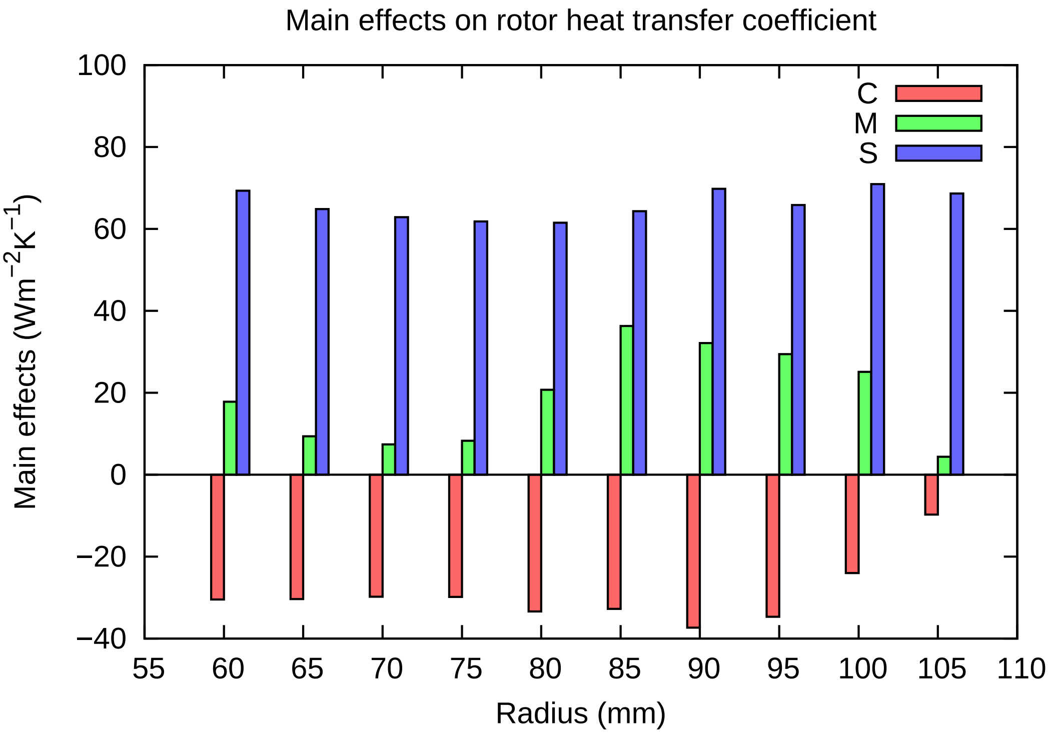

Figure 6.63: Rotor heat transfer coefficient main effects

6.5.2 Interaction effects on the rotor heat transfer coefficient

The interactions of the parameters on the rotor's heat transfer coefficient are very marginal. They are shown in Fig. 6.64 with the same scale as for the main effects.

The '*CM*' interaction effect can be noticed for 80mm $< r <$ 95mm on the rotor surface, and it is negative, which means that a deeper magnet increases the heat transfer coefficient at narrow clearances more than at wide clearances.

The '*CS*' interaction effect is visible for low radii and is negative therefore high speeds enhance the heat transfer coefficient stronger at narrow clearances.

The '*MS*' interaction effect is positive and is noticeable for radii larger than 85mm.

No '*CMS*' interaction effect occurs at any radii.

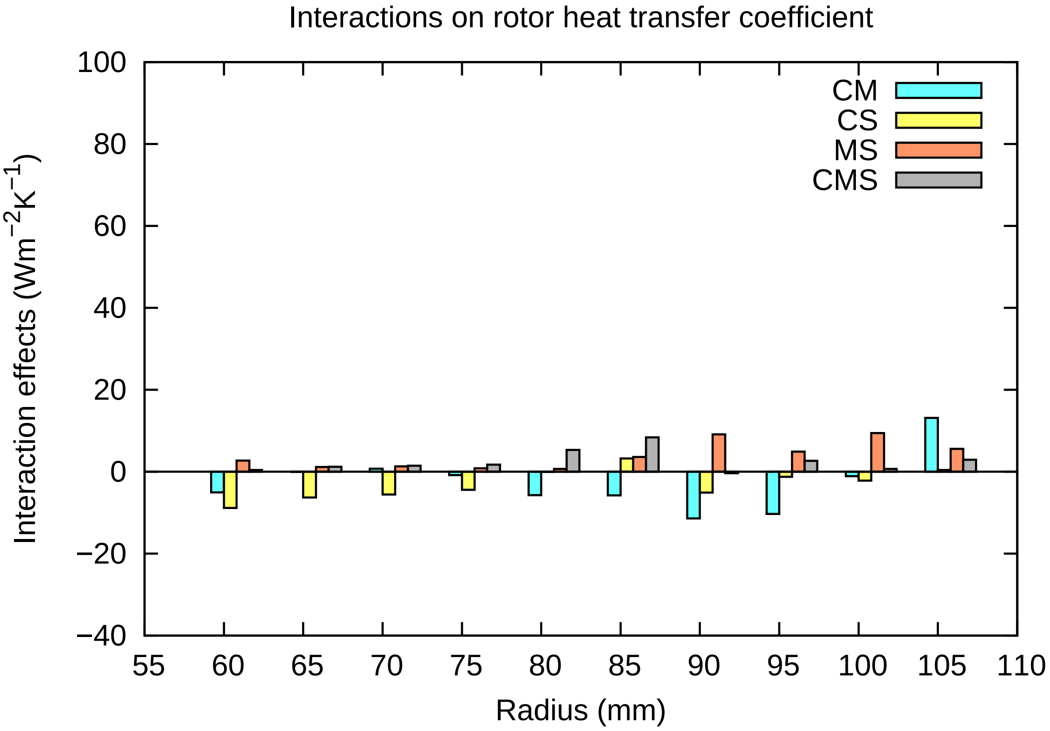

Figure 6.64: Rotor heat transfer coefficient main effects

6.5.3 Rotor heat transfer coefficient first order correlation

First order correlations have been obtained for the heat transfer coefficients on the rotor for the 10 radii into which the domain has been split. As for the heat transfer coefficient on the stator, the least mean squares method has been used for the fitting of the first order polynomial. The equations have the following form:

$$h(r) = b_0(r) + b_1(r)c + b_2(r)m + b_3(r)s \tag{6.10}$$

As in the case of the stator, a graphical representation has been plotted for the correlation of the rotor heat transfer coefficient at three radii. Figs. 6.65 and 6.66 show the correlation at r = 60mm, for the rotational speeds of 1400rpm and 3000rpm, respectively. The plane correlating the parameters with the rotor heat transfer coefficient at $r = 80$mm are displayed in Fig. 6.67 and 6.68 for the rotational speeds of 1400rpm and 3000rpm respectively. The correlations for $r = 100$mm is shown in Figs. 6.69 and 6.70. A reasonable match can be observed between the fitting plane and the available data points from Fluent. The positive influence on the rotor heat transfer coefficient of the magnets is evident at all radii for both speeds. To the contrary, the wider clearance reduces the rotor heat transfer coefficient. This is because, although a wider clearance increases the mass flow rate, the radial velocities reduce due to the larger cross sectional area. The coefficients of the correlation for the heat transfer on the rotor are summarised in Table 6.4 on page 162, where the columns correspond to the radii and the rows to the coefficients.

6.6 Mass flow rate

The mass flow rate through the system has been calculated for all cases of this factorial study (see Table 6.2 on page 122). The main and the interaction effects of the factors have been identified. The original domain includes six magnets and two running clearances. However, only a twelfth of the whole domain has been modelled. The whole domain has been divided to six subdomains due to the 60° periodicity, and to two due to the symmetry in the axial direction. The advantage of symmetry and the periodicity of the systems have been considered in order to reduce the model's size. The mass flow rates shown are relevant to the complete domain. This means that the mass flow rate from the simulations has been multiplied by 12 to obtain the values for the full generator. From the mass flow rate graphs in Fig. 6.71 it can be seen that the widest clearance almost doubles the mass flow rate

Table 6.4: Rotor *h(r)* correlation coefficients

	Radius (mm)									
	60	65	70	75	80	85	90	95	100	105
b_0	50.227500	55.299400	56.053500	56.764400	58.631800	52.901600	49.807000	54.456900	41.280900	38.554300
b_1	-7.618600	-7.597400	-7.443700	-7.455000	-8.351400	-8.189300	-9.333600	-8.678700	-6.006300	-2.439600
b_2	1.111700	0.587658	0.464051	0.516413	1.296900	2.267300	2.007100	1.839500	1.569400	0.274996
b_3	0.043311	0.040517	0.039274	0.038631	0.038459	0.040198	0.043634	0.041145	0.044352	0.042918

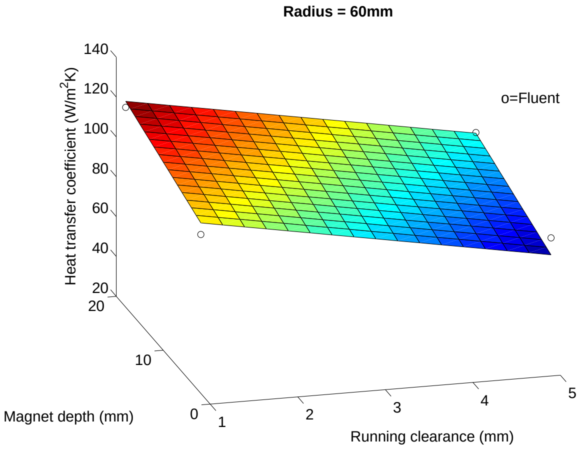

Figure 6.65: Rotor *h(r)*, *r*=60mm, 1400rpm

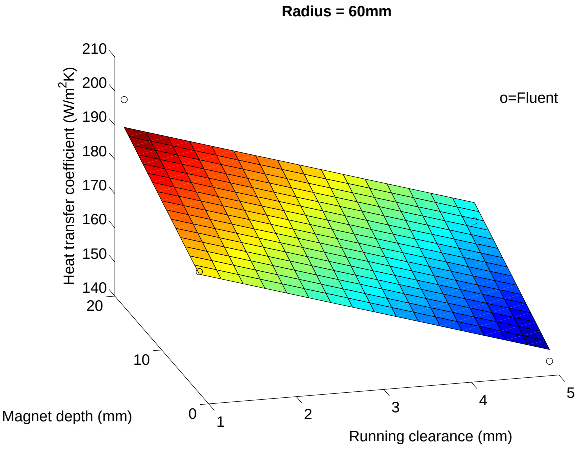

Figure 6.66: Rotor *h(r)*, *r*=60mm, 3000rpm

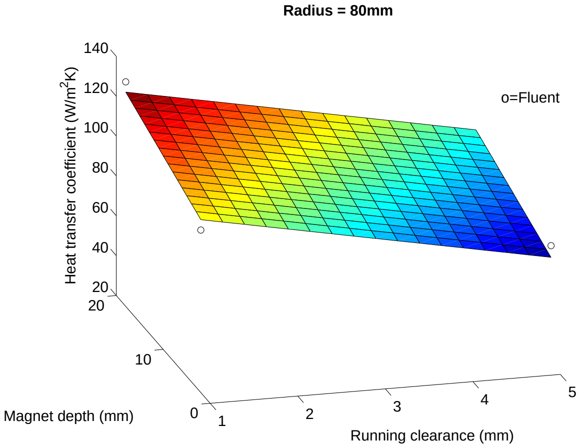

Figure 6.67: Rotor *h(r)*, *r*=80mm, 1400rpm

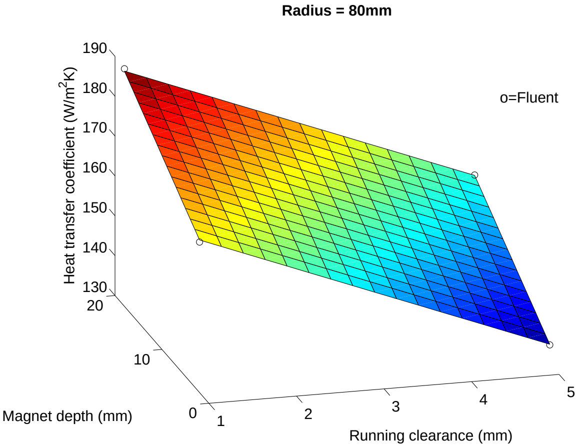

Figure 6.68: Rotor *h(r)*, *r*=80mm, 3000rpm

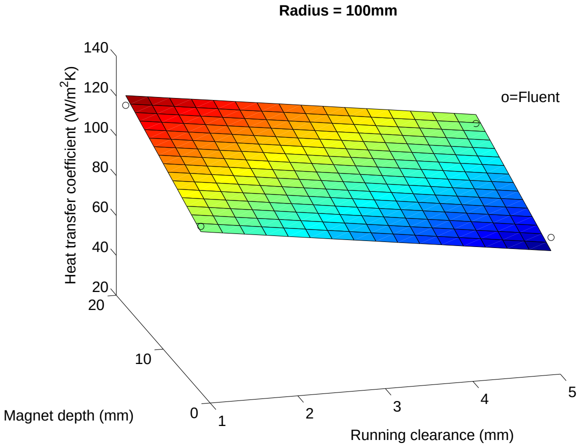

Figure 6.69: Rotor *h(r)*, *r*=100mm, 1400rpm

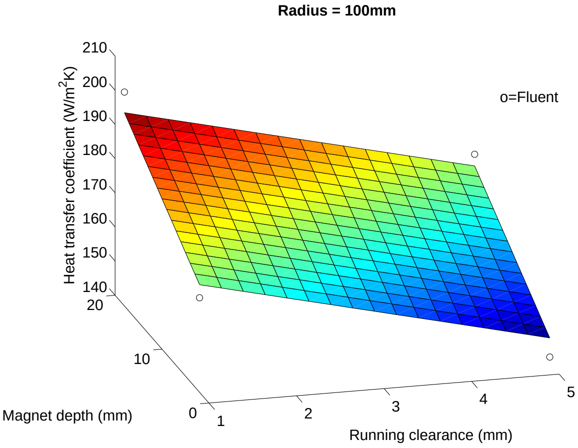

Figure 6.70: Rotor *h(r)*, *r*=100mm, 3000rpm

if the magnets and the rotational speed are kept at their minimum values. However, the factors responsible for the change in the mass flow rate are mainly the magnets' depth and the rotational speed. The wide clearance does not have such a strong effect on the mass flow rate in models with deeper magnets. By comparing the cases 'm' and 'cm' it is clear that the clearance for high magnet values has no influence on the mass flow rate.

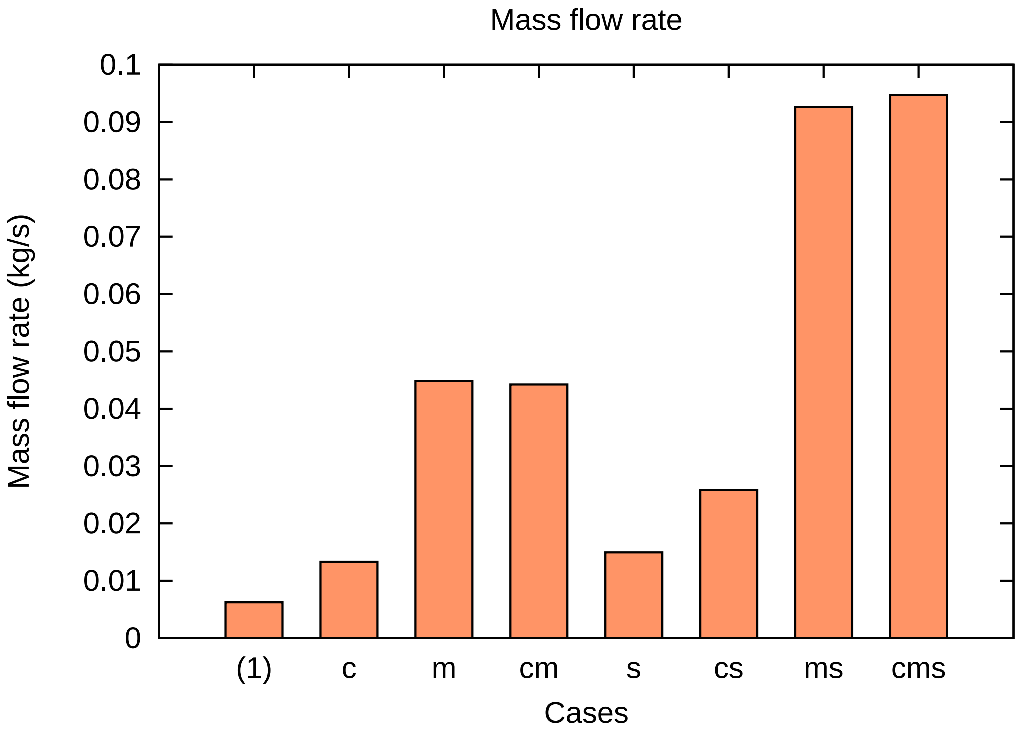

Figure 6.71: Mass flow rate for the factorial study cases

6.6.1 Main effects on mass flow rate

The main and interaction effects are shown in Fig. 6.72. The main effects 'C', 'M', and 'S' are all positive: an increase in each of the above parameters increases the mass flow rate, however the clearance contribution is negligible (one order of magnitude lower) compared to the magnet and the rotational speed effects.

6.6.2 Interaction effects on mass flow rate

The interaction effects '*CM*', '*CS*' and '*CMS*' (Fig. 6.72) are negligible because their magnitude is at least one order of magnitude lower than that of the main effects. Only the '*MS*' interaction is positive and comparable to the '*M*' and '*S*' effects. This means that an increase of the rotational speed has a higher influence on the mass flow rate at the high values of the magnet depth.

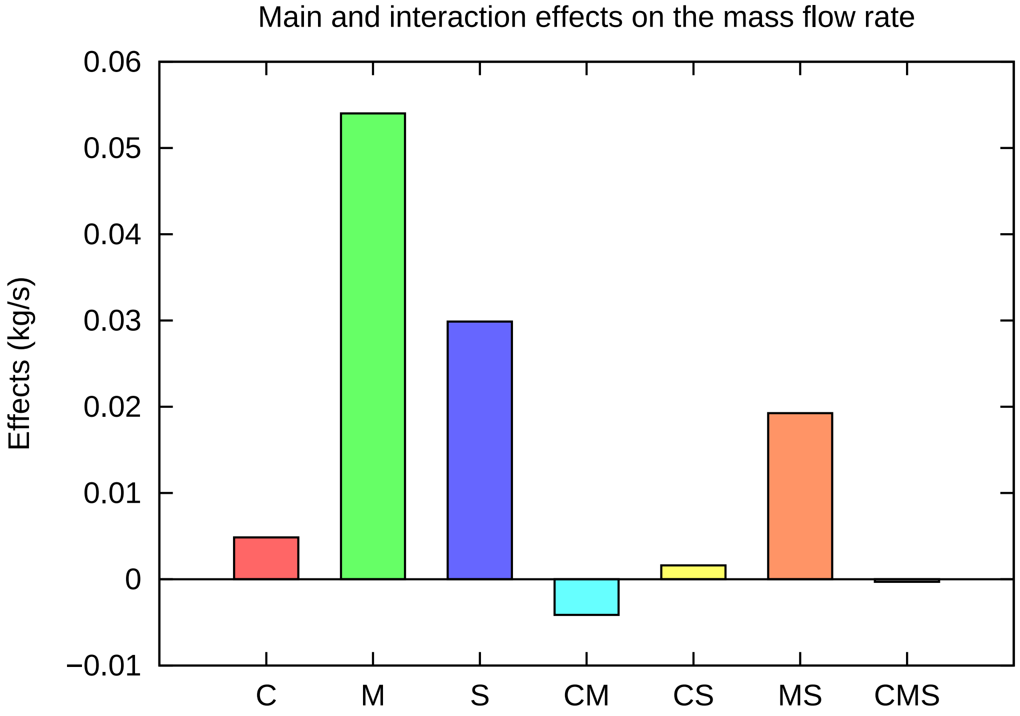

Figure 6.72: Main and interaction effects on the mass flow rate

6.6.3 Mass flow rate first order linear correlation

With the least mean squares method a first order correlation in terms of the three parameters (clearance, magnet, and rotational speed) for the mass flow rate has been obtained as in Eq. 6.11. This is a first order regression function for the mass flow rate in the investigated domain. A higher order regression function can be obtained by increasing the number of tests in the range of variation of the parameters.

$$\dot{m} = -0.036369 + 0.001214c + 0.0033755m + 0.0000186649s \qquad (6.11)$$

where the clearance and the magnet depth are expressed in mm, the rotational speed in rpm and the mass flow rate in kg/s. The plane representing the linear regression of the mass flow rate for the rotational speed of 1400rpm is shown in Fig. 6.73, whereas Fig. 6.74 represents the mass flow rate at 3000rpm. It can be observed that the influence of the deep magnets increases the mass flow rate which, instead, remains independent on the value of the clearance.

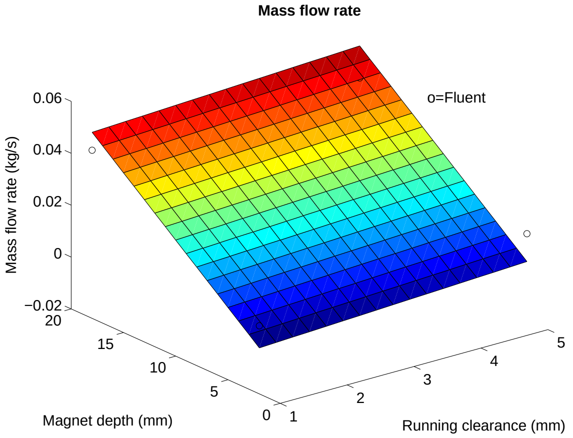

Figure 6.73: Mass flow rate regression plane at s=1400rpm

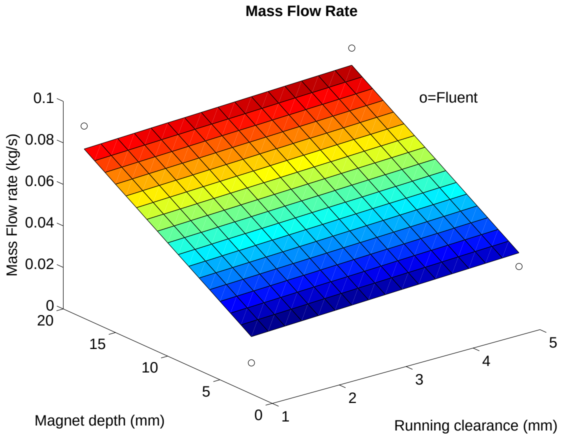

Figure 6.74: Mass flow rate regression plane at s=3000rpm

6.7 Torque and power losses

Two contributions to the torque (one due to the pressure drag and one due to the frictional resistance) have been obtained from the numerical simulations in Fluent. As well as for the mass flow rate, for the torque calculation the results displayed are relevant to the full domain, i.e. the torque values presented are the results from the simulations multiplied by a factor of 12 (Fig. 6.75).

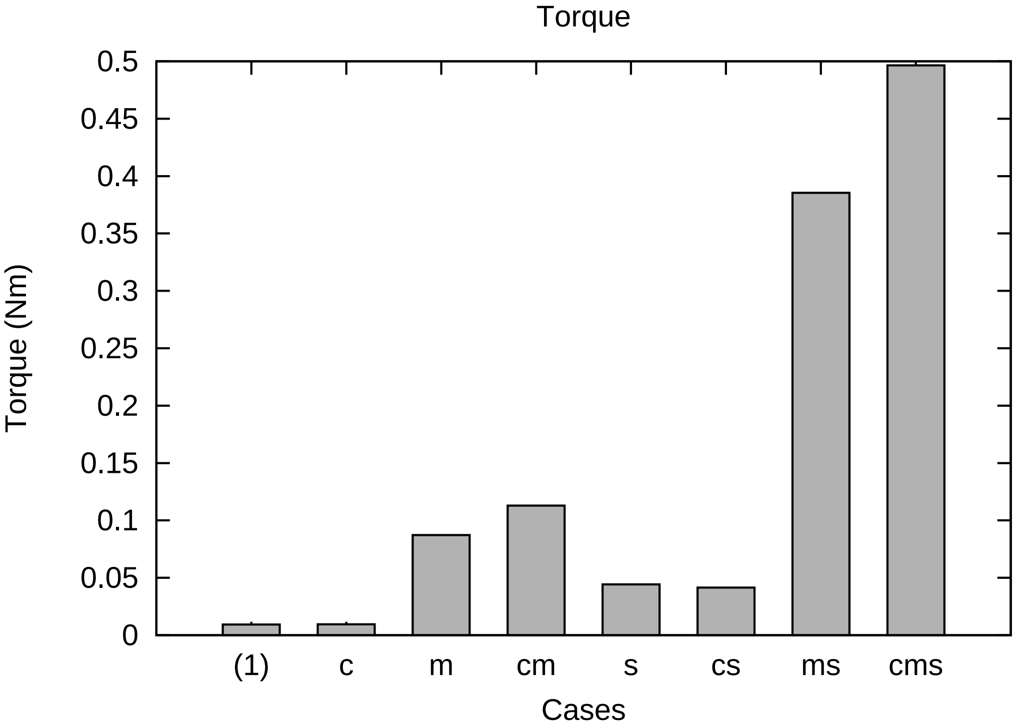

Figure 6.75: Torque for the cases considered

An attempt has been made in order to verify the pressure torque obtained from Fluent by comparing it to the one calculated with the Euler work equation. To obtain the torque the mass flow rate predicted in Fluent is multiplied by the difference of the product of the tangential velocity and the inner and outer radii:

$$T = \dot{m}\left(v_{out} R_{out} - v_{in} R_{in}\right) \tag{6.12}$$

Whereas the order of magnitude between the Euler and the Fluent torques is comparable for all of the eight models tested, an exact match is impossible. This is due to the fact that in the Euler work equation (Eq. 6.12) all the mass flow rate is used to calculate the pressure torque, whereas in Fluent the mass flow rate of air in the clearance is not contributing to the work done by the magnets. In an ideal case where the running clearance is zero the Fluent results would match the theoretical Euler calculation. For this reason the best match between the Euler and the Fluent results is obtained at the narrowest running clearance with the Euler calculation prediction exceeding the Fluent torque by only 19%.

6.7.1 Main effects on the torque

The main and interaction effects of the parameters (clearance, magnet depth and angular speed) on the total torque (pressure and frictional contributions) are reported in Fig. 6.76. These effects resemble the effects already analysed for the mass flow rate. The most significant main effects on the torque are '*M*' and '*S*', both being positive. The '*C*' effect on the torque is insignificant. This means that the total torque increases with the magnets' depth and with the rotational speed, but is independent of the clearance.

6.7.2 Interaction effects on the torque

Among parameters interactions only the '*MS*' effect is notable: the high magnet depth lead to a higher torque at the higher rotational speeds. The '*CM*', '*CS*', and '*CMS*' interactions all have marginal effects on the torque as illustrated in Fig. 6.76.

6.7.3 Torque first order correlation

A first order polynomial regression function has been derived for the total torque. Also in this case the least mean squares method has been used. In Eq. 6.13 the

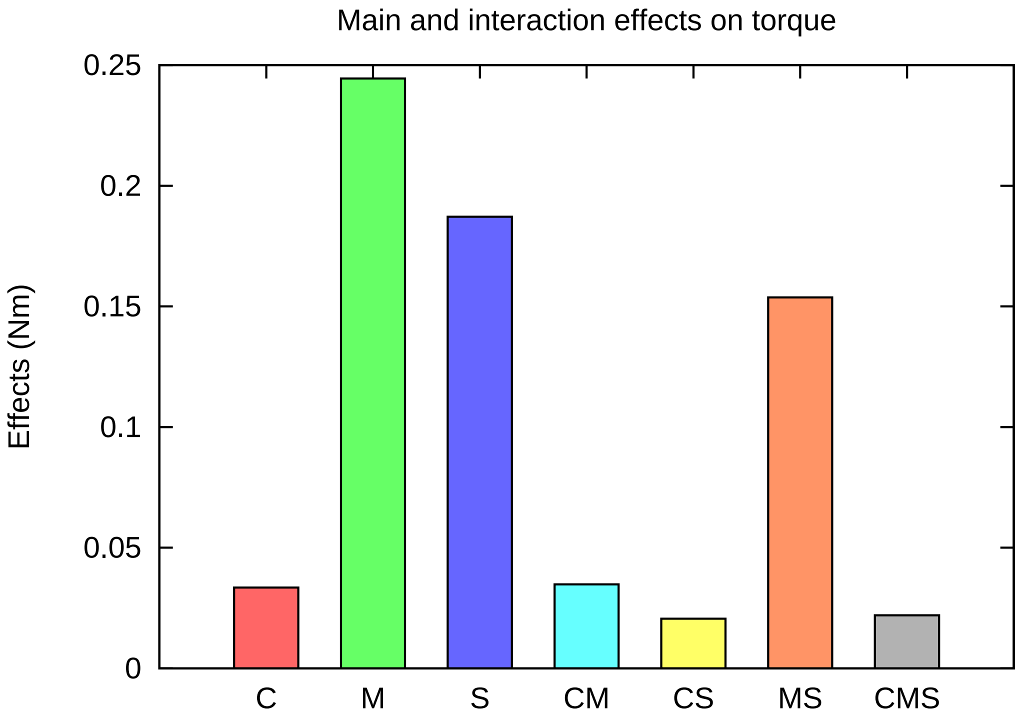

Figure 6.76: Main and interaction effects on the torque

torque is expressed in Nm, the clearance and the magnet in mm, and the rotational speed in rpm.

$$T = -0.2869364 + 0.008368c + 0.0152745m + 0.0001169932s \tag{6.13}$$

The regression planes for the total torque at the rotational speed of 1400rpm and 3000rpm are shown in Fig. 6.77 and Fig. 6.78, respectively. The torque is independent of the running clearance value, whereas it increases considerably for the high value of the magnet's depth; this is valid at both the rotational speeds investigated.

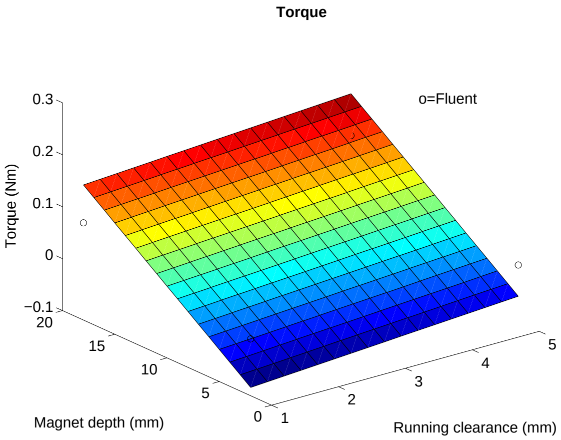

Figure 6.77: Torque plane, s= 1400rpm

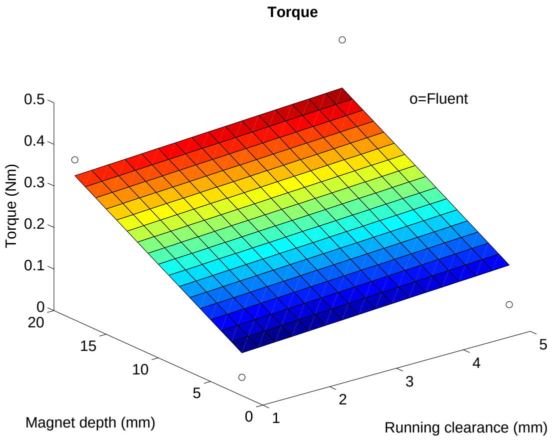

Figure 6.78: Torque plane, s=3000rpm

6.7.4 Power losses

The effect of the factors on the power also has been identified. Since the power depends on the torque through the rotational speed, and the highest rotational speed is twice as much as the lowest, then it is not sufficient to change the order of the magnitude of the power, and the effects remain the same as for the torque case.

6.8 Conclusions

A factorial study has been carried out on the system consisting of the stator and the rotor with protruding magnets. The effects of the three parameters, namely the running clearance, the magnet depth and the rotational speed, on the stator and on the rotor heat transfer coefficients, on the air mass flow rate and on the torque have been found. The main findings can be summarised as follows:

- The magnets' depth and the rotational speed have a positive effect on the stator heat transfer coefficient. However, the effect of the magnet depth is more noticeable at the inlet and at the outlet of the running clearance.

- The running clearance has a negative effect on the stator heat transfer coefficient. An optimal design for the maximum heat transfer on the stator would require a narrow running clearance. A high heat transfer coefficient resulting from a narrow running clearance would not affect the torque and consequently the power required to spin the rotor. On the contrary, high heat transfer coefficients, resulting from high rotational speeds and deep magnets, would increase the windage power losses.

- The interaction effects are generally much weaker than the main effects of the above three parameters. Only the '*CS*' and '*CM*' interactions have been found to influence the stator heat transfer coefficient, even if the main effects are significantly stronger. The '*CS*' interaction is negative on all the stator surface. The 'CM' interaction is negative for $r<$ 80mm and becomes positive for larger radii.

The weakness of the interaction between the parameters has been confirmed. Therefore in chapter 7 a variation of each individual parameter will be performed. This will show the dependency of the target quantities (the heat transfer coefficients on stator and rotor, the air mass flow rate and the torque) from the design and operational parameters and will allow the determination of higher order response functions.

Chapter 7

CFD parametric study

In Chapter 6 a factorial study on the influence of the generator's critical parameters has been completed. The maximum and minimum values of the design and operational parameters (running clearance, magnet depth and rotational speed) define the boundaries of the full investigation. Simulations have been performed at these boundaries with the parameters being at their 'low' or 'high' values.

Due to the nature of the factorial study, which includes two values only for each of the parameters, only linear regressions functions could be obtained. In order to increase the order of the regression function more simulations have been run and the results presented in this chapter.

Five values of the running clearance and of the rotational speed and eight values of the magnet depth have been investigated. This has allowed higher order regression polynomials to be established. The parameters and all the cases considered are shown in Table 7.1. Each of the parameters (the running clearance, the magnet depth, and the rotational speed) has been varied within the range defined in the factorial study, while the others have been kept constant and equal to those in the base case (Clearance = 2 mm; Magnet depth = 8mm; Rotational Speed = 1500rpm). The base case is shown with bold fonts in Table 7.1.

Table 7.1: Cases studied

Case ID	Running clearance (mm)	Magnet depth (mm)	Rotational speed (rpm)
1	1	8	1500
2	**2**	**8**	**1500**
3	3	8	1500
4	4	8	1500
5	5	8	1500
6	2	2	1500
7	2	4	1500
8	2	10	1500
9	2	12	1500
10	2	16	1500
11	2	18	1500
12	2	8	1400
13	2	8	2000
14	2	8	2500
15	2	8	3000

In chapter 6 the linear response functions for the heat transfer coefficients, the torque and the mass flow rate through the machine were presented in the dimensional fashion for the main purpose of showing the heat transfer coefficient patterns and their dependency on the velocities inside the running clearance.

In the part of the study described in this chapter general non-dimensional correlations valid for similar machines have been obtained. Polynomial functions correlating the Nusselt number with the non dimensional running clearance, the non-dimensional magnet depth and the peripheral Reynolds number have been found.

As far as AFPM machines are concerned, there is strong interest in the effect of variation of the machine diameter on the heat transfer coefficient. In this study, models with varying diameter have not been built. Instead, the effect of change in the diameter has been evaluated by using a similarity theory. It has been assumed that the Nusselt number (Nu) on the generator's surfaces is solely dependent on the peripheral Reynolds number (Re_{out}), that there is a unique correspondence between Nu and Re_{out}.

Several simulations have been run in Fluent to confirm this. Fig. 7.1 is an example of the Nusselt number variation on the stator surface along a radial line obtained from two models sharing the same peripheral Reynolds number. In the first case a peripheral radius of 156mm and a rotational speed of 1500rpm have been considered. In the second case the peripheral radius is 110mm, consequently the rotational speed needed to obtain the same Reynolds number is 3000rpm. It can be seen how the Nusselt number equivalence is fulfilled over the whole radius. The dependency of the Nusselt number on the Prandtl number has not been considered as the cooling fluid is always air, hence the Prandtl number is constant in this study. Therefore the heat transfer in a large radius generator has been studied by using a smaller radius generator and by assigning a rotational speed such as to obtain the same peripheral Reynolds number.

Also for these simulations, as for the factorial study, the steady state RANS equations have been solved using the realizable $\kappa - \epsilon$ turbulence model for the closure of the system of equations. The applied boundary conditions and the solution method are the same as those described for the factorial study in chapter 6: at the inlet the total pressure has been specified, at the outlet the static pressure and a constant heat flux has been specified either on the stator or on the rotor walls depending where the heat transfer coefficient needed to be determined.

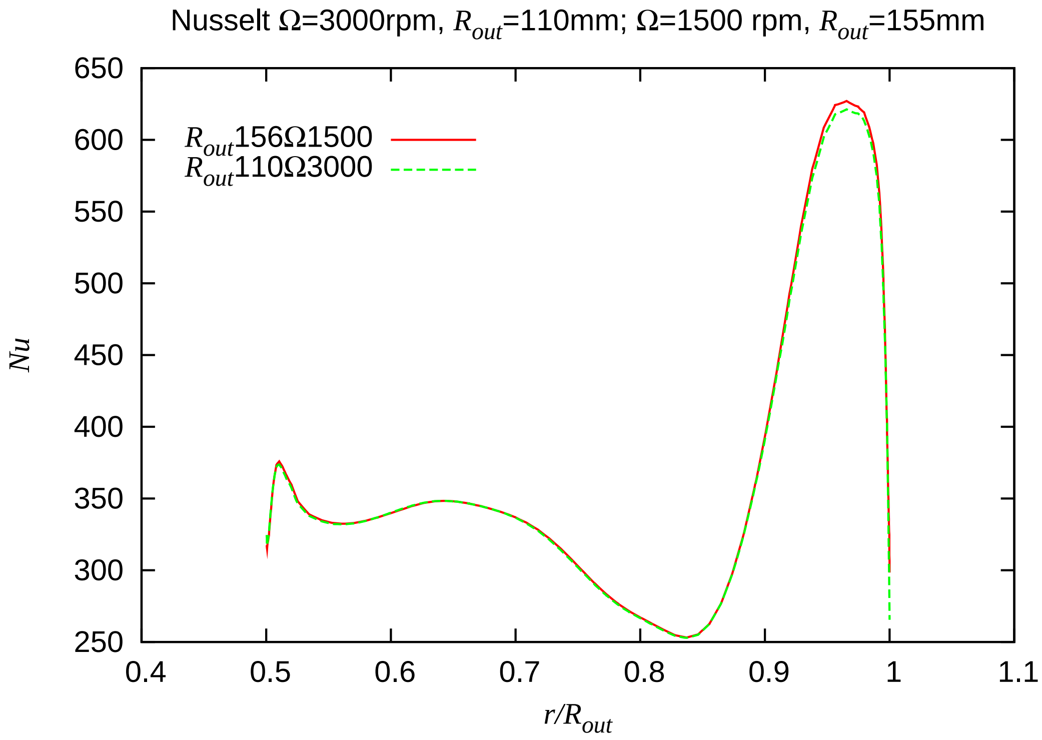

Figure 7.1: Nusselt number equivalence

The heat transfer coefficient on a surface is independent on the heat boundary conditions but, in general, depends on the flow field which develops on this surface and in our case inside the running clearance. Therefore any heat boundary condition could have been applied on the surfaces to find the relevant heat transfer coefficient. It has been chosen to specify the heat flux from the stator wall as 1000W/(m^{2}K) which is close to the values measured in the experiments.

7.1 Stator heat transfer coefficient

The obtained local heat transfer coefficient on the stator surface for the basic configuration of a system with a 2mm running clearance, a 8mm deep magnet and a rotational speed of 1500rpm shown in Fig. 7.2 is relatively independent of the angular position for the central region of the clearance. Differences in the magnitude of the heat transfer coefficient arise at the low radius where the flow is most disturbed due to the inlet and at the outlet where reverse flow occurs on the suction side of the magnet.

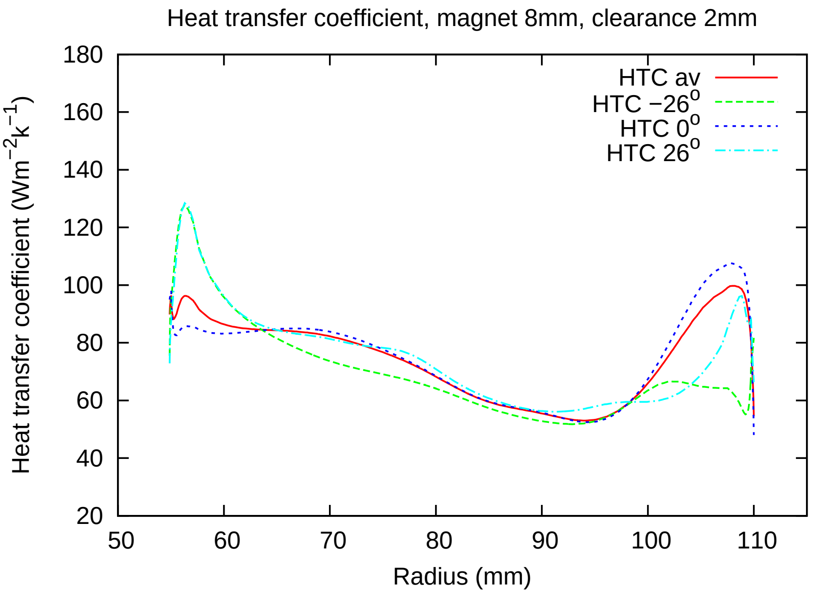

Figure 7.2: Heat transfer coefficient at the three angular locations shown for the base case

7.1.1 Running clearance

For the cases investigated the running clearance has little or no effect on the mass flow rate through the generator and on the resistive power as is illustrated in Fig. 7.3. The small influence on the resistive power is due to two reasons: the major contribution to the mass flow rate is the work done by the side wall of the magnets, and with the magnet depth fixed at 8mm the skin friction contribution of the magnet face to the mass flow rate is negligible. In chapter 6 it has been shown that the circumferential average heat transfer coefficient has been calculated by averaging the values obtained at the three different angular coordinates (namely -26°, 0° and +26°). Here the average heat transfer coefficient has been calculated following the

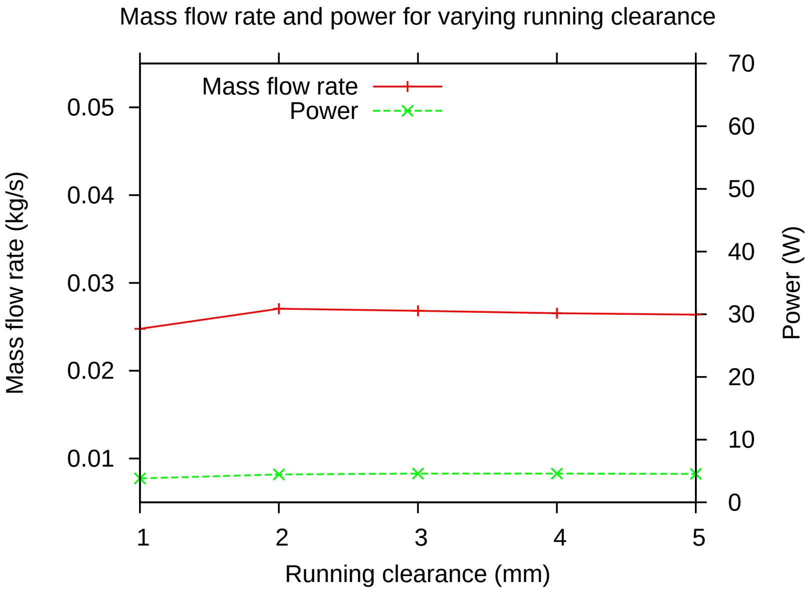

Figure 7.3: Windage losses and mass flow rate

same procedure as in chapter 6. However, only the average heat transfer coefficient is displayed. The heat transfer coefficients on the stator surface calculated at the five running clearances are displayed together in Fig. 7.4.

Results in Fig. 7.4 clearly show that the highest heat transfer coefficient is obtained with the lowest clearance (1mm). The resulting heat transfer coefficient for the 1mm clearance is in the range of 100W/(m^{2}K) whereas for the 5mm clearance is in the order of 40W/(m^{2}K). This is because as the mass flow rate remains constant for a varying running clearance, the radial velocity increases as the clearances reduce, resulting in a higher heat transfer coefficient.

All cases reported in Fig. 7.4 show how the heat transfer coefficient initially increases at the running clearance inlet due to the disturbed flow at the clearance inlet, then it decreases steadily to reach its minimum for r≈90mm where it starts increasing again to reach a relative maximum at the periphery. The range within which the heat transfer coefficient varies over the radius is of about 40W/(m^{2}K) for all cases. The case with the lowest running clearance is an exception and the results are more uniform over the radius: after a steep reduction occurring for 55mm $< r <$ 60mm where the heat transfer coefficient drops from 140 to 100W/(m^{2}K) it remains constant over the rest of the radius. The characteristic pattern of the heat transfer coefficient, which is maximum at the clearance inlet, decreases to reach the minimum for $r \approx$90mm, and then increases to a relative maximum at the stator periphery, is common to most configurations of the rotor-stator system.

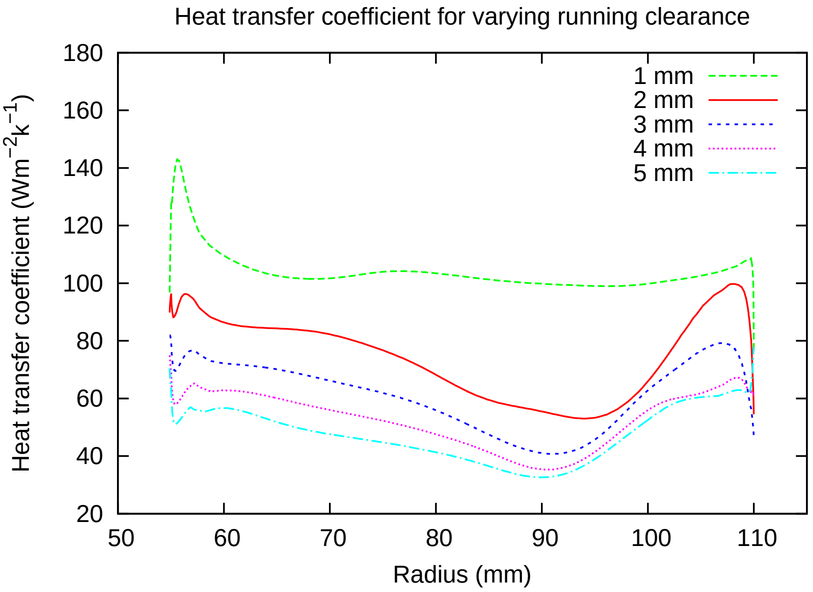

Figure 7.4: Heat transfer coefficient

It can be observed that the heat transfer coefficient on a surface is strongly linked to the velocity of the fluid relative to the surface itself.

Since the stator is stationary, the relative velocity is the velocity of the fluid which consists of the radial and of the tangential velocities components. The axial velocity can be considered negligible in most of the running clearance. The radial component of the velocity is maximum at the clearance inlet, and due to continuity decreases steadily for increasing radii for larger cross sectional areas. Instead, the tangential component of the velocity increases steadily with the radius and reaches its maximum at the clearance periphery.

The velocity vector magnitude is therefore maximum at the clearance inlet (maximum radial velocity equal to 8m/s) as shown in Fig. 7.5, then it decreases and reaches its minimum (4m/s) for $r \approx 90$mm, and increases to reach a maximum at the periphery (maximum tangential velocity).

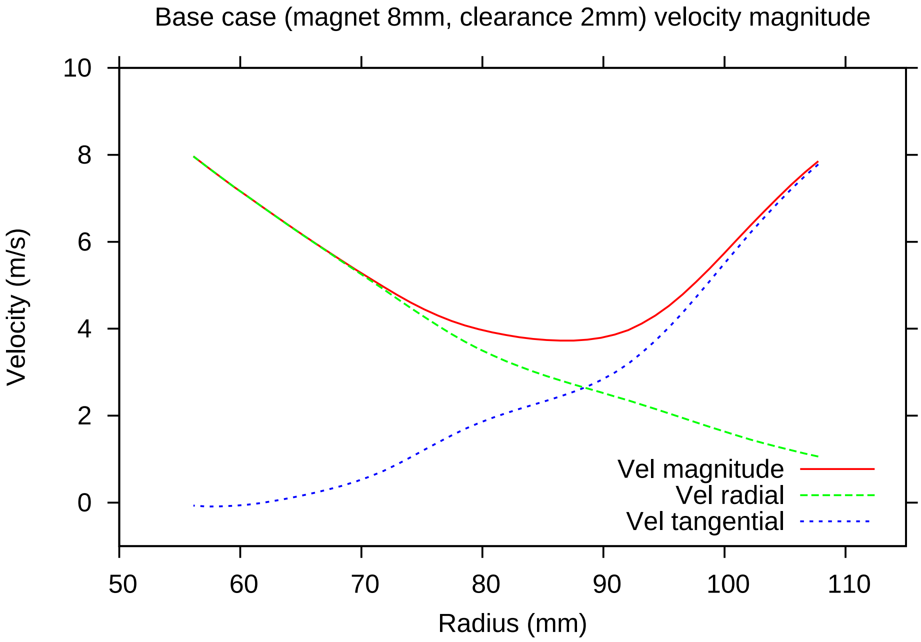

Figure 7.5: Velocities in the clearance for the base case

The heat transfer coefficient at a constant radius of 80mm has been plotted for varying values of running clearance to show the relationship between these two quantities. As shown in Fig. 7.6 the heat transfer coefficient is not a linear function of the running clearance.

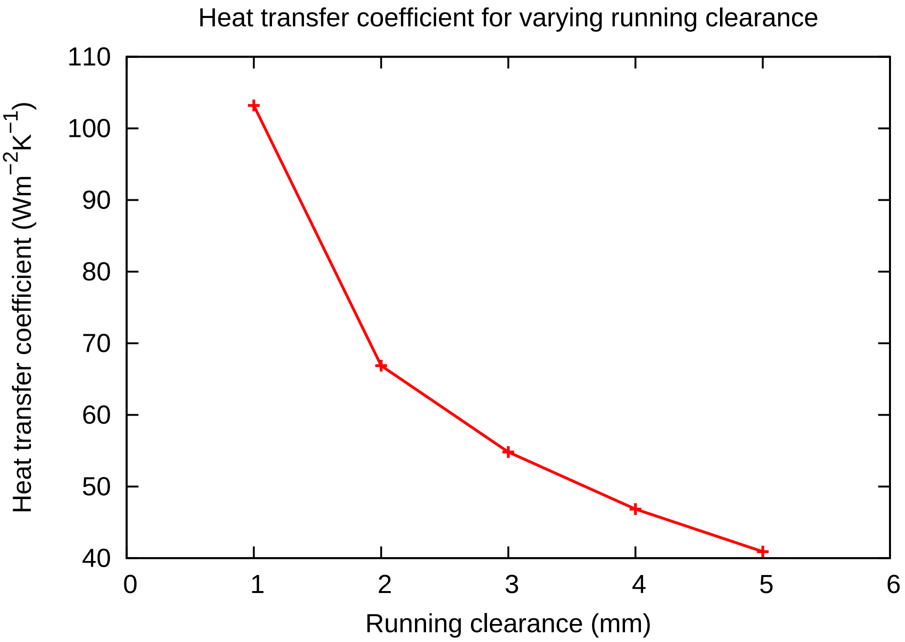

Figure 7.6: Heat transfer coefficient at r=80mm for varying clearances

7.1.2 Magnet groove depth

The heat transfer coefficient for a number of magnet groove depths is shown in Fig.7.8. Two clear air flow patterns occur: one with the magnet groove depth of less than 4mm where the heat transfer coefficient is very uniform along the radius. This pattern is very similar to that found with a flat rotor. The other flow pattern is the one occurring above 4mm where significant variations of heat transfer coefficient occur.

An increasing magnet groove depth increases the air mass flow rate and the windage losses through the generator as shown in Fig. 7.7.

The increase in the groove depth caused by deeper magnets leads to higher mass flow rates, but not to higher radial velocities. In fact the increase in the mass flow rate comes together with an increase in the cross sectional area which contributes to keep the radial velocity roughly constant, and in the case of the deeper magnets to even reduce it.

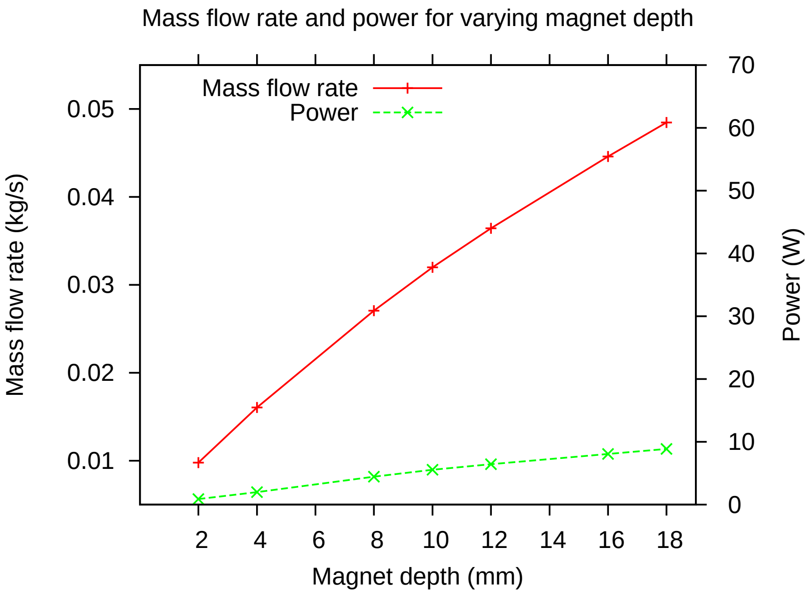

Figure 7.7: Windage losses and mass flow rate

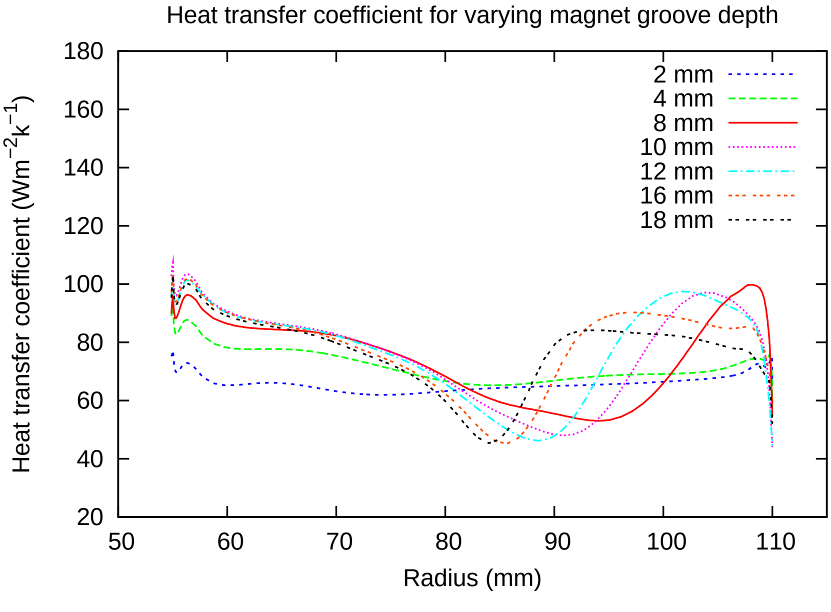

Figure 7.8: Heat transfer coefficient

While the heat transfer coefficient decreases for increasing running clearances regardless of the radius, a unique general conclusion of the dependence of the heat transfer coefficient on the magnet depth can not be drawn. The heat transfer coefficient dependency on the magnet depth varies with the radius. This is shown in

Fig. 7.9 where at $r = 60$mm the heat transfer coefficient is steadily increasing with the magnet depth, and at $r = 80$mm the heat transfer coefficient initially increases until the magnet depth is 8mm, and then starts decreasing.

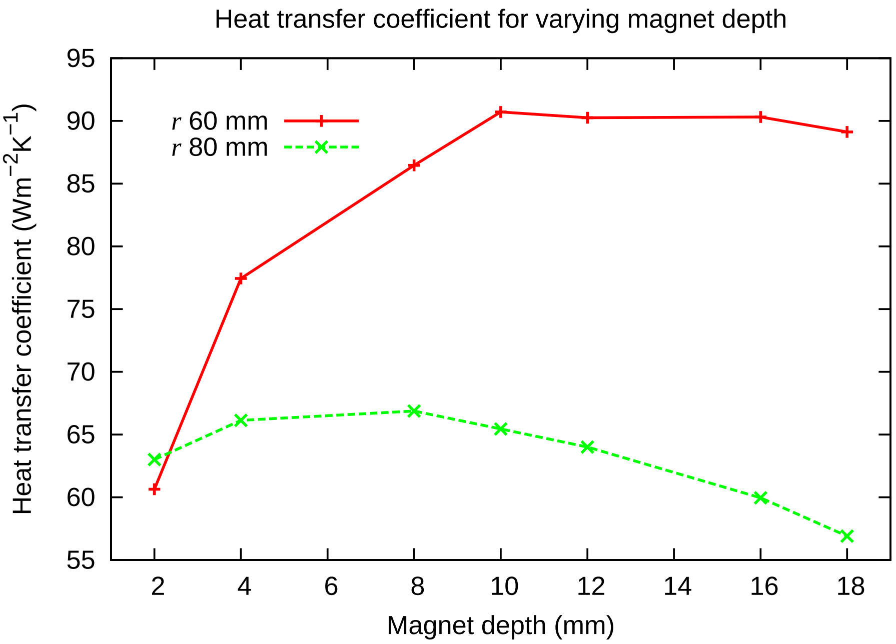

Figure 7.9: Heat transfer coefficient for varying magnet depth

The heat transfer coefficient on the stator peripheral surface increases because of the reversed flow occurring at the outlet boundary. For a greater magnet depth the flow reaches a deeper region of the domain causing the heat transfer coefficient to be higher on a greater area of the stator. However, the heat transfer coefficient peak reduces correspondingly.

7.1.3 Rotational speed

The relationship between the heat transfer coefficient and the rotational speed at any given radius is linear (Fig. 7.12), although the basic pattern of the heat transfer coefficient remains unchanged for varying speeds as shown in Fig. 7.11.

The mass flow rate also rises linearly with the rotational speed as shown in Fig. 7.10. This is in agreement with the findings of Li [42] who found a linear relationship between the mass flow rate and the rotational speed in his CFD study of radial flux machines.

The increase in the rotational speed incurs a steep rise in windage losses: the resisting power varies from 10W at 1500rpm to 68W at 3000rpm (Fig. 7.10).

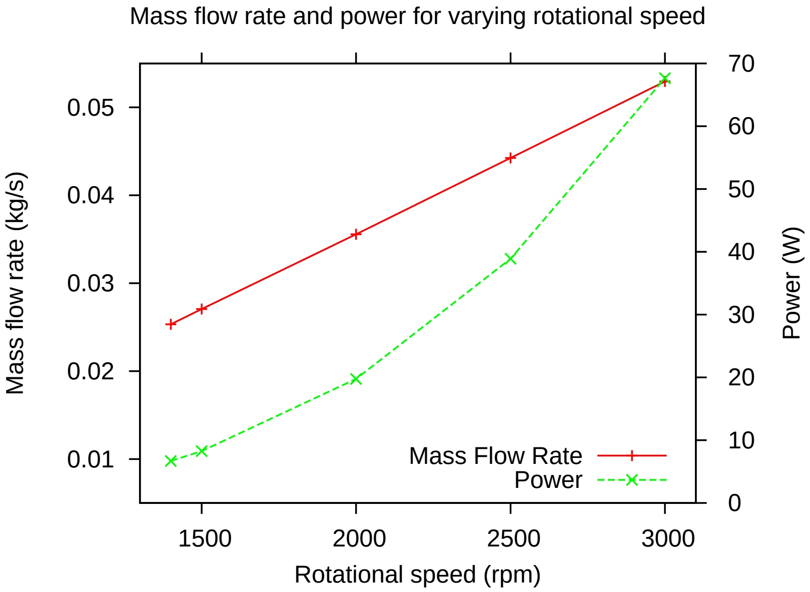

Figure 7.10: Windage losses and mass flow rate

7.1.4 Stator Nusselt number correlations

In the previous sections graphs representing the heat transfer coefficient on the stator and rotor annular surfaces have been shown. In order to obtain general regression functions which are independent of the size of the system, correlations have been found between non-dimensional groups. The Nusselt number has been calculated

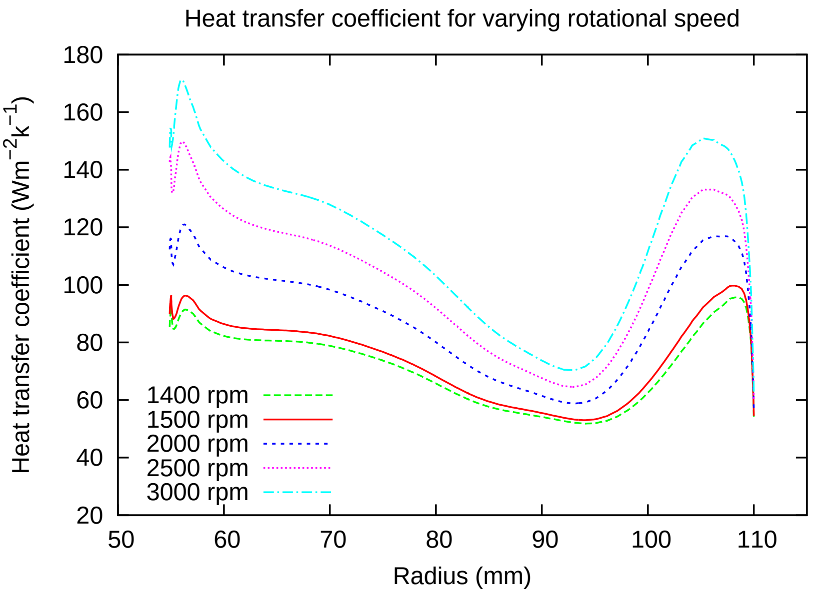

Figure 7.11: Heat transfer coefficient for varying rotational speed

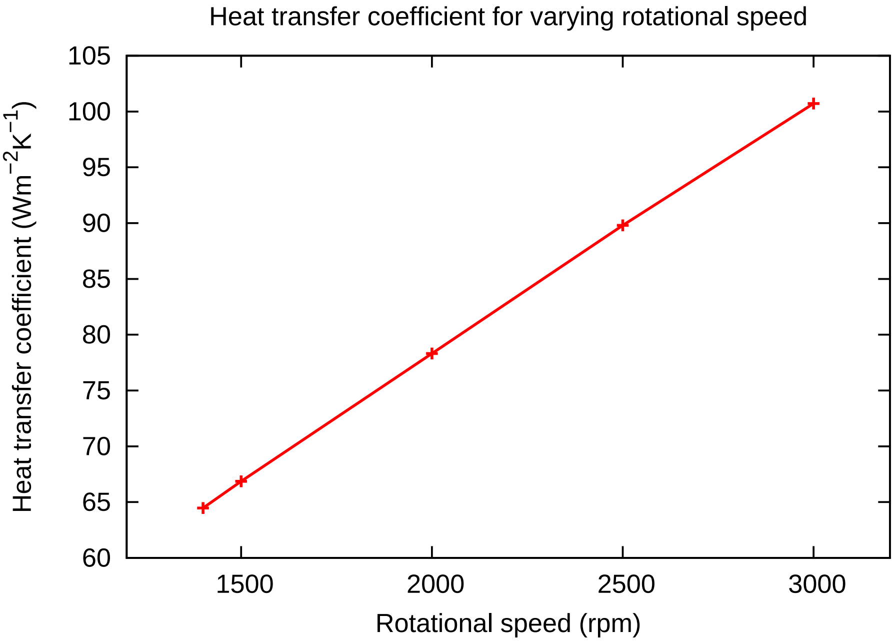

Figure 7.12: Heat transfer coefficient at r=80mm for varying rotational speed

from the heat transfer coefficient obtained from the CFD study according to Eq. 7.1:

$$Nu(r^*) = \frac{h(r)r}{k_{air}} \tag{7.1}$$

where r is the local radius, k_{air} is the air thermal conductivity, *h(r)* is the local heat transfer coefficient and r^* is the non-dimensional radius ($r^* = r/R_{out}$). For geometrically similar systems, with constant ratio between their dimensions, and for a given fluid, the well known relationship in Eq. 7.2 is valid:

$$Nu(r^*) = f\,(Re) \tag{7.2}$$

However, since in this study, in addition to the rotational speed, the geometric proportions of the system have been varied, there is a need to take into account these changes in dimensions. The Nusselt number has been found as a function of the non-dimensional running clearance, the non-dimensional magnet depth and the peripheral Reynolds number which are defined as follows:

$$c^* = \frac{c}{R_{out}}; \tag{7.3}$$

$$m^* = \frac{m}{R_{out}}; \tag{7.4}$$

$$Re = \frac{\rho \Omega R_{out}^2}{\mu}. \tag{7.5}$$

The correlations for the Nusselt number have been derived from the results obtained in this study together with the ones in chapter 6. Table 7.2 summarizes the non-dimensional quantities for which the regression surfaces have been found. A correlating equation has been found for each of the radial regions in which the domain has been divided as shown in Fig. 6.40 on page 145. The functional form which correlates the heat transfer coefficient is the one in Eq. 7.6.

$$\begin{aligned} Nu(r^*) &= b_0(r^*) + b_1(r^*)c^* + b_2(r^*)m^* + b_3(r^*)Re + b_4(r^*)c^{*2} + b_5(r^*)m^{*2} + \\ &+ b_6(r^*)Re^2 + b_7(r^*)c^*m^* + b_8(r^*)m^*Re + b_9(r^*)c^*Re \end{aligned} \tag{7.6}$$

The least mean squares method in Matlab has been used for finding the constant coefficients of this equation.

Table 7.2: Regression function cases

Case ID	c/R$_{out}$	m/R$_{out}$	Re$_{out}$
1	0.009	0.073	129285
2	**0.018**	**0.073**	**129285**
3	0.027	0.073	129285
4	0.036	0.073	129285
5	0.045	0.073	129285
6	0.018	0.018	129285
7	0.018	0.036	129285
8	0.018	0.091	129285
9	0.018	0.109	129285
10	0.018	0.145	129285
11	0.018	0.164	129285
12	0.018	0.073	120727
13	0.018	0.073	172380
14	0.018	0.073	215475
15	0.018	0.073	258701
16	0.009	0.018	120727
17	0.045	0.018	120727
18	0.009	0.164	120727
19	0.045	0.164	120727
20	0.009	0.018	258701
21	0.045	0.018	258701
22	0.009	0.164	258701
23	0.045	0.164	258701

The second order term of the Reynolds number has been included despite the relationship between the Nusselt and the Reynolds numbers being linear as can be seen in Fig. 7.12 presenting the graph linking the relevant dimensional quantities: heat transfer coefficient and rotational speed. The constant coefficients ($b_6(r^*)$) of the Re^2 term have been found to be small enough to consider the contribution of the second order term to be negligible. The Nusselt number is a regression function in three variables therefore in order to visualise it, it is necessary to keep one of the variables constant. It is possible in this way to visualise a three-dimensional surface which represents the Nusselt number as a function of c^* and m^* for a fixed Reynolds number.

Two examples of the Nu surface are displayed at a constant Reynolds number of 129350 at $r^* = 0.59$ and at $r^* = 0.95$ in Figs. 7.13 and 7.14, respectively. The points in these figures represent the results from simulations in Fluent. The coefficients of the polynomial function for each of the radii are reported in Table 7.3.

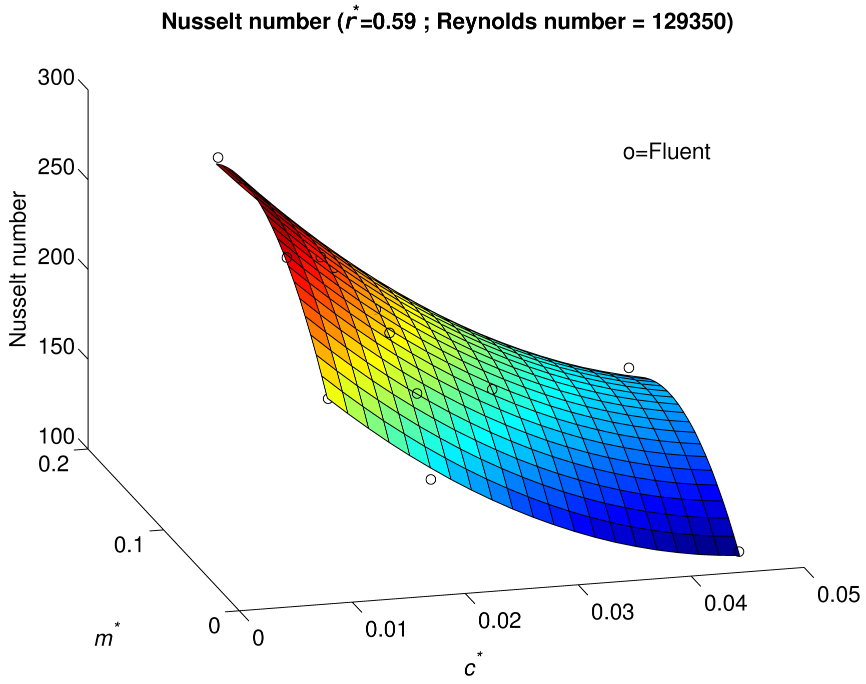

Figure 7.13: Stator Nusselt number for $r^* = 0.59$

Table 7.3: Stator *Nu(r)* correlation coefficients

	Non-dimensional Radius (r^*)									
	0.55	0.59	0.64	0.68	0.73	0.77	0.82	0.86	0.91	0.95
b_0	6.03E+01	9.09E+01	1.35E+02	1.90E+02	2.68E+02	3.92E+02	4.05E+02	3.99E+02	3.04E+02	2.59E+02
b_1	-5.02E+03	-4.55E+03	-6.67E+03	-1.01E+04	-1.47E+04	-2.13E+04	-1.64E+04	-1.42E+04	-1.24E+04	-1.50E+04
b_2	1.69E+03	1.37E+03	1.31E+03	1.28E+03	9.32E+02	-1.14E+02	-1.67E+03	-1.54E+03	4.02E+02	2.60E+03
b_3	1.11E-03	1.11E-03	1.13E-03	1.10E-03	1.03E-03	8.25E-04	7.74E-04	7.81E-04	1.27E-03	1.68E-03
b_4	9.11E+04	6.78E+04	9.09E+04	1.48E+05	2.28E+05	3.24E+05	2.14E+05	1.63E+05	1.55E+05	1.93E+05
b_5	-6.45E+03	-5.66E+03	-5.90E+03	-5.94E+03	-4.68E+03	-1.53E+03	7.69E+03	7.33E+03	-3.22E+03	-1.31E+04
b_6	-3.41E-10	-2.31E-10	-7.57E-10	4.40E-11	3.65E-11	4.38E-10	4.36E-11	7.89E-12	9.54E-11	5.34E-12
b_7	-1.14E+04	-6.03E+03	-2.29E+03	-3.14E+03	-5.80E+03	2.53E+03	9.78E+03	1.57E+04	1.34E+04	7.96E+03
b_8	1.81E-03	1.25E-03	7.12E-04	6.54E-04	1.10E-03	2.24E-03	8.39E-04	1.92E-04	1.86E-03	1.56E-03
b_9	-1.41E-02	-1.48E-02	-1.51E-02	-1.60E-02	-1.67E-02	-1.31E-02	-9.42E-03	-8.12E-03	-1.78E-02	-1.65E-02

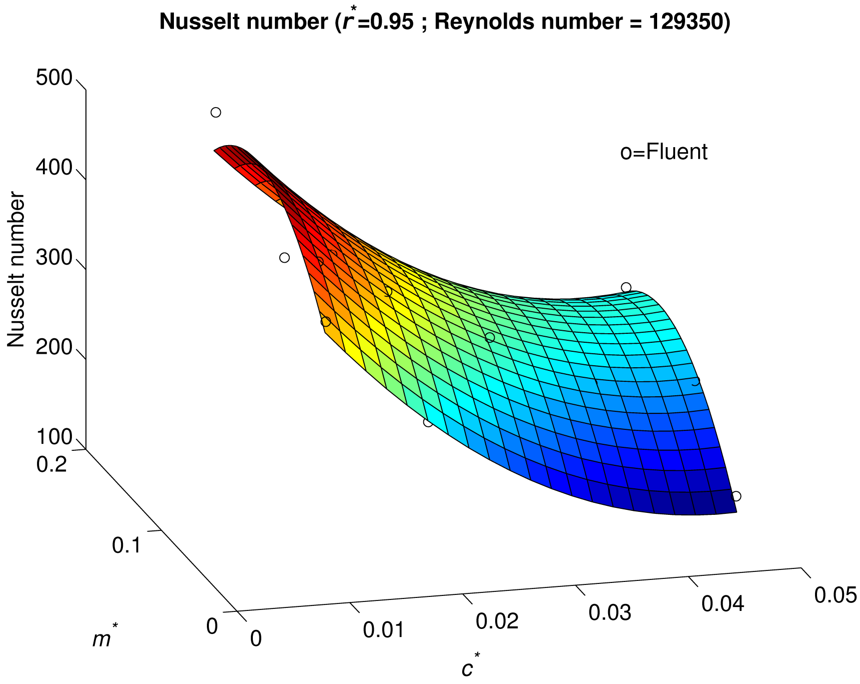

Figure 7.14: Stator Nusselt number for $r^* = 0.95$

7.2 Rotor heat transfer coefficient

The heat transfer coefficient has been calculated on the rotor for the same cases as already described for the stator (see Table 7.1 on page 173). As for the case of the stator one parameter at a time has been varied keeping the other parameters constant and equal to the values in the base case.

7.2.1 Running clearance

Similarly as for the case of the heat transfer coefficient on the stator, the increase of the running clearance results in the reduction of the heat transfer coefficient on the rotor as shown in Fig. 7.15. However the difference is considerably smaller compared to the case of the stator, especially for large radii. The rotor heat transfer coefficient at r = 80mm varies between 93W/(m^{2}K) calculated for the 5 mm clearance and

110W/(m^{2}K) calculated for the 1mm clearance. At the same radius (80mm) the heat transfer coefficient on the stator is 45W/(m^{2}K) for the 5mm clearance and 103W/(m^{2}K) for the 1mm clearance. A considerable difference in the heat transfer coefficient patterns for the stator and the rotor cases can be observed. The heat transfer coefficient on the stator starts at a high value at the clearance inlet, then decreases to reach a minimum at the mid radius before increasing again.

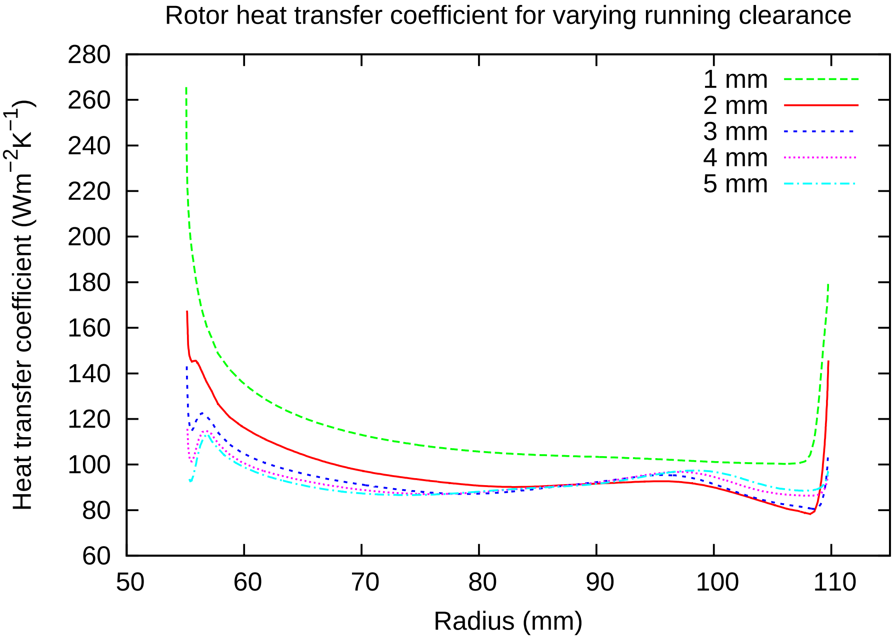

Figure 7.15: Rotor heat transfer coefficient for varying running clearance

The heat transfer coefficient on the rotor surface for all cases is maximum at the clearance inlet then steadily decreases until the periphery. This different pattern can be explained by considering that the heat transfer coefficient on a surface depends on the relative flow velocity. Since the rotor is moving, like the flow inside the clearance, the component of the flow velocity relative to the rotor velocity is the radial one. The heat transfer coefficient pattern follows the radial velocity pattern which decreases with the radius.

7.2.2 Magnet depth

As for the case of the running clearance, the effect of the magnet depth on the rotor heat transfer coefficient is relatively weak, as shown in Fig. 7.16. This is a positive result because it has already been shown that the magnet depth improves the heat transfer from the stator, but the heat transfer to the rotor is undesirable and ideally the whole amount of heat dissipated from the stator should be transferred outside the machine.

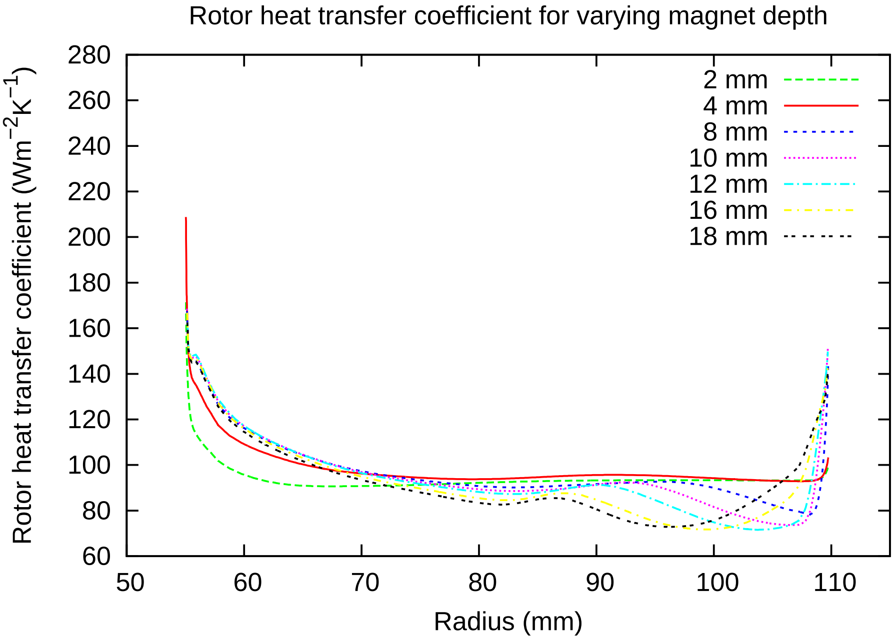

Figure 7.16: Rotor heat transfer coefficient for varying magnet depth

7.2.3 Rotational speed

The rotational speed is the parameter with the largest effect on the rotor heat transfer coefficient. The increase in shear stresses due to the higher rotational speed and the increase of turbulent mixing has a direct impact on the heat transfer coefficient on the rotor surface. While the highest heat transfer from the stator surface can be obtained with the smallest clearance, in the case of the rotor this result can be achieved with the highest speed.

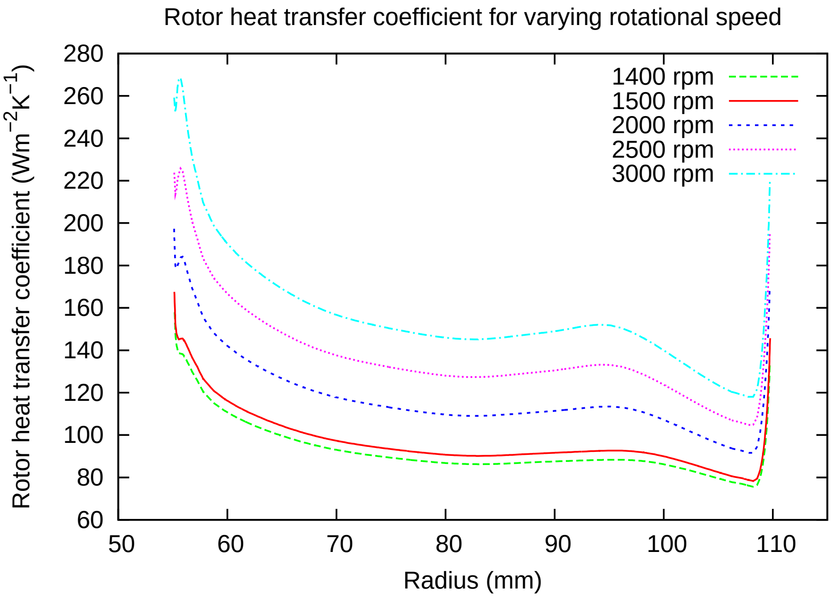

Figure 7.17: Rotor heat transfer coefficient for varying rotational speed

7.2.4 Rotor Nusselt number correlations

Correlations for the Nusselt number on the rotor have been found. The functional form similar to the one previously described for the stator in Eq. 7.6 on page 186 and the corresponding polynomial coefficients have been reported in Table 7.4 on page 199. The Nusselt number surfaces are shown for $Re = 129350$ at $r^* = 0.59$ and $r^* = 0.95$ in Figs. 7.18 and 7.19, respectively.

The fitting surface at the inner radius $r^* = 0.59$ is more accurate than the first order polynomial previously obtained. There is a visible reduction in Nusselt number for an increasing non-dimensional clearance c^* and a small influence of the non-dimensional magnet depth m^* on the Nusselt number.

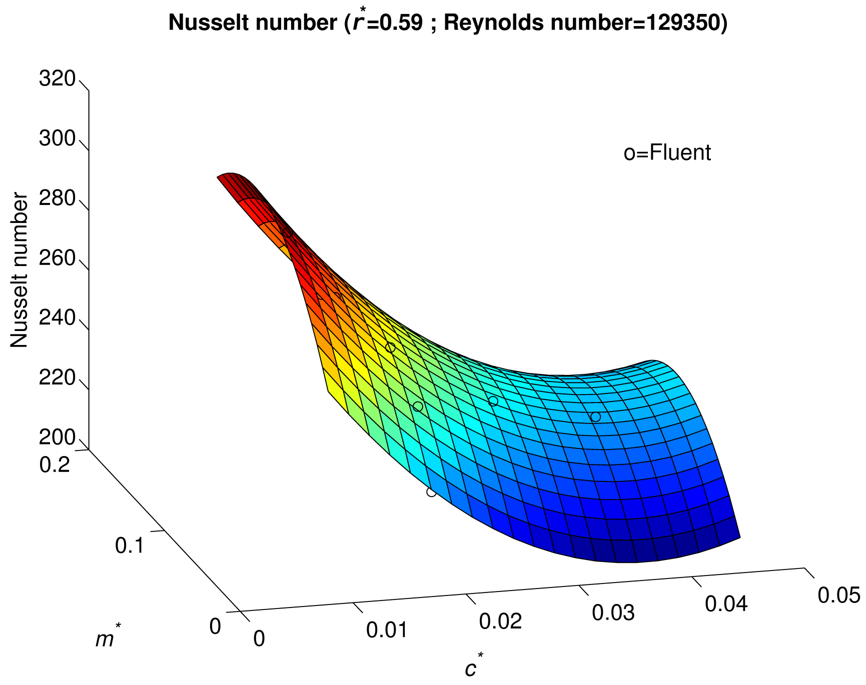

Figure 7.18: Rotor Nusselt number for $r^* = 0.59$

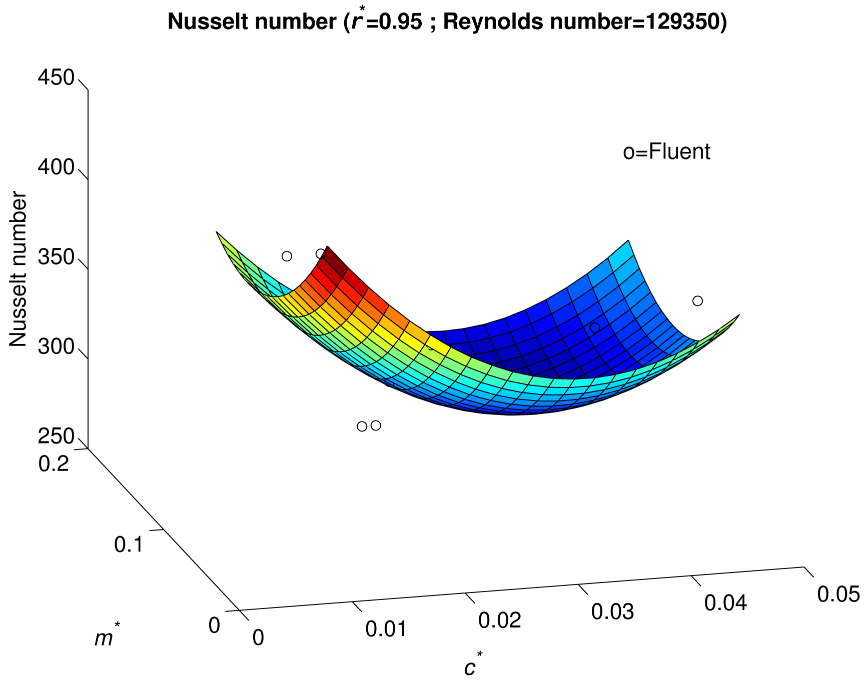

Figure 7.19: Rotor Nusselt number for $r^* = 0.95$

7.3 Non-dimensional mass flow rate

The non-dimensional mass flow rate $\dot{m}^*$ has been calculated using dimensional analysis. The mass flow rate depends on five dimensional variables: $\dot{m} = \dot{m}\left(\Omega, \rho, \mu, R_{out}\right)$ which can be expressed as a function of the three fundamental variables - length, mass, and time. Therefore for similar systems a relationship between two non-dimensional groups can been found. One of these groups is the Reynolds number, and the other is the non-dimensional mass flow rate. However, as mentioned earlier, not all the systems modelled here are similar. Therefore in the response function correlating the non-dimensional mass flow rate, the parameters c^* and m^* had to be included in addition to the peripheral Reynolds number *Re*. Eq. 7.7 represents the non-dimensional mass flow rate obtained with dimensional analysis:

$$\dot{m}^* = \frac{\dot{m}}{\mu R_{out}} \tag{7.7}$$

Also in this case the results from the CFD analysis have been fitted with a second order polynomial (as in the case of Nusselt numbers). The relationship between the non-dimensional mass flow rate and the Reynolds number is linear. This can be observed in Fig. 7.3 which relates the corresponding dimensional quantities: mass flow rate and rotational speed.

Also in this case, as for the stator and the rotor heat transfer coefficients, the second order term of the Reynolds number has been included in the formula for the fitting polynomial curve. However, due to the linear dependency of $\dot{m}^*$ from the Reynolds number the coefficient is small enough to make the Reynolds second order term negligible.

$$\begin{aligned}\dot{m}^* \quad &= -4.445 \cdot 10^3 + 2.280 \cdot 10^5 c^* + 6.578 \cdot 10^4 m^* + 1.901 \cdot 10^{-2} Re + \\ &-3.009 \cdot 10^6 c^{*2} - 2.250 \cdot 10^5 m^{*2} - 3.474 \cdot 10^{-9} Re^{*2} - 6.915 \cdot 10^5 c^* m^* + \\ &+9.546 \cdot 10^{-1} m^* Re + 2.952 \cdot 10^{-1} c^* Re \qquad (7.8)\end{aligned}$$

The surface obtained from the polynomial fitting of the non-dimensional mass flow rate is displayed for the constant Reynolds number ($Re = 129350$). From the surface it can be seen that the non-dimensional mass flow rate is independent of the non-dimensional clearance but, it increases for non-dimensional magnet depths.

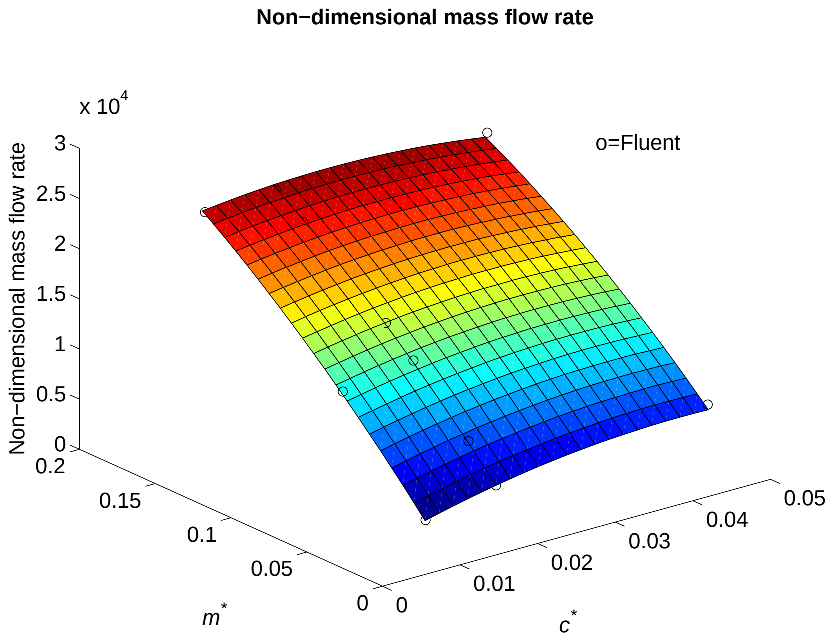

Figure 7.20: Non dimensional mass flow rate for $Re = 129350$

7.4 Non-dimensional torque

Dimensional analysis has been used to calculate the non-dimensional torque. The torque in a generator depends on five dimensional variables: $T = T\left(\Omega, \rho, \mu, R_{out}\right)$. By considering these variables as a function of the three fundamental ones: length, mass and time the two non-dimensional groups namely the Reynolds number and the non-dimensional torque are determined. The expression obtained for the non-dimensional torque T^* is shown in Eq.7.9:

$$T^* = \frac{T\rho}{\mu^2 R_{out}} \tag{7.9}$$

A second order polynomial function (Eq. 7.10) has been used for fitting the torque results obtained through the CFD simulations.

$$\begin{aligned} T^* &= 2.505 \cdot 10^8 - 5.846 \cdot 10^9 c^* - 4.060 \cdot 10^{10} m^* - 3.943 \cdot 10^{10} Re + \\ & -7.632 \cdot 10^{11} c^{*2} - 5.817 \cdot 10^{10} m^{*2} - 2.974 \cdot 10^3 Re^2 + 3.609 \cdot 10^{11} c^* m^* + \\ & +5.204 \cdot 10^5 m^* Re + 2.300 \cdot 10^5 c^* Re \end{aligned} \tag{7.10}$$

In this case, unlike the previous ones, although the second order term of the Reynolds number is smaller in magnitude compared to the other terms, it can not be neglected in the calculations.

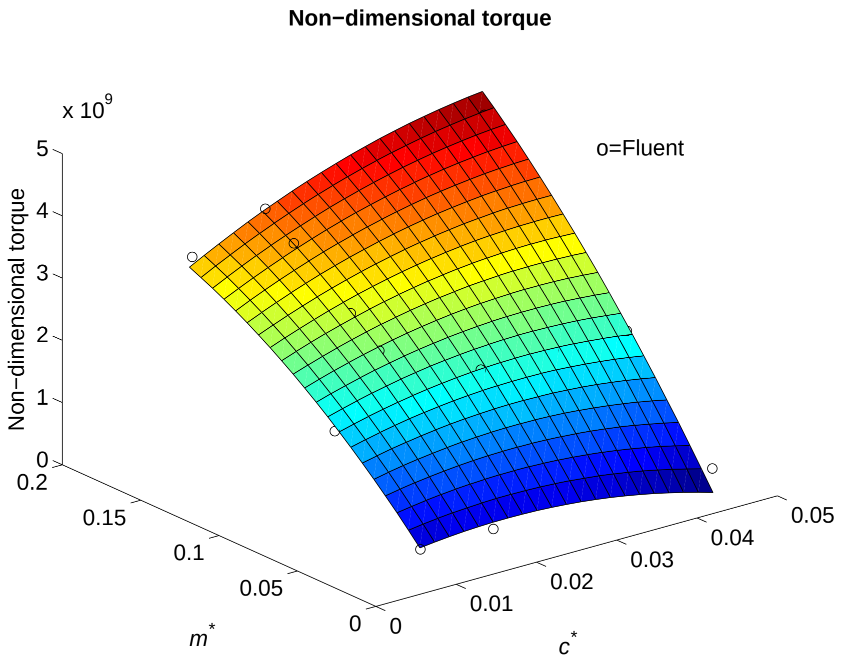

Figure 7.21: Non dimensional torque for $Re = 129350$

7.5 Conclusions

This chapter presented the results from simulations carried out varying one parameter at a time. The main finding from this numerical study are:

- The heat transfer coefficient on the stator and the mass flow rate through the system are linear functions of the rotational speed.
- The relationship of the running clearance and of the magnet depth with the heat transfer coefficient is not linear.
- As already demonstrated in the previous chapter the magnet depth increases the heat transfer coefficient on the stator. However, magnet depths of 8mm on a rotor with $R_{out} = 110$mm which corresponds to a non-dimensional magnet depth $m^* = 0.073$ provide the highest heat transfer. A further increase would unnecessarily augment the resistive torque and the resulting higher mass flow

rate would be distributed in the gap towards the rotor surface rather than close to the stator surface. This would not enhance the cooling of the stator.

- A low running clearance is beneficial and if there are enough passages in the rotor to maintain the necessary mass flow rate then the running clearance should be kept as small as possible. The combination found to have the highest heat transfer coefficient is the one with a clearance of 1mm and the magnet height of 8mm. This corresponds to a non-dimensional clearance $c^* = 9 \times 10^{-3}$ and to a non-dimensional magnet depth $m^* = 7.3 \times 10^{-2}$.

By using the numerical results obtained and the ones in chapter 6 and 7, the second order polynomial correlations have been derived which relate the non-dimensional clearance, the non-dimensional magnet depth and the Reynolds number to the following functions: the Nusselt number on the stator and rotor surfaces, the non-dimensional mass flow rate and the non-dimensional torque.

Table 7.4: Rotor $Nu(r)$ correlation coefficients

	Non-dimensional Radius (r^*)									
	0.55	0.59	0.64	0.68	0.73	0.77	0.82	0.86	0.91	0.95
b_0	9.80E+01	1.25E+02	1.55E+02	1.83E+02	2.23E+02	2.48E+02	2.10E+02	2.09E+02	2.85E+02	3.45E+02
b_1	-4.44E+03	-5.10E+03	-5.85E+03	-6.74E+03	-8.19E+03	-8.45E+03	-6.82E+03	-7.62E+03	-1.03E+04	-1.04E+04
b_2	1.29E+03	8.98E+02	5.28E+02	2.59E+02	-1.01E+02	-4.06E+02	3.22E+02	6.60E+02	-1.34E+02	-1.43E+03
b_3	1.38E-03	1.33E-03	1.33E-03	1.35E-03	1.31E-03	1.32E-03	1.59E-03	1.78E-03	1.65E-03	1.55E-03
b_4	7.73E+04	8.22E+04	9.21E+04	1.05E+05	1.22E+05	1.17E+05	1.11E+05	1.38E+05	1.68E+05	1.60E+05
b_5	-5.81E+03	-4.39E+03	-2.94E+03	-2.16E+03	-1.50E+03	-7.87E+02	-3.29E+03	-5.88E+03	-2.62E+03	5.98E+03
b_6	5.68E-11	3.52E-11	1.50E-10	4.25E-12	6.62E-11	3.42E-12	9.32E-11	9.22E-12	2.33E-11	1.33E-12
b_7	-6.54E+03	-3.07E+03	-1.25E+03	8.01E+02	6.06E+03	1.18E+04	1.37E+03	1.18E+03	9.67E+03	6.23E+03
b_8	1.56E-03	1.16E-03	8.27E-04	8.34E-04	1.34E-03	1.77E-03	5.07E-04	3.11E-04	-1.65E-04	-9.16E-04
b_9	-8.96E-03	-7.33E-03	-6.41E-03	-5.19E-03	-2.37E-03	6.29E-05	-5.67E-03	-9.07E-03	-3.28E-03	5.07E-04

Chapter 8

Conclusions and further work

8.1 Conclusions

In this thesis a CFD study of AFPM machines was presented. As the part of the larger project in which the objective was to build a Lumped Parameter Thermal Network, the work presented in this thesis had the aim of providing the values of the heat transfer coefficient and the flow rate through the machine for varying geometrical parameters. Since the major proportion of the heat in AFPM machines is generated in the stator coils, the focus of the work was on the heat transfer coefficient from the stator surface. A survey of the available literature in the field highlighted the lack of studies concerning heat transfer from a stator. This lack of information was even more obvious for stators facing rotors featuring slots similar to those formed by the presence of magnets in an AFPM generator. Furthermore, the heat transfer coefficient on the surfaces of the machine components strongly depends on the specific geometrical shapes and dimensions. Therefore this study was carried out to provide information on the magnitude of the heat transfer coefficient from the rotor and the stator surfaces and the mass flow rate as a function of specific geometric and operational parameters, such as the magnet depth, the running clearance and the rotational speed. Initially a verification and a validation of the CFD model was carried out in Chapter 4. The verification highlighted that a mesh with at least 23 elements in the running clearance was necessary to obtain a mesh-independent solution.

A first validation was completed by measuring the air mass flow rate, the temperatures and the heat transfer coefficient from two test rigs: one featuring a flat rotor (*flat rotor rig*) and another carrying six segments representing the magnets (*magnet rig*). The air mass flow rate through the experimental system was also measured. The agreement between the quantities predicted by CFD modelling and those measured on the experimental rig was satisfactory. As a part of the validation process, an unsteady simulation of the magnet rig was run to ensure that the heat transfer coefficient on the stator was not affected by large transient effects of the flow. It was found that the pattern of the heat transfer coefficient on the stator was not changing with time and that the heat transfer coefficient did not change relative to the moving rotor. For this reason the system could be studied using steady simulations by considering the flow and heat transfer occurring at a single fixed instant.

A further validation was carried out on the large low-speed rig in chapter 5. The measured and calculated mass flow rate values were in a good agreement. The heat transfer coefficient however, due to the low rotational speed of the rig, was influenced by both forced and natural convection. Since in the CFD model the forced convection only was modelled, then the fraction of the measured heat transfer coefficient determined by the forced convection only was compared with the CFD results. The comparison of the forced convection contribution indicates the high accuracy and reliability of the CFD software and CFD models which can be used with strong confidence for predicting flow rates and heat transfer coefficients in rotating systems. The heat transfer coefficient was found to be independent of the heat flux specified on the surface, therefore in further simulations the solid components were not modelled and a reasonable value of the heat flux only has been specified on the surfaces where the heat transfer coefficient had to be calculated.

After the verification and validation processes were completed, an analysis of the effects that geometrical parameters have on the heat transfer coefficient, on the flow rate and on the torque was conducted, and the relevant results were presented in chapter 6. The investigation was conducted on a simplified generator in which the modelling of the boss and the region inside the boss had been omitted. The effects of the following parameters were investigated by means of a factorial design study: i) the running clearance, ii) the magnet depth, iii) the rotational speed. As a result of the factorial design study, it was found that:

- The effect of the rotational speed and of the magnet depth on the heat transfer coefficient in the considered range is positive: an increase of these factors would lead to an increase in the heat transfer coefficient.
- The effect of the running clearance was instead found to be negative: wider clearances lead to a lower heat transfer coefficient.
- The combined effect of the parameters on the target functions (the heat trans-

fer coefficient, the mass flow rate and the torque) were found to be weak, which indicated that the effect of the parameters could be studied independently.

With the data obtained from the factorial study first order response functions were derived which correlate the heat transfer coefficient on the stator, on the rotor, the mass flow rate and the torque to the values of the above three parameters.

A more detailed study in chapter 7 was conducted where one parameter at a time was varied. The main results from chapter 7 can be summarised as follows:

- By evaluating the heat transfer coefficient at a given radius a linear relationship between the heat transfer coefficient and the rotational speed was established. A linear relationship was also derived between the mass flow rate and the rotational speed. The correlations between the magnet depth and the heat transfer coefficient or between the clearance and the heat transfer coefficient were found to be nonlinear.

- The optimal combination of the magnet depth (8mm) and of the running clearance (1mm) was found to maximise the heat transfer coefficient on the stator. These two values correspond to the non-dimensional magnet depth $m^* = 7.3 \times 10^{-2}$ and to the non-dimensional clearance $c^* = 9 \times 10^{-3}$.

- The increased number of results from this numerical study allowed the derivation of a second order polynomial as a regression function between the target functions and the parameters. Correlations have been found between the non-dimensional target functions (Nusselt number on stator and rotor, non-dimensional mass flow rate and torque) and the non-dimensional parameters (non-dimensional clearance, magnet depth and peripheral Reynolds number).

The form of the correlation for the Nusselt number is described in Eq. 8.1.

$$\begin{aligned} Nu(r^*) &= b_0(r^*) + b_1(r^*)c^* + b_2(r^*)m^* + b_3(r^*)Re + b_4(r^*)c^{*2} + b_5(r^*)m^{*2} + \\ &\quad + b_6(r^*)Re^2 + b_7(r^*)c^*m^* + b_8(r^*)m^*Re + b_9(r^*)c^*Re \end{aligned} \tag{8.1}$$

A similar equation has been derived for each of the control volumes into which the running clearance has been divided. The coefficient relevant to each of these control volumes are listed in Table 8.1 and Table 8.2 for the stator and the rotor, respectively.

The correlation for the non-dimensional mass flow rate and for the non-dimensional torque are described in Eqs. 8.2 and8.3, respectively.

$$\begin{aligned} \dot{m}^* &= -4.445 \cdot 10^3 + 2.280 \cdot 10^5 c^* + 6.578 \cdot 10^4 m^* + 1.901 \cdot 10^{-2} Re + \\ &\quad -3.009 \cdot 10^6 c^{*2} - 2.250 \cdot 10^5 m^{*2} - 3.474 \cdot 10^{-9} Re^{*2} - 6.915 \cdot 10^5 c^* m^* + \\ &\quad +9.546 \cdot 10^{-1} m^* Re + 2.952 \cdot 10^{-1} c^* Re \end{aligned} \tag{8.2}$$

$$\begin{aligned} T^* &= 2.505 \cdot 10^8 - 5.846 \cdot 10^9 c^* - 4.060 \cdot 10^{10} m^* - 3.943 \cdot 10^{10} Re + \\ &\quad -7.632 \cdot 10^{11} c^{*2} - 5.817 \cdot 10^{10} m^{*2} - 2.974 \cdot 10^3 Re^2 + 3.609 \cdot 10^{11} c^* m^* + \\ &\quad +5.204 \cdot 10^5 m^* Re + 2.300 \cdot 10^5 c^* Re \end{aligned} \tag{8.3}$$

The above equations can be used in the designing process of AFPM machines for the calculations of the cooling effect of the air flow.

The original results obtained provide better understanding of the processes of heat transfer from the stator in rotating systems. The case of heat transfer from a stator facing a slotted rotor was thoroughly analysed and described and such was not previously investigated by other authors. The results obtained will contribute to the enhancement of heat transfer and consequently to the improvement of the overall performance of AFPM machines.

The correlations provided constitute a useful tool for the design of AFPM machines. In conjunction with the thermal Lumped parameter model, these correlations can be used for predicting the operational temperatures inside this type of generators in the design phase.

8.2 Further work

Further development of the models can be carried out in both CFD numerical and experimental studies.

8.2.1 Further CFD studies

Further studies could analyse the effect of other parameters (such as the number of magnets, and the ratio between the inner and the outer magnet radii) on the stator heat transfer coefficient, in addition to the parameters investigated in this study (running clearance, magnet depth, and rotational speed). The CFD correlations obtained above are valid for systems with six magnets, each having an angular

Table 8.1: Stator $Nu(r)$ correlation coefficients

	Non-dimensional Radius (r^*)									
	0.55	0.59	0.64	0.68	0.73	0.77	0.82	0.86	0.91	0.95
b_0	6.03E+01	9.09E+01	1.35E+02	1.90E+02	2.68E+02	3.92E+02	4.05E+02	3.99E+02	3.04E+02	2.59E+02
b_1	-5.02E+03	-4.55E+03	-6.67E+03	-1.01E+04	-1.47E+04	-2.13E+04	-1.64E+04	-1.42E+04	-1.24E+04	-1.50E+04
b_2	1.69E+03	1.37E+03	1.31E+03	1.28E+03	9.32E+02	-1.14E+02	-1.67E+03	-1.54E+03	4.02E+02	2.60E+03
b_3	1.11E-03	1.11E-03	1.13E-03	1.10E-03	1.03E-03	8.25E-04	7.74E-04	7.81E-04	1.27E-03	1.68E-03
b_4	9.11E+04	6.78E+04	9.09E+04	1.48E+05	2.28E+05	3.24E+05	2.14E+05	1.63E+05	1.55E+05	1.93E+05
b_5	-6.45E+03	-5.66E+03	-5.90E+03	-5.94E+03	-4.68E+03	-1.53E+03	7.69E+03	7.33E+03	-3.22E+03	-1.31E+04
b_6	-3.41E-10	-2.31E-10	-7.57E-10	4.40E-11	3.65E-11	4.38E-10	4.36E-11	7.89E-12	9.54E-11	5.34E-12
b_7	-1.14E+04	-6.03E+03	-2.29E+03	-3.14E+03	-5.80E+03	2.53E+03	9.78E+03	1.57E+04	1.34E+04	7.96E+03
b_8	1.81E-03	1.25E-03	7.12E-04	6.54E-04	1.10E-03	2.24E-03	8.39E-04	1.92E-04	1.86E-03	1.56E-03
b_9	-1.41E-02	-1.48E-02	-1.51E-02	-1.60E-02	-1.67E-02	-1.31E-02	-9.42E-03	-8.12E-03	-1.78E-02	-1.65E-02

Table 8.2: Rotor *Nu(r)* correlation coefficients

	Non-dimensional Radius (r^*)									
	0.55	0.59	0.64	0.68	0.73	0.77	0.82	0.86	0.91	0.95
b_0	9.80E+01	1.25E+02	1.55E+02	1.83E+02	2.23E+02	2.48E+02	2.10E+02	2.09E+02	2.85E+02	3.45E+02
b_1	-4.44E+03	-5.10E+03	-5.85E+03	-6.74E+03	-8.19E+03	-8.45E+03	-6.82E+03	-7.62E+03	-1.03E+04	-1.04E+04
b_2	1.29E+03	8.98E+02	5.28E+02	2.59E+02	-1.01E+02	-4.06E+02	3.22E+02	6.60E+02	-1.34E+02	-1.43E+03
b_3	1.38E-03	1.33E-03	1.33E-03	1.35E-03	1.31E-03	1.32E-03	1.59E-03	1.78E-03	1.65E-03	1.55E-03
b_4	7.73E+04	8.22E+04	9.21E+04	1.05E+05	1.22E+05	1.17E+05	1.11E+05	1.38E+05	1.68E+05	1.60E+05
b_5	-5.81E+03	-4.39E+03	-2.94E+03	-2.16E+03	-1.50E+03	-7.87E+02	-3.29E+03	-5.88E+03	-2.62E+03	5.98E+03
b_6	5.68E-11	3.52E-11	1.50E-10	4.25E-12	6.62E-11	3.42E-12	9.32E-11	9.22E-12	2.33E-11	1.33E-12
b_7	-6.54E+03	-3.07E+03	-1.25E+03	8.01E+02	6.06E+03	1.18E+04	1.37E+03	1.18E+03	9.67E+03	6.23E+03
b_8	1.56E-03	1.16E-03	8.27E-04	8.34E-04	1.34E-03	1.77E-03	5.07E-04	3.11E-04	-1.65E-04	-9.16E-04
b_9	-8.96E-03	-7.33E-03	-6.41E-03	-5.19E-03	-2.37E-03	6.29E-05	-5.67E-03	-9.07E-03	-3.28E-03	5.07E-04

dimension of 45°. The effect of having a greater number of magnets with a smaller angular size could be analysed. An optimisation study to find the combination of the parameters which gives the highest heat transfer coefficient on the stator could be carried out and managed with the tools available in Matlab. The first mesh of the generator would have to be created in Gambit and a first simulation run in Fluent, then two approaches could be followed. The first would involve re-modelling the domain with different values of the geometrical parameters, then re-meshing the geometry by modifying the Gambit journal file, the new mesh obtained would be read into Fluent and new analysis run. This process would be run iteratively until the optimum value of the monitored quantity would be reached. As a monitor quantity the average heat transfer coefficient on the stator per unit of area should be used. The second approach would not involve any re-meshing of the domain. Instead a dynamic mesh should be used. From the results obtained from the first Fluent simulation the geometry would be modified by changing the dynamic mesh parameters. This operation would still be managed by Matlab. The process would be run iteratively as in the previous case until an optimum average heat transfer coefficient on the stator surface is reached.

8.2.2 Further experimental work

Two possible levels of improvement have been identified for the low-speed large-scale test rig.

The first level does not involve any modification to the rig. A higher number of heat flux sensors could be used so that the heat transfer coefficient can be evaluated at more locations along the radial coordinate and the pattern found with the CFD software can be confirmed with a higher number of points. Furthermore, a Particle Image Velocimetry experiment can be carried out in order to visualise the flow patterns and the flow velocity components inside the test rig which could be then compared to the predicted numerical flow patterns.

A second level of improvement for the test rig would involve a modification of the stator. In order to overcome the challenge of measuring the heat flux from the stator surfaces a stator made of Printed Circuit Boards (PCBs) as described in [70] for a rotor-stator system could be built. The heat flux could then be determined by dividing the power supplied to the tracks on the PCB by their surface exposed to the air flow.

Bibliography

[1] F. Villatico and F. Zuccari. Efficiency comparison between FC and ICE in real urban driving cycles. *International Journal of Hydrogen Energy*, 33(12):3235 – 3242, 2008. 2nd World Congress of Young Scientists on Hydrogen Energy Systems.

[2] Per Roger Johansen, Dean Patterson, Christopher O'Keefe, and John Swenson. The use of an axial flux permanent magnet in-wheel direct drive in an electric bicycle. *Renewable Energy*, 22(1-3):151 – 157, 2001.

[3] F. Feudale, A. Odorico, M. Sica, F. Caricchi, F. Giulii Capponi, and F. Crescimbini. Multi-stage axial-flux pm machine for direct-drive railway traction applications. *SPRTS Ship Propulsion and Railway Traction Systems Conference*, pages 307 – 312, 2005.

[4] Hynek Raisigel, Orphe Cugat, and Jrme Delamare. Permanent magnet planar micro-generators. *Sensors and Actuators A: Physical*, 130-131:438 – 444, 2006. Selected Papers from TRANSDUCERS '05 - The 13th International Conference on Solid-State Sensors, Actuators and Microsystems - Seoul, Korea, 5-9 June 2005.

[5] Florian Herrault, David P. Arnold, Iulica Zana, Preston Galle, and Mark G. Allen. High temperature operation of multi-watt, axial-flux, permanent-magnet microgenerators. *Sensors and Actuators A: Physical*, 148(1):299 – 305, 2008.

[6] B.J. Chalmers and E. Spooner. An axial-flux permanent-magnet generator for a gearless wind energy system. *Energy Conversion, IEEE Transactions on*, 14(2):251–257, Jun 1999.

[7] Bjrn Bolund, Hans Bernhoff, and Mats Leijon. Flywheel energy and power storage systems. *Renewable and Sustainable Energy Reviews*, 11(2):235 – 258, 2007.

[8] F. Caricchi, F. Crescimbini, and O. Honorati. Low-cost compact permanent magnet machine for adjustable-speed pump application. *Industry Applications, IEEE Transactions on*, 34(1):109–116, Jan/Feb 1998.

[9] Maarten J. Kamper Jacek F. Gieras, Rong-Jie Wang. *Axial Flux Permanent Magnet Brushless Machines.* Springer Netherlands, 2008.

[10] M. Aydin, S. Huang, and T.A. Lipo. Axial flux permanent magnet disc machines: A review. *Research report. Unievrsity of Wisconsin-Madison. College of Engineering. Wisconsin Power Electronics Research Center*, 2004.

[11] E. Spooner and B.J. Chalmers. 'TORUS': a slotless, toroidal-stator, permanent-magnet generator. *Electric Power Applications, IEE Proceedings B*, 139(6):497–506, Nov 1992.

[12] J.R. Bumby, R. Martin, M.A. Mueller, E. Spooner, N.L. Brown, and B.J. Chalmers. Electromagnetic design of axial-flux permanent magnet machines. *Electric Power Applications, IEE Proceedings* -, 151(2):151–160, Mar 2004.

[13] Cheng-Tsung Liu, Shih-Chao Lin, and Tsung-Shiun Chiang. On the analytical flux distribution modeling of an axial-flux surface-mounted permanent magnet motor for control applications. *Journal of Magnetism and Magnetic Materials*, 282:346 – 350, 2004. International Symposium on Advanced Magnetic Technologies.

[14] Cheng-Tsung Liu and Shih-Chia Lee. Magnetic field modeling and optimal operational control of a single-side axial-flux permanent magnet motor with center poles. *Journal of Magnetism and Magnetic Materials*, 304(1):e454 – e456, 2006. International Symposium on Spintronics and Advanced Magnetic Technologies and International Symposium on Magnetic Materials and Applications 2005.

[15] F. Caricchi, B.J. Chalmers, F. Crescimbini, and E. Spooner. Advances in the design of TORUS machines. In *Power Electronic Drives and Energy Systems for Industrial Growth, 1998. Proceedings. 1998 International Conference on*, volume 2, pages 516–522, Dec. 1998.

[16] B. J. Chalmers. Developments in electrical machines using permanent magnets. *Journal of Magnetism and Magnetic Materials*, 157-158:131 – 132, 1996. European Magnetic Materials and Applications Conference.

[17] H. K. Versteeg and W. Malalasekera. *An Introduction to Computational Fluid Dynamics. The Finite Volume Method.* Pearson Education Limited, 2007.

[18] B. E. Launder and D. B. Spalding. The numerical computation of turbulent flows. *Computer Methods in Applied Mechanics and Engineering*, 3(2):269 – 289, 1974.

[19] Tsan-Hsing Shih, William W. Liou, Aamir Shabbir, Zhigang Yang, and Jiang Zhu. A new $\kappa - \epsilon$ eddy viscosity model for high Reynolds number turbulent flows. *Computers & Fluids*, 24(3):227 – 238, 1995.

[20] Fluent 6.3.26. *User's guide.* 2005.

[21] J. Blazek. *Computational Fluid Dynamics: Principles and Applications.* Elsivier Science Ltd, 2001.

[22] M. Wolfshtein. The velocity and temperature distribution in one-dimensional flow with turbulence augmentation and pressure gradient. *International Journal of Heat and Mass Transfer*, 12(3):301 – 318, 1969.

[23] W. Rodi. Comparison of LES and RANS calculations of the flow around bluff bodies. *Journal of Wind Engineering and Industrial Aerodynamics*, 69-71:55 – 75, 1997. Proceedings of the 3rd International Colloqium on Bluff Body Aerodynamics and Applications.

[24] J. Abanto, D. Pelletier, A. Garon, J.-Y. Trepanier, and M. Reggio. Verification of some Commercial CFD Codes on Atypical CFD Problems. *43rd AIAAA Aerospace Sciences Meeting and Exibit, Reno*, 2005.

[25] David Lacasse, Éric Turgeon, and Dominique Pelletier. On the judicious use of the $\kappa - \epsilon$ model, wall functions and adaptivity. *International Journal of Thermal Sciences*, 43(10):925 – 938, 2004.

[26] American Institute of Aeronautics and Astronautics. *Guide for Verification and Validation of Computational Fluid Dynamics Simulation. Technical Report AIAA-G-077-1998.* IHS, January 1998.

[27] W. L. Oberkampf and T.G. Trucano. *Verification and Validation in Computational Fluid Dynamics*, volume 38. Elsevier, April 2002.

[28] J. Bellettre, V. Sartre, F. Biais, and A. Lallemand. Transient state study of electric motor heating and phase change solid-liquid cooling. *Applied Thermal Engineering*, 17(1):17 – 31, 1997.

[29] Hossein Rouhani, Jawad Faiz, and Caro Lucas. Lumped thermal model for switched reluctance motor applied to mechanical design optimization. *Mathematical and Computer Modelling*, 45(5-6):625 – 638, 2007.

[30] W. Wu, V. S. Ramsden, T. Crawford, and G. Hill. A low-speed high-torque, direct-drive permanent magnet generator for wind turbines. In *Industry Applications Conference*, volume 1, pages 147–154, 2000.

[31] J.R. Bumby and R. Martin. Axial-flux permanent-magnet air-cored generator for small-scale wind turbines. *IEE PROCEEDINGS-ELECTRIC POWER APPLICATIONS*, 152(5):1065–1075, SEP 2005.

[32] P.H. Mellor, D. Roberts, and D. R. Turner. Lumped parameter thermal model for electrical machines of TEFC design. *Electric Power Applications, IEE Procedings B*, 138(5):205 – 218, 1991.

[33] A.M. EL-Refaie, N.C. Harris, T.M. Jahns, and K.M. Rahman. Thermal analysis of multibarrier interior pm synchronous machine using lumped parameter model. *Energy Conversion, IEEE Transactions on*, 19(2):303–309, June 2004.

[34] S. C. Mukhopadhyay and S. K. Pal. Temperature analysis of induction motors using a hybrid thermal model with distributed heat sources. *Journal of applied physics*, 83:6368–6370, 1998.

[35] Rong-Jie Wang, Maarten J. Kamper, and Robert T. Dobson. Development of a thermofluid model for axial field permanent-magnet machines. *IEEE transactions on energy conversion*, 20(1):80 – 87, 2005.

[36] S. T. Scowby, R. T. Dobson, and M. J. Kamper. Thermal modelling of an axial flux permanent magnet machine. *Applied Thermal Engineering*, 24(2-3):193 – 207, 2004.

[37] E. Belicová and V. Hrabovcová. Analysis of an axial flux permanent magnet machine (AFPM) based on coupling of two separated simulation models (electrical and thermal ones). *Journal of Electrical Engineering*, 58(1):3 –9, 2007.

[38] K. Farsane, P. Desevaux, and P. K. Panday. Experimental study of the cooling of a closed type electric motor. *Applied Thermal Engineering*, 20(14):1321 – 1334, 2000.

[39] Ying Huai, Roderick V. N. Melnik, and Paul B. Thogersen. Computational analysis of temperature rise phenomena in electric induction motors. *Applied Thermal Engineering*, 23(7):779 – 795, 2003.

[40] Hongmin Li. Flow driven by a stamped metal cooling fan - numerical model and validation. *Experimental Thermal and Fluid Science*, 33(4):683 – 694, 2009.

[41] Min-Soo Kim, Kwan-Soo Lee, and Sukkee Um. Numerical investigation and optimization of the thermal performance of a brushless dc motor. *International Journal of Heat and Mass Transfer*, 52(5-6):1589 – 1599, 2009.

[42] Hongmin Li. Cooling of a permanent magnet electric motor with a centrifugal impeller. *International Journal of Heat and Mass Transfer*, 53(4):797 – 810, 2010.

[43] Zlatko Kolondzovski, Anouar Belahcen, and Antero Arkkio. Multiphysics thermal design of a high-speed permanent-magnet machine. *Applied Thermal Engineering*, 29(13):2693 – 2700, 2009.

[44] Cheng-Hung Huang and Hung-Chi Lo. A three-dimensional inverse problem in estimating the internal heat flux of housing for high speed motors. *Applied Thermal Engineering*, 26(14-15):1515 – 1529, 2006.

[45] Ryuichi Ujiie, Raphael Arlitt, and Hirofumi Etoh. Application of Computational Fluid Dynamics (CFD) on Ventilation-Cooling Optimization of Electrical Machines. In *Proc. International Electric Machines and Drive Conference IEMDC*, 2003.

[46] Madiha Bouafia, Abdenacer Ziouchi, Yves Bertin, and Jean-Bernard Saulnier. Étude expérimentale et numérique des transferts de chaleur en espace annulaire sans débit axial et avec cylindre intérieur tournant. Experimental and numerical

study of heat transfer in an annular gap without axial flow with a rotating inner cylinder. *International Journal of Thermal Sciences*, 38(7):547 – 559, 1999.

[47] Marko Tirovic. Energy thrift and improved performance achieved through novel railway brake discs. *Applied Energy*, 86(3):317 – 324, 2009.

[48] J. M. Owen and R. H. Rogers. *Flow and Heat Transfer in Rotating-Disc Systems*, volume 1 - Rotor-Stator systems. Research Studies Press Ltd., 1989.

[49] G. K. Batchelor. Note on a class of solutions of the Navier-Stokes equations representing steady rotationally-symmetric flow. *Q J Mechanics Appl Math*, 4(1):29–41, 1951.

[50] K. Stewartson. On the flow between two rotating coaxial disks. *Mathematical Proceedings of the Cambridge Philosophical Society*, 49(02):333–341, 1953.

[51] K. G. Picha and E. R. G. Eckert. Study of the air flow between coaxial discs rotating with arbitrary velocities in an open or enclosed space. In *Proc. 3rd U.S. Nat. Cong. Appl. Mech.*, pages 791–798, 1958.

[52] John F. Brady and Louis Durlofsky. On rotating disk flow. *Journal of Fluid Mechanics Digital Archive*, 175(-1):363–394, 1987.

[53] J. W. Daily and R. E. Nece. Chamber dimension effects on induced flow and frictional resistance of enclosed rotating disks. *Transactions of the ASME. Series D, Journal of Basic Engineering*, 82:217 – 232, 1960.

[54] R. Debuchy, S. Della Gatta, E. D'Haudt, G. Bois, and F. Martelli. Influence of external geometrical modifications on the flow behaviour of a rotor-stator sys-

tem: numerical and experimental investigation. *Proceedings of the Institution of Mechanical Engineers, Part A: Journal of Power and Energy*, 221:857–863, Jan 2007.

[55] Marc Djaoui, Arthur Dyment, and Roger Debuchy. Heat transfer in a rotor-stator system with a radial inflow. *European Journal of Mechanics - B/Fluids*, 20(3):371 – 398, 2001.

[56] Sebastien Poncet, Marie-Pierre Chauve, and Roland Schiestel. Batchelor versus Stewartson flow structures in a rotor-stator cavity with throughflow. *Physics of fluids*, 17, 2005.

[57] S. Poncet and R. Schiestel. Numerical modeling of heat transfer and fluid flow in rotor-stator cavities with throughflow. *International Journal of Heat and Mass Transfer*, 50(7-8):1528 – 1544, 2007.

[58] E.M. Sparrow and J.L. Goldstein. Effect of rotation and coolant throughflow on the heat transfer and temperature field in an enclosure. *J. Heat Transfer*, 98:387 – 394, 1976.

[59] Julien Pellé and Souad Harmand. Heat transfer measurements in an opened rotor-stator system air-gap. *Experimental Thermal and Fluid Science*, 31(3):165 – 180, 2007.

[60] S. Raguenet and E. Laroche. Une méthode caractérisant l'influence réciproque entre parois: application aux échanges thermiques dans une cavité rotor-stator. A method characterising the respective influence of the heated walls: applica-

tion to the heat transfer in a rotor-stator cavity. *International Journal of Heat and Mass Transfer*, 43(24):4433 – 4445, 2000.

[61] R. P. Roy, G. Xu, and J. Feng. A study of convective heat transfer in a model rotor-stator disk cavity. *J. Turbomach.*, 123(3):621 – 632, 2001.

[62] Rachid Boutarfa and Souad Harmand. Local convective heat exchanges and flow structure in a rotor-stator system. *International Journal of Thermal Sciences*, 42(12):1129 – 1143, 2003.

[63] Julien Pellé and Souad Harmand. Heat transfer study in a rotor-stator system air-gap with an axial inflow. *Applied Thermal Engineering*, 29(8-9):1532 – 1543, 2009.

[64] Souad Harmand, Barbara Watel, and Bernard Desmet. Local convective heat exchanges from a rotor facing a stator. *International Journal of Thermal Sciences*, 39(3):404 – 413, 2000.

[65] H. Iacovides and J. W. Chew. The computation of convective heat transfer in rotating cavities. *International Journal of Heat and Fluid Flow*, 14(2):146 – 154, 1993.

[66] Z. X. Yuan, N. Saniei, and X. T. Yan. Turbulent heat transfer on the stationary disk in a rotor-stator system. *International Journal of Heat and Mass Transfer*, 46(12):2207 – 2218, 2003.

[67] Roger W. Hill and Kenneth S. Ball. Direct numerical simulations of turbulent forced convection between counter-rotating disks. *International Journal of Heat and Fluid Flow*, 20(3):208 – 221, 1999.

[68] G. Airoldi, G.L. Ingram, K. Mahkamov, J.R. Bumby, R.G. Dominy, N.L. Brown, A. Mebarki, and M. Shanel. Computations on heat transfer in axial flux permanent magnet machines. In *Electrical Machines, 2008. ICEM 2008. 18th International Conference on*, pages 1–6, Sept. 2008.

[69] T. Astarita and G. Cardone. Convective heat transfer on a rotating disk with a centred impinging round jet. *International Journal of Heat and Mass Transfer*, 51(7-8):1562 – 1572, 2008.

[70] D.A. Howey, A.S. Holmes, and K.R. Pullen. Radially resolved measurement of stator heat transfer in a rotor-stator disc system. *International Journal of Heat and Mass Transfer*, 53(1-3):491 – 501, 2010.

[71] ESDU07004. *Flow in rotating components. Discs, cylinders and cavities. Engineering Sciences Data Unit.* IHS, August 2007.

[72] J. M. Owen, C. M. Haynes, and F. J. Bayley. Heat Transfer from an Air-Cooled Rotating Disk. *Proceedings of the Royal Society of London. A. Mathematical and Physical Sciences*, 336(1607):453–473, 1974.

[73] G. Airoldi, G.L. Ingram, C. H. Lim, K. Mahkamov, J.R. Bumby, R.G. Dominy, N.L. Brown, A. Mebarki, and M. Shanel. Air flow and heat transfer modeling of an axial flux permanent magnet generator. In *CESSE 2009: International Conference on Computer, Electrical, and Systems Science, and Engineering*, October 2009.

[74] F. A. Watson F. A. Holland, R. M. Moores and J. K. Wilkinson. *Heat Transfer.* Helmann Educational Books Ltd, 1970.

[75] D. P. DeWitt T. L. Bergman F. P. Incropera and A. S. Lavine. *Fundamentals of Heat and Mass Transfer.* John Wiley & Sons, 2007.

[76] S. W. Churchill. A comprehensive correlating equation for laminar, assisting, forced and free convection. *AIChe J.*, 10:10–16, 1977.

[77] S. W. Churchill. Combined free and forced convection around immersed bodies. *Heat exchanger Design handbook*, section 2.5.9:–, 2002.

[78] S. W. Churchill. Combined free and forced convection around immersed bodies. *Heat exchanger Design handbook*, section 2.5.10:–, 2002.

[79] Douglas C. Montgomery and Raymond H. Myers. *Response surface methodology, Process and product optimization using designed experiments.* Wiley-Interscience, 2002.

[80] A. Benabou, S. Georges, and S. Clnet. Permanent magnet modelling for dynamic applications. *Journal of Magnetism and Magnetic Materials*, 320(6):830 – 835, 2008.